Onboard Quantization for Interferometric and Multichannel Synthetic Aperture Radar (SAR) Systems

Zur Erlangung des akademischen Grades eines

DOKTOR-INGENIEURS

von der KIT-Fakultät für
Elektrotechnik und Informationstechnik
des Karlsruher Instituts für Technologie (KIT)

genehmigte

DISSERTATION

von

Michele Martone, M.Sc.
geb. in Neapel, Italien

Tag der mündlichen Prüfung:	15. 11. 2019
Hauptreferent:	Prof. Dr.-Ing. habil. Alberto Moreira
Korreferent:	Prof. Dr. Antonio Iodice

Zusammenfassung

Quantisierung ist der Prozess der Abbildung eines Eingangssignals einer großen Menge meist kontinuierlicher Werte in eine kleinere Menge mit einem endlichen Bereich von diskreten Werten. Quantisierung stellt eine wichtige Operation für praktisch alle Anwendungen im Bereich der digitalen Signalverarbeitung dar, beispielsweise in den Bereichen Audio-, Bild- und Videoproduktion. Dies schließt die Verarbeitung von Fernerkundungsdaten ein, bei der Daten aus einer analogen Quelle in ein numerisches Format umgewandelt werden, um anschließend übertragen, weiterverarbeitet und analysiert werden zu können.

Die vorliegende Arbeit konzentriert sich auf die bordseitige, interne Quantisierung für Radarinstrumente mit synthetischer Apertur (SAR). SAR-Systeme ermöglichen wetter- und tageszeitunabhängige, hochauflösende Aufnahmen und sind daher sehr gefragt für viele wissenschaftliche und kommerzielle Anwendungen der Erd- (oder planetaren) Beobachtung. Allerdings nimmt das bordseitig benötigte Datenvolumen von gegenwärtig geplanten und zukünftigen satellitengestützten SAR-Missionen immer mehr zu, da in modernen Systemen größere Bandbreiten und Mehrfachkanäle zum Einsatz kommen, und außerdem die Abbildung größerer Streifenbreiten bei feinerer räumlicher Auflösung angestrebt wird. Dies impliziert höhere Anforderungen an Bordspeicher und Übertragungskapazitäten, deren begrenzte Ressourcen oft einen Engpass bei der Planung von SAR-Missionen darstellen. In diesem Zusammenhang ist eine geeignete Digitalisierung der vom SAR-Sensor erfassten Rohdaten von großer Bedeutung: die verwendete Anzahl von Bits beeinflusst zum einen die Qualität der resultierenden SAR-Produkte, definiert aber auch andererseits die Menge des gesamten Datenvolumens, das vom System erzeugt wird.

In dieser Dissertation wurde der Einfluss der Quantisierung auf die SAR Leistung und die interferometrische (InSAR) Qualität untersucht. Dafür wurden experimentelle Daten der X-Band SAR-Mission TanDEM-X des Deutschen Zentrums für Luft- und Raumfahrt (DLR) genutzt, die mit unterschiedlichen Systemparametern und SAR-Szeneeigenschaften aufgenommen wurden. Darüber hinaus wurde eine neuartige Quantisierungsmethode vorgestellt, die "qualitätsoptimierte blockadaptive Quantisierung" (Performance-Optimized Block-Adaptive Quantization, PO-BAQ). Diese ermöglicht eine gemeinsame Optimierung der Datenrate und gleichzeitig der interferometrischen Qualität unter Nutzung des a priori Wissens über die Stärke der SAR-Rückstreuung. Ferner wurde eine neuartige SAR-Datenkompressionstechnik entwickelt, die eine effiziente Umsetzung von nicht-ganzzahligen Quantisierungsraten ermöglicht. Die Machbarkeit der vorgeschlagenen "Azimuth-Switched Quantization" (ASQ), die eine höhere Flexibilität in Bezug auf erzielbare Leistung und Ressourcenallokation ermöglicht, wurde anhand von experimentellen TanDEM-X Daten erfolgreich demonstriert.

Der zweite Teil der Dissertation konzentriert sich auf die Entwicklung von innovativen

bordseitigen Datenreduktionsverfahren für zukünftige SAR-Systeme. Insbesondere wurde ein SAR-System untersucht, das mehrere Empfangsaperturen in Längsrichtung nutzt, und so eine hochauflösende Abbildung eines breiten Streifens zulässt, allerdings auf Kosten einer beträchtlichen Erhöhung der Datenmenge. In diesem Kontext wurde eine geeignete Strategie zur Datenreduktion entwickelt, die "mehrkanalige blockadaptive Quantisierung" (Multi-Channel Block-Adaptive Quantization, MC-BAQ). Diese Methode nutzt die bestehende Korrelation zwischen aufeinanderfolgenden Azimut-Samples durch das Ausführen einer diskreten Fourier-Transformation des mehrkanaligen SAR-Datenblocks. Anschließend wird eine Quantisierung mit variabler Bitrate angewendet, was die Optimierung der resultierenden Bildqualität und Datenrate ermöglicht. Schließlich wurde der Einsatz von linearer prädiktiver Kodierung zur bordseitigen Datenreduktion von sogenannten "staggered" SAR-Systemen untersucht. Staggered SAR ist ein innovativer SAR-Aufnahmemodus, der einen breiten Streifen mit hoher Auflösung abbilden kann. Dieser Modus wird realisiert durch eine kontinuierliche Variation des Impulsfolgeintervalls und erfordert eine erhebliche Überabtastung in Azimut-Richtung. Die vorgeschlagene dynamische prädiktive blockadaptive Quantisierung (Dynamic Predictive Block-Adaptive Quantization, DP-BAQ) nutzt die Redundanz im ungleichmäßig abgetasteten Azimut-Rohdatenstrom und ermöglicht eine deutliche Reduzierung des zu übertragenden Datenvolumens zum Boden auf Kosten einer geringfügigen Erhöhung des bordseitigen rechnergestützten Aufwands.

Abstract

Quantization is the process of mapping an input signal from a large set of often continuous values into a smaller one with a finite range of discrete values. Quantization represents a crucial operation for practically all applications in the field of digital signal processing, ranging from audio, image, and video production, including the elaboration of remote sensing data, which are converted from an analog source into a numerical format, in order to be properly transferred and further processed and analyzed.

This work focuses on onboard quantization for synthetic aperture radar (SAR) systems. SAR systems allow for all-weather, day-night high-resolution imaging and are therefore very attractive for a large set of scientific and commercial applications related to Earth (or planetary) observation. For present and next-generation spaceborne SAR missions, an increasing volume of onboard data is going to be required, due to the employment of large bandwidths, multiple channels, and the imaging of large swath widths at fine spatial resolutions. This implies strong requirements in terms of onboard memory and downlink capacity, which are limited resources and often represent a bottleneck in the design of SAR missions. In this context, the proper digitization of the raw data acquired by the SAR sensor represents an aspect of utmost importance, since the number of bits employed to digitize the recorded radar signal, on the one hand, directly affects the performance of the resulting SAR products and, on the other hand, defines the total volume of data to be managed by the system.

In this dissertation, the impact of quantization on SAR and interferometric (InSAR) performance has been investigated using experimental data acquired by the X-band SAR mission TanDEM-X of the German Aerospace Center (DLR) for different system parameters and SAR scene characteristics. Furthermore, a novel quantization method, named performance optimized block-adaptive quantization (PO-BAQ), has been introduced. It allows for a joint optimization of the data rate and, at the same time, of the interferometric performance, by exploiting a priori knowledge about the SAR backscatter information. Furthermore, a novel SAR data compression technique has been developed, which allows for the efficient implementation of non-integer quantization rates. The proposed azimuth-switched quantization (ASQ) has been successfully demonstrated on TanDEM-X data and grants higher flexibility in terms of performance and resource allocation.

In the second part of the thesis, the attention has been focused on the definition of innovative onboard data reduction methods for next-generation SAR systems. In particular, a SAR system exploiting multiple receiving apertures in along-track direction allows for high-resolution imaging of a wide swath, at the cost of the acquisition of a considerable amount of data. In this context, a convenient data reduction strategy has been proposed, named multi-channel block-adaptive quantization (MC-BAQ), which exploits the existing correlation between adjacent azimuth samples by performing a discrete Fourier transform of the multi-channel SAR data block. Then, a variable-bit quantization is applied,

allowing for the optimization of the resulting image quality and data rate.
Finally, the use of linear predictive coding has been investigated for onboard data reduction in staggered SAR systems. Staggered SAR is an innovative high-resolution wide-swath SAR acquisition mode which exploits a continuous variation of the pulse repetition interval and requires, for its operation, a significant azimuth oversampling. The proposed dynamic predictive block-adaptive quantization (DP-BAQ) exploits the redundancy exhibited by the non-uniform azimuth raw data stream and allows for a considerable reduction of the data volume to be transmitted to the ground at the cost of a modest increase of onboard computational effort.

List of Constants

c_0	speed of light in free space	$2.99792458 \cdot 10^8$ m/s
e	Euler's number	2.71828
k_B	Boltzmann constant	$1.38064852 \cdot 10^{-23}$ J/K
π	ratio of a circle's circumference to its diameter	3.14159265

List of Mathematical Operators, Notations, Functions

$\lvert\cdot\rvert$	absolute value
$\angle\cdot$	phase operator
*	complex conjugate of a scalar or vector
$\lfloor\cdot\rfloor$	floor function
$\lceil\cdot\rceil$	ceiling function
$\langle\cdot\rangle$	arithmetic mean
$\in$	set membership
$\cos(\cdot)$	cosine function
$\exp(\cdot)$	natural exponential function
$\log_2(\cdot)$	the logarithm of base 2
$\max(\cdot)$	maximum function
$\min(\cdot)$	minimum function
$\mathrm{rect}[(t-t_0)/T)]$	rectangular window centered in t_0 of width T
$\mathrm{sign}(\cdot)$	sign function
$\sin(\cdot)$	sine function
$\mathrm{sinc}(\cdot)$	cardinal sine function ($\mathrm{sinc}(x)$=$\sin(\pi x)/(\pi x)$)
$\sum$	sum
$\int$	integral and antiderivative
$\mathbb{E}[\cdot]$	expectation operator
$\mathcal{F}$	Fourier transform
F	hypergeometric function
j	imaginary unit ($j=\sqrt{-1}$)
$\mathbb{R}^n$	real coordinate space of n dimensions
Γ	gamma function

$*$		convolution operator

List of Latin Symbols

	Unit	
A		attenuation factor of the received radar pulse
A_i		area under the input pdf within the i-th decision interval
A_q		scaling factor modeling the quantization process
A_{SAR}	m^2	area on ground where raw data responses of the scatterers under illumination overlap with each other
A_σ	m^2	ground area for backscatter normalization
$a(t)$	m	in the context of azimuth focusing, azimuth coordinate of a point target as function of time
B	m	total interferometric baseline
$B_\perp$	m	across-track baseline
B_{D}	Hz	processed Doppler bandwidth
B_R	Hz	bandwidth of the spectral power density function
B_{rg}	Hz	range (chirp) bandwidth
C		bit rate-dependent constant employed in the BAQ algorithm
$\boldsymbol{C}$		covariance matrix of the random process $x[\mathrm{n}]$
$C[i, j]$		correlation between two samples at discrete time instants i and j
c_{v}		coefficient of variation
DR	bits/s	data rate
d	m	in the context of low scatterer errors, total distance between targets
d_{az}	m	in the context of low scatterer errors, azimuth distance between targets
d_i		i-th decision level of the quantizer
$d_{\mathrm{opt},i}$		i-th optimum decision level of the Max-Lloyd quantizer
d_{rg}	m	in the context of low scatterer errors, range distance between targets
d_{step}	m	step length for each PO-BAQ iteration

E		exponent value used in the BAQ algorithm
E_1		BAQ exponent value estimated from the data block
E_{ML}		energy integrated in the mainlobe
$E_{\mathrm{SL},i}$		energy integrated in the i-th sidelobe
$E_{\max}$		maximum exponent value (bit rate-dependent) used in the BAQ algorithm
$\boldsymbol{F}$		discrete Fourier transformation matrix
F_{N}		noise figure
f	Hz	frequency
f_{c}	Hz	radar carrier frequency
$f_{\mathrm{D}}(t)$	Hz	Doppler frequency shift as function of time
$f_{\mathrm{i}}(t)$	Hz	instantaneous chirp frequency as function of time
f_{inf}		relative frequency with which the rate $N_{\mathrm{b,inf}}$ occurs to synthesize a given fractional rate N_{bfrac}
f_{q}		input/output relation of the quantizer
f_{s}	Hz	sampling frequency
G		two-dimensional antenna pattern
$G_{N_{\mathrm{P}}}$		prediction gain resulting from a $N_{\mathrm{P}}^{\mathrm{th}}$-order predictor
G_p^t		p-polarized antenna pattern in transmission
G_p^r		p-polarized antenna pattern in reception
$h(t)$		matched filter as function of time
h_{amb}	m	height of ambiguity
h_{s}	m	satellite orbit height
h_{v}	m	height of the scattering volume
$I(R,a)$		impulse response function as function of the slant range and azimuth coordinate
I_1		master image
I_2		slave image
I_{adc}		in-phase component of the signal at the ADC output
I_{baq}		in-phase component of the BAQ-decoded signal
I_{ML}		peak intensity of the mainlobe
$I_{\mathrm{SL,max}}$		peak intensity of the first sidelobe
$\bar{I}$		signal in-phase component at the ADC output
K		number of DFT coefficients

$K_{\mathrm{I,adc},i}$		i-th bit representing the in-phase component of the signal at the ADC output
$K_{\mathrm{I,baq},i}$		i-th bit representing the in-phase component of the signal at the BAQ output
$K_{\mathrm{Q,adc},i}$		i-th bit representing the quadrature component of the signal at the ADC output
$K_{\mathrm{Q,baq},i}$		i-th bit representing the quadrature component of the signal at the BAQ output
k_{D}	Hz/s	Doppler rate
k_{r}	Hz/s	chirp rate
L_{a}	m	antenna size in azimuth
L_{chirp}	m	chirp slant range extension
L_{e}	m	antenna size in elevation
L_P		length of sequence of coefficients y_k to estimate the power contribution P_k
L_{s}	m	antenna footprint extension in azimuth
L_{seq}	m	extension of the azimuth sequence of length N_{seq}
L_{tot}		total losses
l	m	separation between two azimuth sub-apertures of a multi-channel SAR in azimuth
M_{baq}		mantissa of the signal at the BAQ output
M_{I}		mantissa of the in-phase component of the signal at the BAQ output
M_{max}		maximum mantissa value (bit rate-dependent) used in the BAQ algorithm
M_{Q}		mantissa of the quadrature component of the signal at the BAQ output
N_{acq}		number of available interferometric acquisitions
N_{ch}		number of channels of a SAR system
N_{b}	bits/sample	number of bits for quantization
$\bar{N}_{\mathrm{b}}$	bits/sample	mean bit rate
$N_{\mathrm{b,ASQ}}$	bits/sample	ASQ rate
$N_{\mathrm{b,frac}}$	bits/sample	fractional bit rate
$N_{\mathrm{b},k}$	bits/sample	bit rate used for the k-th DFT channel (MC-BAQ) or k-th bit rate to synthesize a given ASQ rate $N_{\mathrm{b,ASQ}}$

$N_{\mathrm{b,high}}$	bits/sample	largest quantization rate used according to MC-BAQ
$N_{\mathrm{b,inf}}$	bits/sample	next smaller integer rate to synthesize a given fractional rate $N_{\mathrm{b,frac}}$
$N_{\mathrm{b,low}}$	bits/sample	lowest quantization rate used according to MC-BAQ
$N_{\mathrm{b,M}}$	bits/sample	bit rate used for the master acquisition
$N_{\mathrm{b,mid}}$	bits/sample	mid quantization rate used according to MC-BAQ
$N_{\mathrm{b,min}}$	bits/sample	minimum allowed bit rate
$N_{\mathrm{b,max}}$	bits/sample	maximum allowed bit rate
$N_{\mathrm{b,req}}$	bits/sample	bit rate required for quantization
$N_{\mathrm{b,S}}$	bits/sample	bit rate used for the slave acquisition
$N_{\mathrm{b,sup}}$	bits/sample	next greater integer rate to synthesize a given fractional rate $N_{\mathrm{b,frac}}$
N_{block}		size of the raw data block for the BAQ algorithm
N_{l}		number of looks
N_{op}		number of onboard operations
N_{P}		order of prediction
N_{seq}		length of the ASQ rate sequence $\mathbf{S}_{N_{\mathrm{b,ASQ}}}$
$\mathrm{NESZ}_{\mathrm{quant}}$		NESZ degradation due to quantization
$\mathrm{NESZ}_{\mathrm{sys}}$		NESZ including all error contributions except quantization
n		discrete time
n		rank of the radar system
$n_{\mathrm{rg,max}}$		maximum number of range lines to be taken into account for determining the effective ASQ rate
$n(t)$		additive Gaussian noise as a function of time
o_{f}		oversampling factor
P_k	W	power associated to the k-th transformed coefficient
P_{l}	W	power of the weak scatterer
P_{ratio}		power ratio
P_{s}	W	power of the strong scatterer
$P_x(f)$		Doppler power spectral density of x
P_q^r	W	received q-polarized power
P_p^t	W	transmitted p-polarized power
$\mathrm{PRF}_{\mathrm{eff}}$	Hz	effective PRF on receive for a multi-channel SAR system

$\mathrm{PRF}_{\mathrm{sys}}$	Hz	transmit PRF for a multi-channel SAR system
$p_Q(q)$		probability density function of the quantization error between two interferometric SAR channels
$p_X(x)$		probability density function of the quantizer input
$p_{X_\mathrm{q}}(x_\mathrm{q})$		probability density function of the quantizer output
$p_\varphi(\varphi)$		probability density function of the phase difference between two interferometric SAR channels
$Q(f)$		amplitude weighting of the Doppler spectrum in the processing
$\bar{Q}$		signal quadrature component at the ADC output
Q_adc		quadrature component of the signal at the ADC output
Q_baq		quadrature component of the BAQ-decoded signal
q		quantization error
$R(t)$	m	time-varying slant range distance
R_0	m	slant range distance perpendicular to the flight direction (zero Doppler)
R_tot	bits/sample	total bit rate used to quantized N_acq acquisitions
$R_x(\tau)$		normalized azimuth autocorrelation function of x as function of the time lag τ
r_clip		maximum output value of the quantizer
$r_{\mathrm{opt},i}$		i-th optimum reconstruction level of the Max-Lloyd quantizer
r_i		i-th reconstruction value of the quantizer
S_p^i	$\mathrm{W/m^2}$	p-polarized power density intercepted by the target
S_q^s	$\mathrm{W/m^2}$	q-polarized power density backscattered to the sensor
$\mathbf{S}_{N_\mathrm{b,ASQ}}$	bits/sample	vector of length N_seq containing the bit rate values which synthesize a given ASQ rate $N_\mathrm{b,ASQ}$
$\mathrm{SQNR}_\mathrm{frac}$		SQNR associated to the non-integer rate $N_\mathrm{b,frac}$
$\mathrm{SQNR}_\mathrm{inf}$		SQNR associated to the non-integer rate $N_\mathrm{b,inf}$
$\mathrm{SQNR}_\mathrm{sup}$		SQNR associated to the non-integer rate $N_\mathrm{b,sup}$
$s(t)$		continuous-time continuous-amplitude signal transmitted by the radar system
$s_\mathrm{I,adc}$		sign bit for the in-phase component of the signal at the ADC output
$s_\mathrm{I,baq}$		sign bit for the in-phase component of the signal at the BAQ output

$s_{\mathrm{Q,adc}}$		sign bit for the quadrature component of the signal at the ADC output
$s_{\mathrm{Q,baq}}$		sign bit for the quadrature component of the signal at the BAQ output
T_{r}	K	receiver temperature
t	s	continuous time variable
t_{int}	s	integration time
u		independent variable of the characteristic function (pdf transformed domain)
V_{clip}		maximum input (clipping) value of the quantizer
v_{s}	m/s	satellite velocity
v_{T}	m/s	target velocity
W_{g}	m	ground swath width
$W_{\mathrm{g,eff}}$	m	effective imaged swath width
$W_{\mathrm{g,max}}$	m	maximum imaged swath width
W_{q}		random variable describing the stochastic process $w_{\mathrm{q}}[\mathrm{n}]$
$w(a)$		echo received by the sensor from a point target with azimuth coordinate a
w_{q}		additive Gaussian noise term modeling the quantization process
X		random variable describing the stochastic process $x[\mathrm{n}]$
X_{q}		random variable describing the stochastic process $x_{\mathrm{q}}[\mathrm{n}]$
$X(f)$		spectrum of $x(t)$
$x(t)$		continuous-time continuous-valued echo received by the radar system
$x[\mathrm{n}]$		in the context of SAR raw data quantization, discrete-time (sampled) continuous-valued version of $x(t)$
x_{adc}		signal at the ADC output
x_{in}		signal at the ADC input
x_{max}		maximum value of the quantizer input signal, assuming bounded support
$x_{\mathrm{q}}[\mathrm{n}]$		discrete-time (sampled) discrete-valued (quantized) version of $x(t)$

$x_{\mathrm{q,MR}}$		output of a midrise quantizer
$x_{\mathrm{q,MT}}$		output of a midtread quantizer
$\tilde{x}[\mathrm{n}]$		estimate of the sample $x[\mathrm{n}]$
$y_k[\mathrm{n}]$		k-th DFT coefficient of the multi-channel SAR echo received at discrete time n
z	m	height of the target

List of Greek Symbols

	Unit	
α	rad	local terrain slope
β	m^{-1}	one-way extinction coefficient
$\boldsymbol{\beta}$		set of weights for linear predictive coding
β_k		prediction weight associated to the k-th preceding sample
γ		interferometric coherence
γ_{Amb}		ambiguity correlation factor
γ_{Az}		Doppler shift correlation factor
γ_{clip}		signal-to-clipping ratio
γ_{Quant}		quantization correlation factor
γ_{Rg}		baseline correlation factor
γ_{SNR}		signal-to-noise correlation factor
γ_{Temp}		temporal correlation factor
γ_{Vol}		volume correlation factor
$\hat{\gamma}$		estimated coherence
Δ		quantization step size
Δh	m	relative height error affecting a DEM
$\Delta h_{90\%}$	m	90% point-to-point relative height error
$\Delta h_{90\%,h_{\mathrm{amb}}}$		relative height error degradation due to quantization, normalized with respect to the height of ambiguity
$\Delta N_{\mathrm{b},k}$	bits/sample	bit rate contribution to be added or subtracted to the k-th channel with respect to the average rate $\bar{N}_{\mathrm{b}}$
Δp_a	m	interferometric posting in azimuth
Δp_r	m	interferometric posting in ground range
ΔR	m	travel path difference between master and slave sensor

ΔT_{acq}	s	acquisition duration
Δt	s	time delay of the radar pulse between transmission and reception
$\Delta\varphi$	rad	interferometric phase error (confined to the interval $[-\pi,\pi]$)
$\Delta\varphi_{N_{\mathrm{acq}},R_{\mathrm{tot}}}$	rad	phase error after combination of N_{acq} acquisitions for a constant total bit rate of R_{tot} bits/sample
$\Delta\varphi_{N_{\mathrm{acq}},N_{\mathrm{b}}}$	rad	phase error after combination of N_{acq} acquisitions each quantized with N_{b} bits/sample
$\Delta\varphi_{\mathrm{req}}$	rad	maximum allowed phase error degradation
$\Delta\varphi_{N_{\mathrm{b}}}$	rad	interferometric phase error from a single acquisition which has been quantized using N_{b} bits/sample
$\Delta\varphi_{\delta}$	rad	differential phase between the non-compressed interferogram and the quantized one (confined to the interval $[-2\pi,2\pi]$)
δa_{RAR}	m	azimuth resolution of a real aperture radar
δa	m	azimuth resolution of a SAR
δf_{D}	Hz	Doppler frequency resolution
δr_{rect}	m	slant range resolution when transmitting a rectangular pulse
δr	m	slant range resolution when transmitting a chirp pulse
δr_{g}	m	ground range resolution when transmitting a chirp pulse
$\varepsilon[\mathrm{n}]$		prediction error for the n-th sample
$\varepsilon_{\mathrm{q}}[\mathrm{n}]$		quantized prediction error
η	rad	angle of incidence
θ_{e}	rad	elevation angle
$\imath_p$		p-th pixel of the non-quantized SAR image $\imath$
$\imath_{\mathrm{q},p}$		p-th pixel of the quantized SAR image $\imath_{\mathrm{q}}$
κ_x		loading (crest) factor of the signal x
λ	m	radar wavelength
μ_X		expectation (statistic mean) of the random variable X
μ_γ		mean coherence from a single TanDEM-X scene
ν		focused (compressed) azimuth impulse response
ξ_i		i-th quantization interval

$\xi_{\mathrm{opt},i}$		i-th optimum interval of the Max-Lloyd quantizer
$\boldsymbol{\rho}$		vector of correlation values of the random process $x[\mathrm{n}]$
ρ_k		correlation between the sample to be predicted and the k-th preceding sample
$\rho_{\Delta\varphi}$		phase error degradation due to quantization with respect to the total performance
$\rho_{\Delta\varphi_{N_{\mathrm{acq}},R_{\mathrm{tot}}}}$		ratio of the phase error resulting from the combination of $N_{\mathrm{acq}} > 1$ acquisitions to the one resulting from $N_{\mathrm{acq}} = 1$, for a given total data rate R_{tot}
σ^0_{pq}		radar cross section per unit area (backscattering coefficient) for p-polarization in transmission and q-polarization in reception (often without subscript, σ^0)
$\sigma^0(z)$		vertical scattering profile, as function of the volume height
$\sigma_{\varepsilon,N_{\mathrm{P}}}$		standard deviation of the prediction error resulting from a $N_{\mathrm{P}}^{\mathrm{th}}$-order predictor
σ_{pq}	m^2	radar cross section for p-polarization in transmission and q-polarization in reception
σ_Q		standard deviation of the quantization error
$\sigma_{Q,\mathrm{c}}$		standard deviation of the quantization noise due to clipping errors
$\sigma_{Q,\mathrm{g}}$		standard deviation of the quantization noise due to granular errors
$\sigma_{Q,\mathrm{I}}$		standard deviation of the in-phase component of the quantization error
$\sigma_{Q,\mathrm{Q}}$		standard deviation of the quadrature component of the quantization error
σ_X		standard deviation of the quantizer input signal
$\sigma_{X,\mathrm{I}}$		standard deviation of the in-phase component of the quantizer input signal
$\sigma_{X,\mathrm{Q}}$		standard deviation of the quadrature component of the quantizer input signal
σ_k		square root of the power associated to the k-th subband integrated over the processed bandwidth
σ_γ		standard deviation of the coherence from a single TanDEM-X scene
$\sigma_{\Delta\varphi}$	rad	phase error standard deviation due to quantization

$\sigma_{\Delta\varphi,\mathrm{req}}$	rad	allowed (required) phase errors standard deviation
$\sigma_{\Delta\varphi_{\mathrm{Tot}}}$	rad	phase error standard deviation of the compressed interferogram including all decorrelation sources
$\sigma_{\Delta\varphi_{\mathrm{Tot,bypass}}}$	rad	phase error standard deviation of the non-compressed interferogram including all decorrelation sources
σ_{σ^0}		standard deviation of the SAR backscatter
σ_{φ}	rad	standard deviation of the interferometric phase error
τ	s	time lag in the azimuth dimension
τ_{p}	s	pulse duration
υ		SAR interferogram
$\Phi_X(u)$		characteristic function of the random variable X as function of the variable in the transformed domain u
ϕ_0	rad	initial phase shift
ϕ_1	rad	phase of the master image
ϕ_2	rad	phase of the slave image
$\phi(t)$	rad	azimuth phase variation as function of time
ϕ_{a}	rad	azimuth angle between the transmitter and the target
$\phi_{\mathrm{scat},1}$	rad	scattering phase of the master image
$\phi_{\mathrm{scat},2}$	rad	scattering phase of the slave image
φ	rad	interferometric phase
$\varphi_{90\%}$	rad	90% point-to-point interferometric phase errors
φ_{abs}	rad	interferometric absolute phase
χ		focused (compressed) range impulse response
Ψ		repetition frequency of the characteristic function
$\psi(t)$	rad	azimuth angles with respect to the radar sensor, as function of time
ψ_{a}	rad	off-center angle in azimuth
$\psi_{\mathrm{a,3dB}}$	rad	half-power off-center angle in azimuth
ψ_{e}	rad	off-center angle in elevation
$\psi_{\mathrm{e,3dB}}$	rad	half-power off-center angle in elevation

List of Acronyms

AASR	Azimuth Ambiguity-to-Signal Ratio
ADC	Analog-to-Digital Converter

ASF DAAC	Distributed Active Archive Center of the Alaska SAR Facility
ALOS	Advanced Land Observing Satellite
ASI	Agenzia Spaziale Italiana (Italian Space Agency)
ASQ	Azimuth-Switched Quantization
AWGN	Additive White Gaussian Noise
BAQ	Block-Adaptive Quantization
BLU	Best Linear Unbiased (Interpolation)
BRM	Bit Rate Map
CAST	China Association for Science and Technology
CDTI	Centre for the Development of Industrial Technology
CNN	Convolutional Neural Network
CF	Characteristic Function
CLT	Central Limit Theorem
CONAE	Comisión Nacional de Actividades Espaciales (Argentine National Space Activities Commission)
COSMO-SkyMed	Constellation of Small Satellites for Mediterranean Basin Observation
CRESDA	China Center for Resources Satellite Data and Applications
CSA	Canadian Space Agency
DBF	Digital Beamforming
DC	Direct Coupling
DEM	Digital Elevation Model
DFT	Discrete Fourier Transform
DLR	Deutsches Zentrum für Luft- und Raumfahrt (German Aerospace Center)
DP-BAQ	Dynamic Predictive Block-Adaptive Quantization
DPCM	Differential Pulse Code Modulation
ENVISAT/ASAR	Environmental Satellite / Advanced Synthetic Aperture Radar
ERS	European Remote Sensing Satellite
ESA	European Space Agency
EWL	Echo Window Length
FDBAQ	Flexible Dynamic Block-Adaptive Quantization
FPGA	Field Programmable Gate Array
GIS	Geographic Information System

GmbH	Gesellschaft mit beschränkter Haftung (company with limited liability)
GPS	Global Positioning System
HJ-1C	Huan Jing 1C, Chinese SAR satellite in S band
HH	horizontal transmit and horizontal receive polarization
HR	Institut für Hochfrequenztechnik und Radarsysteme (Microwaves and Radar Institute)
HRWS	High-Resolution Wide-Swath
HV	horizontal transmit and vertical receive polarization
InSAR	Synthetic Aperture Radar Interferometry
IRF	Impulse Response Function
ISLR	Integrated Sidelobe Ratio
ISRO	Indian Space Research Organisation
ITP	Interferometric TanDEM-X Processor
JERS-1	Japanese Earth Resource Satellite 1
JPL	Jet Propulsion Laboratory
KARI	Korea Aerospace Research Institute
KOMPSAT-5	Korea Multi-Purpose Satellite 5
LFM	Linear Frequency Modulation
LPC	Linear Predictive Coding
LTI	Linear Time-Invariant
LUT	Look-Up Table
MAC	Multiple Azimuth Channels
MC-BAQ	Multi-Channel Block-Adaptive Quantization
MLE	Maximum Likelihood Estimator
MMSE	Minimum Mean Square Error
MoD	Ministry of Defense
NASA	National Aeronautics and Space Administration
NESZ	Noise Equivalent Sigma Zero
NRL	Naval Research Laboratory
NRSCC	National Remote Sensing Center of China
P-BAQ	Predictive Block-Adaptive Quantization
pdf	probability density function
pmf	probabiliy mass function

PO-BAQ	Performance-Optimized Block-Adaptive Quantization
PRF	Pulse Repetition Frequency
PRI	Pulse Repetition Interval
PSLR	Peak Sidelobe Ratio
radar	Radio Detection and Ranging
RADARSAT	Radar Satellite
RAR	Real Aperture Radar
RASR	Range Ambiguity-to-Signal Ratio
RCM	RADARSAT Constellation Mission
R-D	Rate-Distortion (Theory)
RISAT-1	Radar Imaging Satellite 1
SAOCOM	Satélite Argentino de Observación Con Microondas (Argentine Microwaves Observation Satellite)
SAR	Synthetic Aperture Radar
SCORE	Scan-on-Receive
SIR	Spaceborne Imaging Radar
SLC	Single-Look Complex
SNR	Signal-to-Noise Ratio
SQNR	Signal-to-Quantization Noise Ratio
SRTM	Space Radar Topography Mission
SSTL	Surrey Satellite Technology
TanDEM-X	TerraSAR-X add-on for Digital Elevation Measurement
TDX	TanDEM-X satellite
TAXI	TanDEM-X Interferometric Processor
TOPS	Terrain Observation with Progressive Scan
TSX	TerraSAR-X satellite
UK	United Kingdom
UKSA	UK Space Agency
USA	United States of America
VH	vertical transmit and horizontal receive polarization
VV	vertical transmit and vertical receive polarization

Contents

List of Figures

List of Tables

1 Introduction

Radar is the acronym for "radio detection and ranging" and indicates an active system which uses radio waves to detect objects and determine their position, angle of observation, and/or velocity. The history of radar dates back to the last decades of the 19$^{\text{th}}$ century, when Heinrich Hertz proved the existence of electromagnetic waves [1], previously predicted and formalized in equations by James C. Maxwell [2]. Between 1886 and 1888, Hertz conducted a series of experiments to demonstrate that radio waves can actually be reflected by metallic and dielectric objects. Then, in 1904, Christian Hülsmeyer invented the first device which utilizes radio waves to detect the presence of distant objects, the so-called *Telemobiloscope* [3], [4], mainly intended to prevent collisions between ships in foggy conditions. Relevant experiments were conducted during the following two decades by Guglielmo Marconi together with Charles S. Franklin, and by the researchers at the Naval Research Laboratory (NRL), United States of America (USA). However, despite the promising results, it was only right before the outbreak of World War II that radar technology experienced a rapid development concurrently in several countries, such as Great Britain, France, Italy, Germany, the Netherlands, the Soviet Union, Japan, and the USA.

A significant development in radar history is then represented by the invention of the side looking airborne radar (SLAR) in the 1950s, which allowed for the imaging of ground areas from airborne platforms for military reconnaissance purposes. In 1951, the working principle of synthetic aperture radar (SAR) was conceived by Carl A. Wiley. SAR allows for high-resolution imaging, independently of the range distance, by exploiting the relative motion of the radar antenna in the along-track dimension over the target under illumination [5]. A detailed description of the SAR principle and of the most relevant SAR systems and performance parameters is provided in Chapter 2. Since its invention, SAR has been universally acknowledged as a fundamental discovery in the field of radar for remote sensing applications, and up to the present day a number of airborne and spaceborne missions have been developed, by progressively and significantly improving the sensor capabilities and the provided image quality. Table 1.1 shows the frequency bands and the corresponding wavelength ranges commonly employed for spaceborne imaging radar systems. The radar wavelength λ is related to the radar carrier frequency f_{c} by the relation

$$\lambda = \frac{c_0}{f_{\text{c}}}, \tag{1.1}$$

being c_0 the speed of light in free space. Each of the frequency bands is characterized by different interaction and penetration capabilities of the electromagnetic waves in media, and is therefore selected depending on the specific target application. A detailed historical overview of the most relevant spaceborne SAR missions is presented in the next

Table 1.1: Frequency bands (and corresponding frequency and wavelength ranges) typically used for SAR systems.

Frequency Band	**Frequency [GHz]**	**Wavelength [cm]**
P	0.25-0.5	60-120
L	1-2	15-30
S	2-4	7.5-15
C	4-8	3.75-7.5
X	8-12	2.5-3.75
K_u	12-18	1.67-2.5
K	18-26.5	1.3-1.67
K_a	26.5-40	0.75-1.3

section.

1.1 Spaceborne SAR: Historical Overview and State of the Art

Table 1.2 provides a historical overview of the civilian spaceborne SAR missions. All satellites which are still in operation (as indicated in the second column of the table) were launched within the last 10-15 years, and their frequency bands, except for a few cases, range from L band to X band. After the invention of the SAR principle in the beginning of the 1950s, it took almost 30 years until the first civilian SAR satellite, Seasat, was launched into space by the Jet Propulsion Laboratory (JPL) of the National Aeronautics and Space Administration (NASA) in 1978 [6]. Seasat was equipped with an L-band antenna with the main scope of providing relevant information about oceanographic processes, such as wave heights and ocean surface winds and temperature, with a mission duration of about three months. The left-hand side of Figure 1.1 shows an artistic view of the Seasat sensor, while the right-hand side depicts the SAR amplitude acquired by Seasat over the Columbia River and the Oregon coastline. Successively, the L-band Shuttle Imaging Radar SAR missions SIR-A [7], [8] and SIR-B [9], mounted on board the Space Shuttle, were launched in 1981 and 1984, respectively. In particular, the SIR-B mission, during its eight days of operation, acquired for the first time SAR data takes from multiple incidence angles, thanks to its ability to mechanically tilt the SAR antenna in elevation.

The first spaceborne SAR mission developed by the European Space Angency (ESA) was the C-band ERS-1 [10], launched in 1991 and in operation until 2000. Its follow-on satellites ERS-2 (1995-2011) and ENVISAT/ASAR (2002-2012) provided a fundamental continuity in data acquisition and distribution [11], [12]. This aspect has been further assured by the development of the C-band Sentinel-1a and Sentinel-1b satellites, launched in 2014 and 2016, respectively, in the frame of the European Union's Earth

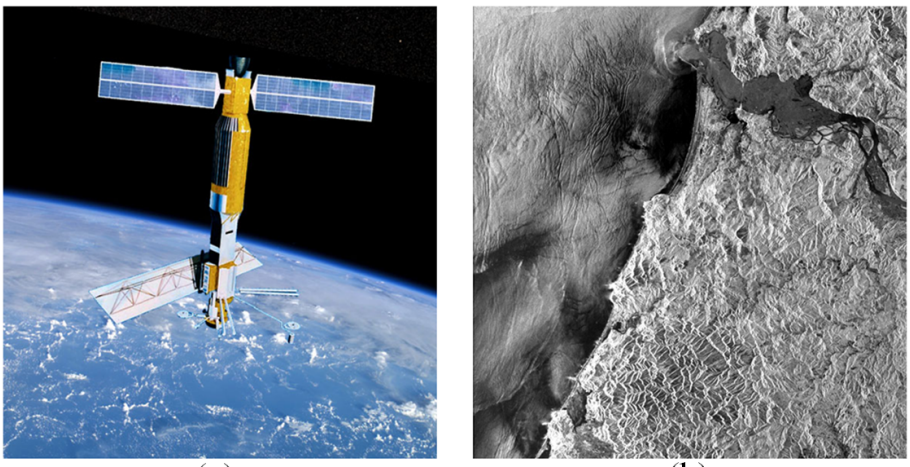

(a) (b)

Figure 1.1: (a) Artist's illustration of the NASA's Seasat satellite, launched on June 28, 1978. (b) Seasat SAR image over the Mouth of the Columbia River and the Oregon coastline, Oregon (USA), acquired on August 10, 1978 (Credits: NASA 1978, processed by ASF DAAC 2013).

observation program Copernicus [13], and providing enhanced capabilities in terms of SAR image quality, revisit time, and coverage.

The two C-band SAR missions RADARSAT-1 and RADARSAT-2 were developed by the Canadian Space Agency and launched in 1995 and 2007, respectively. They are characterized by swath width capabilities of up to 500 km and aim at the supply and distribution of data for commercial applications as well as for remote sensing science [14], [15]. The follow-on RADARSAT Constellation Mission (RCM) was launched on June 12, 2019. The Japanese Space Agency (JAXA) developed a series of L-band spaceborne SAR sensors, JERS-1 in 1992, ALOS in 2006, and ALOS-2 in 2014 [16], [17], with main purposes in the fields of cartography, regional observation, disaster monitoring, and resource surveying.

The SIR-C/X-SAR missions, developed in a joint partnership between NASA JPL, the German Aerospace Center (DLR), and the Italian Space Agency (ASI) [18], operated on two Space Shuttle flights in April and October 1994, and were equipped with L-, C-, and X-bands SAR antennas, representing the first demonstration of multi-frequency SAR in space. This successful cooperation continued with the development of the Shuttle Radar Topography Mission (SRTM) [19]. SRTM was launched in February 2000 and, during its eleven days of mission operation, acquired data in C and X band for the generation of a nearly global Digital Elevation Model (DEM) of the Earth's landmasses (latitudes between 56° S and 60° N).

Table 1.2: Overview of civilian spaceborne SAR sensors.

Sensor	Lifetime	Frequency Band	Institution, Country
Seasat	1978	L	NASA/JPL, USA
SIR-A/B	1981/1984	L	NASA/JPL, USA
ERS-1/2	1991-2000 1995-2011	C	ESA, Europe
JERS-1	1992-1998	L	JAXA, Japan
SIR-C/X-SAR	1994	L/C/X	NASA/JPL, USA DLR, Germany ASI, Italy
RADARSAT-1 RADARSAT-2	1995-2013 2007-today	C	CSA, Canada
SRTM	2000	C/X	NASA/JPL, USA DLR, Germany ASI, Italy
ENVISAT/ASAR	2002-2012	C	ESA, Europe
ALOS/PalSAR	2006-2011	L	JAXA, Japan
TerraSAR-X TanDEM-X	2007-today 2010-today	X	DLR/Airbus, Germany
COSMO-SkyMed-1/4	2007...2010-today	X	ASI/Italian MoD, Italy
RISAT-1	2012-today	C	ISRO, India
HJ-1C	2012-today	S	CRESDA/CAST/ NRSCC, China
Kompsat-5	2013-today	X	KARI, South Korea
Sentinel-1a/1b	2014/2016-today	C	ESA, Europe
ALOS-2	2014-today	L	JAXA, Japan
PAZ	2018-today	X	CDTI, Spain
NovaSAR-1	2018-today	S	SSTL/Airbus/UKSA, UK
SAOCOM-1a SAOCOM-1b	2018-today Scheduled in 2020	L	CONAE, Argentina
ICEYE Constellation	2018/2019-today	X	Iceye Oy, Finland
RCM	2019-today	C	CSA, Canada

The constellation of the four X-band satellites COSMO-SkyMed for Earth observation was launched into space between 2007 and 2010 [20]. The SAR satellites have been developed by ASI in cooperation with the Italian Ministry of Defence (MoD) for dual use applications, both military and civilian. Further on-going spaceborne SAR missions that deserve to be mentioned are the Indian C-band quad-polarization mission RISAT-1 (2012) [21], S-band sensors HJ-1C (2012) [22] from China and NovaSAR (2018) [23]

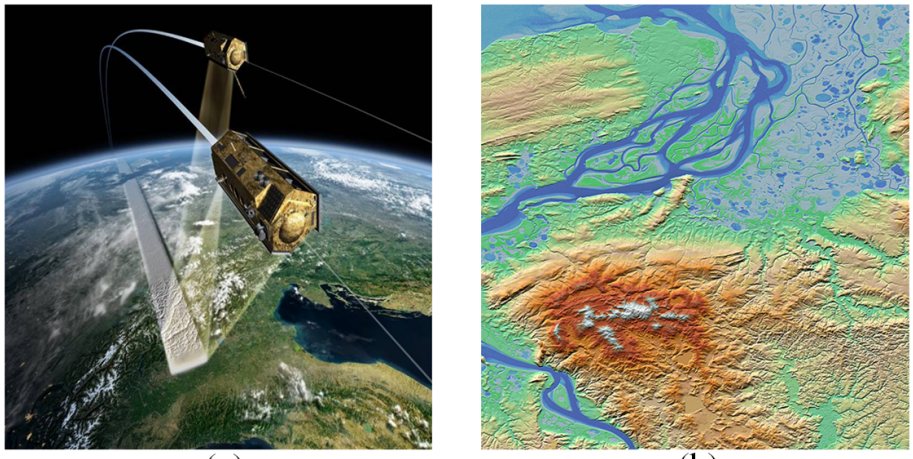

(a) (b)

Figure 1.2: (a) Artist's illustration of the DLR's TerraSAR-X and TanDEM-X satellites. (b) Color-coded TanDEM-X DEM over the Pyasina Delta and Kara Sea, Russia (Credits: DLR).

from UK, the X-band SAR satellites Kompsat-5 (South Korea, 2013) [24] and PAZ (Spain, 2018) [25], and the Argentinean L-band SAOCOM-1a (2018) [26] (the launch of the companion satellite SAOCOM-1b is scheduled for 2020).

The first German SAR satellite, TerraSAR-X, was developed under a public-private-partnership between DLR and Airbus Defence & Space and launched in June 2007. TerraSAR-X operates at X band and provides SAR imagery with excellent radiometric and geometric accuracies [27], spatial coverage up to 250 km (Wide ScanSAR mode [28]) and resolutions down to 20 centimeters (Staring Spotlight mode [29]). In June 2010, TerraSAR-X was enhanced by its almost twin satellite TanDEM-X, to begin the first bistatic spaceborne SAR mission ever comprising two separate spacecrafts. Since then, the two X-band SAR satellites have been flying in a close orbit formation at a few hundred meters distance acting as a large single-pass radar interferometer, with the opportunity for flexible along- and across-track baseline selection and allowing for the acquisition of high-resolution interferograms [30]. The primary objective of the TanDEM-X mission (which stands for "TerraSAR-X add-on for Digital Elevation Measurement") was the generation of a worldwide and consistent DEM with unprecedented accuracy, which was successfully completed in 2016 (an additional change-DEM layer is foreseen to be delivered by 2021 [31]). The left-hand side of Figure 1.2 shows an artistic view of the TerraSAR-X and TanDEM-X satellites, while the right-hand side depicts the color-coded TanDEM-X DEM over the Pyasina Delta and Kara Sea, Russia. Nowadays, TanDEM-X is able to provide the remote sensing scientific community with a unique data set and to apply innovative techniques for a broad range of commercial and scientific ap-

plications, such as the monitoring of terrain deformation [32], flooding [33], ice melting [34], and deforestation events [35]. While being very flexible and powerful systems, the acquisition capabilities of the TerraSAR-X and TanDEM-X satellites are limited by their relatively short orbit duty cycle (about 3 minutes per orbit) and small onboard memory (of 256 Gbit and 512 Gbit, respectively), which pose constraints on the achievable data rate during the mission. This aspect represents a critical issue for all spaceborne SAR missions and, in turn, directly dictates a trade off between the quality of the resulting SAR products and the sensor acquisition capabilities: indeed, about an entire year was required by TanDEM-X to complete one global interferometric acquisition of the Earth's landmasses fulfilling the specified mission requirements [30].

1.2 Motivation and Objectives of the Work

Synthetic aperture radar (SAR) allows for all-weather, day-night high-resolution imaging and is therefore very attractive for a large number of scientific as well as commercial applications. For present and next-generation spaceborne SAR missions, an increasing volume of onboard data is going to be required, due to the employment of large bandwidths, multiple channels, and the imaging of large swath widths at fine spatial resolutions. An example is Tandem-L, a DLR proposal for a single-pass interferometric and fully polarimetric L-band radar mission, which exploits innovative high-resolution wide-swath SAR modes with the main objective of systematically monitoring dynamic processes of the Earth system, such as deformation events, forest height and biomass change, and ice/glacier velocity fields [36], [37]. The resulting increase of required data rate implies hard requirements in terms of onboard memory and downlink capacity. In this context, a proper quantization of the raw data acquired by the SAR sensor is of utmost importance, since the number of bits employed to digitize the recorded radar signal, on the one hand, directly affects the performance of the resulting SAR products and, on the other hand, defines the total amount of data to be managed by the system, hence identifying a key aspect for the design of future SAR missions.

One of the most widely recognized standards for SAR raw data compression is the block-adaptive quantization (BAQ) [38], [39], which provides a good compromise between implementation complexity, granted image quality, and achievable compression ratio. In this dissertation, different quantization strategies as well as efficient data volume reduction methods for SAR systems are proposed and, in all cases, BAQ has been considered as the state-of-the-art quantization scheme.

This work focuses on the onboard quantization of synthetic aperture radar (SAR) systems and is the result of the research activities carried out at the Microwaves and Radar Institute (HR) of DLR, Germany. The main content and objectives of the thesis are summarized in the following:

1. Assess the impact of raw data quantization on SAR and InSAR performance for

different SAR image characteristics and system parameters. For this purpose, bistatic images acquired by the TanDEM-X mission are investigated. Starting from the obtained results, a novel method, denoted as performance-optimized block-adaptive quantization (PO-BAQ), is introduced, which exploits the a priori knowledge about the SAR backscattered information to adjust the resource allocation and, at the same time, to control the interferometric performance degradation.

2. Develop a novel SAR data compression technique, named azimuth-switched quantization (ASQ), which allows for the efficient implementation of non-integer quantization rates, hence enabling finer granularity in terms of achievable performance and resource allocation for the design of SAR systems. The proposed method has been successfully demonstrated on experimental data acquired by TanDEM-X.

3. Introduce a new strategy for onboard data reduction for multi-channel SAR systems [40], which exploits the transform coding paradigm by taking advantage of the existing correlation between adjacent azimuth samples. The proposed method, named multi-channel block-adaptive quantization (MC-BAQ), allows for the optimization of the resulting performance and data rate.

4. Address data volume reduction in the context of staggered SAR systems [41]. The proposed dynamic predictive block-adaptive quantization (DP-BAQ) exploits the redundancy in the non-uniform staggered SAR azimuth raw data stream and allows for a significant reduction of the data volume to be downlinked to the ground at the cost of a modest increase of the onboard computational effort.

The goals of this thesis can be therefore categorized in two main parts: the first one (corresponding to objectives 1. and 2.) focuses on the analysis and the optimization of SAR performance with respect to raw data quantization, and to this purpose investigations on experimental TanDEM-X data have been conducted; the second part (objectives 3. and 4.) addresses innovative onboard data reduction methods for next-generation SAR systems, whose effectiveness is demonstrated by means of analytical formulations as well as of Monte-Carlo simulations.

Each of the above mentioned objectives is elaborated in a dedicated chapter of the dissertation, whose detailed structure is described in the next section.

1.3 Thesis Structure

The thesis is structured as follows:

- A short review of SAR remote sensing is presented in Chapter 2: the SAR acquisition principle and image formation process are recalled, together with an overview of the main SAR and interferometric SAR (InSAR) system and performance parameters and a summary of the most relevant acquisition and operation modes.

- In Chapter 3 the compression of SAR raw data is discussed. State-of-the-art quantization schemes for SAR systems are reviewed and the impact of quantization errors is evaluated by means of a dedicated simulation framework for different target scenarios. Chapter 2 and Chapter 3 are intended to provide all necessary concepts for the understanding of the work developed in the subsequent chapters.

- The impact of quantization on SAR and interferometric (InSAR) performance is evaluated in Chapter 4 on experimental TanDEM-X bistatic data for different system parameters and SAR scene characteristics. For this, an overview of the TanDEM-X mission is provided, and the consequent adaptation of the resource allocation strategy for the global TanDEM-X DEM acquisition is presented as well. In addition, a novel performance-optimized block-adaptive quantization (PO-BAQ) is introduced, which allows for adjusting the target data rate depending on the specific SAR backscatter information and, at the same time, to control the interferometric performance degradation.

- Chapter 5 presents a novel SAR data compression technique, named azimuth-switched quantization (ASQ), which allows for the efficient implementation of non-integer quantization rates. By this, higher flexibility in terms of resource allocation and achievable SAR performance is enabled. The proposed method is tested on experimental TanDEM-X data.

- Chapter 6 describes a new method for onboard data reduction for SAR systems using multiple receiving channels mutually displaced in the along-track direction, which allows for high-resolution imaging of a wide swath. The proposed multi-channel block-adaptive quantization (MC-BAQ) exploits the existing correlation within each multi-channel raw data block by jointly applying a discrete Fourier transform together with an efficient selection of the quantization rates, hence allowing for the optimization of the resulting performance and data rate.

- Chapter 7 introduces a novel strategy for data volume reduction in the context of staggered SAR systems [41]. Staggered SAR requires a higher azimuth oversampling with respect to a conventional SAR. Hence, the use of linear predictive coding is investigated, which exploits the correlation properties exhibited by the non-uniform azimuth raw data stream. The proposed dynamic predictive block-adaptive quantization (DP-BAQ) allows for a significant reduction of the data volume to be downlinked to the ground at the cost of a slight increase of the onboard implementation effort.

- Finally, the conclusions of the thesis are drawn in Chapter 8, together with an outlook on future research activities.

2 Synthetic Aperture Radar (SAR) Remote Sensing

Synthetic Aperture Radar (SAR) is an active microwave sensing technique which is capable of acquiring high-resolution images at day and night. Moreover, since weather phenomena, such as precipitation or the presence of clouds, do not significantly affect the microwave propagation, high-quality imaging is achieved regardless of the specific weather condition. This represents a great advantage with respect to optical sensors, which need sunlight and clear sky to be able to image the area of interest. Since its discovery in the early 1950s, an increasing interest has arisen on the utilization of SAR in remote sensing, representing nowadays a well-recognized and powerful technique to be applied for a wide range of geoscience applications, such as geology, physical geography, glaciology, agriculture, forestry, oceanography, and environmental monitoring. In this chapter, the SAR acquisition principle and image formation process are recalled, together with an overview of the main SAR performance parameters and of the most relevant SAR acquisition modes and imaging systems. Afterwards, the basic concepts of SAR interferometry (InSAR), its acquisition geometry and operation modes, and the main parameters describing the quality of InSAR products are introduced. An exhaustive treatise on SAR theory, algorithms, and implementation aspects is provided, among others, in [42], [43], [44], [45], [46].

2.1 Acquisition Geometry and Basic Principles

In a simplified representation, a monostatic SAR imaging system consists of a microwave transmitter and receiver, which is placed on a moving platform such as an airplane or a satellite, as shown in Figure 2.1. The radar sensor flies at an approximately constant height h_{s} above the ground and speed v_{s} along the radar track (or azimuth, or along-track) direction. The antenna height and length is indicated by L_{e} and L_{a} (where the subscripts stand for elevation and azimuth, respectively). The slant range identifies the direction perpendicular to the radar track pointing to the target T, whereas the ground range is the projection of the slant range on ground, i.e., the vector connecting the point of closest approach on the nadir track and the scatterer T. Let R_0 be the slant range distance of closest approach between the sensor and the target T, after the pulse transmission an echo will be received by the radar with a time delay

$$\Delta t = \frac{2R_0}{c_0}. \tag{2.1}$$

Hence, discrimination of objects at different range distances is made possible by the SAR side-looking imaging geometry. The microwave energy radiated by the antenna illuminates an area on ground which is defined as the antenna footprint. This extends

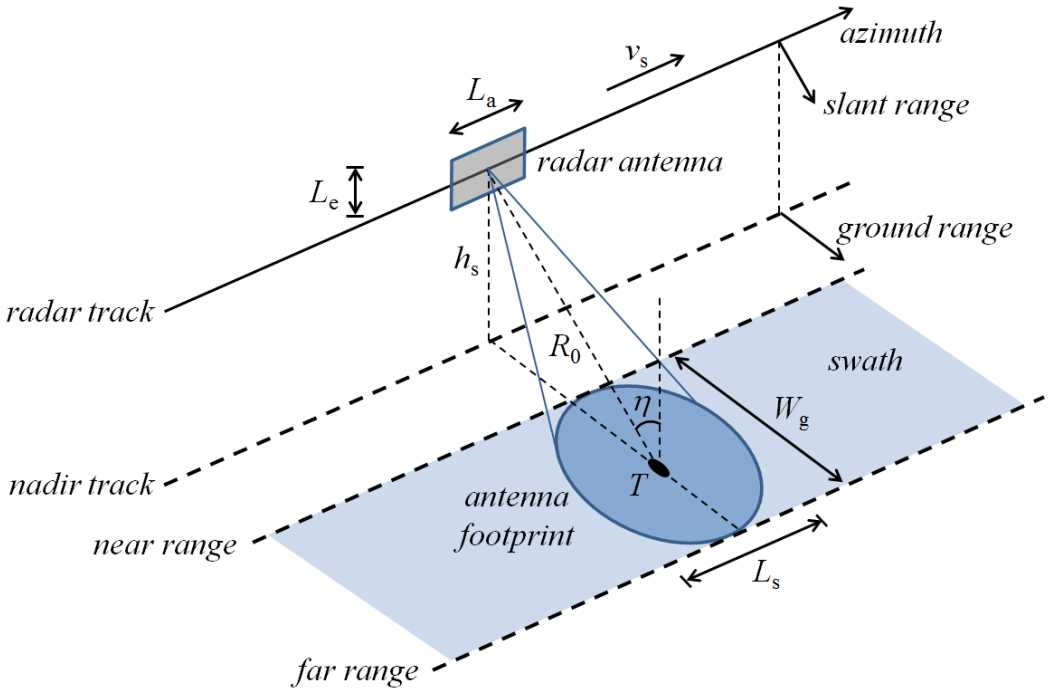

Figure 2.1: Schematic SAR acquisition geometry.

over L_s along azimuth direction and W_g from near to far range (the so-called swath width), which are expressed as

$$L_s = \frac{\lambda R_0}{L_a}, \tag{2.2}$$

$$W_g = \frac{\lambda R_0}{L_e \cdot \cos(\eta)}, \tag{2.3}$$

being η the angle of incidence as in Figure 2.1. The SAR transmitter unit typically emits short pulses of electromagnetic radiation each of duration τ_p (and spatial length $c_0\tau_p$) at a constant pulse repetition frequency (PRF), as depicted in Figure 2.2. For spaceborne SAR the resulting PRF values are typically in the range of a few kilohertz (kHz). The echo window length (EWL) is the time interval allowed for the echo reception. Due to the large range distance, each pulse typically takes several pulse repetition intervals (PRIs, being $\text{PRI} = 1/\text{PRF}$) to travel from the sensor to the target T and back, i.e., $\Delta t \approx n \cdot \text{PRI}$, where n is also known as *rank*. Given a range R_0, the *rank* of a SAR system is defined as

$$rank(R_0) = \left\lfloor \frac{2R_0}{c_0} \cdot \frac{1}{\text{PRI}} \right\rfloor. \tag{2.4}$$

As an example, for TerraSAR-X $R_0 = 600$ km and PRF = 3000 Hz, which results in *rank* = 12. The echo window length (EWL) as in Figure 2.2 directly determines the effective imaged swath width $W_{\mathrm{g,eff}}$ as follows

$$W_{\mathrm{g,eff}} = \frac{c_0 \cdot (\mathrm{EWL} - \tau_{\mathrm{p}})}{2 \cdot \sin(\eta)}. \tag{2.5}$$

The maximum swath width $W_{\mathrm{g,max}}$ is achieved by selecting the largest possible EWL, which is given by

$$\mathrm{EWL}_{\mathrm{max}} = \mathrm{PRI} - \tau_{\mathrm{p}}. \tag{2.6}$$

SAR is a coherent radar system, hence it records the amplitude and the phase of the received echoes, which are affected by the physical and dielectric properties of the illuminated target, such as its roughness or permittivity, as well as by the characteristics of the imaging system, such as the radar wavelength, the imaging geometry, and the polarization channel, the latter describing the geometric orientation of the radar wave oscillations in the plane perpendicular to the direction of propagation. For this, different target responses are possible depending on the polarizations used in transmission and reception. Often the combination of two linear polarizations, H (horizontal) and V (vertical) is used. For this, the antenna alternates the transmission of pulses with horizontal and vertical polarizations. The echoes are then simultaneously recorded using two separate channels with horizontal and vertical polarizations, respectively. In this way, different polarization combinations can be implemented: HH, HV, VH, and VV (in monostatic SAR observations, the reciprocity theorem results in the symmetric assumption of the cross-pol channels, i.e. the HV and VH channels carry the same information). In addition, by combining the polarization components and varying their phase shift and intensity in time, circularly, elliptically, or linearly (e.g., 45° inclined) polarized waves can be synthesized as well [47].

The received echo is weighted by the radar antenna pattern (which also depends on the specific polarization combination). For a rectangular aperture, the two-dimensional antenna pattern G can be approximated as

$$G(\psi_{\mathrm{a}}, \psi_{\mathrm{e}}) = \mathrm{sinc}^2\left(\frac{L_{\mathrm{a}}}{\lambda}\psi_{\mathrm{a}}\right) \cdot \mathrm{sinc}^2\left(\frac{L_{\mathrm{e}}}{\lambda}\psi_{\mathrm{e}}\right), \tag{2.7}$$

where ψ_{e} and ψ_{a} are the off-boresight angles in elevation and azimuth dimension, respectively, while L_{e} and L_{a} are the corresponding antenna height and length, according to Figure 2.1. In the above formula, the sinc function denotes the cardinal sinc function which, for a generic independent variable y, is defined as

$$\mathrm{sinc}(y) = \frac{\sin(\pi y)}{\pi y}, \tag{2.8}$$

and appears squared in (2.7) since the patterns are considered both in transmission and reception. Usually, in radar systems the energy of the antenna pattern is considered

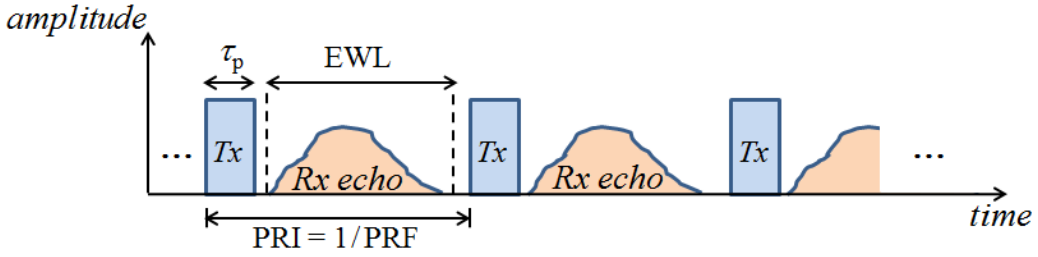

Figure 2.2: Sequence of transmitted SAR pulses (Tx), each one of duration τ_p and spaced out by the pulse repetition interval (PRI). The echo window length (EWL) is the time interval allowed for the echo reception, which directly defines the imaged swath width. For each transmitted pulse, an echo is received (Rx) by the sensor after a time delay Δt as in (2.1). Such a delay typically lasts several pulse repetition intervals and is not shown in the figure.

within the half power beam width ($\psi_{e,3dB}, \psi_{a,3dB}$) which, for a sinc pattern, can be well approximated by a

$$\psi_{e,3dB} \approx 0.886 \frac{\lambda}{L_e}, \tag{2.9}$$

$$\psi_{a,3dB} \approx 0.886 \frac{\lambda}{L_a}. \tag{2.10}$$

2.2 SAR Image Formation

Differently from optical sensors, which provide ready-to-use information on the imaged scene almost at the same time of acquisition, each of the echoes received by a SAR sensor is composed by the superposition of responses from the group of scatterers on the ground located within the antenna beam. The echoes are arranged into a two-dimensional array where the coordinates are given by the time delay and the pulse number in slant range and azimuth direction, respectively, and are referred to as *raw data*. Due to the large number of scatterers contributing to each received radar echo, its In-phase (I) and Quadrature (Q) components can be well approximated as zero-mean Gaussian stationary and independent processes, as a consequence of the central limit theorem (CLT) [42]. According to the SAR acquisition geometry, the range time is typically referred to as *fast* time, since the time delay between transmission and reception of the SAR pulse is in the order of milliseconds and, for typical bandwidth values, adjacent range samples are a few nanoseconds apart. On the other hand, the azimuth time is referred to as *slow* time, as the SAR survey typically extends over several seconds. Figure 2.3 depicts a

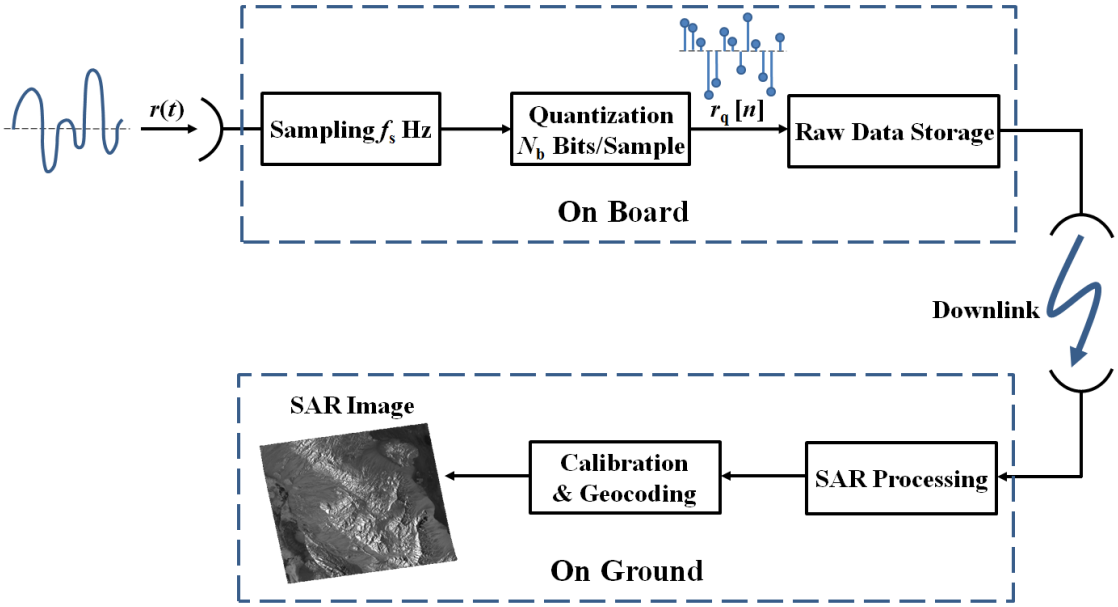

Figure 2.3: Schematic SAR workflow.

schematic workflow of the relevant steps for SAR imaging. The received analog signal $x(t)$ is conveniently sampled (discrete-time) at a certain range sampling frequency f_s and quantized (discrete-amplitude) with a pre-defined number of bits per sample N_b by an analog-to-digital converter (ADC), and the output signal $r_q[n]$ is stored on board in digital format. Once the SAR data take is completed, the raw data are downloaded to the ground (for spaceborne SAR typically a network of ground stations is employed). Since the individual targets are *defocused* in both range and azimuth directions in the SAR raw data matrix, proper SAR processing needs to be applied in order to reconstruct a two-dimensional image. Finally, calibration and geocoding are applied to convert the complex-valued SAR data to a meaningful and georeferenced measurement. These on-ground processing steps are explained in the following.

2.2.1 Range Focusing

Let $s(t)$ be a waveform which is modulated and transmitted at a certain time t by the SAR sensor. The signal which is scattered back from a point-like target (i.e., a target whose response dominates on the other targets within a single resolution cell) located at a slant range (line-of-sight) distance R and received back by the radar antenna $x(t)$, after coherent demodulation, will be an attenuated, delayed, and phase-shifted version of $s(t)$,

summed with an additive white Gaussian noise (AWGN) contribution $n(t)$

$$x(t) = A \cdot s\left(t - \frac{2R}{c_0}\right) \cdot \exp\left(-j\frac{4\pi R}{\lambda}\right) + n(t). \tag{2.11}$$

In the above equation, A represents the attenuation factor (i.e. $A < 1$), j is the imaginary unit, and the factor 2 multiplied by the slant range R takes into account the distance of the pulse traveling from the sensor to the target and back (see also (2.1)). Given these assumptions, it is known that the optimal linear time-invariant (LTI) filter for maximizing the output signal-to-noise ratio (SNR) is the so-called *matched filter*, whose impulse response is the conjugated (*) time-reversed replica of the transmitted signal [42], [48]

$$h(t) = s^*(-t). \tag{2.12}$$

Hence, the focusing process is achieved by convolving the received signal with its matched filter

$$\chi(t) = x(t) * h(t) = \int_{-\infty}^{+\infty} x(\tau)s^*(-(t-\tau))d\tau, \tag{2.13}$$

where $*$ denotes the convolution operator. Different scatterers on ground can be effectively detected only if their echoes are separated by sufficient time delays. If considering a rectangular pulse with duration τ_p used in transmission, one can show that the spatial resolution in the slant range direction δr_rect is approximately given by

$$\delta r_\mathrm{rect} \approx \frac{c_0 \tau_\mathrm{p}}{2}. \tag{2.14}$$

The above equation tells that higher resolutions can be only achieved by shortening the pulse length τ_p, which, in turn, implies a reduction of the radiated energy (which is proportional to τ_p), and hence of the resulting SNR after matched filtering (unless very high peak power is used for the pulse, which is also limited by technical constraints). In order to overcome this limitation, radar systems generally transmit a complex linear frequency modulated (LFM) pulsed waveform known as *chirp*, which is expressed as

$$s(t) = \exp\left[j\left(\phi_0 + 2\pi f_\mathrm{c} t + \pi k_\mathrm{r} t^2\right)\right] \cdot \mathrm{rect}\left(\frac{t}{\tau_\mathrm{p}}\right), \tag{2.15}$$

where t represents the range or *fast* time and f_c is the carrier frequency. The limited duration of the waveform is indicated by the rectangular rect function, which is defined as

$$\mathrm{rect}\left(\frac{t}{\tau_\mathrm{p}}\right) = \begin{cases} 1, |t| \leq \tau_\mathrm{p}/2 \\ 0, |t| > \tau_\mathrm{p}/2. \end{cases} \tag{2.16}$$

The instantaneous frequency of the chirp is

$$f_\mathrm{i}(t) = f_\mathrm{c} + k_\mathrm{r} t, \tag{2.17}$$

where k_r is the chirp rate. If a positive (negative) value of k_r is employed, a so-called up-chirp (down-chirp) is obtained. In both cases, the chirp bandwidth can be derived as

$$B_\mathrm{rg} = |k_\mathrm{r}|\tau_\mathrm{p}. \tag{2.18}$$

The amplitude of the chirp signal stays constant throughout the entire transmission, whereas the phase quadratically varies during the pulse extension (ϕ_0 is the initial phase shift). If a chirp signal as in (2.15) is employed, the normalized output $\chi(t)$ of the matched filter, for large values of the time-bandwidth product $B_\mathrm{rg}\tau_\mathrm{p}$ and aside from a scaling factor, can be well approximated by

$$\chi(t) \approx \mathrm{sinc}(B_\mathrm{rg} t). \tag{2.19}$$

As $R = c_0 t/2$, the above equation can be rewritten as

$$\chi(R) \approx \mathrm{sinc}\left(\frac{2B_\mathrm{rg}}{c_0} R\right). \tag{2.20}$$

The resulting range resolution is related to the width of the main lobe of $|\chi(R)|^2$. If the width between the maximum and the first null of $|\chi(R)|^2$ is considered (according to the definition of Rayleigh resolution), the attainable slant range resolution δr is given by

$$\delta r \approx \frac{c_0}{2B_\mathrm{rg}}. \tag{2.21}$$

Differently from δr_rect defined in (2.14), chirp signals achieve better resolutions when longer waveforms are radiated, according to (2.18), which also allow for the transmission of a larger amount of energy, hence resulting in higher SNRs. The ground range resolution δr_g is obtained by projecting the slant range resolution as

$$\delta r_\mathrm{g} = \frac{\delta r}{\sin(\eta)}. \tag{2.22}$$

Hence, the ground resolution varies with the incidence angle η along the swath. This variation is much larger for airborne SAR, where η may vary up to several tens of degrees within a stripmap scene, than for spaceborne configurations (only a few degrees), due to the different sensor altitude. For modern SAR systems, B_rg typically ranges between few tens up to several hundreds of MHz, so that range resolutions in the order of a few meters can be achieved. Figure 2.4 shows an exemplary chirp signal: its real and imaginary part are depicted in Figure 2.4 (a) and Figure 2.4 (b), respectively. Figure 2.4 (c) shows the instantaneous chirp frequency (for this example, a chirp pulse duration $\tau_\mathrm{p} = 20\ \mu$s and a range bandwidth $B_\mathrm{rg} = 10$ MHz are considered), and Figure 2.4 (d) depicts the signal obtained after matched filtering. Due to the property of the matched filter of concentrating the signal energy and increasing the resulting SNR, the described process is also referred to as *range focusing*, and the filtered data ($\chi(t)$ in (2.13)) are also known as range-compressed (or range-focused) data.

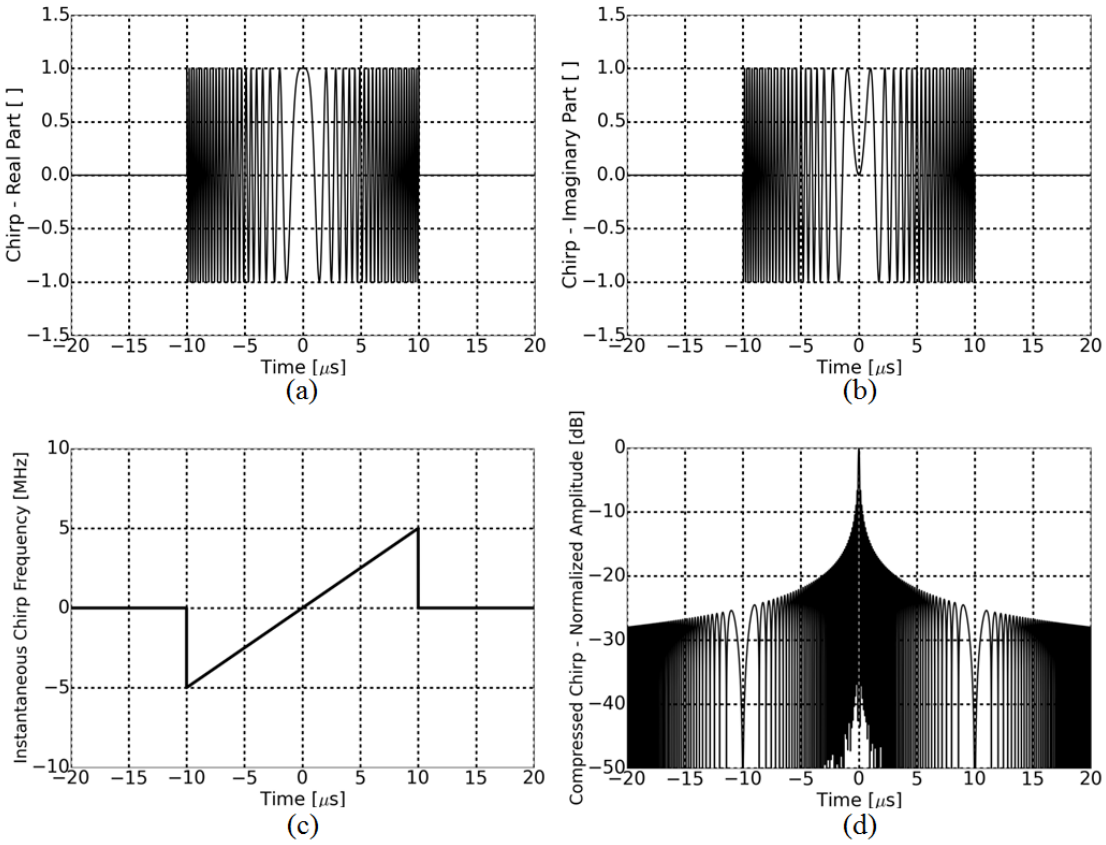

Figure 2.4: (a) Real part and (b) imaginary part of an exemplary chirp signal; (c) Instantaneous frequency shift; (d) Pulse-compressed amplitude.

2.2.2 Azimuth Focusing

In the azimuth direction, the resolution of a real aperture radar (RAR) system, i.e., if no additional processing is applied, is directly related to the size of the azimuth antenna footprint on ground, as in (2.2), which is recalled here

$$\delta a_{\mathrm{RAR}} = L_{\mathrm{s}} = \frac{\lambda R_0}{L_{\mathrm{a}}}. \tag{2.23}$$

As an example, the DLR satellites TerraSAR-X and TanDEM-X have an azimuth antenna length $L_{\mathrm{a}} = 4.8$ m and operate at X band (i.e., $\lambda = 3.1$ cm). By assuming a slant range R_0 of about 600 km, an azimuth resolution of $\delta a_{\mathrm{RAR}} \approx 4$ km is obtained, which is clearly not sufficient for most applications requiring high-resolution imaging. A better δa_{RAR} could be achieved by, e.g., increasing the antenna length, using shorter wavelengths, or reducing the distance between sensor and scatterer, but these requirements can not be

accomplished due to technical limitations.

The basic principle of synthetic aperture radar exploits the fact that, due to the movement of the sensor, a scatterer stays in the antenna beam (which has an angular aperture $\psi_a = \lambda / L_a$, as shown in Figure 2.5 (a)) for a time interval, also referred to as *integration time* t_{int}, which is given by

$$t_{int} = \frac{L_s}{v_s} = \frac{\lambda R_0}{L_a v_s}. \tag{2.24}$$

In particular, the echo received by the sensor at azimuth position $a(t)$ from a point target, assuming a rectangular antenna pattern, can be expressed as

$$w(a) = \exp\left(- j \frac{4\pi R(a)}{\lambda} \right) \cdot \mathrm{rect}\left(\frac{a}{L_s} \right), \tag{2.25}$$

where, for the sake of notation simplicity, the time dependence of the azimuth coordinate $a(t)$ has been omitted. At a certain azimuth or *slow* time t, the distance between the radar moving at constant velocity v_s and the point on the ground is obtained by using the Pythagorean theorem as

$$R(a) = \sqrt{R_0^2 + a^2} \approx R_0 + \frac{a^2}{2R_0} \tag{2.26}$$

As typically $R_0 >> L_s$, Taylor series expansion of $R(a)$ to the 1^{st}-order term is sufficient. The range distance R can be rewritten as function of the azimuth time (being $a = v_s t$) as follows

$$R(t) \approx R_0 + \frac{(v_s t)^2}{2R_0}. \tag{2.27}$$

Hence, the azimuth phase history $\phi(t) = 4\pi R(t)/\lambda$ has, with good approximation, a quadratic behavior. Figure 2.5 (b) shows the response of a non-moving target T (i.e., $v_T = 0$) in the data after range compression (see previous section): it is spread over several range cells, it is curved and the curvature varies along range. This phenomenon is also referred to as range cell migration and needs to be accurately corrected during the focusing operation [45].

Similarly to the range dimension, it can be demonstrated that the output of the matched filter applied to the azimuth signal $w(a)$ can be well approximated by [42]

$$v(a) = \mathrm{sinc}\left(\frac{2}{L_a} a \right). \tag{2.28}$$

The best azimuth resolution attainable by a SAR δa is related to the width of the main lobe of $|v(a)|^2$ and is given by

$$\delta a \approx \frac{L_a}{2}. \tag{2.29}$$

Hence, a finer azimuth resolution can, in principle, be achieved by reducing the azimuth antenna size. Moreover the resolution is independent of the range distance R and of the wavelength λ, as a result of the increasing length of the synthetic aperture (i.e., the larger the footprint, the longer the integration time, the sharper the resulting Doppler beam).

Another way to approach to the same problem is by considering that, during the time interval t_{int} (2.24), the target is located at distinct azimuth angles ψ with respect to the radar sensor. Therefore, it returns echoes each with a different instantaneous Doppler frequency shift f_{D} relative to the carrier frequency, which, in case the target T is fixed can be expressed as

$$f_{\text{D}}(t) = \frac{2v_{\text{s}}\sin(\psi(t))}{\lambda} \approx \frac{2v_{\text{s}}a(t)}{\lambda R_0} = -\frac{2v_{\text{s}}^2}{\lambda R_0}t. \tag{2.30}$$

In the above equation, the small angle approximation for ψ has been made. From the last term of (2.30) the Doppler rate can be derived as

$$k_{\text{D}} = \frac{\partial f_{\text{D}}(t)}{\partial t} = -\frac{2v_{\text{s}}^2}{\lambda R_0}, \tag{2.31}$$

similarly to the range chirp rate (see (2.17) and (2.18)). Figure 2.5 (c) shows the Doppler frequency shift resulting from the SAR configuration in Figure 2.5 (a) as a function of the azimuth time (or, equivalently, of the platform position). The analysis of the resulting Doppler frequency spectrum allows to improve the azimuth resolution, as discussed in the following. In particular, the Doppler frequency resolution δf_{D} can be approximated as the reciprocal of the integration time t_{int} in (2.24)

$$\delta f_{\text{D}} = \frac{1}{t_{\text{int}}} = \frac{L_{\text{a}}v_{\text{s}}}{\lambda R_0}. \tag{2.32}$$

By substituting in (2.30) one can finally derive the azimuth resolution for a SAR system as

$$\delta a \approx \frac{\lambda R_0}{2v_{\text{s}}}\delta f_{\text{D}} = \frac{\lambda R_0}{2v_{\text{s}}}\frac{L_{\text{a}}v_{\text{s}}}{\lambda R_0} = \frac{L_{\text{a}}}{2}, \tag{2.33}$$

which is equivalent to the result obtained in (2.29). Moreover, similarly to the definition of the range bandwidth in (2.18), the Doppler bandwidth can be expressed as the reciprocal of the time interval employed by the SAR to "travel" through one resolution cell or, equivalently, as a function of the Doppler rate k_{D}

$$B_{\text{D}} = \frac{v_{\text{s}}}{\delta a} = |k_{\text{D}}|t_{\text{int}} = \frac{2v_{\text{s}}}{L_{\text{a}}}. \tag{2.34}$$

Typically, an azimuth low-pass filter of width $B_{\text{D}} < \text{PRF}$ is applied to the focused SAR image to meet ambiguity requirements (as later on discussed in Section 2.3.4), which leads to an alternative definition of the best attainable azimuth resolution

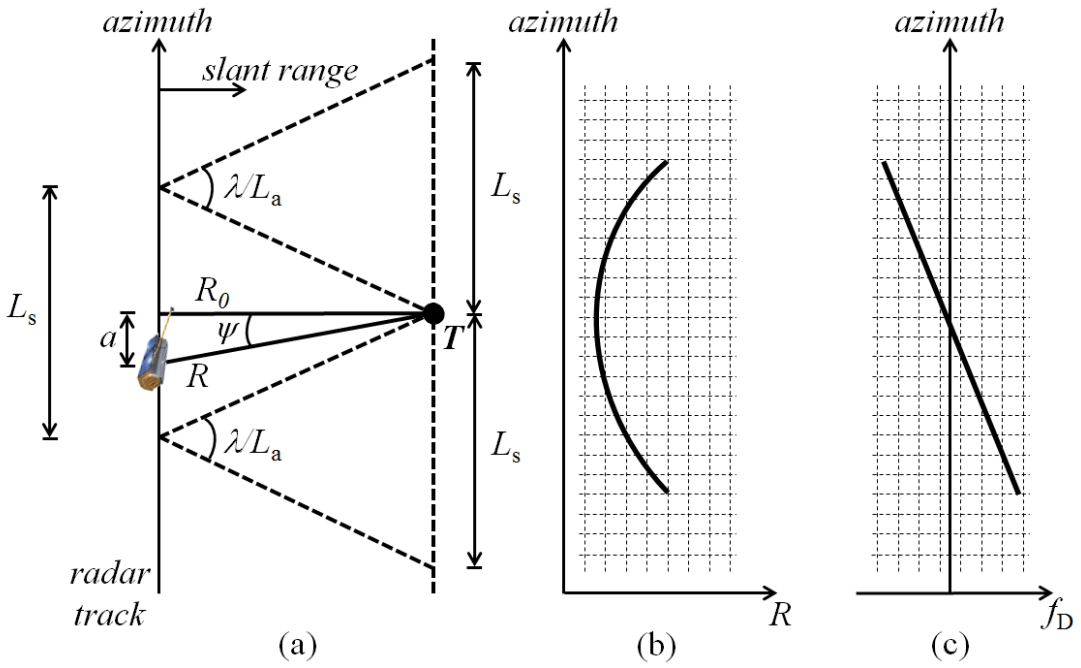

Figure 2.5: (a) Synthetic aperture; (b) Range cell migration; (c) Doppler frequency shift.

$$\delta a = \frac{v_s}{B_D}. \tag{2.35}$$

In conclusion, SAR processing basically consists of two linear filtering operations in range and azimuth dimension, respectively, to obtain focused SAR images. These are typically complex-valued two-dimensional matrices which are displayed as intensity values, often referred to as *digital numbers*. The so-called absolute calibration represents the subsequent necessary step to convert such numeric values into a physical quantity (such as the backscattering coefficient, see 2.3.2), which can be effectively used for information retrieval and/or to compare different sensors, e.g., operating at different frequency bands. Absolute calibration is typically carried out by using passive or active reference targets, such as corner reflectors and transponders, respectively [49], [50].

Focused SAR images are projected in radar coordinates, or slant-range geometry, which means that the position of each pixel depends on the corresponding range time delay and azimuth pulse number (or fast-slow times, respectively). Geocoding allows to locate each pixel into its georeferenced (latitude/longitude) position and, for this purpose, the precise knowledge of the sensor position (derived from the so-called *orbit state vectors*), the timing information associated to the SAR pulses, together with a sufficiently accurate reference digital elevation model (DEM) are needed as input. In case of a multi-polarization acquisition, the mentioned processing steps (focusing, calibration,

geocoding) are carried out for each channel, which can be then jointly exploited in order to retrieve relevant information on the scattering properties of the imaged scene [47].

2.2.3 SAR Acquisition Modes

By properly controlling the radiation pattern of the SAR antenna (see also Section 2.1), data acquisitions can be carried out in different modes, whose main characteristics are recalled in the following [46]:

- *Stripmap*: represents the "classical" SAR operation mode, where the antenna radiation pattern points to a fixed direction, so that the swath width remains constant over time and a single continuous strip is covered on ground (as shown in Figure 2.1). An expression of the Stripmap resolution in azimuth is derived in (2.33). For, e.g., an X-band SAR such as TanDEM-X, the swath width is typically of about 30 km and an azimuth resolution of about 3 m (in single polarization) can be attained.

- *ScanSAR*: Similarly to Stripmap, the ScanSAR mode is also a continuous imaging mode, meaning that the acquisition is in principle not limited along the azimuth direction. However, the swath width position is adjusted by continuously and cyclically switching the elevation angle of the antenna radiation pattern (hence in range direction), which allows for the acquisition of multiple sub-swaths and hence of a wider resulting swath. This increase in imaged swath width (up to several hundreds of kilometers) requires a proportional degradation in azimuth resolution (typically 20 m or larger). Moreover, due to the continuous beam switching, each target is illuminated by a different portion of the antenna pattern, which results in a periodic amplitude fluctuation in the resulting SAR image, also known as scalloping.

- *Spotlight*: The antenna pattern is steered in the azimuth direction so that a defined area on ground is illuminated for a longer time as the antenna moves along the flight path. This, in turn, results in an improved azimuth resolution, which is typically in the order of 1 m, even though a limited area of a few kilometers in azimuth can be acquired (in this sense, spotlight is not a continuous imaging mode).

- *Terrain Observation with Progressive Scan (TOPS)*: As for ScanSAR, in *TOPS* mode [51] multiple sub-swaths are acquired quasi-simultaneously by switching the antenna pattern from burst to burst, and the increased swath coverage is achieved at the cost of a reduced azimuth resolution. Nevertheless, in TOPS mode a dynamic antenna steering along azimuth in the opposite direction as done in Spotlight mode is added. In this way, the same performance in terms of coverage and resolution as ScanSAR is achieved, but with a more uniform image performance (drastic mitigation of scalloping effects).

Table 2.1: Acquisition modes and corresponding azimuth resolution and swath width for the imaging modes available for the TerraSAR-X system.

Mode	Azimuth Resolution [m]	Swath Width [km]
Wide ScanSAR	40	250
ScanSAR	18	100
Stripmap	3	30
Sliding Spotlight	1	10
Staring Spotlight	0.2	5

As an example, Table 2.1 summarizes the performance in terms of swath width and azimuth resolution achieved by the different acquisition modes available for the TerraSAR-X system [52], [53], [28]. The parameters are considered for single-polarization mode. It can be noticed that, in general, a better azimuth resolution has to be traded with a smaller swath width.

In the last decades, innovative spaceborne radar techniques have been proposed to overcome these limitations, allowing for high-resolution imaging of a wide swath. For this purpose, multiple azimuth channels (MAC) [40] or the cyclic variation of the system PRI (so-called staggered SAR mode [41]) can be exploited together with digital beamforming (DBF) in elevation to achieve Scan-on-Receive (SCORE), [54], [55], [56], [57], [58]. The resulting improvements in coverage and azimuth resolution imply a proportional increase in terms of data volume which has to be managed by the SAR system, hence requiring efficient strategies for onboard data volume reduction, as it will be further detailed in Chapter 6 and Chapter 7.

2.2.4 Geometric Distortions

Due to the peculiar side-looking operation of SAR sensors, SAR images are typically affected by geometric distortions, which occur because the radar projects the three-dimensional scene under illumination into a two-dimensional plane (also called slant-range geometry). Such distortions are independent of the antenna footprint and are caused by the specific relation between the elevation angle θ_e employed by the sensor for the SAR survey and the local terrain slope α. They are shortly recalled in the following:

- *Foreshortening*: If the terrain slope is positive ($\alpha > 0$, i.e., facing towards the sensor) a compression of the distances with respect to the sensor is observed in the SAR image. The larger the local slope α, the stronger the foreshortening, which can be effectively resolved after image geocoding;

- *Layover*: Above the limit where $\alpha > \theta_e$, the region is said to be in layover, which results in a point inversion in the SAR image. This is shown in Figure 2.6 (a),

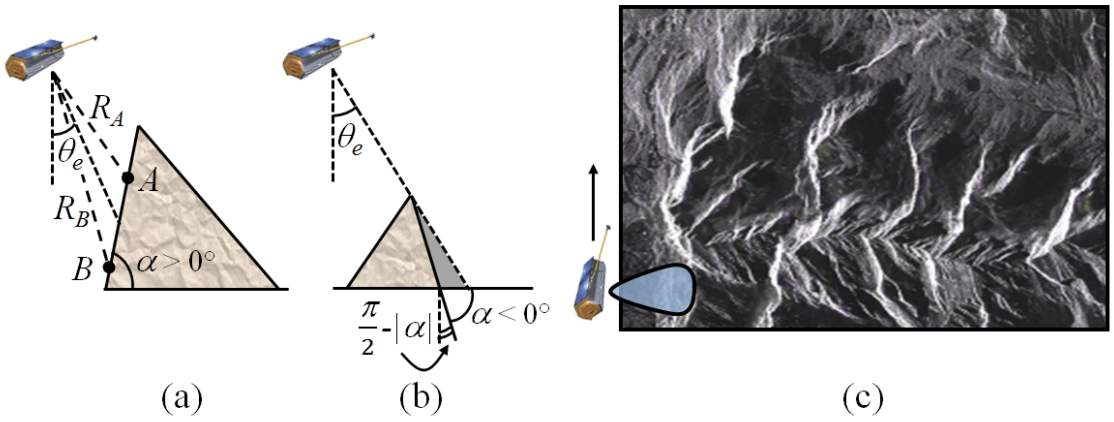

Figure 2.6: (a) Condition for layover: if $\alpha > \theta_e$ the radar echo associated to the target A is received by the sensor before the one associated to the target B, being $R_A < R_B$, which results in a point inversion in the SAR image; (b) If $\alpha < 0$ and $\frac{\pi}{2} - |\alpha| < \theta_e$ shadow occurs, which is highlighted by the gray area; (c) SAR amplitude acquired the over Austrian Alps by the TanDEM-X satellite on April 11, 2012 which shows perspective deformations: extremely bright and dark areas correspond to layover and shadow, respectively.

where the distance between the sensor and the target A (R_A) is smaller than the distance between the sensor and the target B (R_B);

- *Shadowing* corresponds to ground areas which are not illuminated by the radar beam because they are hidden behind high-relief terrain. Shadow areas occur when $\alpha < 0$ (i.e., the terrain faces away from the sensor) and $\frac{\pi}{2} - |\alpha| < \theta_e$ and appear as missing data in the SAR image, as shown in Figure 2.6 (b). In addition, areas for which the above conditions are not met may be shadowed by parts of the imaged surface at smaller slant range.

In general, the observation angle θ_e of the sensor should be chosen to balance, and to minimize, the occurrence of layover and shadow. Figure 2.6 (c) shows the SAR amplitude of an area in the Austrian Alps acquired by the TanDEM-X satellite and affected by geometric distortions: the mountains look compressed towards the sensor (which flies bottom-left to top-left of the image) as a consequence of foreshortening; bright and dark areas correspond to layover and shadow, respectively.

2.3 System and Performance Parameters

In this section the main parameters and performance figures of a SAR system, which are relevant for the proper system design with respect to typical applications, are reviewed.

2.3.1 Resolution and Sidelobes

In Section 2.2 the system resolution has been derived from the two-dimensional (azimuth-range) response from a single point target in the scene. This is typically referred to as the SAR impulse response function (IRF) and can be well approximated as the product of the output of the matched filter $\chi(R)$ and $\nu(a)$, which have been defined in (2.20) and (2.28) as a function of the slant range and azimuth coordinate, respectively. The two-dimensional IRF $I(R,a)$ is expressed as

$$I(R,a) \approx \chi(R) \cdot \nu(a) = \operatorname{sinc}\left(\frac{2B_{\mathrm{rg}}}{c_0}(R-R_0)\right) \cdot \operatorname{sinc}\left(\frac{2}{L_{\mathrm{a}}}(a-a_0)\right), \tag{2.36}$$

being R_0 and a_0 the slant range and azimuth coordinates where the point target is located. The SAR impulse response has a mainlobe centered in $(R,a) = (R_0,a_0)$, and the half-power widths in the two perpendicular dimensions correspond to the slant range and azimuth resolution, as in (2.21) and (2.33), respectively. However, $I(R,a)$ also presents sidelobes, which affect the image quality possibly leading to the masking of neighboring weaker targets. A way to mitigate sidelobes is by employing additional weighting to the transfer function of the matched filters, which however implies a degradation in the resulting resolution [59].

The presence of sidelobes is quantified by the peak sidelobe ratio (PSLR), which is equal to the ratio between the peak intensity of the highest (usually the first) sidelobe $I_{\mathrm{SL,max}}$ and the peak intensity of the mainlobe I_{ML}

$$\mathrm{PSLR} = \frac{I_{\mathrm{SL,max}}}{I_{\mathrm{ML}}}. \tag{2.37}$$

Alternatively, the integrated sidelobe ratio (ISLR) is the ratio of the energy outside the mainlobe integrated over a region of size $20\delta a \times 20\delta r$, E_{SL}, to the energy integrated over the mainlobe E_{ML}, which is defined as lying within an area of size $2\delta a \times 2\delta r$ centered on the IRF peak

$$\mathrm{ISLR} = \frac{E_{\mathrm{SL}}}{E_{\mathrm{ML}}}. \tag{2.38}$$

2.3.2 Radar Backscatter and Speckle

As observed by a SAR sensor, the scatterers can generally be categorized in two types:

- A *point target* is characterized by the presence of a single dominant scatterer within the resolution cell. Let us consider a single point target located at distance R from the sensor. The target is illuminated by the antenna beam, transmitting at polarization p, and reflects the radiated energy in different directions. Therefore, only a fraction of the scattered energy at polarization q is received by the sensor, which is described by the *point target radar equation* [60]. For a monostatic radar, it can be expressed as follows

$$P_q^r = \frac{P_p^t G_p G_q \lambda^2}{(4\pi)^3 R^4} \sigma_{pq}, \tag{2.39}$$

  where P_p^t and P_q^r are the transmitted p-polarized power and the received q-polarized power, respectively (the p and q indices may correspond, e.g., to the linear horizontal polarization H and/or the vertical polarization V). Using the same notation, G_p and G_q are the transmit and receive antenna gains for the p and q polarization channels, respectively (for a monostatic radar, given a p-polarization, it holds $G_p^t = G_p^r = G_p$). Finally, σ_{pq} is the so-called *radar cross section*, which is a measure of the fraction of power density effectively re-radiated (backscattered) to the sensor S_q^s with respect to the power density intercepted by the target S_p^i, and is defined as [60]

$$\sigma_{pq} = \lim_{R\to\infty} \left(4\pi R^2 \frac{S_q^s}{S_p^i} \right). \tag{2.40}$$

  The above equation is valid in far-field approximation, denoted by the limit $R \to \infty$.

- Differently from point targets, *distributed targets* can be understood as the ensemble of many non-dominant scatterers within a single resolution cell. According to this, distributed targets can be modeled as Gaussian random variables, as a consequence of the central limit theorem.

  The radar equation for distributed targets is derived by integrating (2.39) over the illuminated area A_σ:

$$P_q^r = \iint_{A_\sigma} \frac{P_p^t G_p(\theta_\mathrm{e}, \phi_\mathrm{a}) G_q(\theta_\mathrm{e}, \phi_\mathrm{a}) \lambda^2}{(4\pi)^3 R^4} \sigma_{pq}^0 \, dA_\sigma, \tag{2.41}$$

  where θ_e and ϕ_a are the boresight elevation angle and the squint angle of the transmitter, respectively, and identify the direction to a point inside the considered area A_σ with respect to the sensor. σ_{pq}^0 represents the backscattering coefficient per unit area. It is a dimensionless number and is defined as the radar cross section σ_{pq} of a distributed target of area A_σ, normalized with respect to A_σ itself:

$$\sigma^0_{pq} = \lim_{A_\sigma \to 0} \left(\frac{\sigma_{pq}}{A_\sigma} \right). \tag{2.42}$$

A SAR image consists of pixels of varying intensities, any one of which is obtained as coherent combination of all point scatterers lying within the corresponding resolution cell. Due to the random distribution of the scatterers, this superposition effect implies areas having the same backscatter coefficient σ^0_{pq} to show different pixel intensities. Such spatial variance of the pixels' intensity is also referred to as *speckle*. Speckle can be modeled as a multiplicative disturbance source, i.e., its variance increases with the signal intensity [46], hence it cannot be mitigated by simply increasing the transmit power and/or the antenna gain. On the other hand, speckle can be reduced by applying a non-coherent averaging (i.e., only the pixels' intensity or amplitude is averaged) to the radar image, a technique which is known as *multi-looking* [48]. In particular, if N_l pixels of the same region are averaged together, a consistent degradation of the resolution by a factor N_l is observed in the multi-looked image, together with a reduction of the standard deviation of the backscatter by a factor $\sqrt{N_\mathrm{l}}$ (despeckling). This implies an improvement in terms of radiometric resolution and, in general, may greatly improve the interpretability of the final SAR image. In this sense, multi-looking can be considered as a low-pass filter applied to the processed SAR image, which can be implemented in different domains:

- *Spatial domain*: Adjacent pixels within a window with fixed dimension are averaged over the number of pixels;
- *Time domain*: The synthetic aperture of the antenna is separated into N_l shorter segments (temporal sub-looks), and each segment is separately processed, resulting in a set of N_l SAR images at lower resolution;
- *Frequency domain*: Similarly to the multi-looking in time domain, the Doppler spectrum of the raw data is split into segments (frequency sub-looks) and then separately processed.

2.3.3 Noise Equivalent Sigma Zero

The signal-to-noise ratio (SNR) describes how much a signal has been corrupted by noise and is a measure of image quality for remote sensing systems. The SNR is maximized after matched filtering and, from a processed pq-polarized SAR image, it can be computed as follows

$$\mathrm{SNR}_{pq} = \frac{\sigma^0_{pq}}{\mathrm{NESZ}_{pq}}, \tag{2.43}$$

being NESZ the noise equivalent sigma zero. It describes the sensitivity of a SAR system to areas of low radar backscatter and includes contributions such as the antenna gain, the

instrument thermal noise, and the processing filters. The SNR depends on the local backscatter distribution, whereas the NESZ corresponds to the backscattering coefficient that leads to SNR = 1, hence giving information about the system sensitivity to low backscatter intensities. The NESZ can be derived from the radar equation as

$$\mathrm{NESZ}_{\mathrm{pq}} = \frac{4^4 \pi^3 R^3 v_{\mathrm{s}} \sin(\eta) k_{\mathrm{B}} T_{\mathrm{r}} B_{\mathrm{rg}} F_{\mathrm{N}} L_{\mathrm{tot}}}{P_p^t G_p G_q \lambda^3 c_0 \tau_{\mathrm{p}} \mathrm{PRF}}, \tag{2.44}$$

where k_{B} is the Boltzmann constant, T_{r} is the receiver temperature, F_{N} is the noise figure, and L_{tot} includes all loss contributions (such as, e.g., system, processor, atmosphere). On spaceborne SAR, NESZ is typically estimated by means of receive-only pulses, which are commanded during each imaging data take.

2.3.4 Ambiguities and Nadir Returns

As a consequence of the Shannon sampling theorem, the pulse repetition frequency (PRF) used for transmission must be larger than the signal Doppler bandwidth

$$\mathrm{PRF} \geq B_{\mathrm{D}} \tag{2.45}$$

or, equivalently,

$$v_{\mathrm{s}} \cdot \mathrm{PRI} \leq \frac{L_{\mathrm{a}}}{2}. \tag{2.46}$$

In general, the finite sampling of the Doppler spectrum at frequency PRF causes aliasing in the processed SAR image and increases the so-called azimuth ambiguities, which correspond to those portions of the signal which fold back into the main part of the processed spectrum. Azimuth ambiguities are typically visible over weak backscatter regions close to strong ones (e.g., the sea closed to an urban area) and are quantified by the azimuth ambiguity-to-signal ratio (AASR), defined as the ratio between the local power of the ambiguous signal and the local power of the main signal as

$$\mathrm{AASR} = \frac{\sum\limits_{\substack{m=-\infty, \\ m\neq 0}}^{+\infty} \int_{f=-B_{\mathrm{D}}/2}^{B_{\mathrm{D}}/2} G^2(f + m \cdot \mathrm{PRF}) \cdot Q^2(f) df}{\int_{f=-B_{\mathrm{D}}/2}^{B_{\mathrm{D}}/2} G^2(f) \cdot Q^2(f) df}, \tag{2.47}$$

where f is the Doppler frequency, $Q(f)$ accounts for the amplitude weighting of the Doppler spectrum in the processing, $B_{\mathrm{D}} < \mathrm{PRF}$ is the processed Doppler bandwidth and G^2 represents the two-way antenna power pattern. For the sake of simplicity, the dependency on the polarization has been here neglected, hence $G_p = G_q = G$, differently from the previous equations, e.g., (2.44). According to (2.46), the radar must send at least one

pulse before moving by half of the antenna length L_a to achieve the best achievable resolution and to avoid the emergence of ambiguities. Moreover, a finer azimuth resolution is attained by increasing the Doppler bandwidth of the received signal (as in (2.35)). This, in turn, increases the required PRF, hence limiting the extension of the swath width W_g as in (2.5).

Range ambiguities arise from echoes which precede and/or follow the desired returns and are received by the radar all together. Range ambiguities are therefore generated from regions outside the focused image and their impact is evaluated by means of the RASR (range ambiguity-to-signal ratio), which is a function of the elevation angle θ_e and is defined as follows

$$\mathrm{RASR}(\theta_\mathrm{e}) = \frac{\displaystyle\sum_{j=1}^{N_\mathrm{A}} \frac{\sigma^0(\eta_j)\displaystyle\int_{f=-B_\mathrm{D}/2}^{B_\mathrm{D}/2} G^2(\theta_{\mathrm{e},j},f)\cdot Q^2(f)df}{R_j^3\sin(\eta_j)}}{\dfrac{\sigma^0(\eta_\mathrm{main})\displaystyle\int_{f=-B_\mathrm{D}/2}^{B_\mathrm{D}/2} G^2(\theta_{\mathrm{e,main}},f)\cdot Q^2(f)df}{R_\mathrm{main}^3\sin(\eta_\mathrm{main})}}, \tag{2.48}$$

where the subscript j ($j = 1,...,N_\mathrm{A}$) refers to the N_A ambiguous returns preceding and following the desired return, which is indicated with the subscript "main".

Summarizing, the PRF is constrained by the following

$$\frac{2\,v_\mathrm{s}}{L_\mathrm{a}} < \mathrm{PRF} < \frac{c_0}{2W_\mathrm{g}\,\sin(\eta)}, \tag{2.49}$$

which implies the constraint

$$W_\mathrm{g} < \frac{c_0\,L_\mathrm{a}}{4\sin(\eta)}. \tag{2.50}$$

In addition to that, the PRF needs to be selected in order to accurately synchronize the transmission and the reception of the radar pulse. Indeed, for spaceborne SAR, each pulse typically takes several PRIs to travel from the sensor to the target and back (the so-called rank), as it has been illustrated in Section 2.1. Moreover, for each pulse the first echo is received from the nadir, i.e., the direction pointing vertically from the sensor to the ground. Due to the coherent backscatter over a large area, nadir echoes can have very strong response. Hence, the PRF must be selected such that nadir echoes are sufficiently attenuated by the antenna gain or, if this is not possible, they must be received outside the receive echo window (e.g., during a pulse transmission, when the system is blind to reception).

2.4 SAR Interferometry

SAR interferometry (InSAR) represents nowadays a well-recognized technique for many remote sensing applications. It exploits the *phase difference* of at least two complex SAR images, acquired from different orbit positions and/or at different times. This derived information allows for the estimation and assessment of many geophysical parameters, such as ocean currents, ground deformations, and Earth's topography by generation of digital elevation models (DEMs). About four decades of research studies, technical progress, and developments in the field have demonstrated the potentials of spaceborne and airborne InSAR systems, and DEMs are widely employed in a broad range of commercial and scientific applications, such as, for example, Geographic Information System (GIS), Global Positioning System (GPS), as well as many geoscience fields, like geology, physical geography, glaciology, and oceanography. A comprehensive overview of the most relevant concepts and applications of SAR interferometry can be found in [61], [62], [63], [64]. The basic principles of InSAR and its different modes of operations are shortly described in the following.

2.4.1 Geometry and Operation Modes

Figure 2.7 shows two SAR sensors S_1 and S_2 at approximate orbit height h_s and elevation angle θ_e. They observe a target T at height z from different positions and fly in a direction perpendicular to the plane of the figure, as indicated by the symbol on the right-hand side. The slant range distances are denoted with R_1 and R_2, respectively, and the distance between the two sensors B is the interferometric baseline. If two images are simultaneously acquired, then the interferometric acquisition is said to be in *single-pass* mode. If, on the other hand, the two images are acquired at different times, it is said to be in *repeat-pass* mode. In this case the individual acquisitions can be carried out by the same or by different sensors revisiting the area of interest. Furthermore, the InSAR acquisition can be performed in *monostatic* or *bistatic* configuration. In the former both satellites are used for transmission and reception, whereas in the latter either S_1 or S_2 is used for transmission and both satellites simultaneously record the signal backscattered from the Earth's surface. If the two SAR antennas are aligned in the flight direction and are separated by a certain distance (so-called along-track baseline, which is ideally equal to zero in Figure 2.7) then *along-track* interferometry is performed. This mode is employed, e.g., for the estimation of ocean currents, and is typically carried out in single-pass mode. If the two SAR antennas are separated in the plane perpendicular to the flight direction, like in Figure 2.7, *across-track* interferometry is considered. Across-track interferometry can be performed both in single-pass and repeat-pass configurations and is primarily used for topography estimation (DEM). For this, the baseline perpendicular to the line of sight (or across-track baseline $B_\perp$) is relevant for the interferometric height inversion and for the resulting accuracy, as it will be clarified in the next subsec-

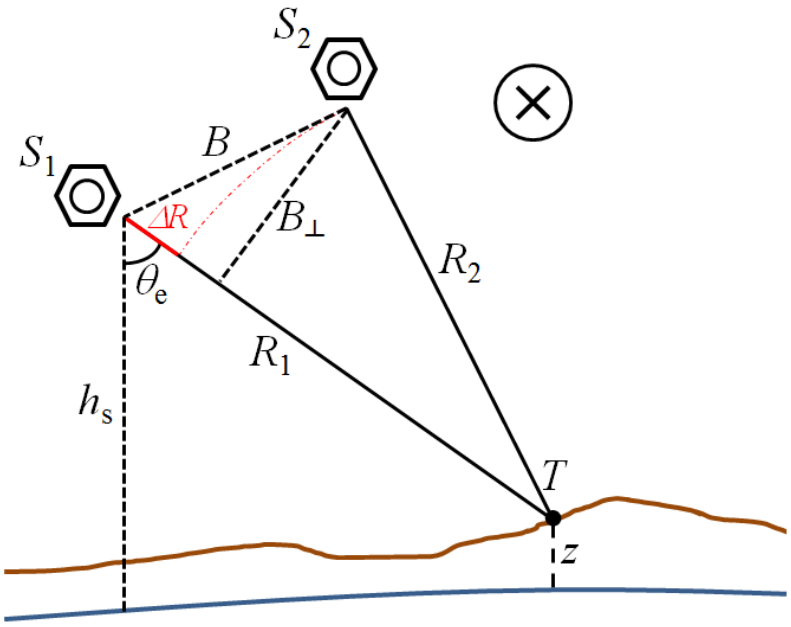

Figure 2.7: Interferometric SAR geometry in across-track configuration.

tion. Looking at Figure 2.7, the topographic height z can be derived using trigonometric relations as

$$z = h_s - R_1 \cos(\theta_e). \tag{2.51}$$

The two-dimensional image obtained as the product of the reference image (or *master*, e.g., I_1) and the conjugate of the *slave* image I_2 defines the *interferogram* υ

$$\upsilon = I_1 \cdot I_2^* = |I_1||I_2| e^{j(\phi_1 - \phi_2)}. \tag{2.52}$$

The phase recorded by each SAR sensor $\phi_{1,2}$ is composed of two terms: the propagation phase, which is proportional to the distance between the sensor and the target, and the backscattered phase, which is influenced by the surface backscattering characteristics (such as, e.g., moisture and roughness). Assuming a repeat-pass monostatic configuration, for the sensor S_1 the phase of each complex pixel of the SAR image I_1 is then given by

$$\phi_1 = -\frac{4\pi}{\lambda} R_1 + \phi_{\text{scat},1}, \tag{2.53}$$

and for the image I_2 acquired by the sensor S_2 it is given by

$$\phi_2 = -\frac{4\pi}{\lambda} R_2 + \phi_{\text{scat},2}. \tag{2.54}$$

According to the acquisition geometry depicted in Figure 2.7, and assuming the scattering phase to be the same in both images (i.e., $\phi_{\text{scat},1} = \phi_{\text{scat},2}$) the *interferometric phase* φ can be expressed as

$$\varphi = \angle \underline{v} = \phi_1 - \phi_2 = \frac{4\pi}{\lambda} \Delta R, \tag{2.55}$$

where $\Delta R = |R_1 - R_2|$ represents the travel path difference between the signals received by S_1 and S_2, and is highlighted by the bold red segment in Figure 2.7. Hence, the InSAR phase is a very sensitive measure for the range difference, and with this it is possible to measure small path length differences with centimetric or even millimetric accuracy, which is independent of the distance between the radar and the target.

Clearly, the interferometric phase difference is still ambiguous (i.e., "wrapped") to within integer multiples of 2π, which leads to the well-known interferometric "fringes". Therefore, to reconstruct the topographic height, the wrapped interferometric phase needs to be properly converted into an absolute phase φ_{abs}, a process which is known as *phase unwrapping*. Several methods and different algorithms have been developed throughout the years to solve the unwrapping problem, the most important of those are presented in [65], [66], [67], [68]. The final phase-to-height conversion is carried out by means of the so-called *height of ambiguity* h_{amb}, which represents the height difference corresponding to a complete 2π cycle of the interferometric phase and is defined as

$$h_{\text{amb}} = \frac{\lambda R \sin(\theta_{\text{e}})}{p B_{\perp}}, \tag{2.56}$$

being $R \approx (R_1 + R_2)/2$ the mean slant range and p a scaling factor which depends on the specific acquisition configuration: in the monostatic case $p = 2$, whereas in the bistatic configuration (single-pass mode) $p = 1$. Hence, the phase-to-height scaling resulting from bistatic InSAR is twice as much with respect to the one from a monostatic acquisition operated with the same interferometric baseline $B_{\perp}$.

2.4.2 Interferometric Coherence

One of the key parameters used to evaluate the quality and performance of InSAR products is the interferometric coherence γ. It represents the normalized complex correlation coefficient between master I_1 and slave I_2 acquisitions and provides information about the amount of noise in the interferogram [63], [69], [70]

$$\gamma = |\gamma| \cdot e^{j\angle\gamma} = \frac{\mathbb{E}[I_1 \cdot I_2^*]}{\sqrt{\mathbb{E}[|I_1|^2] \cdot \mathbb{E}[|I_2|^2]}}, \tag{2.57}$$

where $\mathbb{E}[\cdot]$ represents the expectation operator. The magnitude of coherence values ranges from 0 (no correlation) to 1 (perfect correlation). The higher the coherence, the

more accurate the resulting DEM will be. Practically, due to the non-stationarity of the imaged SAR scene, for each pixel of indices $[m,n]$ the coherence is estimated from the interferometric pair within a typically rectangular window W centered on the pixel of interest and extending up to a few tens of pixels in azimuth and range [70]. For performance assessment the absolute value of the estimated coherence $\hat{\gamma}$ is taken into account

$$|\hat{\gamma}[m,n]| = \frac{\left|\sum_{W} I_1[m,n] I_2^*[m,n]\right|}{\sqrt{\sum_{W} |I_1[m,n]|^2 \sum_{W} |I_2^*[m,n]|^2}}. \tag{2.58}$$

Before coherence computation, proper *coregistration* of the two complex SAR images needs to be applied to compensate for the different acquisition geometry: each pixel of the slave image must be resampled to the corresponding pixel location in the master one, and an accuracy in the order of a small fraction of an image pixel is required for typical interferometric applications. As an example, Figure 2.8 (a) shows the SAR amplitude (in slant-range coordinates) acquired by TanDEM-X for an area located in Death Valley (Nevada, USA) and Figure 2.8 (b) depicts the wrapped interferometric phase (for this bistatic data take, $h_{\text{amb}} \approx 30$ m). Figure 2.8 (c) illustrates the geocoded coherence map (0: black, 1: white) and 2.8 (d) represents the resulting color-coded digital elevation model. As it can be seen, different areas of the coherence map show different degrees of correlation. Indeed, several error sources may contribute to a loss in the interferometric coherence, which, assuming statistical independence, can be rewritten as [30], [63], [69], [71], [72]

$$\gamma = \gamma_{\text{SNR}} \cdot \gamma_{\text{Vol}} \cdot \gamma_{\text{Amb}} \cdot \gamma_{\text{Rg}} \cdot \gamma_{\text{Az}} \cdot \gamma_{\text{Temp}} \cdot \gamma_{\text{Quant}}, \tag{2.59}$$

where each correlation factor on the right-hand side describe coherence loss due to: limited signal-to-noise ratio (γ_{SNR}), volume decorrelation (γ_{Vol}), ambiguities (γ_{Amb}), baseline decorrelation (γ_{Rg}), errors due to relative shift of Doppler spectra (γ_{Az}), temporal decorrelation (γ_{Temp}). The last term γ_{Quant} represents the coherence loss due to raw data quantization. In general, the use of lower bit rates for the onboard raw data digitization results in an increased loss of coherence (hence smaller values of γ_{Quant}), and vice versa. Clearly, there exists a trade off between the quantization rate employed and, eventually, the total number of acquisitions achievable within a certain time interval, which both directly impact the total data rate and the resulting interferometric image quality. This trade off must be carefully taken into account due to typical limitations in the downlink capacity and due to mission constraints. The investigation and assessment of quantization errors on interferometric SAR performance, specifically in the context of the TanDEM-X mission, is investigated in detail in Chapter 4.

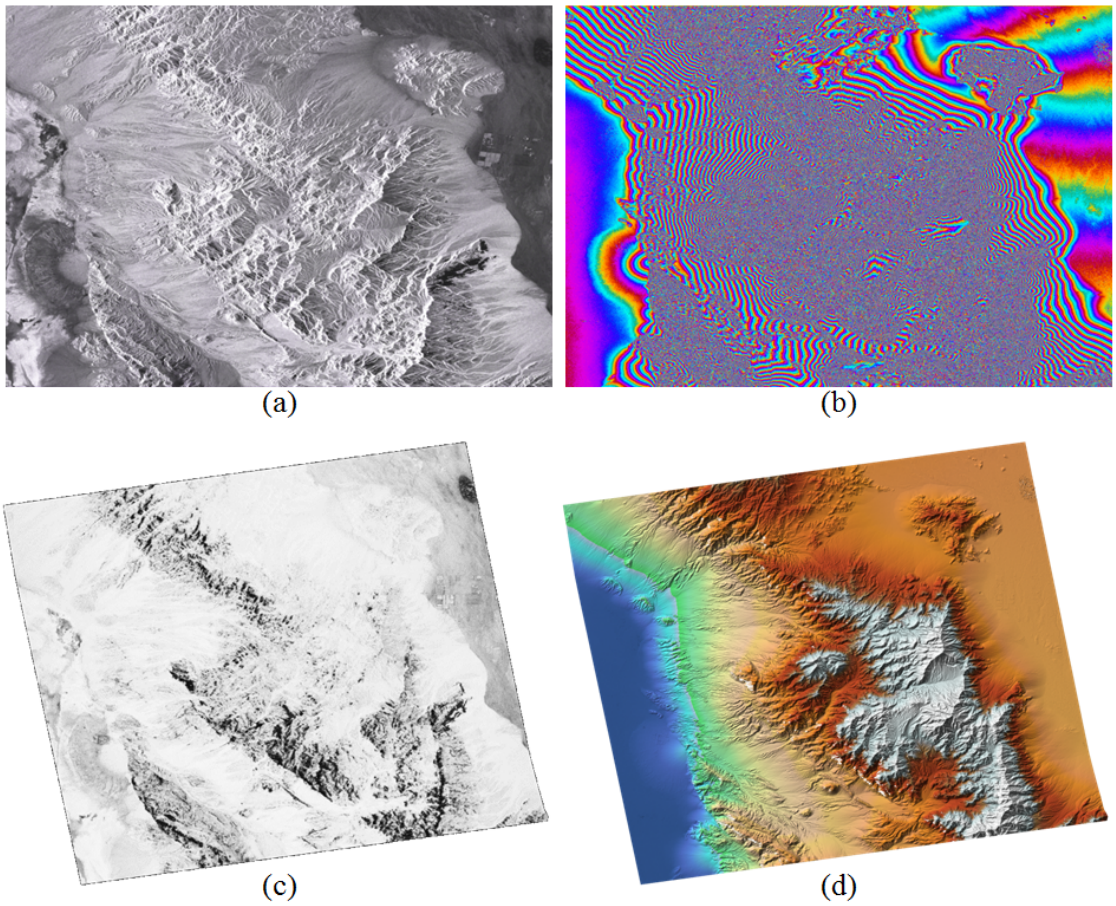

Figure 2.8: (a) SAR amplitude and (b) interferometric phase after flat-Earth removal, both in slant-range geometry; (c) Geocoded interferometric coherence and (d) digital elevation model of the Death Valley (Nevada, USA) acquired by TanDEM-X on June 9, 2012.

In addition to quantization, it is worth recalling the error sources which typically most affect the performance of interferometric SAR. In particular, the limited system sensitivity causes a loss in the SNR which, in turn, degrades the quality of the measured phase and the interferometric coherence as [63]

$$\gamma_{\mathrm{SNR}} = \frac{1}{\sqrt{(1+\mathrm{SNR}_1^{-1})\cdot(1+\mathrm{SNR}_2^{-1})}}, \tag{2.60}$$

where SNR_1 and SNR_2 are the signal-to-noise ratio (SNR) estimates for the interferometric channels associated to I_1 and I_2, respectively, as defined in (2.43). Deviations

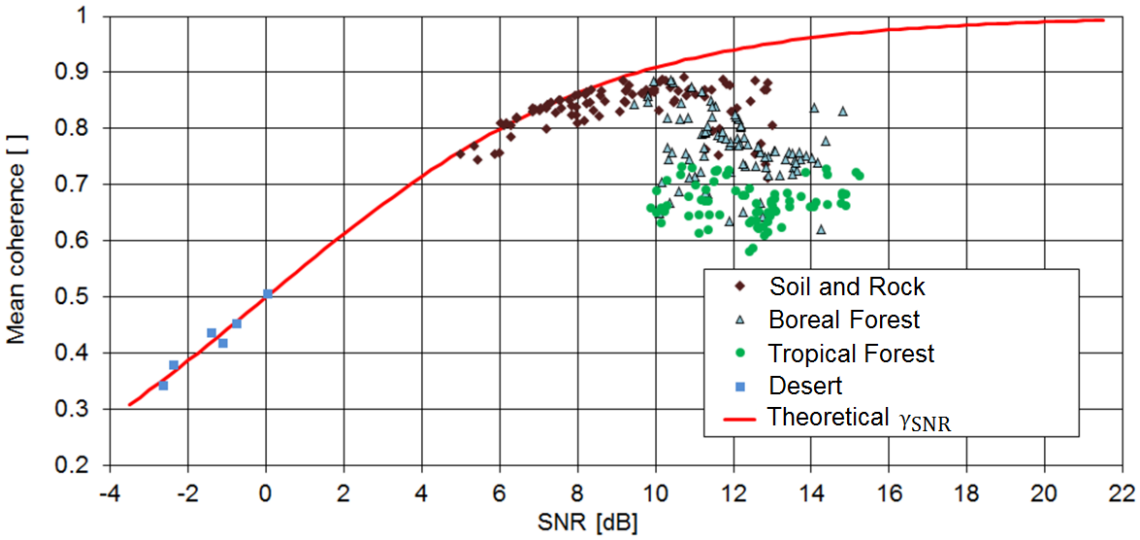

Figure 2.9: Estimated interferometric coherence $\hat{\gamma}$ over signal-to-noise ratio (SNR). The red line indicates the theoretical SNR correlation factor γ_{SNR}, as defined in (2.60).

between SNR_1 and SNR_2 may be due to changes in the scene backscatter or due to differences/changes in the antenna patterns among the two channels.

Figure 2.9 [71] shows the estimated interferometric coherence $\hat{\gamma}$ as a function of SNR for single-pass interferograms acquired by TanDEM-X over test sites showing different vegetation and soil characteristics (for TanDEM-X, the SNR difference between the two channels of a single bistatic acquisition is typically very small, in the order of a fraction of a dB, hence $\mathrm{SNR}_1 \approx \mathrm{SNR}_2$ with reasonable approximation). The red line on the top of the figure indicates the theoretical SNR coherence as defined in (2.60), i.e., the expected coherence as if the finite sensitivity of the SAR system was the only error source, which proves, indeed, the presence of additional decorrelation (as in (2.59)). For most of the land cover types SNR values typically higher than 5-6 dB and coherence almost always greater than 0.6 is obtained. However, performance over sandy desert (blue squares in Figure 2.9) is strongly affected by the weak power of the backscattered signal from sand: for SNR smaller than 2 dB a coherence above 0.5 can be rarely observed. For this reason, an optimization of the imaging geometry over sandy regions has been carried out during the TanDEM-X mission, mainly by employing steeper incidence angles (for TanDEM-X, the nominal incidence angle interval ranges between about 30° and 50°). This allowed for the maximization of the backscatter power over such low backscatter areas and for the improvement of the overall interferometric performance, as discussed in [73], [74]. On the other hand, areas characterized by tropical rainforest (marked in green) and boreal forest (light blue triangles) additionally degrade the coherence due to the existence of a

scattering volume within each single resolution cell (a similar mechanism occurs over snow/ice covered areas), an effect which is known as volume decorrelation (γ_{Vol} term in (2.59), [69], [75]). According to this, each scatterer is located at a different height z and contributes with a different interferometric phase $\varphi = \frac{2\pi z}{h_{\text{amb}}}$. The resulting correlation factor is obtained from the ensemble average over all scatterers within the volume [76]

$$\gamma_{\text{Vol}} = \frac{\int_0^{h_{\text{v}}} \sigma^0(z) \cdot \exp\left(j2\pi \frac{z}{h_{\text{amb}}}\right) dz}{\int_0^{h_{\text{v}}} \sigma^0(z) \cdot dz}, \tag{2.61}$$

where h_{v} is the volume height and $\sigma^0(z)$ is the vertical scattering profile. By assuming a defined extinction rate through a homogeneous medium, $\sigma^0(z)$ is modeled as [76]:

$$\sigma^0(z) = \exp\left[-2 \cdot \beta \cdot \frac{h_v - z}{\cos(\eta)}\right], \tag{2.62}$$

being β the one-way extinction coefficient. Figure 2.10 shows the estimated volume correlation factor $\hat{\gamma}_{\text{Vol}}$ as a function of the ambiguous height h_{amb}, which has been retrieved by inverting (2.58) for a time series of TanDEM-X bistatic data takes over a test area in the Amazon rainforest, acquired with incidence angles of 30° (blue dots) and 48° (red), respectively [75]. The theoretical volume correlation factor γ_{Vol} as in (2.61) is shown for both the 30° and the 48° incidence angle case, by the turquoise and brown lines, respectively. The resulting extinction coefficient β is of about 0.4 dB/m, which is in good agreement with typical values over forest at X band [77]. For a given h_{amb}, smaller coherence values are observed for steeper incidence angles, because of the larger number of scatterers projected within a single resolution cell. On the other hand, for shallow incidence angles a more "surface-like" volume is imaged, which in turn results into higher coherence values. On the other hand, as shown in Figure 2.9, non-vegetated areas are not affected by volume decorrelation effects. This aspect makes the volume correlation factor very helpful for, e.g., classification purposes. As an example, a classification method for the generation of a global forest/non-forest classification map from TanDEM-X interferometric data is presented in [35], [78], and an approach for discriminating Greenland snow facies by using the combined information of volume correlation and backscatter is described in [79].

Finally, the term γ_{Temp} in (2.59) describes the so-called temporal decorrelation, which is due to possible changes of the scatterer structure between the two interferometric acquisitions. This term can be neglected for single-pass interferometry (i.e., $\gamma_{\text{Temp}} = 1$), like for the TanDEM-X mission [30], [71].

In conclusion, constraints on the temporal baseline, in case of repeat-pass configuration, and on the interferometric (spatial) baseline $B_\perp$ are typically imposed in order to

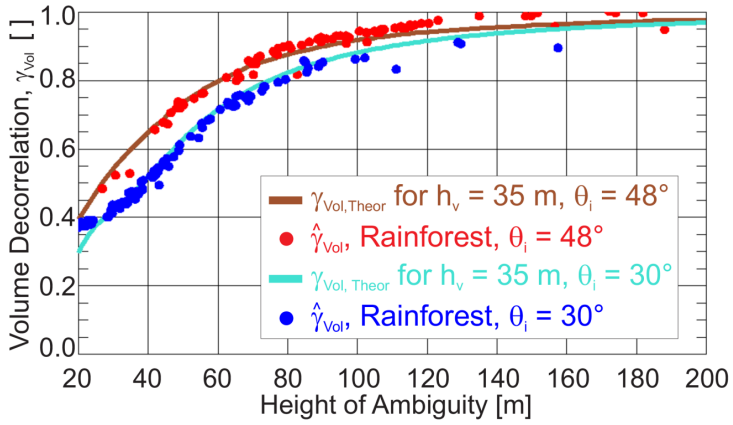

Figure 2.10: Estimated volume correlation factor $\hat{\gamma}_{\mathrm{Vol}}$ over height of ambiguity retrieved from repeated TanDEM-X acquisitions over a single test area in the Amazon rainforest, with incidence angles of 30° (blue circles) and 48° (in red). The theoretical γ_{Vol} as in (2.61) is depicted for the steeper incidence angle (turquoise line), and for the shallower one (in brown) as well.

ensure a sufficient correlation between the two interferometric SAR images and hence to fulfill the specified performance requirements.

2.4.3 Interferometric Phase Errors

As explained in the previous section, a loss in the interferometric coherence γ implies an increase of the associated interferometric phase errors. In order to reduce the phase noise, *multi-looking* is usually applied, which consists in averaging N_{l} values of the complex interferogram before estimating the phase value of interest. Hence, the knowledge of the total coherence $\hat{\gamma}$ and of the independent number of looks N_{l} used for multi-looking allows for a statistical description of the interferometric phase errors. The probability density function (pdf) of the random variable describing the phase difference between two interferometric SAR channels φ can be expressed as [30], [80]

$$p_{\varphi}(\varphi) = \frac{\Gamma\left(N_{\mathrm{l}}+\frac{1}{2}\right)\left(1-\hat{\gamma}^2\right)^{N_{\mathrm{l}}}\hat{\gamma}\cos(\varphi)}{2\sqrt{\pi}\Gamma(N_{\mathrm{l}})\left(1-\hat{\gamma}^2\cos^2(\varphi)\right)^{N_{\mathrm{l}}+\frac{1}{2}}} + \frac{\left(1-\hat{\gamma}^2\right)^{N_{\mathrm{l}}}}{2\pi} F\left(N_{\mathrm{l}},1;\frac{1}{2};\hat{\gamma}^2\cos^2(\varphi)\right), \quad (2.63)$$

where Γ is the gamma function and F denotes the hypergeometric function [81]. The standard deviation of the single-point phase errors is typically used for performance assessment and is defined as

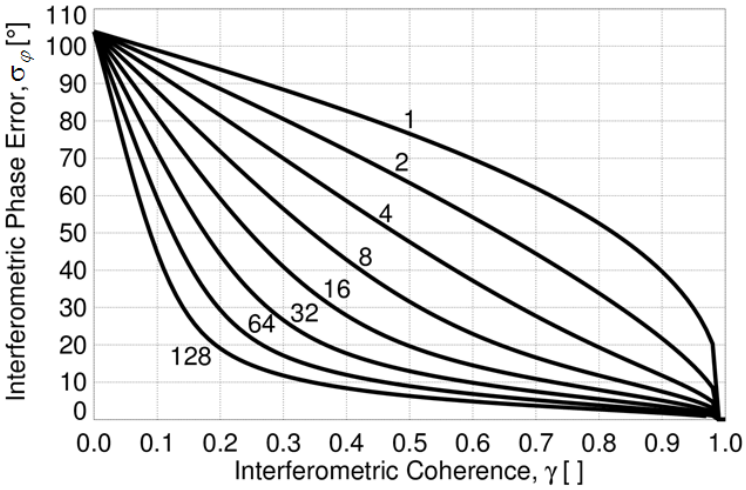

Figure 2.11: Standard deviation of the interferometric phase errors, as function of the coherence and of the number of looks (indicated close to each curve).

$$\sigma_\varphi = \sqrt{\int_{-\pi}^{\pi} \varphi^2 p_\varphi(\varphi) \cdot d\varphi}. \tag{2.64}$$

In general, a decrease in the coherence γ results in an increase in the standard deviation of the phase errors σ_φ, as shown in Figure 2.11 for different number of looks (indicated above each curve). Alternatively, the 90% point-to-point phase error $\varphi_{90\%}$ can be considered [30]. For this, the difference between two random variables, each one describing the fluctuation of a single phase estimate, must be computed. The corresponding pdf results from the convolution $*$ between the two pdfs and is finally derived as [30]

$$\int_{-\varphi_{90\%}}^{\varphi_{90\%}} \left[p_\varphi(\varphi) * p_\varphi(\varphi) \right] \cdot d\varphi = 0.9. \tag{2.65}$$

Assuming the pdf in (2.63) to be approximated by a Gaussian probability distribution [82], the 90% point-to-point height errors can be expressed, for a sufficiently large number of looks, as

$$\varphi_{90\%} \approx 2.33 \cdot \sigma_\varphi, \tag{2.66}$$

being σ_φ the standard deviation of the single-point phase error defined in (2.64).

Regarding the estimation of the independent number of looks N_l used for multi-looking, in practice, for real SAR mission scenarios a target azimuth and range independent interferometric posting Δp_a, Δp_r is imposed, and the actual number of looks N_l is determined

by the azimuth resolution δa and range resolution δr of the SAR system as

$$N_{\mathrm{l}} \approx \frac{\Delta p_a}{\delta a} \cdot \frac{\Delta p_r}{\delta r}. \tag{2.67}$$

For TanDEM-X, the ground range and azimuth resolution is of about 3 meters (in particular, the ground range resolution also depends on the incidence angle, as in (2.22)), and a final independent posting $\Delta p_a = \Delta p_r = 12$ m is set such that N_{l} typically ranges in the interval between 16 and 32 looks [30].

2.4.4 Relative Height Errors for DEMs

The interferometric phase error affects the performance of the resulting DEMs. In particular, the relative height error is defined as the uncertainty on a height estimation due to random noise-like disturbance contributions and can be derived as

$$\Delta h = h_{\mathrm{amb}} \cdot \frac{\Delta \varphi}{2\pi}, \tag{2.68}$$

where $\Delta\varphi$ is given by either σ_φ or $\varphi_{90\%}$. The product specifications for digital elevation measurements are typically expressed as 90% linear error of the point-to-point relative height accuracy. From real DEM data, the point-to-point estimation of the relative height errors can be assessed by subtracting two repeated DEM acquisitions with identical imaging geometry and configuration parameters, each of them affected by independent noise components [82]. After that, a high pass filter is performed to remove slowly varying error sources such as baseline and orbit uncertainties [83] to finally derive the relative height error contribution.

The impact of SAR raw data quantization on interferometric performance (coherence, phase errors, and resulting DEM accuracy) is investigated in detail in Chapter 4.

2.5 Chapter Summary

This chapter aims at providing the reader with the fundamental background on synthetic aperture radar (SAR) remote sensing and SAR interferometry, which is necessary for a complete understanding of the analyses and investigations presented in the following chapters.

The reader should now be aware of the basic principles of SAR, specifically regarding: the processing steps required to obtain range/azimuth focused images from SAR raw data; the different SAR acquisition modes, which trade off the resulting azimuth resolution and achievable swath width; and the perspective distortions depending on the specific acquisition geometry and terrain slope. The most representative system performance parameters have been introduced, such as the resolution and sidelobes, which are derived from the impulse response function (IRF), together with the concepts of radar

backscatter and speckle. The system sensitivity (or noise equivalent sigma zero, NESZ), range/azimuth ambiguities, and nadir returns represent key performance measures, and have been described to provide a complete overview on the different aspects to be considered for SAR system design.

In the second part of the chapter, the basic concepts of SAR interferometry (InSAR), its acquisition geometry, and possible operation modes have been recalled, together with parameters describing the quality of InSAR products, such as the interferometric coherence, phase errors, and relative height accuracy of the resulting digital elevation model (DEM). The knowledge of these performance measures is of importance to understand the investigations presented in the following chapters, where the impact of raw data digitization on SAR and InSAR data acquired by the TanDEM-X mission is presented. For this purpose, a detailed introduction on SAR data quantization, including a description of typical quantization errors, supported by simulation results on a variety of SAR image scenarios, is presented in the next chapter.

3 SAR Raw Data Quantization

In this chapter, quantization of SAR raw data is addressed. In its most general formulation, quantization can be defined as the process of mapping a large (continuous or discrete) set of input values to a countable smaller one. As outlined in Figure 3.1, each radar echo $x(t)$ received by the SAR antenna is an analog (i.e., continuous-time continuous-valued) signal, which needs to be conveniently sampled (discrete-time n) at a certain range sampling frequency f_s and quantized (discrete-amplitude x_q) with a predefined number of bits per sample N_b. Both, sampling and quantization are deterministic operations, and the hardware or software block implementing the described signal digitization is usually referred to as *analog-to-digital converter* (ADC). In the context of SAR, lossy compression schemes are typically used (i.e., the output of the quantizer $x_\mathrm{q}[\mathrm{n}]$ is a distorted copy of the input signal $x[\mathrm{n}]$), due to the limited capacity in terms of data rate achievable by the system (the loss introduced by the quantization is usually larger for spaceborne than for airborne SAR systems, due to the more constrained onboard resources and acquisition requirements typical of spaceborne SAR). The discrete-time discrete-valued signal $x_\mathrm{q}[\mathrm{n}]$ is then stored in the onboard digital memory and, successively, downloaded to ground for further data processing and elaboration, as discussed in Chapter 2. It is well known [42] that the In-phase (I) and Quadrature (Q) components of the received SAR echo $x(t)$ can be described as zero-mean Gaussian stationary and independent processes, as a consequence of the central limit theorem (CLT). Hence, $x[\mathrm{n}]$ and $x_\mathrm{q}[\mathrm{n}]$ are typically modeled as stochastic processes as well. Clearly, both f_s and N_b are directly proportional to the resulting data rate *DR* to be managed by the system, which is measured in bits per second and can be expressed as follows

$$DR = (2 \cdot N_\mathrm{b}) \cdot f_\mathrm{s} \cdot \mathrm{EWL} \cdot N_\mathrm{ch} \cdot \mathrm{PRF}, \tag{3.1}$$

being EWL the echo window length (as in Figure 2.2) and N_ch the number of channels ($N_\mathrm{ch} > 1$ for, e.g., multi-polarimetric SAR systems or for a SAR including multiple azimuth apertures [40]). Since the SAR raw data are complex numbers, a Cartesian quantizer is typically applied, which operates independently on the real and imaginary part, and justifies the factor 2 in the above equation. The azimuth sampling frequency (PRF) does not appear in the schematic description in Figure 3.1, where a single SAR echo is considered. If, on the one hand, the range sampling frequency f_s is determined by the target range resolution and, hence, by the chirp bandwidth B_rg (according to (2.18) and (2.21)), on the other hand, the degree of fidelity of the signal after the digitization process directly affects the resulting SAR image quality. For this reason, the number of bits per sample N_b allocated must be traded off between a sufficiently accurate data reconstruction (N_b too low may irreparably degrade the quality of the obtained SAR products, making their interpretation impossible) and the resulting volume of data to be managed by the system (N_b too large leads to the overflow of onboard memory, hence limiting the

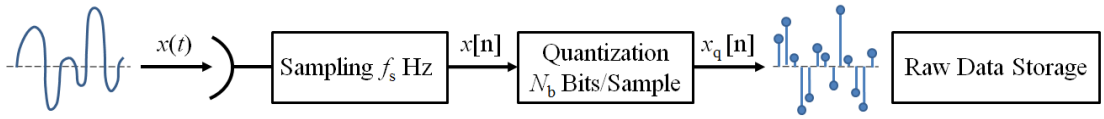

Figure 3.1: Block diagram of an analog-to-digital converter (ADC) at the radar front end. Each analog radar echo received by the SAR antenna $x(t)$ is sampled at a certain range sampling frequency f_s and quantized with a pre-defined number of bits per sample N_b. The digital signal $x_q[n]$ is then stored in the onboard memory. The signals $x(t)$ and, consequently, $x[n]$ and $x_q[n]$ are typically modeled as stochastic processes.

acquisition capabilities of the system). In this scenario, efficient techniques for onboard data reduction are of utmost importance, yet the computational complexity needs to be kept as low as possible to ensure high performance and throughput while requiring minimal satellite resources. An exhaustive description of quantization theory, algorithms and implementation aspects is provided, among others, in [84], [85], [86].

3.1 Fundamentals of Quantization Theory

Quantization typically refers to the operation of mapping the amplitude of the input signal with the nearest value out of a set of predefined possible outputs, which cover the signal amplitude range [84]. The discretization process always introduces a certain error, i.e., it is a lossy operation. The limited amount of reconstructed values is defined by the number of bits used for each sample, which identifies the *alphabet* of the quantizer. Since digitized signals are typically encoded in binary representation, the length of the quantizer alphabet is usually $M = 2^{N_b}$. Clearly, the higher the resolution of the quantizer (i.e., larger N_b values), the smaller the resulting reconstruction error, and vice versa. In the next sections, different possible quantizer settings and characteristics are discussed, and a detailed description of the error contribution introduced by data compression is recalled.

3.1.1 Quantizer Types and Description

Figure 3.2 shows the typical input-output function of a quantizer, characterized by a non-linear staircaise-like function with M levels and bounded between the maximum and minimum output values $\pm r_{clip}$, since the input signal values outside the interval $[-V_{clip}, +V_{clip}]$ (with $V_{clip} > 0$) are "clipped" to the corresponding boundary value (in

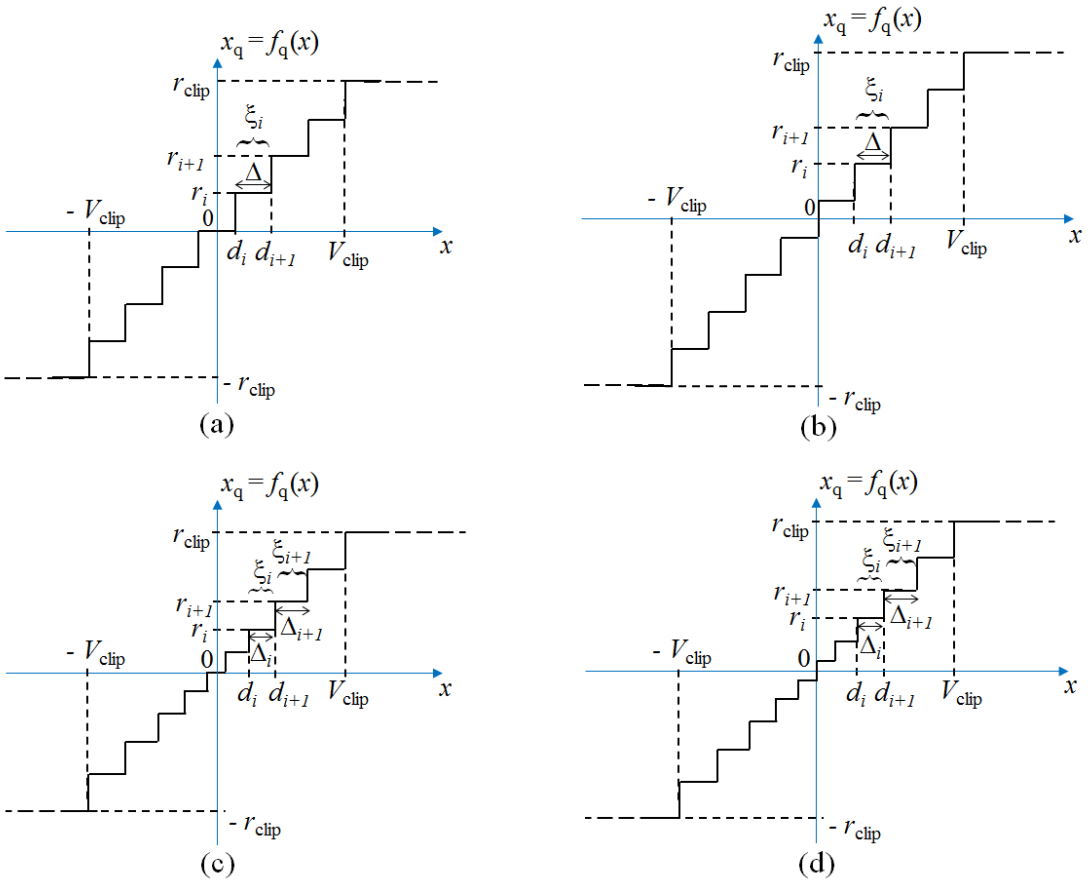

Figure 3.2: Graphic representation for the function relating the input x to the output x_q for a (a) uniform midtread, (b) uniform midrise, (c) non-uniform midtread, and (d) non-uniform midrise quantizer.

principle, the clipping and corresponding reconstruction value may coincide, i.e., $V_{clip} = r_{clip}$). According to the schemes depicted in Figure 3.2 the operation performed by the quantizer can be divided in two steps: the first step consists of splitting the input domain in a set of M intervals $\boldsymbol{\xi}$

$$\boldsymbol{\xi} = \{\xi_1, \xi_2, \ldots, \xi_M\}. \tag{3.2}$$

Then, every input signal sample x (i.e., the realization of the stochastic process $x[\mathrm{n}]$ at the time instant n) contained in the i-th interval ξ_i will be described as:

$$\xi_i : (d_i < x < d_{i+1}), \quad i = 1, 2, \ldots, M, \tag{3.3}$$

where the d_i and d_{i+1} are the end points (or *decision levels*) delimiting the i-th quantization interval. The second step consists in mapping each interval ξ_i into an amplitude x_q, which must belong to the set of possible outputs (or *reconstruction levels*) of the quantizer $\{r_i\}$

$$x_\mathrm{q} \in \{r_1, r_2, \ldots, r_M\}. \tag{3.4}$$

In conclusion, the input/output relation of a quantizer $f_\mathrm{q}(\cdot)$ can be described as follows

$$x_\mathrm{q} = f_\mathrm{q}(x) = r_i \quad \text{if} \quad x \in \xi_i \tag{3.5}$$

and is depicted in Figure 3.3.

Figure 3.2 (a) and (b) show the input-output function for a *uniform* quantizer, where the step size Δ, representing the interval of the input signal mapped to each output value, is constant for all quantization levels. This implies that the decision levels of the quantization intervals and the reconstruction levels are uniformly spaced. On the other hand, a quantizer having a variable step size is said to be *non-uniform*, as shown in Figure 3.2 (c) and (d). In this case, the decision levels are densely located for low-amplitudes and coarsely elsewhere, hence tolerating larger errors for higher signal amplitude, and vice versa. In addition, depending on the position of the decision levels within the signal dynamic range, it is possible to define a *midtread* and a *midrise* quantizer. A midtread quantizer (Figure 3.2 (a) and (c)) has a zero-valued reconstruction value $x_\mathrm{q} = 0$. As an example, the input-output relation for the midtread (MT) uniform quantizer in Figure 3.2 (a) can be expressed as

$$x_{q,\mathrm{MT}} = f_\mathrm{q}(x) = \Delta \cdot \left\lfloor \frac{x}{\Delta} + \frac{1}{2} \right\rfloor \quad \text{if} \quad x \in [-V_\mathrm{clip}, +V_\mathrm{clip}], \tag{3.6}$$

where $\lfloor \cdot \rfloor$ returns the greatest integer less than or equal to its argument (so-called "floor" function). Hence, an input value with magnitude less than $\Delta/2$ is mapped to 0 without considering its sign. On the other hand, a midrise scheme (Figure 3.2 (b) and (d)) has a decision threshold d_i at zero, meaning that this value is not present in the possible output. For the midrise (MR) uniform quantizer in Figure 3.2 (b), the input-output relation can be expressed as

$$x_{q,\mathrm{MR}} = f_\mathrm{q}(x) = \Delta \cdot \left(\left\lfloor \frac{x}{\Delta} \right\rfloor + \frac{1}{2} \right) \quad \text{if} \quad x \in [-V_\mathrm{clip}, +V_\mathrm{clip}]. \tag{3.7}$$

3.1.2 Quantization Errors

As it has been previously explained, the digitization of an analog signal is an irreversible process which leads to an information loss and represents a critical aspect for data compression, as the reconstructed signal will be a distorted version of the input depending on the bit rate and on the particular quantization scheme used. The difference

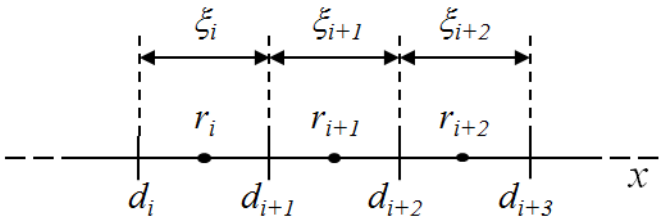

Figure 3.3: Quantization of a signal x as defined in (3.5).

between input and corresponding output is therefore often referred to as *quantization error* q

$$q = x - x_{\mathrm{q}} = x - f_{\mathrm{q}}(x). \tag{3.8}$$

This error (or noise) contribution is totally deterministic, since for a given input always the same (single) output is returned. On the other hand, if the input x has a random nature, the error q can be reasonably modeled as an additive and signal-correlated random noise contribution [85] (this assumption strictly holds for the so-called *granular* errors, but it is not valid for *overload* errors, which are described in the following).

Let X be the random variable describing the stochastic processes $x[\mathrm{n}]$ at the time instant n. Without loss of generality, X has zero mean and variance σ_X^2 and is described by the probability density function (pdf) $p_X(x)$, i.e.,

$$\mu_X = \mathbb{E}[X] = \int_{-\infty}^{+\infty} x\, p_X(x)\, dx = 0 \implies \sigma_X^2 = \mathbb{E}\left[X^2\right] = \int_{-\infty}^{+\infty} x^2\, p_X(x)\, dx, \tag{3.9}$$

where $\mathbb{E}[\cdot]$ represents the expectation operator. If $\mu_X \neq 0$, it can be opportunely subtracted from the input signal and added back after quantization, an operation that is equivalent to a shift of the quantizer to the input mean value μ_X. Due to the random nature of the input signal, the quantizer output x_{q} is modeled as a random variable $X_{\mathrm{q}} = f_{\mathrm{q}}(X)$. According to this, the quantization error q is also a zero-mean random variable $Q = X - X_{\mathrm{q}}$ characterized by its pdf $p_Q(q)$ and variance

$$\sigma_Q^2 = \mathbb{E}\left[Q^2\right] = \int_{-\infty}^{+\infty} \left[x - f_{\mathrm{q}}(x)\right]^2 p_X(x)\, dx, \tag{3.10}$$

where, in the above calculation, the pdf of the input signal $p_X(x)$ needs to be considered. Assuming N_{b} bits allocated for the quantizer, the quantization error power is finally obtained by integrating over the $M = 2^{N_{\mathrm{b}}}$ decision levels and (3.10) becomes

$$\sigma_Q^2 = \mathbb{E}\left[Q^2\right] = \sum_{k=1}^{M} \int_{d_k}^{d_{k+1}} (x - r_k)^2\, p_X(x)\, dx, \tag{3.11}$$

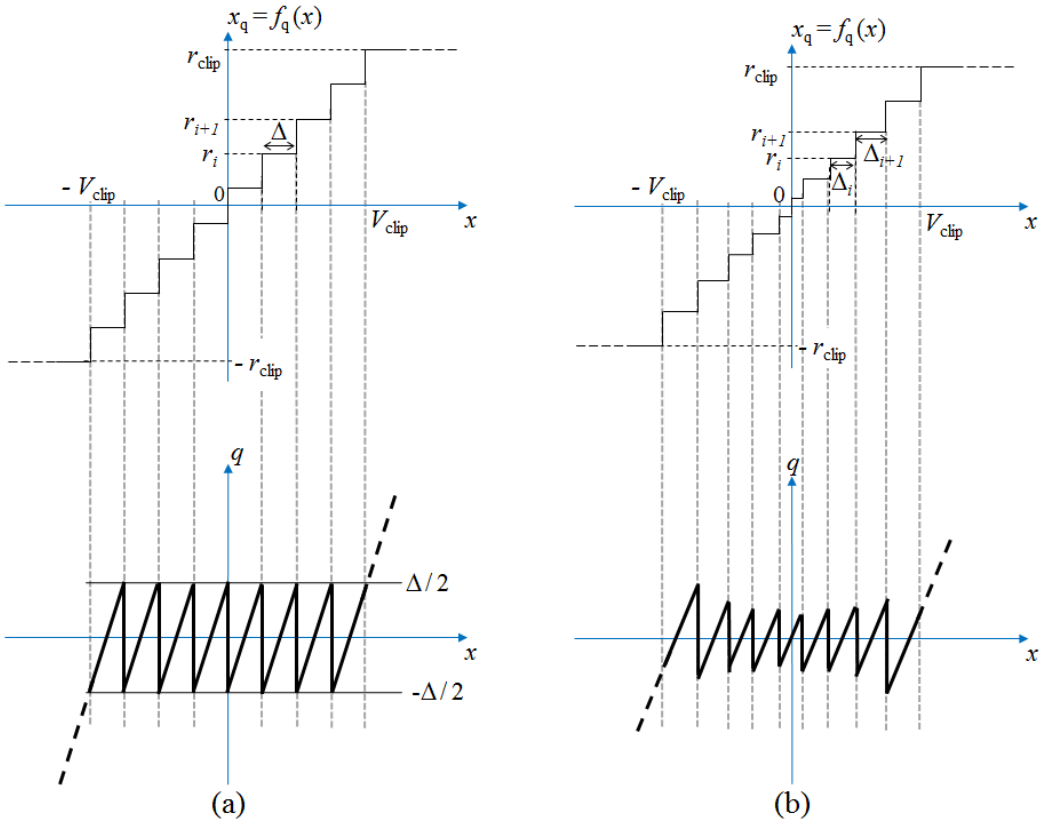

Figure 3.4: Graphic reppresentation of the quantization error q (bottom) for (a) midrise uniform and (b) midrise non-uniform quantizer, as a function of the input signal x. The corresponding input-output functions are given on the top of the figure.

being $d_1 = -\infty$ and $d_{M+1} = +\infty$. In order to describe the performance of a quantizer, the *signal-to-quantization noise ratio* (SQNR) is typically used, which is defined as the ratio between the input signal variance σ_X^2 and the quantization noise variance σ_Q^2

$$\text{SQNR} = \frac{\sigma_X^2}{\sigma_Q^2}. \tag{3.12}$$

Figure 3.4 depicts the deterministic nature of the quantization error (bottom of the figure) for an exemplary uniform (Figure 3.4 (a)) and non-uniform (Figure 3.4 (b)) midrise quantizer, whose input-output functions $f_q(\cdot)$ are depicted on the top of the figure. A quantizer typically has a limited dynamic range, which truncates the input signal to a

maximum and minimum level given by $\pm V_{\text{clip}}$. If the input signal x has unbounded support, the clipping introduces a distortion, which is referred to as *overload* error and is indicated by the diverging dashed lines at the bottom of Figure 3.4. On the other hand, the quantization step $\Delta > 0$ defines the accuracy of the reconstruction values within the supported range, and the distortion introduced by this finite spacing is referred to as *granular* error, as depicted by the bold lines at the bottom of Figure 3.4. According to the definition of quantization noise power derived in (3.11) and to the schemes in Figure 3.4, the granular and clipping noise power contributions can be expressed as

$$\sigma_{Q,\text{g}}^2 = \sum_{k=2}^{M-1} \int_{d_k}^{d_k+1} (x - r_k)^2 \, p_X(x) \, dx, \tag{3.13}$$

$$\sigma_{Q,\text{c}}^2 = \int_{-\infty}^{-V_{\text{clip}}} (x + r_{\text{clip}})^2 \, p_X(x) \, dx + \int_{+V_{\text{clip}}}^{+\infty} (x - r_{\text{clip}})^2 \, p_X(x) \, dx, \tag{3.14}$$

respectively, and the total quantization error power can be derived as the sum of granular and overload error variances [85]

$$\sigma_Q^2 = \sigma_{Q,\text{g}}^2 + \sigma_{Q,\text{c}}^2. \tag{3.15}$$

In the case of a uniform quantizer, the step size Δ is constant and each reconstruction value is chosen as midpoint of the corresponding decision levels (as shown in Figure 3.4 (a)), as

$$r_i = \frac{d_i + d_{i+1}}{2} \quad \text{if} \quad 1 < i < M. \tag{3.16}$$

If the input signal x has bounded support, i.e., $x \in [-x_{\max}, x_{\max}]$, it is straightforward to design the optimum midrise quantizer such that $V_{\text{clip}} = x_{\max}$ and

$$|x| \leq V_{\text{clip}} = \frac{\Delta 2^{N_\text{b}}}{2} = \Delta 2^{N_\text{b}-1}. \tag{3.17}$$

If the step size of the quantizer is sufficiently small, then it can be reasonably assumed the granular error to be uniformly distributed in the interval $[-\Delta/2, \Delta/2]$ (so-called "high-rate approximation" [85]) and the probability density function of the error is given by

$$p_Q(q) = \begin{cases} 1/\Delta & \text{if } |q| \leq \Delta/2 \\ 0 & \text{otherwise.} \end{cases} \tag{3.18}$$

In this case, the variance of the quantization noise can be derived according to (3.11) as

$$\sigma_Q^2 = \Delta^2/12 = \frac{1}{3} V_{\text{clip}}^2 \, 2^{-2N_\text{b}}. \tag{3.19}$$

Hence, under the assumption of high-rate approximation, the power of the quantization error quadratically increases with the step size Δ and exponentially decreases with the bit rate N_b.

It is now worth recalling the definition of *loading (or crest) factor* of a random process X, κ_X, as the ratio between its peak value and its root mean square value

$$\kappa_X = \frac{X_\mathrm{max}}{\sigma_X}. \tag{3.20}$$

This allows one to finally express the signal-to-quantization noise ratio SQNR for a uniform quantizer, according to (3.12), in logarithmic scale, (or decibel, dB), as

$$\mathrm{SQNR}|_\mathrm{dB} = 10\log_{10}\left(\frac{\sigma_X^2}{\sigma_Q^2}\right) = 10\log_{10}\left(\frac{3\,\sigma_X^2}{V_\mathrm{clip}^2}2^{2N_\mathrm{b}}\right) \approx 6N_\mathrm{b} - 10\log_{10}\left(\frac{\kappa_X^2}{3}\right) \text{ if } N_\mathrm{b} \gg 1. \tag{3.21}$$

The above equation shows that if a binary code is used for the reconstruction levels of a uniform quantizer, the resulting SQNR increases by about 6 dB for each additional quantization bit, which is a known result from the rate-distortion theory [85].

3.1.3 Quantizing Theorem

Figure 3.5 sketches an exemplary pdf of the quantizer input X, $p_X(x)$, and the resulting probability mass function (pmf) of the quantizer output X_q, $p_{X_\mathrm{q}}(x_\mathrm{q})$. The graphic is provided for a uniform (Figure 3.5 (a)) and non-uniform (Figure 3.5 (b)) quantizer, and the input signal is assumed to be continuous, whereas the output one is obviously discrete. Following the discussion in [87], it is possible to demonstrate that the output signal is related to the input one through a specific sampling operation. Indeed, the output pmf is represented by the Dirac impulses, each one located at the corresponding reconstruction level, and whose area A_i is just the area under the input pdf within the corresponding decision interval

$$A_i = \int_{d_i}^{d_{i+1}} p_X(x)\,dx. \tag{3.22}$$

In this sense, quantization can be understood as a sampling of the probability density function of the input signal (hence operating in the amplitude domain instead of in the "classical" time domain), an operation which is often referred to as *area sampling* [87]. In this context, it is worth first recalling the concept of *characteristic function* (CF) as the Fourier transform of the pdf

$$\Phi_X(u) = \int_{-\infty}^{+\infty} p_X(x)e^{jux}\,dx = \mathbb{E}\left[e^{juX}\right], \tag{3.23}$$

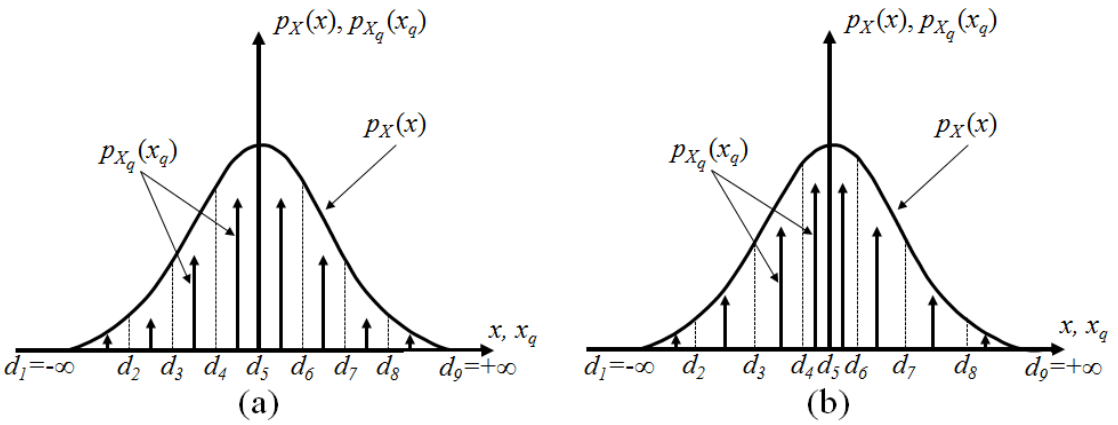

Figure 3.5: Quantization as area sampling of the continuous input pdf $p_X(x)$. The probability mass function (pmf) of the quantized signal $p_{X_q}(x_q)$ is represented by the Dirac impulses, each one located in the corresponding reconstruction level. (a) Uniform and (b) non-uniform quantizer. The Lloyd-Max quantizer optimizes the distribution of the decision and reconstruction levels in order to minimize the quantization error variance σ_Q^2.

where u represents the transformed domain of the CF (pdf frequency). According to this, the *Quantizing Theorem* [87] can be formulated as follows: let Δ be the quantization step and Ψ the corresponding "repetition frequency" of the CF given by

$$\Psi \triangleq \frac{2\pi}{\Delta}. \tag{3.24}$$

If the CF of X is band-limited, so that,

$$\Phi_X(u) = 0 \quad \text{for} \quad |u| > \frac{\pi}{\Delta} = \frac{\Psi}{2} \tag{3.25}$$

then

- the CF of X can be derived from the CF of X_q, and
- the pdf of X can be derived from the pmf of X_q.

This theorem derives a sufficient condition such that, given a quantized signal, it is possible to capture all the information from the original band-limited continuous-amplitude signal. This theorem represents a sort of equivalent in quantization of the well-known Nyquist-Shannon sampling theorem, which establishes a sufficient condition for the sampling rate of a discrete sequence of values to capture all the information from a continuous-time signal of finite bandwidth.

If, on the other hand, in the frequency domain the signal is not band-limited, an anti-aliasing filter is typically applied to it before sampling in order to remove undesired portions of the spectrum. For this purpose, filtering is applied either in time domain (by convolution of the direct signals) or in frequency domain (by multiplication of their spectra). Analogously, in the quantization domain a product of characteristic functions corresponds to a convolution of the probability density functions. In turn, pdf convolution is obtained by summing the corresponding independent random variables. Therefore, the band Ψ of the CF as in (3.24) can be limited by adding a properly defined independent random variable with limited CF bandwidth, which is often referred to as *dither* in the context of analog-to-digital conversion and digital signal processing [87], [88], [89], [90]. It is worth to point out that the described low-pass filter in the CF domain deserves careful consideration, since its inverse transform (i.e., the associated signal pdf) must be a non-negative function.

3.1.4 Lloyd-Max Optimum Quantizer

Although representing the simplest compression scheme, uniform quantization is not necessarily the most effective one. If, as an example, a normally distributed input is considered (which is a suitable model for SAR raw data, as it has been discussed in Chapter 2), a uniform quantizer will assign the same resources to reconstruct the equally spaced intervals, disregarding whether they are more or less likely to occur, as shown in Figure 3.5 (a). Instead, a more plausible choice to increase the overall reconstruction quality would intuitively consist in allocating more resources (i.e., tinier decision intervals) for value ranges occurring with larger probability, and vice versa, as depicted in Figure 3.5 (b). In this scenario, a reasonable criterion for the design of the optimum quantizer is therefore to define the distribution of the decision and reconstruction levels, for a given number of bits N_b, in order to minimize the quantization noise power σ_Q^2 (or, equivalently, to maximize the SQNR),

$$\left\{\boldsymbol{d}_\mathrm{opt}, \boldsymbol{r}_\mathrm{opt}\right\} = \underset{\{\boldsymbol{d},\boldsymbol{r}\}}{\operatorname{argmin}} \;\; \sigma_Q^2(N_\mathrm{b}). \tag{3.26}$$

If the pdf of the input signal is known, a necessary condition for minimizing the quantization error is that the derivative of σ_Q^2 with respect to the decision and reconstruction levels (obtained from (3.11)) is zero [91], which leads to the following conditions,

$$\frac{\partial \sigma_Q^2}{\partial d_k} = 0 \implies (d_k - r_{k-1})^2 = (d_k - r_k)^2 \quad \text{if} \;\; p_X(d_k) \neq 0, \quad k = 2,3,\ldots,M \tag{3.27}$$

and

$$\frac{\partial \sigma_Q^2}{\partial r_k} = 0 \implies \int_{d_k}^{d_{k+1}} (x - r_k)\, p_X(x)\, dx = 0, \quad k = 1,2,\ldots,M\,, \tag{3.28}$$

being $M = 2^{N_\mathrm{b}}$. According to the relations in (3.27) and (3.28) the optimum decision level $d_{\mathrm{opt},k}$ and reconstruction level $r_{\mathrm{opt},k}$ can be finally derived as

$$d_{\mathrm{opt},k} = \frac{\left(r_{\mathrm{opt},k} + r_{\mathrm{opt},k-1}\right)}{2} \quad k = 2,\ldots,M, \;\; d_{\mathrm{opt},1} = -\infty, \;\; d_{\mathrm{opt},M+1} = +\infty \tag{3.29}$$

and

$$r_{\mathrm{opt},k} = \frac{\int_{d_{\mathrm{opt},k}}^{d_{\mathrm{opt},k+1}} x\, p_X(x)\, dx}{\int_{d_{\mathrm{opt},k}}^{d_{\mathrm{opt},k+1}} p_X(x)\, dx} \quad k = 1,2,\ldots,M. \tag{3.30}$$

Hence, the optimum decision levels are in the mid-point between neighboring reconstruction levels, which, in turn, must be set as the centroid of the pdf (i.e., its expected value) in the corresponding decision interval. The obtained quantizer minimizes the resulting mean square error (MMSE), and is also referred to as the *Lloyd-Max quantizer* [91]. It is straightforward to demonstrate that, if the input signal is uniformly distributed, $d_{\mathrm{opt},k}$ and $r_{\mathrm{opt},k}$ are equally spaced, hence leading to a uniform quantizer. In all other cases, the optimum decision and reconstruction levels are non-uniformly distributed (such as, e.g., the ones obtained for the normally distributed signal in Figure 3.5 (b)). However, for a generic input pdf an analytical solution of (3.29) and (3.30) does not exist, which is therefore computed numerically as an iterative procedure as follows: the initial value for the first reconstruction level $r_{\mathrm{opt},1}$ is chosen and the succeeding $d_{\mathrm{opt},k}$ and $r_{\mathrm{opt},k}$ are derived by using the relations in (3.27), (3.28), (3.29), and (3.30). If the last $r_{\mathrm{opt},M}$ is actually the centroid of the last interval $\xi_M = \left[d_{\mathrm{opt},M}, +\infty\right]$ then the guess estimation of $r_{\mathrm{opt},1}$ was correct, otherwise it must be chosen again. Hence, the choice of employing a uniform quantizer instead of a non-uniform one depends on the statistics of the quantizer input, if known. As an example, the optimum sets $\left\{\boldsymbol{d}_{\mathrm{opt}}, \boldsymbol{r}_{\mathrm{opt}}\right\}$ obtained for a normally distributed input with zero mean and unitary variance (hence resulting in a symmetric quantizer), are listed in [91] for different number of levels M.

These results allow for deriving interesting properties about the quantization error statistics [85]. In particular, the reconstruction values derived in (3.30) can be seen as the expectation of the input random variable X conditioned to $X \in \xi_{\mathrm{opt},k}$

$$r_{\mathrm{opt},k} = \mathbb{E}\left[X \mid X \in \xi_{\mathrm{opt},k}\right]. \tag{3.31}$$

This implies that for a Lloyd-Max quantizer the quantization error Q in each decision interval $\xi_{\mathrm{opt},k}$ has zero mean, i.e.,

$$\mathbb{E}\left[X - r_{\mathrm{opt},k} \mid X \in \xi_{\mathrm{opt},k}\right] = \mathbb{E}\left[Q \mid X \in \xi_{\mathrm{opt},k}\right] = 0, \tag{3.32}$$

which is also a direct consequence of (3.28). By summing up all error contributions weighted by the output probability mass function $p_{X_\mathrm{q}}(x_{\mathrm{q},k})$ it follows that also the unconditioned mean of the quantization noise Q is zero, i.e.,

$$\sum_{k=1}^{M} \mathbb{E}\left[X - r_{\mathrm{opt},k} \mid X \in \xi_{\mathrm{opt},k}\right] p_{X_\mathrm{q}}(x_{\mathrm{q},k}) = \mathbb{E}\left[Q\right] = 0, \tag{3.33}$$

where

$$p_{X_\mathrm{q}}(x_{\mathrm{q},k}) = \int_{d_{\mathrm{opt},k}}^{d_{\mathrm{opt},k+1}} p_X(x)\,dx, \tag{3.34}$$

which is indicated, e.g., by the Dirac impulses in Figure 3.5. By multiplying (3.33) with $r_{\mathrm{opt},k}$, one obtains

$$\mathbb{E}\left[QX_\mathrm{q}\right] = 0, \tag{3.35}$$

i.e., the quantization error is orthogonal to the output of the Lloyd-Max quantizer. On the other hand, the input signal and the quantization error are correlated, since

$$\mathbb{E}\left[XQ\right] = \mathbb{E}\left[Q(Q+X_\mathrm{q})\right] = \sigma_Q^2. \tag{3.36}$$

The variance of the output signal can be finally derived as

$$\sigma_{X_\mathrm{q}}^2 = \mathbb{E}\left[X_\mathrm{q}^2\right] = \mathbb{E}\left[(X-Q)^2\right] = \mathbb{E}\left[X^2\right] + \mathbb{E}\left[Q^2\right] - 2\cdot\mathbb{E}\left[XQ\right] = \sigma_X^2 - \sigma_Q^2. \tag{3.37}$$

Hence, the power of the output signal is always smaller than the power of the input one, which is due to the non-zero probability of clipping events [85]. This effect becomes negligible for a sufficiently large bit rate N_b (i.e., $M \to +\infty$), which implies $\sigma_Q^2 \to 0$ and therefore $\sigma_{X_\mathrm{q}}^2 \to \sigma_X^2$. Another interesting result can be derived on the variance of the quantization error from (3.29) and (3.30):

$$p_{X_\mathrm{q}}(x_{\mathrm{q},m})\cdot\mathbb{E}\left[Q^2 \mid X \in \xi_{\mathrm{opt},m}\right] = p_{X_\mathrm{q}}(x_{\mathrm{q},n})\cdot\mathbb{E}\left[Q^2 \mid X \in \xi_{\mathrm{opt},n}\right] \quad \forall\ m,n, \tag{3.38}$$

which means that, even if the step size changes, the expected error variances (i.e., weighted by the probability value of X being in the m-th interval $\xi_{\mathrm{opt},m}$, $p_{X_\mathrm{q}}(x_{\mathrm{q},m})$) are identical for all decision intervals.

As a consequence of the findings discussed in this section, the quantization process can be properly modeled as a scaling of the discrete-time input signal x by a factor $A_\mathrm{q} < 1$, which accounts for the power reduction as in (3.37), followed by an additive noise source w_q, such that

$$x_\mathrm{q} = A_\mathrm{q}\cdot x + w_\mathrm{q}, \tag{3.39}$$

as depicted in Figure 3.6. According to this model, the variance of the quantized signal is derived as

$$\sigma_{X_\mathrm{q}}^2 = \mathbb{E}\left[X_\mathrm{q}^2\right] = \mathbb{E}\left[(A_\mathrm{q}X + W_\mathrm{q})^2\right] = A_\mathrm{q}^2\sigma_X^2 + \sigma_{W_\mathrm{q}}^2, \tag{3.40}$$

where the variables expressed in capital letters refer to the associated random variables and

$$A_\mathrm{q} = \sqrt{\frac{\sigma_{X_\mathrm{q}}^2 - \sigma_{W_\mathrm{q}}^2}{\sigma_X^2}}. \tag{3.41}$$

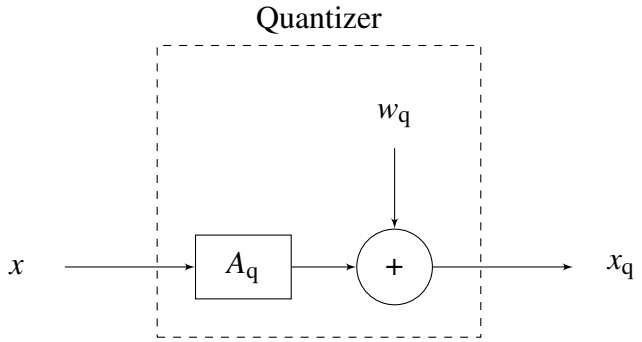

Figure 3.6: A quantizer can be modeled as a variable gain amplifier $A_q < 1$ and an additive noise source w_q; hence the output signal x_q is a distorted copy of the input x.

3.1.5 Relevant Parameters and Performance Measures

In this subsection the most relevant parameters used to describe a quantizer and its performance are recalled.

Signal-to-clipping ratio, γ_{clip}: Given an input signal x with standard deviation σ_x and being V_{clip} the clipping value of the quantizer, the *signal-to-clipping ratio* γ_{clip} is defined as

$$\gamma_{clip} = \frac{\sigma_x}{V_{clip}} = \frac{\sqrt{\sigma_{x,I}^2 + \sigma_{x,Q}^2}}{V_{clip}}, \tag{3.42}$$

where $\sigma_{x,I}^2$ and $\sigma_{x,Q}^2$ are the powers of the In-phase (I) and Quadrature (Q) components of the quantizer input x, which is modeled as a complex signal as for the case of SAR raw and focused data. Once fixed the number of bits N_b and the dynamic range of the quantizer V_{clip}, if the statistics of the input signal are known, γ_{clip} should be neither too small (i.e., $\sigma_x << V_{clip}$) in order to mitigate granular errors, nor too large (i.e., σ_x comparable to V_{clip}) to reduce the occurrence of clipping errors.

Signal-to-Quantization Noise Ratio, SQNR: It has been defined in (3.12) and represents the figure of merit of a quantizer describing how much the output signal has been corrupted by quantization noise. It is defined as the power ratio of the input signal x to the quantization error $q = x - x_q$, being x_q the quantized signal, and is given by

$$\text{SQNR} = \frac{\sigma_x^2}{\sigma_q^2} = \frac{\sigma_{x,I}^2 + \sigma_{x,Q}^2}{\sigma_{q,I}^2 + \sigma_{q,Q}^2}, \tag{3.43}$$

where $\sigma^2_{q,I}$ and $\sigma^2_{q,Q}$ are the power of the In-phase (I) and Quadrature (Q) component of the complex quantization noise, respectively. If an SQNR map has to be estimated from a SAR image $\imath$ and its compressed version $\hat{\imath}$, for the p-th image pixel it is simply calculated as

$$\mathrm{SQNR}_p = \frac{\left|\imath_p\right|^2}{\left|\imath_p - \hat{\imath}_p\right|^2}. \tag{3.44}$$

The SQNR for a normally distributed complex signal obtained at the output of a uniform ADC is plotted in Figure 3.7 (a) as a function of γ_{clip} and for different bit rates N_{b}, depicted with different colors. For low values of γ_{clip} (i.e., the signal dynamic is small compared with the dynamic range of the quantizer) the SQNR is degraded predominantly due to the occurrence of granular errors, whereas, in the case of large γ_{clip} values, clipping errors mostly affect the resulting performance. As expected, a larger number of bits used for quantization results in high SQNR and vice versa.

Quantization Coherence, γ_{Quant}: As recalled in Section 2.4.2 the quantization coherence γ_{Quant} describes the amount of noise affecting a SAR interferogram due to quantization and can be derived from the SQNR as

$$\gamma_{\mathrm{Quant}} = \frac{1}{1+\frac{1}{\mathrm{SQNR}}} = \frac{\mathrm{SQNR}}{\mathrm{SQNR}+1}. \tag{3.45}$$

The quantization coherence resulting from the SQNR in Figure 3.7 (a) is shown in Figure 3.7 (b) as a function of γ_{clip} and for different bit rates N_{b}, depicted with different colors.

Phase Errors, $\Delta\varphi$: Once γ_{Quant} and the number of looks N_{l} employed for multilooking are known, one can derive the interferometric phase errors as expressed by (2.63) in Section 2.4.2. In general, the relation between coherence and phase errors is highly non-linear, as shown in Figure 2.11. From real or simulated data, the single-point phase error can be evaluated as the phase difference between the compressed x_{q} and the original signal x as

$$\Delta\varphi = \mathrm{atan}(x \cdot x_{\mathrm{q}}^*). \tag{3.46}$$

The standard deviation of the phase errors $\sigma_{\Delta\varphi}$ for the Gaussian signal of Figure 3.7 (a) is shown in Figure 3.7 (c) as function of γ_{clip} and for different ADC rates N_{b}, depicted with different colors.

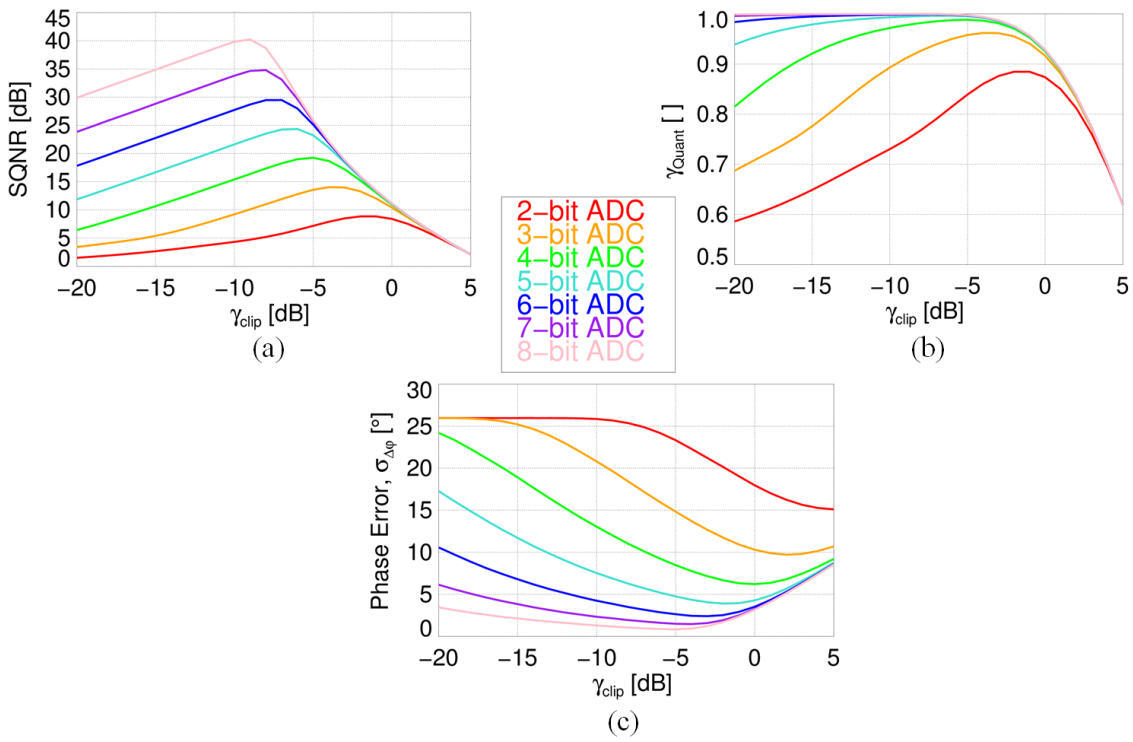

Figure 3.7: (a) SQNR, (b) quantization coherence γ_{Quant}, and (c) standard deviation of the phase error $\sigma_{\Delta\varphi}$ for a Gaussian signal after uniform ADC, as a function of γ_{clip} and for N_{b} varying between 2 and 8 bits/sample.

3.2 Quantization Schemes for SAR Systems: State of the Art

3.2.1 Block-Adaptive Quantization (BAQ)

During the imaging survey, the SAR system transmits radar pulses and receives echoes backscattered from the Earth's surface. These include responses from both, low- and high-backscatter regions, hence the resulting amplitude values in the SAR raw data are space-varying. In order to handle such a varying dynamic range, a conventional quantizer would require a large number of bits/sample N_{b} to keep a sufficient image quality for most SAR applications. To overcome this limitation, adaptive quantizers are typically employed for SAR systems, which trade off an increased scheme complexity with a reduced date rate required for a target performance.

One of the most widely recognized methods for raw data compression for SAR systems is the block-adaptive quantization (BAQ) [38], [39]. BAQ is a lossy data reduction technique which uses local statistics of raw data blocks in order to set the re-quantization decision levels: a space-varying estimation of raw data statistics is performed for each

block of the input data, which is then used to determine the quantization decision levels that best match with the observed statistics. The raw data blocks typically have a fixed size of N_{block} samples. N_{block} must be sufficiently large to allow for a correct estimation of the local statistics, but, at the same time, it should be sufficiently small to include regions with similar power statistics (for this, the weighting effect of the range/azimuth SAR antenna patterns must be taken into account as well). The compression can be applied either directly on the SAR raw data (i.e., in "time" domain) or in frequency domain after proper signal transformation. The former leads to a good signal-to-quantization noise ratio, but it does not optimize the compression scheme according to the frequency envelope of the signal power in range/azimuth directions. On the other hand, the compression in frequency domain increases the performance, at the cost of a significant effort for its onboard implementation [92]. Due to the limited resources available for onboard processing operations, block-adaptive quantization of the SAR raw data (i.e., in time domain) is typically employed on spaceborne SAR systems. BAQ represents a good compromise between scheme complexity (a simple scalar quantization algorithm), granted image quality, and achievable compression ratio, and is therefore an attractive solution for spaceborne SAR systems, where a huge amount of onboard data need to be stored and then transmitted to the ground.

In this dissertation, quantization effects on interferometric SAR data acquired by the TanDEM-X mission are investigated in Chapter 4 and Chapter 5. Hence, in the following, the BAQ algorithm implemented on the TerraSAR-X and TanDEM-X satellites is detailed and is taken as reference quantization method, whereas an overview of the TanDEM-X mission is given in Section 4.2.

On both SAR satellites, the BAQ compression rate is individually configured before every data take by instrument commanding and is kept constant for the whole acquisition. In particular, the BAQ is separately applied for the in-phase (I) and quadrature (Q) channel and the decision and reconstruction levels are adapted to the local statistics of the received SAR data block.

The input analogue signal is first scaled and clipped within the range $[-V_{\text{clip}}, +V_{\text{clip}}]$ (V_{clip} = 250 mV) and then digitized using an 8-bit analog-to-digital converter (ADC). At the ADC output, the I- and Q-component of each sample $x_{\text{adc}} = [I_{\text{adc}}, Q_{\text{adc}}]$ is an 8-bit number in signed magnitude as

$$I_{\text{adc}} \rightarrow \mathbf{K}_{I,\text{adc}} = \left[K_{I,\text{adc},1}, K_{I,\text{adc},2}, \ldots, K_{I,\text{adc},8}\right], \tag{3.47}$$

$$Q_{\text{adc}} \rightarrow \mathbf{K}_{Q,\text{adc}} = \left[K_{Q,\text{adc},1}, K_{Q,\text{adc},2}, \ldots, K_{Q,\text{adc},8}\right], \tag{3.48}$$

where $K_{I,\text{adc},i}$ and $K_{Q,\text{adc},i}$ is the value of the i-th bit (0 or 1) for the in-phase and quadrature component at the ADC output, respectively. The corresponding decimal interpretation is simply obtained from

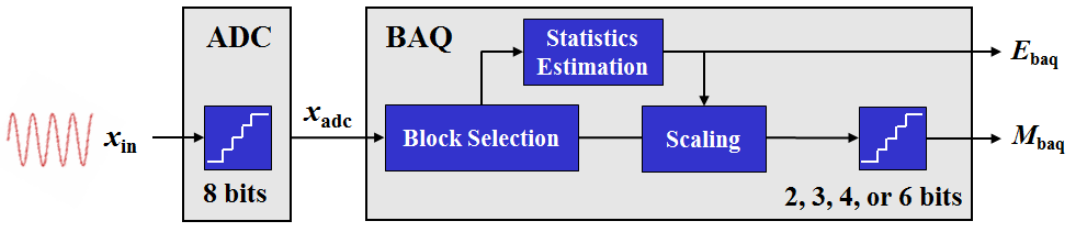

Figure 3.8: Flow diagram of the block-adaptive quantizer (BAQ). The input is encoded in mantissa M_{baq} and exponent E_{baq} which are stored in the onboard register in binary format.

$$I_{\text{adc}} = (-1)^{s_{I,\text{adc}}} \cdot \left(0.5 + \sum_{i=2}^{8} K_{I,\text{adc},i} \cdot 2^i\right), \tag{3.49}$$

$$Q_{\text{adc}} = (-1)^{s_{Q,\text{adc}}} \cdot \left(0.5 + \sum_{i=2}^{8} K_{Q,\text{adc},i} \cdot 2^i\right), \tag{3.50}$$

being $s_{I,\text{adc}} = K_{I,\text{adc},1}$ and $s_{Q,\text{adc}} = K_{Q,\text{adc},1}$ the sign bit for the in-phase and quadrature component at the ADC output, respectively, whose values range in the interval $[-127.5, +127.5]$. The ADC-quantized signal is then provided as input to the block-adaptive quantizer (BAQ), which is described in the following.

BAQ Algorithm: The block diagram for the BAQ implementation is shown in Figure 3.8. For TerraSAR-X and TanDEM-X, possible compression rates are 8:2, 8:3, 8:4, 8:6 and 8:8, where, e.g., 8:2 indicates that the data are digitized from the 8-bit ADC to the 2-bit BAQ, and the latter 8:8 corresponds to BAQ bypass [27], [93], [94]. Table 3.1 contains the values of the parameters used for the different compression rates N_{b} in the BAQ algorithm, which consists of the following steps:

Step 1: The ADC digitized raw data I_{adc} and Q_{adc}, given in (3.49) and (3.50), respectively, are divided into blocks of $N_{\text{block}} = 128$ range samples (corresponding to a slant range extension of about 70-200 m);

Step 2: Depending on the quantization rate N_{b} used for compression, the corresponding C value is taken from Table 3.1 and the value E_1 is calculated as follows

$$E_1 = 4 \cdot \log_2\left(1 + \frac{1}{N_{\text{block}}} \sum_{n=1}^{N_{\text{block}}} \left(|I_{\text{adc},n}| + |Q_{\text{adc},n}|\right)\right) - C, \tag{3.51}$$

Table 3.1: Parameters used for the BAQ algorithm for different compression rates as implemented on the TerraSAR-X and TanDEM-X satellites.

Compression Rate, N_b	C **Value**	E_max **Value**	M_max **Value**
8:2	2.20374	24	1
8:3	5.28038	20	3
8:4	8.50475	16	7
8:6	15.2549	8	31

where $\log_2$ is the logarithm of base 2. The value E_1 provides an estimate of the average magnitude of the complex raw data block of length N_block;

Step 3: The obtained E_1 value is compared with the corresponding E_max value in Table 3.1. The exponent E is finally derived as follows

$$E = \min\big\{E_\mathrm{max}, \lfloor E_1 \rfloor\big\}, \tag{3.52}$$

where $\lfloor E_1 \rfloor$ denotes the closest integer less than or equal to E_1 and $\min\{\cdot\}$ gives the minimum of its arguments. For TanDEM-X, the exponent E is coded using 5 bits in the register;

Step 4: Once obtained the exponent value E, the I_adc and Q_adc samples are scaled as follows

$$\bar{I} = \frac{I_\mathrm{adc}}{2^{E/4}} \quad \text{and} \quad \bar{Q} = \frac{Q_\mathrm{adc}}{2^{E/4}}; \tag{3.53}$$

Step 5: The BAQ quantized I and Q channels are obtained by comparing the scaled $\bar{I}$ and $\bar{Q}$ values, respectively, with M_max taken from Table 3.1 according to the BAQ rate used. The resulting mantissa $M_\mathrm{baq} = [M_I, M_Q]$ is given by

$$M_I = \frac{\bar{I}}{|\bar{I}|} \cdot \min\big\{|\bar{I}|, M_\mathrm{max}\big\} \quad \text{and} \quad M_Q = \frac{\bar{Q}}{|\bar{Q}|} \cdot \min\big\{|\bar{Q}|, M_\mathrm{max}\big\}, \tag{3.54}$$

where $\bar{I}/|\bar{I}| = \pm 1$;

Step 6: As last step, M_I and M_Q are uniformly quantized in the range between $[-M_\mathrm{max} - 0.5, M_\mathrm{max} + 0.5]$ and encoded in binary representation using N_b bits/sample

$$M_I \rightarrow \mathbf{K}_I = \left[K_{I,\mathrm{baq},1}, K_{I,\mathrm{baq},2}, \ldots, K_{I,\mathrm{baq},N_\mathrm{b}}\right], \tag{3.55}$$

$$M_Q \rightarrow \mathbf{K}_Q = \left[K_{Q,\text{baq},1}, K_{Q,\text{baq},2}, \ldots, K_{Q,\text{baq},N_\text{b}}\right], \tag{3.56}$$

where $K_{I,\text{baq},i}$ and $K_{Q,\text{baq},i}$ is the value of the i-th bit (0 or 1) for the in-phase and quadrature component, respectively. Summarizing, the input signal is encoded in mantissa M_baq and exponent E_baq and stored in the onboard register in binary format.

According to the described algorithm, the quantized blocks are encoded, stored in the on board memory, and then transmitted to ground. Here, the SAR raw data are reconstructed and, after decoding, each sample $x_\text{baq} = \left[I_\text{baq}, Q_\text{baq}\right]$ is simply given by

$$I_\text{baq} = (-1)^{s_{I,\text{baq}}} \cdot \left(0.5 + \sum_{i=2}^{N_\text{b}} K_{I,\text{baq},i} \cdot 2^i\right) \cdot 2^{E/4}, \tag{3.57}$$

$$Q_\text{baq} = (-1)^{s_{Q,\text{baq}}} \cdot \left(0.5 + \sum_{i=2}^{N_\text{b}} K_{Q,\text{baq},i} \cdot 2^i\right) \cdot 2^{E/4}. \tag{3.58}$$

being $s_{I,\text{baq}} = K_{I,\text{baq},1}$ and $s_{Q,\text{baq}} = K_{Q,\text{baq},1}$ the sign bit for the in-phase and quadrature component of the mantissa, respectively.

3.2.2 Polar Block-Adaptive Quantization

The SAR raw data exhibit a circular Gaussian symmetry [42], so polar quantization can be considered as a possible alternative to a Cartesian quantization scheme for efficient SAR raw data compression. According to that, input I/Q values are transformed to magnitude-phase representation using rectangular to polar conversion. Since the obtained polar components are not independent from each other, they must be jointly quantized. Polar block-adaptive quantization is investigated in [95], where a detailed description of the design of the polar quantizer is provided as well (i.e., the optimum decision sectors and reconstruction values as derived in Section 3.1.4 [91]). However, it is shown that polar quantization does not improve much the resulting image quality, being the gain in terms of phase errors in order of 1° [95]. Hence, if considering the additional implementation complexity required for the polar quantizer, the traditional Cartesian BAQ remains a more attractive solution for efficient SAR raw data compression.

3.2.3 Flexible Dynamic Block-Adaptive Quantization (FDBAQ)

The SAR Sentinel-1a and Sentinel-1b SAR satellites have been launched in 2014 and 2016, respectively, in the frame of the European Union's Earth observation program Copernicus [13], with the main goal of providing enhanced capabilities in terms of SAR image quality, revisit time, coverage, timeliness, and reliability for operational services and applications. The Sentinel-1 satellites operate at C band ($\lambda \approx 5.5$ cm) and employ the so-called flexible dynamic block-adaptive quantization (FDBAQ) [96] for onboard data

compression. The FDBAQ extends the concept of block-adaptive quantization (BAQ), by adaptively adjusting the quantization rate according to the local signal-to-noise ratio (SNR): raw data showing large SNR values are quantized with more bits/sample, whereas, on the other hand, for regions affected by poor SNRs, smaller bit rates are allocated, since the performance gain would be negligible [96]. In this way, the resulting data rate is correspondingly reduced. Such an optimization procedure, in terms of local SNR estimation and data rate selection, is entirely done on board, which means that for the FDBAQ implementation no additional information has to be transmitted to the satellite (apart of the look-up tables linking the bit rates to the corresponding raw data power intervals); this implies that the data volume required for a specific acquisition cannot be accurately estimated before the commanding of each data take. Finally, the FDBAQ optimizes the performance and data rate in the raw data domain, and therefore the actual degradation in the final (focused) SAR and InSAR products is not considered in the algorithm.

In the last decade, alternative compression schemes for SAR systems based on the FDBAQ principle have been implemented to allow for a finer performance and resource optimization, by following the quantizer (commonly based on a BAQ scheme) with additional software/hardware blocks (as, e.g., an entropy or Huffman coder) at the cost of increasing the overall system complexity [97], [98]. A comprehensive overview of several algorithms for SAR raw data compression is provided in [92].

3.2.4 Efficient Onboard Quantization for Future SAR Systems

In the context of the design of future SAR systems, novel methods for efficient data volume reduction for multi-channel SAR [40] based on the joint use of transform coding and BAQ have been developed in [99] and [100], the latter being described in Chapter 6. Finally, in [101] a new approach based on linear predictive coding is suggested for efficient data volume reduction on staggered SAR systems [102], which is further detailed in Chapter 7.

3.3 BAQ and Low-Amplitude Errors

As it has been described in Section 3.1.2, quantization errors are mainly given by the sum of two contributions, the granular and the overload noise: the first one is due to the finite number of output decision levels within the supported range, whereas the second one is introduced by the clipping of input signals exceeding the supported range.

In addition to granular and clipping errors, inhomogeneities in the SAR backscatter distribution cause a further signal-dependent performance degradation due to quantization. This occurs, for example, in urban areas, where a high dynamic range of backscatter can be expected. Such an effect is also known as low scatterer suppression [103], it is

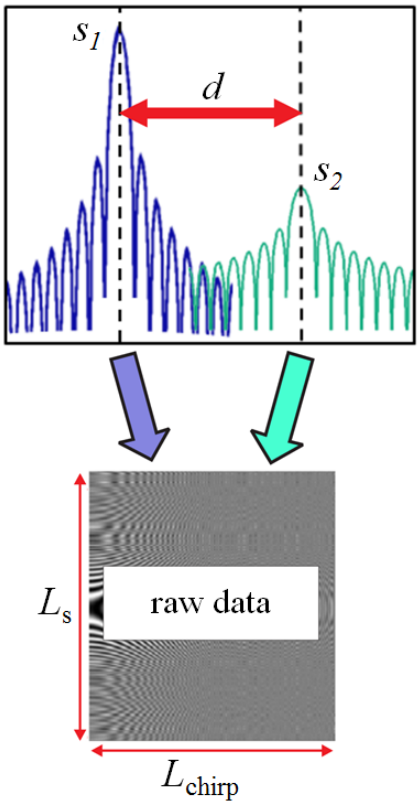

Figure 3.9: The impulse response of the two point scatterers s_1 and s_2 overlap in the raw data domain if their distance d is small with respect to the synthetic antenna L_s and the chirp length L_{chirp}, respectively, as shown in (3.59) and (3.60).

peculiar of the SAR acquisition principle and has to be considered as an additional quantization error source, different from granular and clipping noise, since it is visible only after SAR processing. Figure 3.9 shows two targets, s_1 and s_2, with different magnitude response. They overlap in the raw data domain if both the azimuth and range distances d_{az} and d_{rg} are small with respect to the synthetic antenna L_s and the chirp length L_{chirp}, respectively

$$d_{az} << L_s = \lambda \frac{R_0}{L_a}, \tag{3.59}$$

$$d_{rg} << L_{chirp} = \frac{c_0 \tau_p}{2}. \tag{3.60}$$

As an example, for the TerraSAR-X and TanDEM-X satellites, values of L_s and L_{chirp} are commonly in the order of a few kilometers. According to the BAQ algorithm, the decision levels and the clipping thresholds for the compression are determined by the

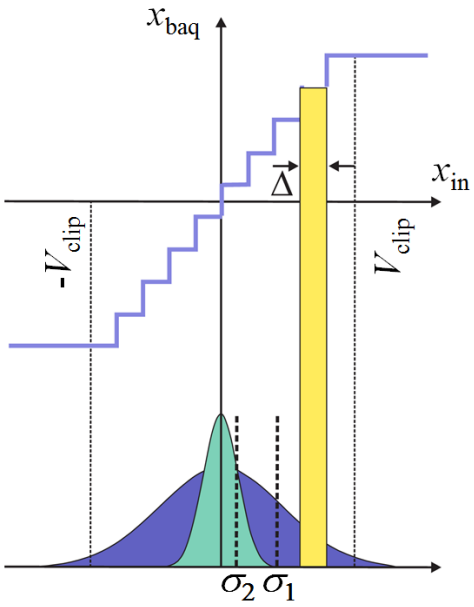

Figure 3.10: (Bottom) probability density functions for the two targets in Figure 3.9, sketched with different colors. (Top) according to the BAQ algorithm, the decision levels Δ, as well as the dynamic range of the quantizer $\pm V_{clip}$, are set as a function of the mean power of the raw data block, which, in this example, is mostly determined by s_1 (since $\sigma_1 >> \sigma_2$). Therefore, if two overlapping targets have different power responses, the strong signal is better reconstructed, whereas the weak one is heavily distorted.

mean power for each raw data block, as shown in Figure 3.10. Therefore, if two overlapping targets have different magnitude responses, the strong signal is better reconstructed, whereas the weak one is heavily distorted. In order to quantify the described effect, different simulations on two one-dimensional azimuth-compressed point targets have been carried out: the power of the strong target P_s is kept constant, whereas the power of the low one P_l is varying, to evaluate the distortion for different power ratios between the two. The targets are located at about 50 meters distance in azimuth, in order to ensure a sufficient overlapping of the echo responses in the raw data. The resulting performance degradation is shown in Figure 3.11, where the phase error is plotted for the available BAQ rates and along the power ratio P_{ratio}

$$P_{ratio} = \frac{P_s}{P_l}. \tag{3.61}$$

The phase error is obtained as the phase difference evaluated at the peak of the point target with lower amplitude, and is calculated for different BAQ rates with reference

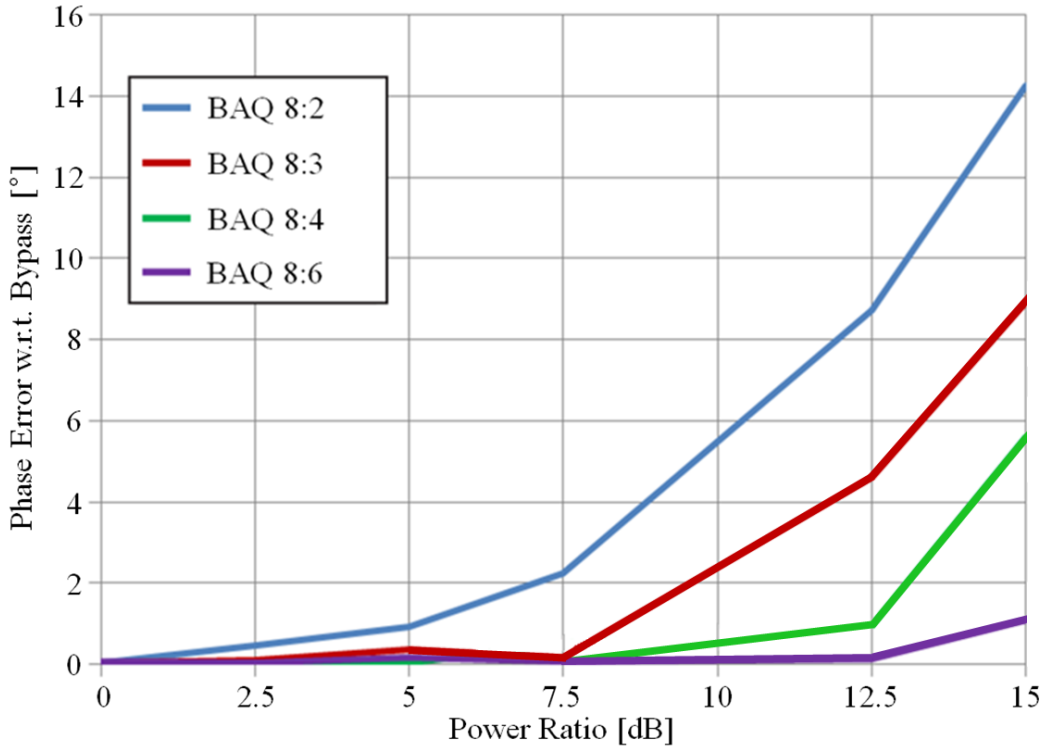

Figure 3.11: Low scatterer suppression effects are evaluated by means of simulations of two azimuth-compressed point-like targets: the power of the strong target P_s is kept constant, whereas the power of the low one P_l varies. The phase error is derived taking as reference the data quantized with 8 bits/sample and is evaluated at the peak of the compressed target with lower amplitude and is plotted for the available BAQ rates and along the power ratio, expressed as in (3.61).

to the data quantized with 8 bits/sample (the latter corresponding to the BAQ-bypass case). From Figure 3.11 it can be noticed that the phase error strongly depends on the power ratio of the two targets and, at the same time, on the quantization rate employed for compression: while for the case of 6 bits/sample almost no degradation is observed (less than 1°), a significant performance loss is shown when reducing the quantization rate to 2 bits/sample, for which a phase error of about 14° (for a power ratio of 15 dB) is obtained. The phase error has been evaluated for the strong magnitude target as well and, as expected, it has been found to be independent of the power ratio (the dependence on the quantization ratio, of course, remains).

Based on the present investigations, one can conclude that, in the most general case, quantization errors are to be treated as a nonlinear and signal-dependent error source affecting SAR data, for which the correlation between noise and data can not be neglected.

The impact of the described low-amplitude errors on simulated SAR data as well as on real TanDEM-X acquisitions is further discussed in Chapter 4 and Chapter 5.

3.4 Chapter Summary

This chapter aims at providing the reader with the fundamental background on quantization theory, specifically applied to synthetic aperture radar (SAR) data, which is necessary for the understanding of the analyses and investigations presented in the next chapters.

The relevant parameters, which define the quantizer type (e.g., uniform, non-uniform) and its performance, are recalled, together with a description of the system and signal models and of the typical sources of quantization errors. The constraints for designing the MMSE (or Lloyd-Max) quantizer are provided along with the definition of the quantizing theorem, which derives a sufficient condition, so that it is possible to reconstruct all the information of a quantized signal from the original band-limited continuous-amplitude one (thus representing a sort of equivalent in quantization of the well-known Nyquist-Shannon sampling theorem).

The reader should be aware of the state-of-the-art quantization schemes for SAR systems, such as the well-established block-adaptive quantization (BAQ), and of the so-called low-amplitude errors, which are introduced by the use of adaptive quantizers and cause an increased reconstruction error for weak targets in close vicinity of stronger ones in SAR raw data. Indeed, in addition to the well known granular and clipping errors, inhomogeneities in the SAR backscatter distribution cause a further performance degradation due to raw data quantization. This has to be therefore treated as a nonlinear and signal-dependent error source affecting the SAR performance, for which the correlation between noise and data cannot be neglected. A few simulation results are shown, whereas, in the next chapter, an extensive analysis on the impact of raw data quantization on TanDEM-X interferometric SAR data is presented.

4 Quantization Effects in TanDEM-X Data

In this chapter, the impact of quantization on TanDEM-X monostatic and interferometric data is investigated. For this purpose, key quantities in estimating interferometric and SAR image quality, like NESZ, coherence, phase errors, and resulting DEM inaccuracies, are evaluated in detail. From this, a statistical characterization of the resulting performance degradation is provided and a novel method, named performance-optimized block-adaptive quantization (PO-BAQ), is introduced, which allows for an optimization of the resource allocation and, at the same time, for controlling the interferometric performance degradation, by exploiting a priori knowledge about the SAR backscatter information. Part of the analyses presented in this chapter have been published in [94].

4.1 Introduction

SAR interferometry (InSAR) represents a well-recognized technique for many remote sensing applications. About three decades of research studies, technical progress, and developments in the field have demonstrated the potential of spaceborne InSAR systems for the assessment and monitoring of many geophysical parameters, such as ground deformations, ocean currents, and Earth's topography by generation of digital elevation models (DEMs). In 2000, the Shuttle Radar Topography Mission (SRTM) created the first elevation data on a nearly global scale, limited to a latitude range from 56° S to 60° N [19]. Ten years later, TanDEM-X (TerraSAR-X add-on for Digital Elevation Measurement) has opened a new era in spaceborne radar remote sensing, by generating a global, high-resolution DEM with unprecedented accuracy [104]. The next big challenge to be addressed by future spaceborne remote sensing missions is now turning to the estimation and the long-term monitoring of dynamic processes in the Earth environmental system, such as surface deformation, forest height and biomass change, ice/glacier melting, as well as ocean currents. This represents the main objective of Tandem-L, a DLR single-pass interferometric and fully polarimetric L-band radar mission proposal, which exploits innovative high-resolution wide-swath SAR modes, together with the use of large bandwidths, high pulse repetition frequencies (PRFs), and multiple acquisition channels [37], [105]. Definitely, this is associated with the clear demand of gathering an increasing amount of information in a shorter time interval, which implies, from mission design, stronger requirements in terms of onboard memory and downlink capacity (a strategy for data volume reduction for Tandem-L-like SAR systems is presented in Chapter 7).

In this scenario, SAR raw data quantization represents an aspect of primary importance, since the data rate employed to digitize the recorded radar signal defines on the one hand the amount of data to be collected and transmitted to the ground, and also, on the other hand, directly affects the performance of the SAR products. The impact

of raw data quantization on the SAR image quality is often considered as an additive white Gaussian noise source. However, quantization effects strongly depend on the specific characteristics of the SAR scene, and have to be treated as a signal-dependent and highly nonlinear error source, as shown in Chapter 3. The goal of this chapter is therefore to assess the impact of raw data quantization on SAR imaging and interferometric performance using bistatic TanDEM-X data. In the next section a short overview on the TanDEM-X mission is provided, and the investigation approach followed for the present analyses is shown. In Section 4.3 the impact of raw data quantization is evaluated on key InSAR performance descriptors such as the noise equivalent sigma zero (NESZ), the interferometric coherence, the interferometric phase errors, and the relative height accuracy in DEMs. In particular, the attention is focused on those scene and system parameters which most affect quantization errors in SAR data (in addition, of course, to the quantization rate N_b), such as the degree of inhomogeneities in the backscatter response, described by the standard deviation of the SAR backscatter σ_{σ^0}, the number of interferometric acquisitions N_acq, and the number of looks N_l. Based on the obtained results, a novel performance-optimized block-adaptive quantization (PO-BAQ) method is introduced in Section 4.4, which allows for an optimization of the compression rate to control the resulting image degradation by exploiting a priori knowledge about the SAR backscatter information of the imaged scene. The chapter is concluded in Section 4.5 with a summary and outlook for future research.

4.2 The TanDEM-X Mission

TanDEM-X (TerraSAR-X add-on for Digital Elevation Measurement) is the first operational spaceborne bistatic SAR system, which comprises two separate spacecrafts. Developed under a public-private partnership between the German Aerospace Center (DLR) and Airbus Defense & Space (ADS) [30], [106], the TerraSAR-X SAR satellite (TSX, launched in 2007) is enhanced by its twin radar satellite TanDEM-X (TDX, launched in 2010). A list of the main TanDEM-X system parameters is given in Table 4.1. After six months of commissioning phase, the mission officially started in December 2010. Since then, the two satellites have been operationally acquiring interferometric SAR images in stripmap single HH polarization mode, with a typical resolution of about 3 meters in azimuth and range. Both satellites have been flying in a closely controlled orbit formation with the opportunity for flexible along- and across-track baseline selection and the primary objective of generating a global, consistent and high-precision digital elevation model (DEM) [30] at a final independent posting of 12 m $\times$ 12 m. TanDEM-X nominally operates in bistatic SAR acquisition mode, i.e. either TerraSAR-X or TanDEM-X is used as a transmitter (master) and both satellites (master and slave) simultaneously record the signal scattered back from the Earth's surface. By this, TanDEM-X provides the community with a unique data set to be exploited for a broad range of commercial and scientific

Table 4.1: System parameters for the TanDEM-X mission.

Parameter	**Value**
Satellite Height (Equator), h_s	514 km
Carrier Frequency, f_c	9.65 GHz
Radar Wavelength, λ	3.11 cm
Chirp Bandwidth, B_{rg}	100 MHz
Chirp Pulse Duration, τ_p	10 - 60 μs
Antenna Size, $L_a \times L_e$	4.8 m $\times$ 0.8 m
Incidence Angles, η	29° - 48°
Available BAQ Rates, N_b	2, 3, 4, 6, 8 bits/sample
Satellite Memory	TSX: 256 Gbit, TDX: 512 Gbit
Downlink Capacity	$\sim$260 Mbits/s (total net data rate)

applications. The global TanDEM-X DEM has been finalized and delivered in September 2016 [104] and is shown in Figure 4.1. In Table 4.2 the specifications for SRTM [107] and TanDEM-X [108] missions are compared. Such high-demanding requirements have been achieved by performing at least two global mappings of the Earth's land masses and multiple acquisitions over selected regions (such as mountainous terrain, forested areas, or sandy desert regions) to improve the overall product accuracy [109]. Since the beginning of the mission, more than half a million high-resolution bistatic scenes, extending over an area of about 30 km in range by 50 km in azimuth, have been acquired and processed, with incidence angles ranging between 30° and about 50°. For the first DEM global coverage of TanDEM-X, the height of ambiguity (h_{amb}, defined in (2.56)) was typically between 45 m and 60 m, ensuring good unwrapping quality over most land types. For the second one, larger baselines were considered (h_{amb} around 35 m), in order to increase the final DEM accuracy. The combination of at least two acquisitions by means of multi-baseline phase unwrapping algorithms allowed then to fully meet the mission requirements [110].

On board the TerraSAR-X and TanDEM-X satellites, the received backscattered signal is first digitized by an 8-bit analog-to-digital converter (ADC) and then further compressed by a block-adaptive quantizer (BAQ), which has been introduced in Section 3.2. For the space-varying estimation of raw data statistics blocks of fixed size of $N_{block} = 128$ range samples are used, for the in-phase (I) and quadrature (Q) channels separately. This information is then employed to determine the quantization decision levels that

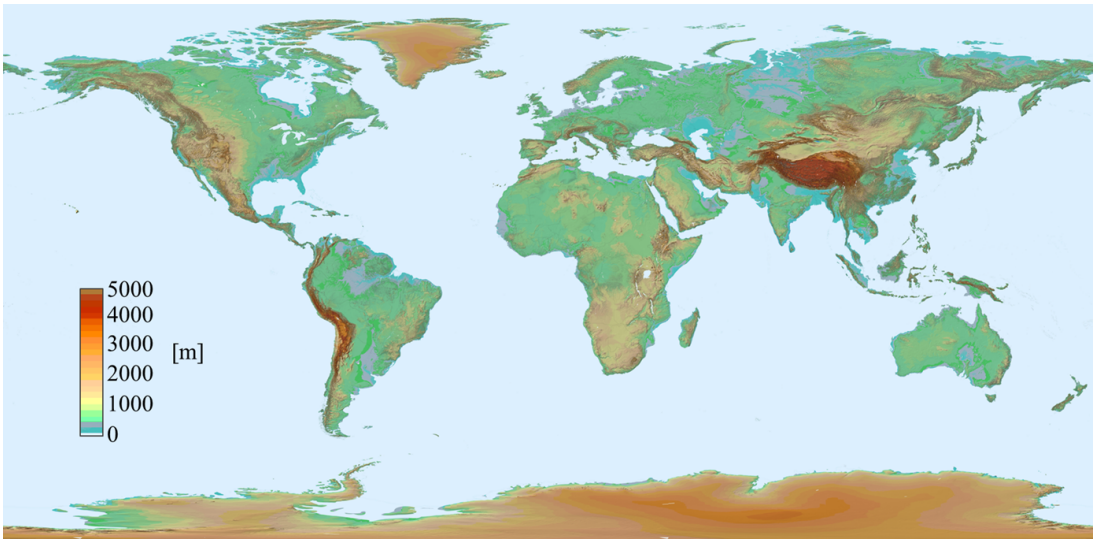

Figure 4.1: The global TanDEM-X DEM.

Table 4.2: Comparison of SRTM and TanDEM-X specifications.

Requirement	**Specification**	**SRTM**	**TanDEM-X**
Relative Vertical Accuracy	90% linear point-to-point error over a 1° x 1° cell	12 m (slope < 20%) 15 m (slope > 20%)	2 m (slope < 20%) 4 m (slope > 20%)
Absolute Vertical Accuracy	90% linear error	18 m	10 m
Absolute Horizontal Accuracy	90% circular error	23 m	10 m
Spatial Resolution	independent pixels	30 m (1 arc sec at equator)	12 m (0.4 arc sec at equator)

best match with the observed statistics. Possible compression rates are 8:2 (i.e., from 8-bit ADC to 2-bit BAQ), 8:3, 8:4, 8:6 and 8:8, where the latter corresponds to BAQ bypass [27], [93]. The compression rate is individually configured before every data take by instrument commanding and is kept constant for the whole acquisition.

For the raw data acquired by TSX and TDX, the granular noise can be considered as the dominant error source caused by quantization, as the instrument parameters are set to minimize the occurrence of saturation effects. In particular, in [27] the overflow rate occurring in the raw data is investigated for the TerraSAR-X satellite: several hundreds of data takes are considered and each one is divided into raw data blocks, and it is verified that for more than 99% of the blocks the occurrence of signal saturation remains below 1%. Similar results have been obtained for the TanDEM-X satellite from analyses conducted during the initial commissioning phase, few months after its launch. Moreover, in [30] it is verified that the performance loss due to raw data digitization within TanDEM-X, resulting from the quantization process, matches quite well with the the-

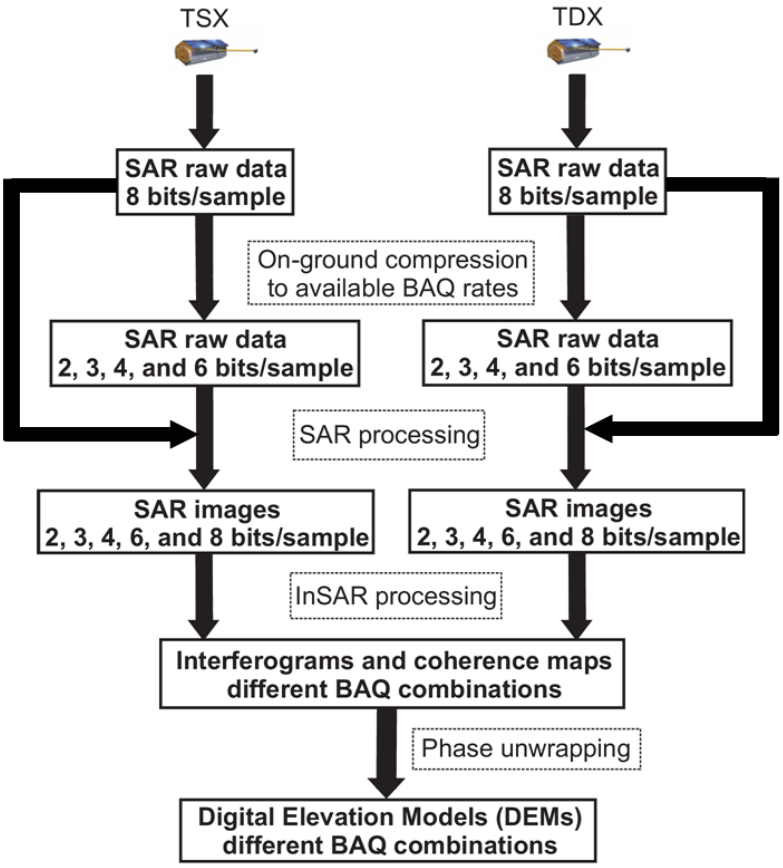

Figure 4.2: Workflow for test data acquisition, on-ground quantization, and processing. Raw data commanded with BAQ bypass are compressed on ground into multiple data sets using all available quantization rates. The obtained products are then processed into SAR images, from which interferograms, coherence maps, and DEMs are derived.

oretic predictions for an optimum uniform Cartesian quantizer (i.e., where no clipping effects exist).

4.2.1 Investigation Approach

The steps performed to evaluate quantization effects on TanDEM-X data are sketched in Figure 4.2: bistatic acquisitions are commanded with BAQ bypass in both TSX and TDX SAR instruments. The recorded SAR raw data are compressed on ground into multiple data sets using all available BAQ rates. The employment of different BAQ settings for the two satellites (e.g., TSX 8:4 and TDX 8:3) allows to further refine the

Table 4.3: Test sites for quantization analysis. For each test site, bistatic acquisitions have been commanded with BAQ bypass in both TSX and TDX SAR instruments.

Test Site	**Land Cover**	**[Lat./Lon.]**
1. Salar de Uyuni (Bolivia)	Salt Lake	[20° S, 67° W]
2. Amazon Forest 1 (Brazil)	Rainforest	[4° S, 64° W]
3. Amazon Forest 2 (Brazil)	Rainforest	[7° S, 66° W]
4. Amazon Forest 3 (Brazil)	Rainforest	[6° S, 63° W]
5. Greenland	Ice and Snow	[71° N, 42° W]
6. Antarctica	Ice and Snow	[74° S, 10° W]
7. Las Vegas	Urban Area	[36° N, 115° W]
8. Mexico City	Urban Area	[19° N, 99° W]
9. Borneo Forest (Indonesia)	Tropical Forest	[3° S, 113° E]
10. Appalachian (USA)	Mountainous Forest	[35° N, 82° E]
11. Death Valley (USA)	Soil and Rocks	[41° N, 119° W]
12. Taklamakan Desert (China)	Sandy Desert	[39° N, 82° E]
13. Iowa (USA)	Agricultural Area	[41° N, 93° W]

granularity of the achievable performance, and is investigated as well. The obtained raw data products are then processed into single-look complex (SLC) SAR images, with a ground-range resolution of about 3 m. From SLC images, interferograms, coherence maps, and DEMs are derived. The interferometric products have a final ground-range resolution of approximately 12 m, obtained by applying a boxcar multi-looking to the bistatic interferogram. The total number of independent looks N_l is mostly between 16 and 32, depending on the incidence angle (specified in Table 4.1) as well as on the processed bandwidths [30]. Each bistatic scene typically extends over 30 km in range and 50 km in azimuth and the complete SAR and InSAR processing is performed by the Interferometric TanDEM-X Processor (ITP) [111]. By reprocessing the same data acquisitions with different BAQ rates, the effects of quantization are isolated from other error sources. For the present investigations, dedicated acquisitions were carried out on defined test sites showing different land cover types and topography characteristics, which are listed in Table 4.3. From each of these sites, up to six product sets, obtained from different compression rates, were then generated for performance comparison.

4.3 Performance Analysis

In this section the performance impact of different raw data quantization rates on TanDEM-X data is presented. As key SAR parameters, the NESZ (investigated in Section 4.3.1), the interferometric coherence (Section 4.3.2), and the phase errors (Section 4.3.3) are investigated. For this, a detailed assessment on parameters influencing quantization errors is provided, such as the degree of inhomogeinities in the SAR backscatter, the number of interferometric acquisitions, and the number of looks. Finally, quantization effects on the DEM relative height accuracy (Section 4.3.4) are investigated.

4.3.1 Noise Equivalent Sigma Zero (NESZ)

The noise equivalent sigma zero is a measure of the system sensitivity to areas of low radar backscatter. It is described in (2.44), and represents the value of the backscatter coefficient corresponding to a signal-to-noise ratio (SNR) equal to one. The NESZ quantifies the system noise floor and includes contributions induced by the system, like antenna pattern, instrument thermal noise, as well as processing filters [42]. In order to quantitatively estimate the noise power affecting TanDEM-X SAR products, a distributed target analysis over regions characterized by very low backscatter has been carried out. In particular, areas covered by water bodies almost completely reflect the radar signal in specular direction. Hence, the signal received by the antenna over such low backscatter areas can be approximated with the system noise. The procedure adopted for NESZ estimation is shown in Figure 4.3. The test area depicted on the top of the figure is located in the Amazon rainforest and is entirely crossed by one river from near to far range. Forested areas are identified as pixels with $\sigma^0 > -17$ dB (a threshold value which can be slightly adapted for each scene), they correspond to the black areas in the mask in the middle and are filtered out. Then, water pixels (white areas in the mask) are averaged along the azimuth direction, to finally derive the corresponding NESZ profile shown at the bottom of Figure 4.3. For the present analysis, incidence angles going from 39° to 48° have been investigated over different test areas, and the NESZ has been estimated for the master satellite (however, for TSX and TDX, the observed difference in terms of NESZ is usually less than 1 dB [112], [113]). The NESZ profile curves, resulting from an interpolation along range of the measured values, are depicted in Figure 4.4 (a) for each quantization rate of four different data acquisitions over the salt lake of Uyuni (Bolivia) and over the Amazon rainforest, corresponding to the test sites 1, 2, 3, and 4 of Table 4.3 (the respective NESZ profiles in Figure 4.4 are numbered accordingly).

In order to validate the present results, they have been compared with the NESZ degradation estimated by adopting the theoretical model presented in [93], where a performance analysis of BAQ is carried out by simulating the complete system and signal

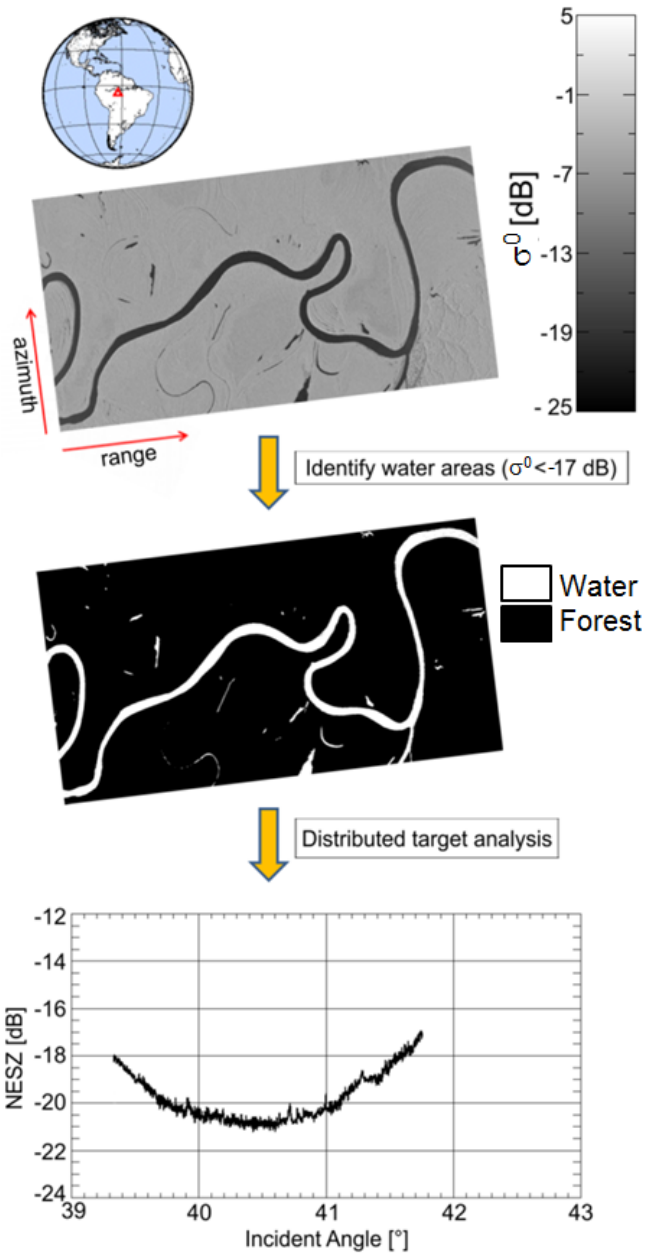

Figure 4.3: Steps followed for NESZ estimation. (Top) The test site is located in the Amazon rainforest and is crossed by one river from near to far range. (Middle) A threshold on backscatter is applied to locate water bodies and the corresponding pixels are depicted in white. (Bottom) The NESZ profile curves are finally derived by averaging the water pixels along azimuth.

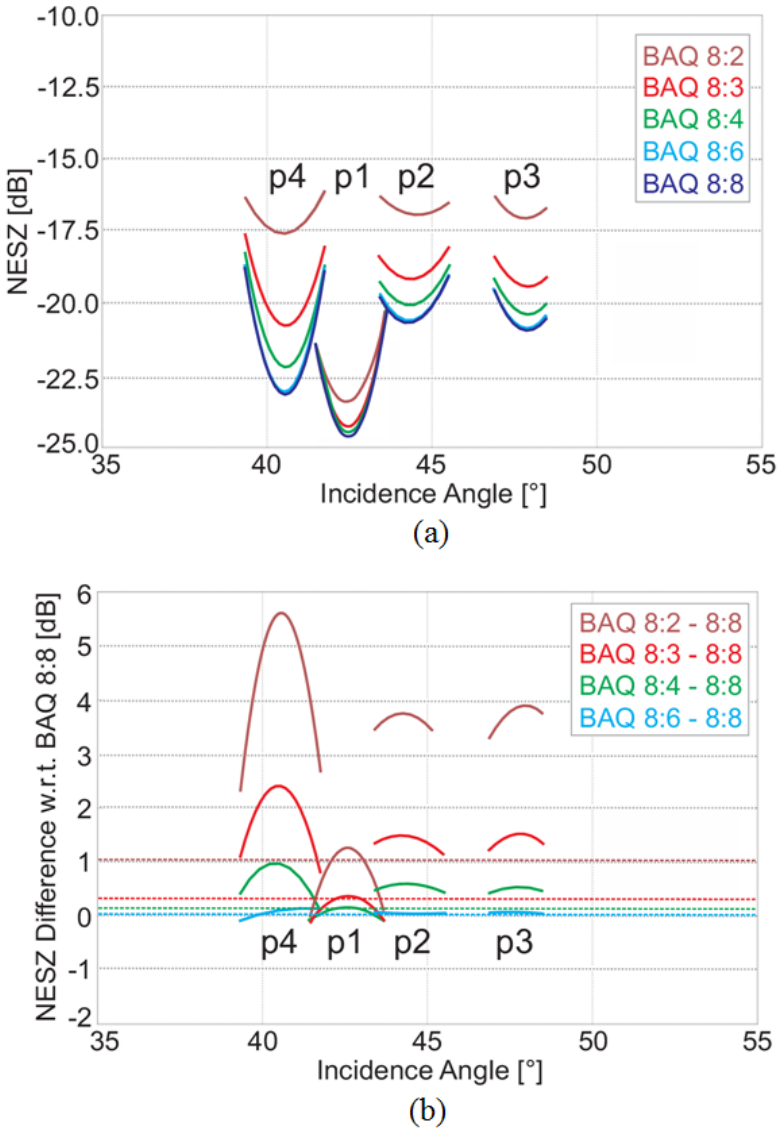

Figure 4.4: (a) NESZ over incidence angle for different BAQ rates (depicted with different colors), derived as explained in Figure 4.3. The four profiles p1-p4 correspond to data acquired over different areas, corresponding to the test sites 1, 2, 3, and 4 of Table 4.3. The highest and lowest curve indicate the NESZ for the case of BAQ 8:2 and BAQ 8:8 (bypass), respectively. (b) NESZ degradation introduced by quantization with respect to the bypass case. The theoretical degradation has been derived for the different quantization rates according to [93] and is represented by the horizontal lines. Only the profile p1 matches quite well with the theoretical predictions (see also Figure 4.5).

models for the TSX and TDX satellites. According to the NESZ definition, quantization effects are evaluated considering the SNR degradation when assuming a unitary input SNR, which is kept constant and homogeneous in all simulations.

Figure 4.4 (b) shows the NESZ degradation with respect to the bypass case (for each data take all the other acquisition and processing parameters are the same), and the NESZ degradation with reference to BAQ 8:8 obtained by simulations is indicated with horizontal lines depicted with different colors, each one representing the compression rate indicated in the figure legend. A general underestimation of the employed model is evident, except for the profile p1. In order to better understand the observed discrepancy, the backscatter distribution of the considered scenes has to be inspected. A representative scene, from which the profiles p2, p3, and p4 are derived, is depicted in Figure 4.3. Here, the rivers considered for NESZ estimation are usually not more than a few hundreds meter wide, about one order of magnitude smaller than the typical synthetic antenna and the chirp length for TanDEM-X. Therefore, the responses from the close and stronger backscatter area (such as forest, soil and rocks) considerably overlap with the ones coming from the water area, and the consequent setting of the quantization decision levels is biased by the strong target responses, leading to a suppression of the low backscatter region (as explained in Section 3.3). This results in an increase of the noise floor (i.e., of the NESZ degradation), that becomes more evident when fewer bits are employed for quantization, and explains the observed inconsistency with the simulation results, where a uniform and homogeneous backscatter response was considered. Indeed, the performance resulting from BAQ with 6 bits/sample and 8 bits/sample is practically the same for all the analyzed test sites and in good agreement with the simulation results, whereas a substantial degradation in terms of radiometric accuracy up to 6 dB is observed for the profiles p2, p3, and p4 when employing 2 bits/sample. This is due to the described low scatterer suppression effect: even if 75% of memory consumption could be spared for one acquisition, such a configuration setting causes a noticeable loss in the SAR image quality, and should be avoided when possible. On the other hand, the SAR image, from which the profile p1 is derived, is shown in Figure 4.5. It is located in the salt lake of Uyuni (test site 1 in Table 4.3), and low backscatter due to the temporary presence of water (most probably caused, in turn, by a rain event) is observed on an area extending by about 4 km along azimuth, which is comparable to the synthetic antenna length. Therefore, the setting of the quantization decision levels over the salt lake is on average little influenced by the neighboring high backscatter areas. The resulting NESZ degradation of p1, depicted in Figure 4.4 (b), matches quite well with the theoretic prediction. Therefore, the backscatter characteristics of the imaged scene strongly impact the sensitivity of a SAR system, especially when low BAQ rates are used, an aspect which needs to be necessarily taken into account for performance definition and design.

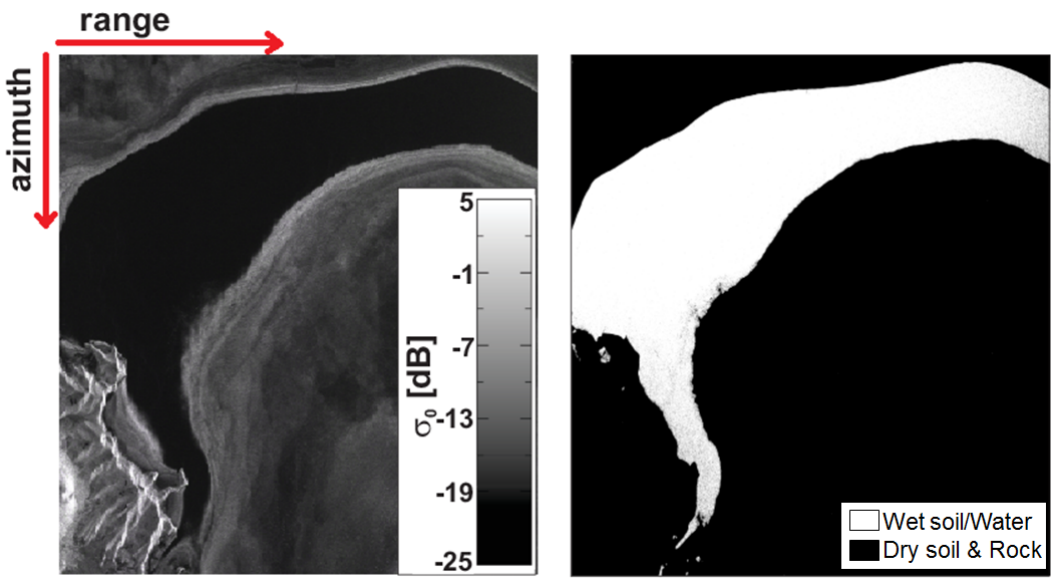

Figure 4.5: (Left) SAR amplitude of the salt lake of Uyuni, Bolivia. (Right) Mask used for NESZ estimation. The low backscatter region, highlighted in white, is probably due to a rain event where the area was temporarily flooded. It extends by about 4 km along azimuth direction (which is comparable to the synthetic antenna length), and entirely from near to far range. It can be therefore assumed that the quantization decision levels in the low backscatter zones are less influenced by the adjacent high backscatter areas. The resulting NESZ degradation corresponds to the profile p1 in Figure 4.4 and agrees quite well with the simulation results in [93].

4.3.2 Interferometric Coherence

The key quantity to evaluate InSAR performance is the interferometric coherence. As already introduced in Section 2.4.2, it represents the normalized correlation coefficient between the master (monostatic channel) and the slave (bistatic channel) acquisition, and its absolute value provides valuable information about the amount of noise affecting the interferogram. Several error sources contribute to coherence loss in bistatic TanDEM-X data [71]. In the Interferometric TanDEM-X Processor (ITP) [111], the interferometric coherence is estimated from the full-resolution SAR images pair by using an estimation window of typically 11×11 pixels in azimuth and range. Areas showing different land cover characteristics have been acquired with different polarization channels, incidence angles, and baselines (corresponding to the test sites 1, 2, and 5-13 of Table 4.3). For each scene, the mean coherence over land has been evaluated by applying a water mask.

Figure 4.6 (a) depicts the interferometric coherence for the analyzed scenes and BAQ

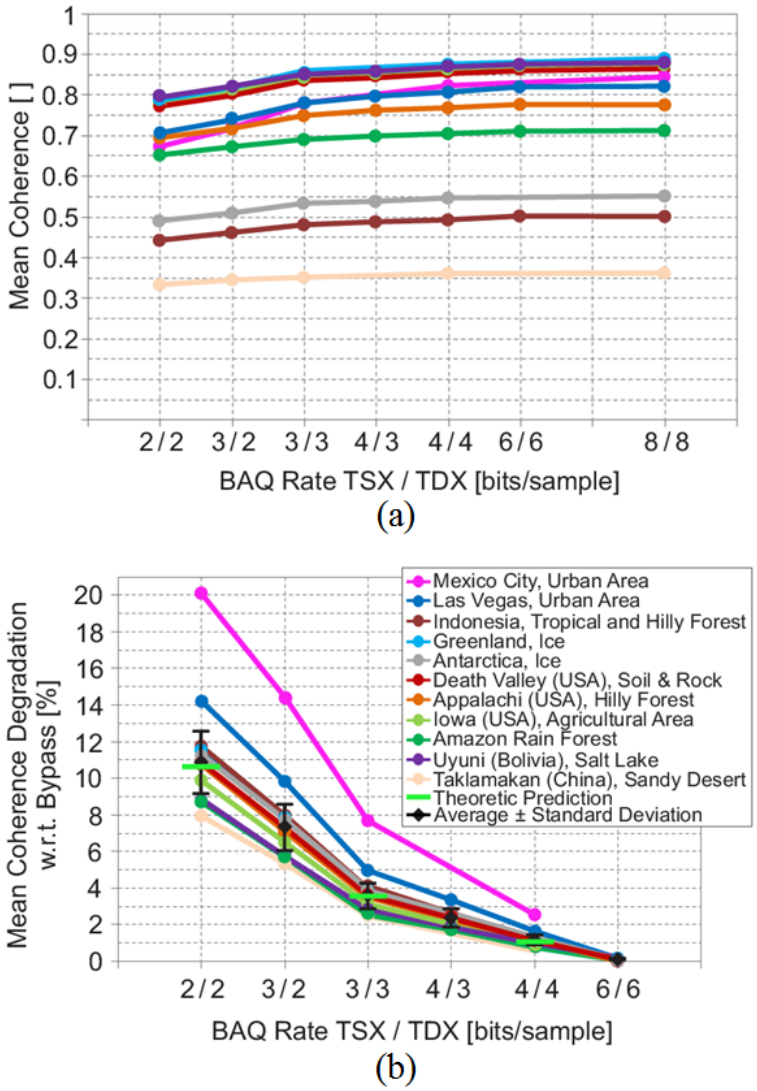

Figure 4.6: (a) Interferometric coherence over BAQ rates and (b) coherence degradation with respect to the bypass case (8:8), for different test sites (depicted with different colors). Different BAQ settings for the two satellites (e.g., TSX 8:4 and TDX 8:3) are investigated as well. The black bars in the bottom plot represent the average and the standard deviation of the estimated degradations for each BAQ rate, while the short horizontal green lines indicate the theoretical prediction for the case of 2, 3, and 4 bits/sample, as derived in [30]. Each curve corresponds to one acquisition compressed and reprocessed for different BAQ rates.

rates. As expected, lower coherence values are observed, for the same test site, when fewer bits are employed for quantization. The results plotted in Figure 4.6 are obtained for quantization rates of 2, 3, 4, and 6 bits/sample. Additionally, bistatic acquisitions with different quantization rates between master and slave SAR images have been generated as well. For example, 3 bits/sample for TSX has been combined with 2 bits/sample on TDX and, secondly, 4 bits/sample on TSX together with 3 bits/sample on TDX. By doing so, also the non-integer quantization rates of 2.5 and 3.5 bits/sample, respectively, can be implemented and investigated. Figure 4.6 (b) shows the resulting coherence degradation with respect to the bypass case. Each curve describes the performance of one acquisition, which has been compressed to different BAQ rates. In particular, an average coherence degradation of about 1% and 3.5% is noticed by using rates of 4 and 3 bits/sample for both satellites, respectively, which are the nominal configurations which have been used for the first global DEM acquisition of TanDEM-X. The black bars represent the average and the standard deviation of the estimates for each BAQ rate, and a good agreement with the theoretic prediction is observed, marked by the green lines for the case of 2, 3, and 4 bits [30]. It can be noticed that the standard deviation of the estimates increases when reducing the quantization rate. Again, an explanation of this effect is given by looking at the backscatter distribution within the scene: in Figure 4.7, the coherence degradation for the case of 2 bits/sample (for which the dispersion is most evident) is plotted over the standard deviation of the measured radar backscatter σ^0, which gives information about the degree of homogeneity in the backscatter response of the imaged area. The observed quantization decorrelation is approximately 8% for flat and homogeneous areas with standard deviations typically smaller than 2.5 dB like the Taklamakan desert (China) and the salt lake of Uyuni (Bolivia), depicted in flesh tone and violet, respectively. On the other hand, a quantization decorrelation up to 20% is observed for the urban area of Mexico City, marked in pink. Here, the backscatter distribution is very inhomogeneous (showing high standard deviations above 6 dB). Moreover, over urban areas the performance is further degraded due to the presence of additional geometric distortions, such as multiple reflections, which increase the noise in the interferometric phase (see also next section). Low scatterer suppression effects represent therefore an additional non-linear and signal-dependent error, which vitiates the hypothesis of additive independent Gaussian noise for quantization errors, and needs to be taken into account when defining resource allocation strategies for SAR missions.

4.3.3 Interferometric Phase Error

As it has been described in Section 2.4.3, the error affecting the interferometric phase is directly related to the coherence and to the equivalent number of looks N_{l} employed within the multi-looking process [30], [80]. The error affecting the interferometric phase is a key quantity for the assessment of interferometric SAR data quality. For this anal-

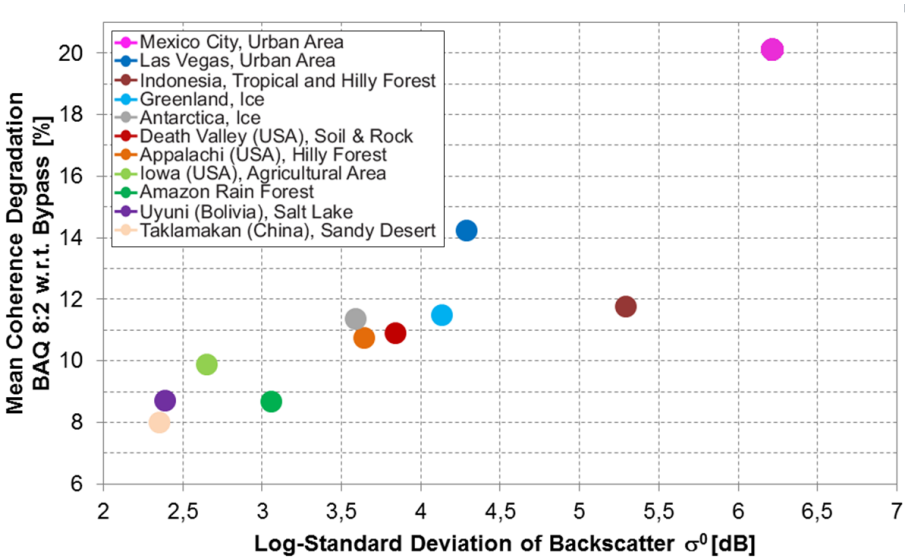

Figure 4.7: Increase of coherence loss for BAQ 8:2 with respect to the bypass case, due to inhomogeneities in the backscattered response, represented by the standard deviation of the measured radar backscatter σ^0 over a test site.

ysis, interferograms with different compression rates have been obtained by using the experimental TanDEM-X processor (TAXI), developed at the Microwaves and Radar Institute, DLR [114]. The interferometric azimuth and ground-range resolution is about 12 m, corresponding to N_l values typically between 16 and 32. The impact of raw data quantization on the interferometric phase has been evaluated by comparing, for a single data take, the non-compressed interferograms φ_bypass with the ones generated by different BAQ rates φ_{N_b}

$$\Delta\varphi_\delta = \varphi_\mathrm{bypass} - \varphi_{N_\mathrm{b}}, \tag{4.1}$$

where N_b indicates the used compression rate (in bits/sample). The differential phase $\Delta\varphi_\delta$ is nominally confined in the interval $[-2\pi, 2\pi]$. However, the maximum real phase error achievable is equal to $\pm\pi$, and all possible values outside the interval $[-\pi,\pi]$ are wrapped around the corresponding bound, i.e.

$$\Delta\varphi_\delta : \pm\pi \pm \varepsilon \equiv \mp\pi \pm \varepsilon, \forall\varepsilon \in [0,\pi]. \tag{4.2}$$

Taking into account the above equivalence, the phase error due to quantization for the case of N_b bits/sample may be finally expressed as:

$$\Delta\varphi = \begin{cases} \Delta\varphi_\delta, & \text{if } |\Delta\varphi_\delta| \leq \pi \\ -\mathrm{sign}(\Delta\varphi_\delta)\cdot(2\pi - |\Delta\varphi_\delta|), & \text{if } |\Delta\varphi_\delta| > \pi, \end{cases} \tag{4.3}$$

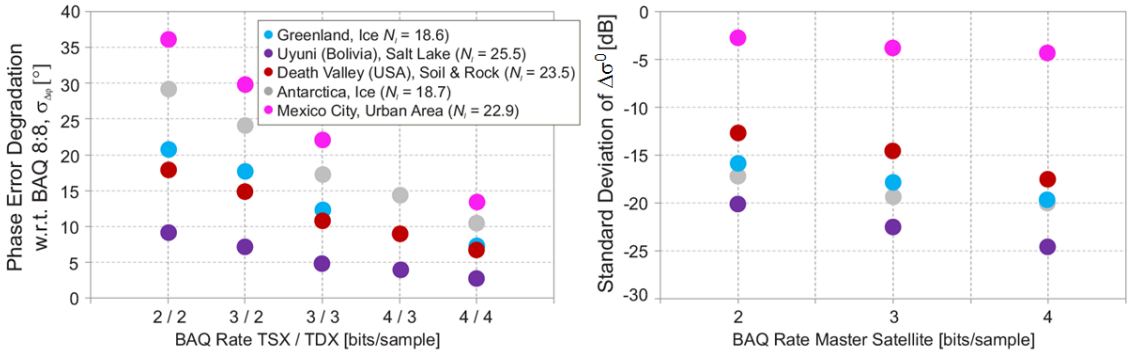

Figure 4.8: (Left) Increase of the interferometric phase error due to quantization. Each value represents the standard deviation of the differential interferometric phase for each compression rate with reference to the bypass case $\sigma_{\Delta\varphi}$ (being $\Delta\varphi$ derived as in (4.3)), for a given acquisition. The total equivalent number of looks N_l for each test site is specified in the legend. (Right) Increase of the errors introduced in the SAR amplitude due to quantization. Each value represents the standard deviation of the radar backscatter difference $\Delta\sigma^0$ (of the master acquisition) for different compression rates with respect to the bypass case.

being $\Delta\varphi_\delta$ defined in (4.1). In general, $\Delta\varphi$ can be well approximated by a zero-mean random variable (as described in Section 3.1.4), independently of the employed quantization rate. On the other hand, its standard deviation gives information about the dispersion of the phase errors, and has therefore been chosen as a quality parameter for performance assessment. The increase of the interferometric phase errors due to quantization is shown on the left-hand side of Figure 4.8. Each value represents the standard deviation of the phase error, $\sigma_{\Delta\varphi}$ for each compression rate with reference to the bypass case. For this analysis, the test sites 1, 5, 6, 8, and 11 of Table 4.3 have been investigated. For the case of $N_\mathrm{b} = 3$ bits/sample, which is typically selected for nominal TanDEM-X acquisitions, phase errors between 5° and about 22° are observed for the (flat and homogeneous) salt lake of Uyuni and the urban area of Mexico City, respectively. It is worth recalling that the interferograms used for comparison have been generated from the same original raw data, i.e., they differ only in the quantization rate employed for compression. Therefore, the observed phase error degradation is solely due to an increase in the quantization noise, as all other error contributions, such as limited SNR or volume scattering, affect the data in the same way (for a given test site). On the right-hand side of Figure 4.8, the standard deviation of the difference between the radar backscatter (of the master acquisition) generated from BAQ bypass and the ones from different BAQ rates $\Delta\sigma^0$ is depicted for the same test areas. The highest deviation is again observed for the urban area of Mex-

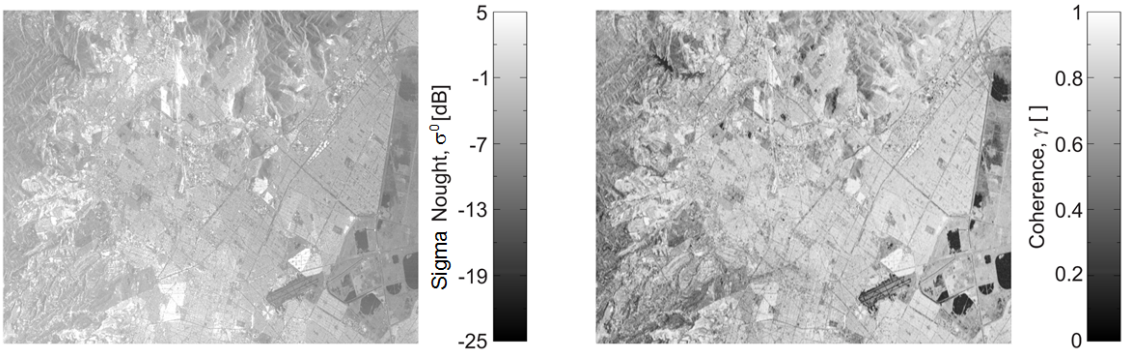

Figure 4.9: (Left) Radar backscatter map of the urban area of Mexico City. (Right) Corresponding coherence map. The area is characterized by a very high dynamic range of backscatter due to the combined presence of man-made structures as well as rugged topography.

ico City, which is characterized by a very high dynamic range of backscatter due to the dominant presence of man-made structures, as well as of rugged topography, as shown in Figure 4.9. Here, the amplitude and coherence maps prior to quantization are depicted on the left-hand and right-hand side, respectively. The absolute value of the phase error for the case of $N_\mathrm{b} = 2$ bits/sample is shown on the left-hand side of Figure 4.10, and the phase error is plotted as function of the signal-to-noise ratio (SNR) for each pixel on the right-hand side of the figure. The SNR is derived as in (2.43), and a detailed description about the procedure for estimating the signal-to-noise ratio from TSX and TDX data, together with a quantitative assessment on the interferometric performance of TanDEM-X is provided in [71]. The red line shows the standard deviation of the phase error distributions as a function of the SNR. It can be noticed that higher phase errors are located in areas of lower backscatter. This aspect is due to the fact that low backscatter areas are more strongly affected by the nonlinear distortions introduced by the Cartesian I/Q quantization. In particular, for low amplitude signals, only few discrete phase values are obtainable at the output of the quantizer, whereas, for high amplitude signals, more phase values are available, and therefore smaller errors, resulting from different quantization settings, are observed in the interferometric phase [95]. In addition to that, low scatterer suppression effects (as described in Section 3.3) also degrade the performance, whereas, on the other hand, for very high SNRs the phase errors due to quantization asymptotically tend to zero, showing that an increase of the compression rate has, over such areas, a negligible impact on the absolute performance degradation.

Furthermore, it is of interest to evaluate the impact of raw data quantization on the overall end-to-end interferometric performance. The interferometric phase errors can be estimated by means of the well-established theoretical model proposed in [80] for

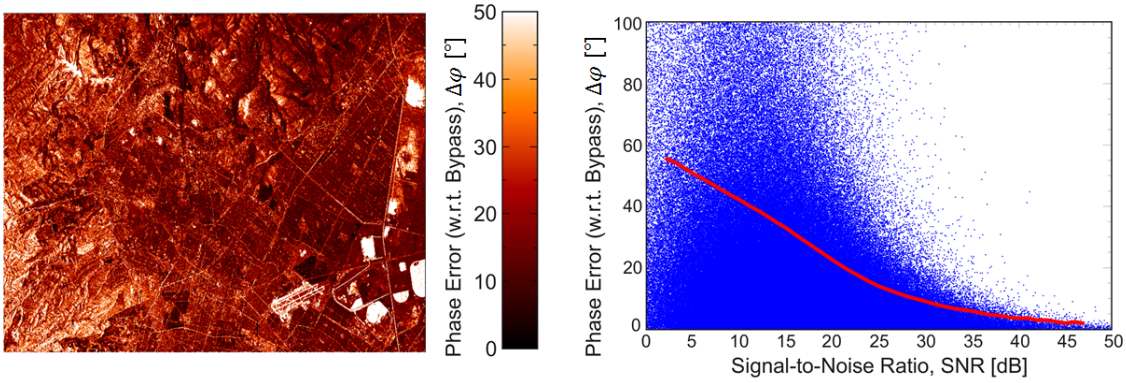

Figure 4.10: (Left) Phase error map $\Delta\varphi$ of the urban area of Mexico City, obtained as in (4.3), for $N_\mathrm{b} = 2$ bits/sample. (Right) Phase error over signal-to-noise ratio (SNR), derived from the map on the left-hand side. The red line shows the standard deviation of the phase error distributions, as a function of the SNR. Higher phase errors are located in areas of lower backscatter (and vice versa) as a consequence of nonlinearities introduced by the quantization together with the occurrence of low scatterer suppression effects.

the statistical determination of the interferometric quality descriptors. According to the model, the interferometric phase error is estimated directly from the coherence γ and the independent number of looks N_l employed within the multi-looking process. In particular, the coherence includes all decorrelation contributions, due to, e.g., limited SNR or volume scattering effects, therefore the resulting phase error is referred to as $\Delta\varphi_\mathrm{Tot}$. The probability density function of the phase difference between two interferometric SAR channels is provided in (2.63) [80]. Hence, from each value of a coherence map originated with N_b bits/sample, the corresponding standard deviation of the phase error $\sigma_{\Delta\varphi_\mathrm{Tot}}$ is estimated according to [80], whereas the standard deviation of the phase error generated from the non-compressed (i.e., BAQ bypass) coherence is indicated with $\sigma_{\Delta\varphi_\mathrm{Tot,bypass}}$, since it includes all decorrelation sources except the one due to quantization. The performance degradation due to quantization is finally expressed by the phase error ratio

$$\rho_{\Delta\varphi} = \frac{\sigma_{\Delta\varphi_\mathrm{Tot}}}{\sigma_{\Delta\varphi_\mathrm{Tot,bypass}}} \tag{4.4}$$

and is depicted in Figure 4.11 for different compression rates. Each value represents the ratio between the mean values $\langle\cdot\rangle$ of the corresponding phase error maps, $\langle\sigma_{\Delta\varphi_\mathrm{Tot}}\rangle$, $\langle\sigma_{\Delta\varphi_\mathrm{Tot,bypass}}\rangle$. For the Antarctica test site (gray circles) a small phase error degradation lower than 20% is observed. The same area shows a poor coherence of about 0.55 (see Figure 4.6 (a)), which is mainly due to the occurrence of SNR and volume decorrelation effects. Therefore, the impact of quantization errors on the overall

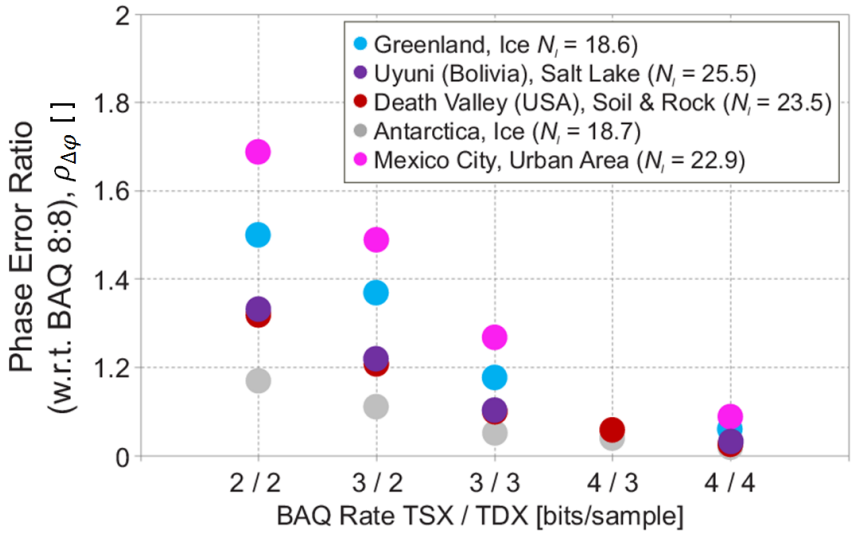

Figure 4.11: Phase error ratio $\rho_{\Delta\varphi}$ estimated according to (4.4) for different compression rates and test sites. Each value represents the ratio between the mean values of the corresponding phase error maps. The total equivalent number of looks N_l for each test site is specified in the legend.

performance decreases. On the other hand, for the urban area of Mexico City a degradation up to 70% is observed. The corresponding phase error ratio map for the case of $N_\mathrm{b} = 2$ bits/sample (calculated according to (4.4)) is shown on the left-hand side of Figure 4.12, and the phase error ratio over the coherence prior to quantization is depicted on the right-hand side of Figure 4.12. The red line shows the mean value of the phase error ratio distributions as a function of the coherence. As previously explained, over low-coherence areas other decorrelation sources, such as limited SNR and/or volume scattering, become dominant. There, phase errors due to quantization are indeed high, but their relative impact on the overall performance is smaller (for this the left-hand side of this figure should be compared also with Figure 4.9 and Figure 4.10).

Based on the present results, in the following the attention is focused on those system and scene parameters which most affect the interferometric phase errors due to quantization. In addition to the BAQ compression rate N_b, which has been already discussed, the degree of inhomogeneities in the backscatter distribution, quantified by the standard deviation of the SAR backscatter σ_{σ^0}, and the number of interferometric looks N_l are investigated. Finally, the combined effect of quantization rate and number of available

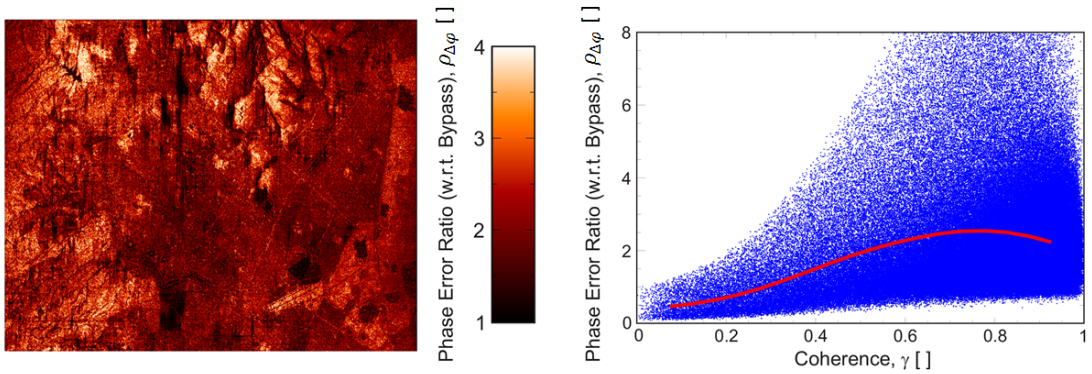

Figure 4.12: (Left) Phase error ratio map $\rho_{\Delta\varphi}$ of the urban area of Mexico City, obtained as in (4.4), for $N_b = 2$ bits/sample. (Right) Phase error ratio over coherence prior to quantization, derived from the map on the left. The red line shows the mean value of the phase error ratio distributions, as a function of the coherence. Over low-backscatter/coherence areas, other phase error sources (such as limited SNR and/or volume scattering) become dominant and quantization errors have a smaller impact on the overall performance.

acquisitions N_{acq} on the resulting phase errors is assessed for a fixed data rate.

Backscatter Inhomogeneities: As it has been recalled many times in the previous sections, quantization errors are significantly affected by the local SAR backscatter distribution, and it has been shown that homogeneous areas are in general less affected by quantization errors, when compared to regions showing heterogeneities in the backscatter response. Looking at local scale, an example of low scatterer suppression caused by raw data quantization in presence of inhomogeneities in the backscatter distribution is given in Figure 4.13. On the left-hand side, the radar backscatter (sigma-nought, σ^0) for an area located in the Death Valley (USA) is depicted (test site 13 in Table 4.3). The region extends by about 5 km in azimuth and range direction. The backscattered signal shows a discontinuity along the range direction, due to a change of the land cover characteristics from rocky to sparsely vegetated terrain. For the present analysis, the subset marked in pink has been considered and the measured σ^0 together with the corresponding interferometric phase error, the latter calculated as in (4.3), have been evaluated. The resulting phase error profiles (their absolute value has been considered, i.e., $|\Delta\varphi|$) are depicted on the right-hand side of Figure 4.13 for different compression rates. In correspondence of a sudden decrease of about 6 dB in the backscatter response, a clear jump in the interferometric phase error is visible and, as expected, a raw data quantization with fewer bits results in a higher degradation in the phase error (i.e., the "height" of

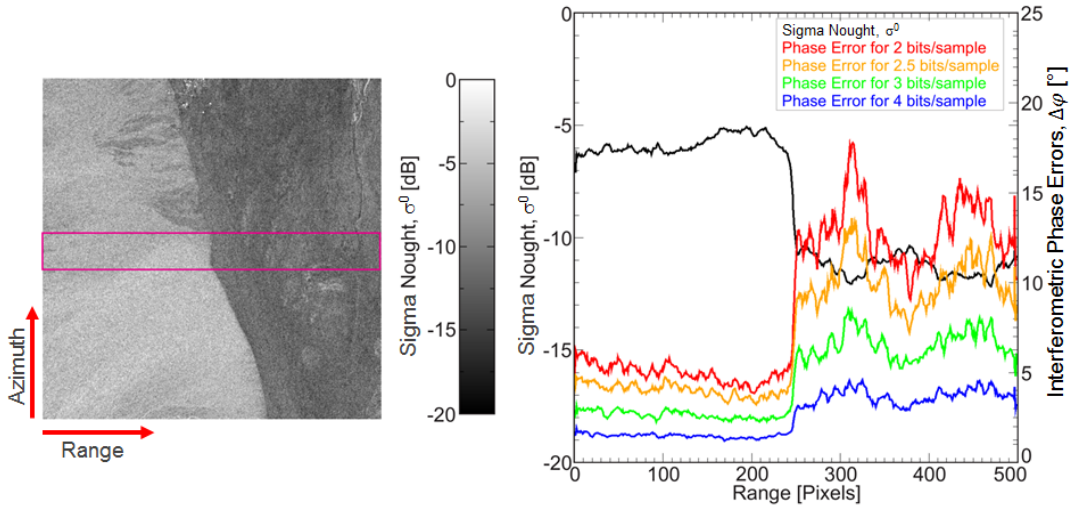

Figure 4.13: (Left) Radar backscatter map σ^0 of an area located in Death Valley (USA). Over the area highlighted in pink, the σ^0 and interferometric phase error profiles $\Delta\varphi$ are sketched for different quantization rates (right). A notable degradation of the phase is observed in case of sudden variations in the backscatter response, as a consequence of the low scatterer suppression effect.

the jump). For the case of 4 bits/sample (blue line in Figure 4.13), the phase error goes from about 2° in the high backscatter area to 4° in the low backscatter one. Therefore, an additional degradation of about 2° due to the low scatterer suppression is observed. On the other hand, for the case of 2 bits/sample (red line in Figure 4.13), the phase error goes from 5° in the high backscatter region to approximately 13° in the low backscatter one: the low scatterer suppression effect for the case of 2 bits/sample causes therefore an additional degradation of about 8°. In correspondence to the low backscatter area, it can be noticed that the error profiles are very sensitive to the backscatter behavior and look almost "complementary" to it, showing higher values exactly where the corresponding σ^0 becomes lower, and this effect is more visible, if fewer bits are employed for compression. However, one has to consider that phase errors are of course already higher in the low backscatter area and, therefore, the additional effect from quantization may be less severe than it may appear from the results shown here. On the other hand, only a slight dependence of the phase noise on backscatter is observed for all compression rates within the slice showing higher backscatter (left side of the image). The strong dependency on backscatter of the interferometric phase errors due to quantization needs to be strictly taken into account for the performance budget definition, since errors in the interferogram affect both the relative height accuracy (as discussed in the next section), and the phase unwrapping quality, which represents a critical step for DEM generation.

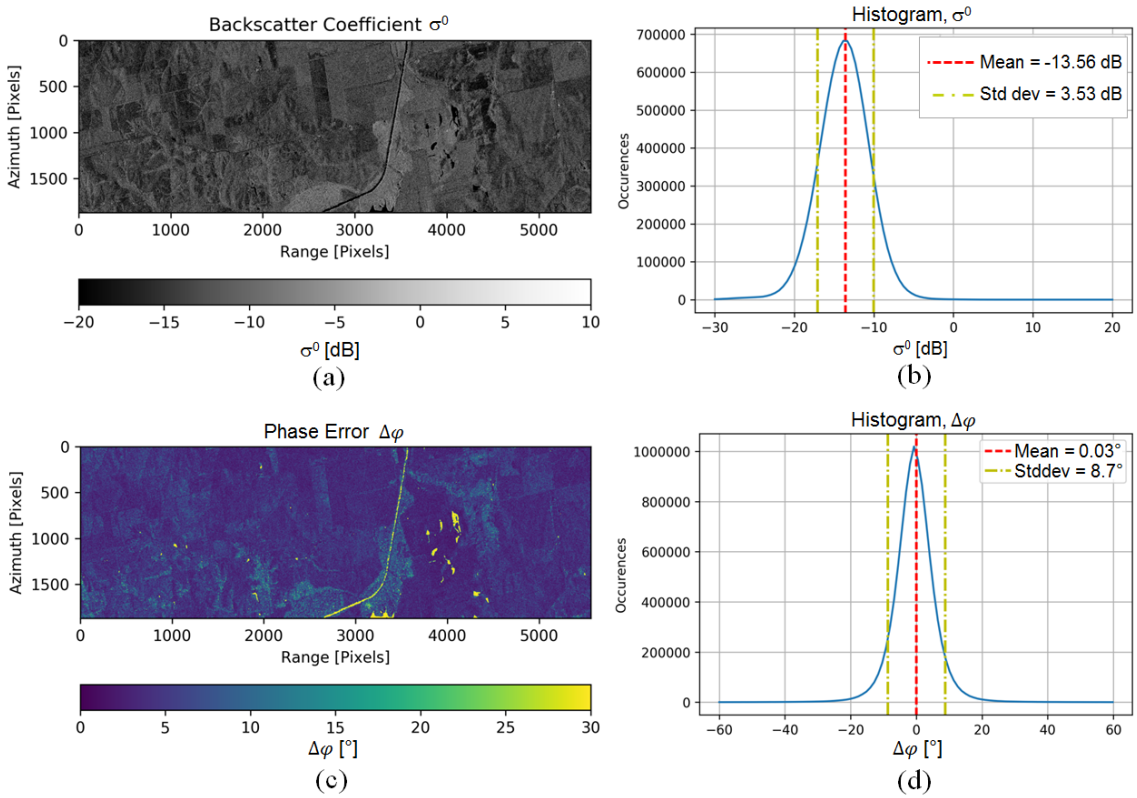

Figure 4.14: (a) Radar backscatter map σ^0 of an agricultural region located in Iowa (USA) and (b) corresponding histogram. The area is quite flat and homogeneous, and a $\sigma_{\sigma^0} \approx 3.5$ dB is observed (c) Phase error map $\Delta\varphi$ and (d) corresponding histogram for $N_\mathrm{b} = 3$ bits/sample, and a phase error standard deviation $\sigma_{\Delta\varphi} \approx 8.7^\circ$ is obtained.

Indeed, for the global DEM produced by TanDEM-X, at least two interferometric acquisitions are required in order to meet the mission specification [103] and to ensure, in most cases, a sufficient phase unwrapping quality [110].

As further examples, the interferometric phase errors have been evaluated for areas showing different degrees of inhomogeneity in the backscatter distribution. This can be quantified by means of the standard deviation of the SAR backscatter σ_{σ^0}. Figures 4.14, 4.15, and 4.16 show the two-dimensional maps and the corresponding histograms of σ^0 and of the resulting interferometric phase error $\Delta\varphi$ obtained as in (4.3) for the areas over Iowa, Death Valley, and Mexico City, respectively (corresponding to the test sites 13, 11, and 8 in Table 4.3). All maps are derived for a BAQ rate $N_\mathrm{b} = 3$ bits/sample and $N_\mathrm{l} = 9$ looks. As expected, the phase error has zero mean in all cases, and its standard deviation is positively correlated with the degree of inhomogeneities of σ^0. Indeed, σ_{σ^0} ranges from about 3.5 dB for the homogeneous agricultural area in Iowa, to more than 6 dB for

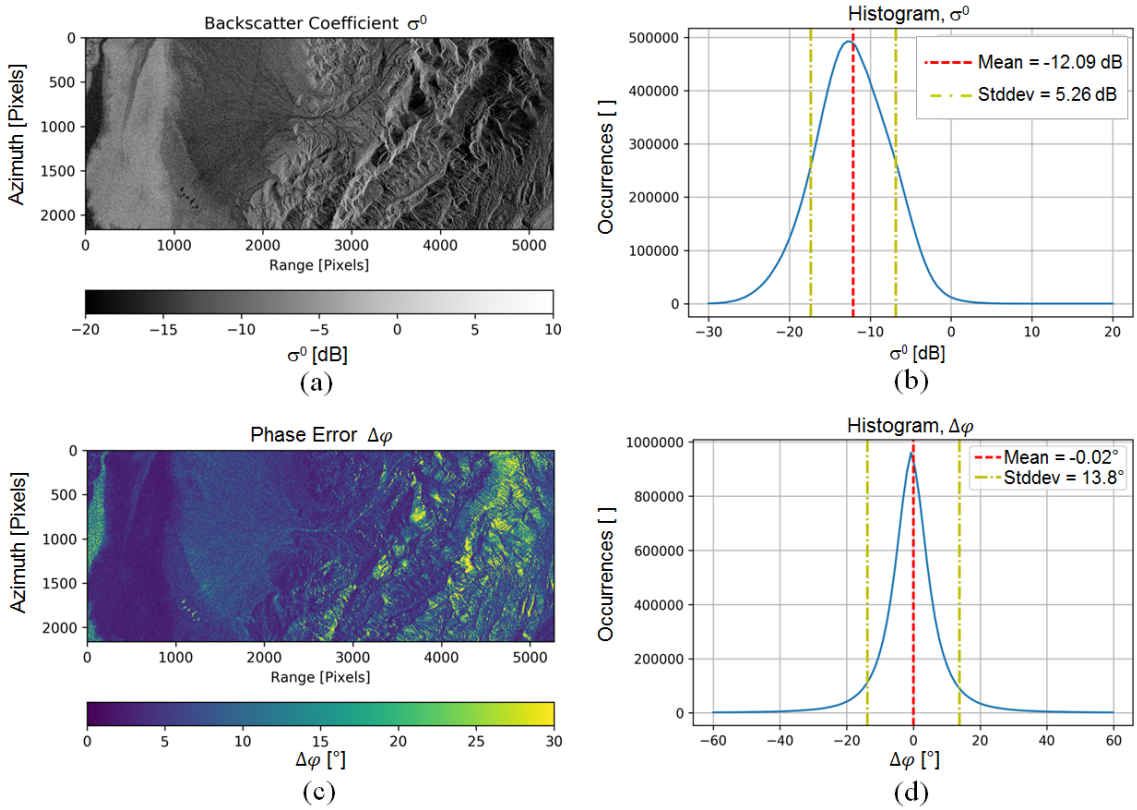

Figure 4.15: (a) Radar backscatter map σ^0 of an area located in the Death Valley (USA) and (b) corresponding histogram. The region shows rugged terrain, and a $\sigma_{\sigma^0} \approx 5.3$ dB is observed. (c) Phase error map $\Delta\varphi$ and (d) corresponding histogram for $N_\mathrm{b} = 3$ bits/sample, for which a phase error standard deviation $\sigma_{\Delta\varphi} \approx 13.8°$ is obtained.

the highly inhomogeneous urban area of Mexico City, which corresponds to $\sigma_{\Delta\varphi}$ ranging between 8.7° and 22.6°.

As it can be noticed, in all cases lower backscatter values (dark areas in Figure 4.14-4.16 (a)) are associated to larger errors in the interferometric phase (green-yellow pixels in Figure 4.14-4.16 (c)), and vice versa.

Number of Looks: In SAR interferometry, multi-looking is typically applied to mitigate the noise affecting the interferometric phase, as it has been introduced in Section 2.3.2. Multi-looking typically consists in averaging N_l pixels of the same region together. Hence, a consistent degradation of the resolution by a factor N_l is observed in the multi-looked image, together with a reduction of the standard deviation of the backscatter (de-speckling) by a factor $\sqrt{N_\mathrm{l}}$. In this sense, multi-looking can be considered as a low-pass

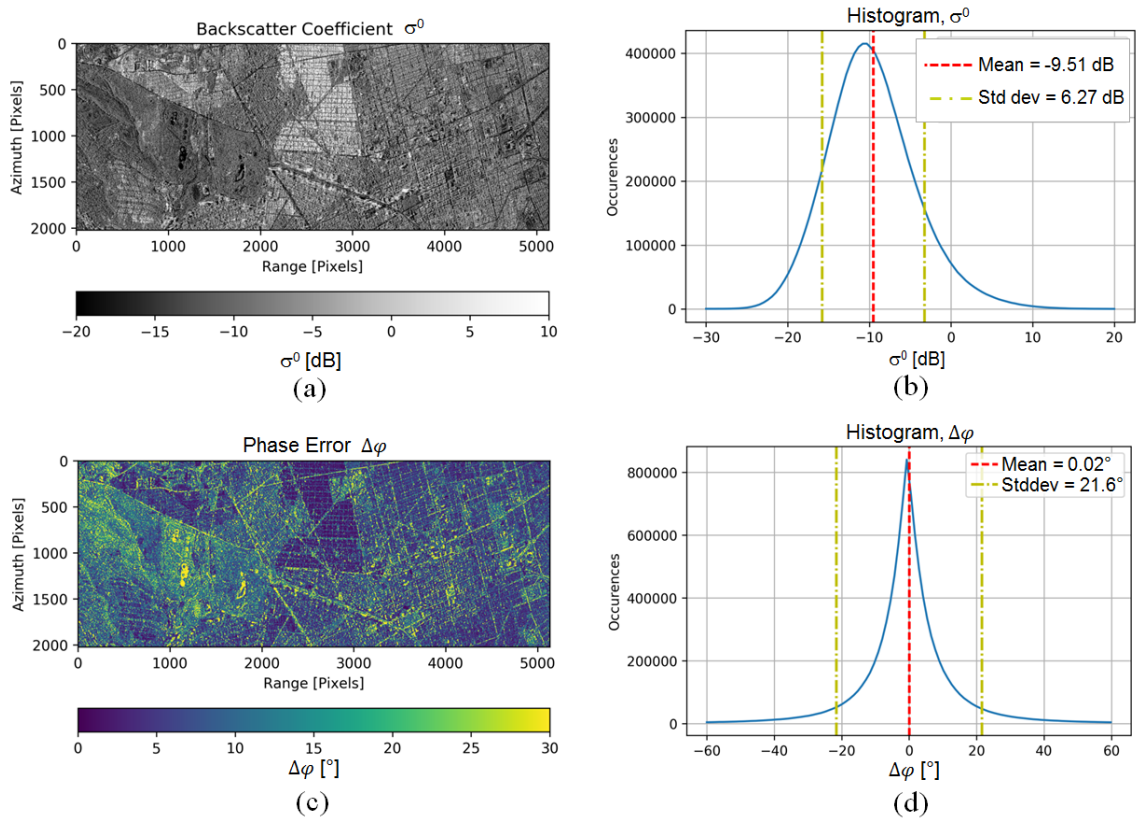

Figure 4.16: (a) Radar backscatter map σ^0 for the urban area of Mexico City (Mexico) and (b) corresponding histogram. The region shows a high dynamic range of backscatter, due to the presence of man-made structures (such as buildings and roads), which results in a $\sigma_{\sigma^0} \approx 6.3$ dB. (c) Phase error map $\Delta\varphi$ and (d) corresponding histogram for $N_\mathrm{b} = 3$ bits/sample, for which an increased phase error $\sigma_{\Delta\varphi} \approx 22.6^\circ$ is obtained.

filter applied to the SAR interferogram, which may greatly improve the interpretability of the resulting InSAR products.

For TanDEM-X, the ground range and azimuth resolution is about 3 meters (in particular, the ground range resolution depends also on the incidence angle, as in (2.22)). Hence, according to (2.67) the final DEM posting $\Delta p_a = \Delta p_r = 12$ m results in number of looks N_l typically in the range between 16 and 32 looks [30]. As an example, Figure 4.17 shows the phase error for an area over the Amazon rainforest (corresponding to the test site 3 in Table 4.3), which is characterized by a flat terrain and a homogeneous backscatter distribution. The BAQ compression rate has been fixed to $N_\mathrm{b} = 2.5$ bits/sample (obtained by setting 3-bit BAQ for the TerraSAR-X acquisition and 2-bit

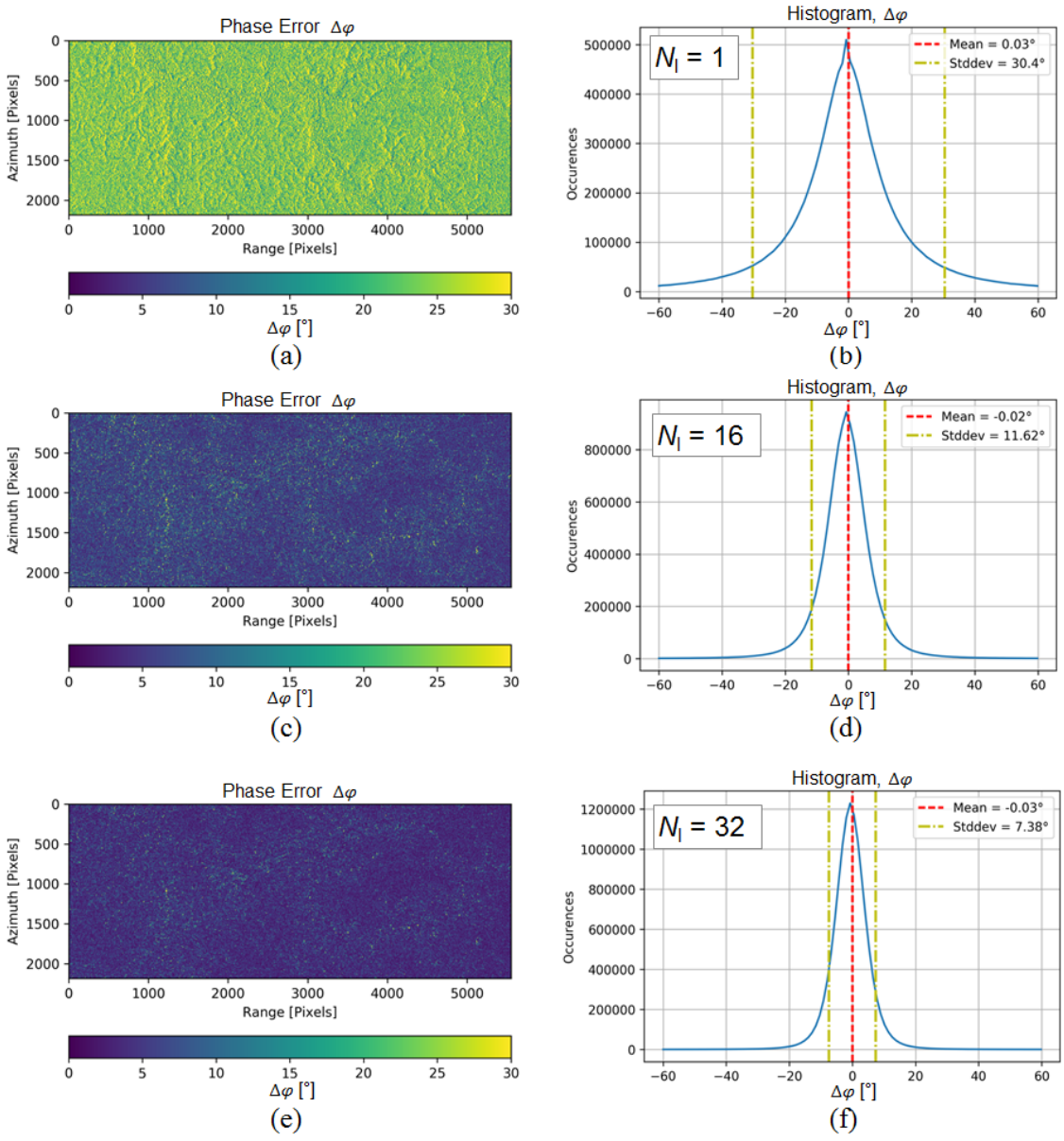

Figure 4.17: (a) Phase error map and (b) corresponding histogram for a homogeneous area located in the Amazon rainforest and obtained from interferograms with $N_\mathrm{l} = 1$ look (i.e., no multi-looking has been applied), resulting in $\sigma_{\Delta\varphi} \approx 30°$. (c) phase error map and (d) corresponding histogram for $N_\mathrm{l} = 16$ looks, and $\sigma_{\Delta\varphi} \approx 11.6°$. (e) Phase error map and (f) corresponding histogram for $N_\mathrm{l} = 32$ looks, and the phase error deviation decreases to about 7.4°. The quantization rate is fixed to $N_\mathrm{b} = 2.5$ bits/sample.

BAQ for the TanDEM-X one), and phase error maps originating from interferograms with N_l set to 1 (i.e., no multi-looking applied), 16, and 32 looks have been generated. Figure 4.17 (a), (c), and (e) shows the phase error maps for different N_l values, which are indicated in the corresponding histograms on the right-hand side (Figure 4.17 (b), (d), and (f), respectively). As expected, lower phase errors are obtained for larger values of N_l (the increase in performance matches quite well with the theoretical model in [80]), which clearly plays a key role in defining the performance degradation due to quantization in interferometric products.

Number of Acquisitions: As it has been pointed out, the limited onboard memory and downlink capacity often represent a bottleneck which directly affect the acquisition capabilities of SAR systems and may impact, e.g., the required mission duration to fulfill the given requirements and product specification [108]. In this context, it is of interest to investigate the joint effect on the final performance of the quantization rate N_b and of the number of acquisitions N_acq, which can be commanded over the same area, given a fixed total data rate R_tot, such that

$$R_\mathrm{tot} = N_\mathrm{acq} \cdot N_\mathrm{b} \quad \text{bits/sample.} \tag{4.5}$$

In case, e.g., a single acquisition is considered (i.e., $N_\mathrm{acq} = 1$), the maximum data rate $N_\mathrm{b} = R_\mathrm{tot}$ can be then employed and low quantization errors are consequently obtained; if, on the other hand, multiple data takes $N_\mathrm{acq} > 1$ are commanded over a certain area, the available data rate per acquisition is given by $N_\mathrm{b} = R_\mathrm{tot}/N_\mathrm{acq}$, resulting in larger quantization errors affecting each acquisition. The obtained phase error after combination $\Delta\varphi_{N_\mathrm{acq},R_\mathrm{tot}}$ is derived from the maximum-likelihood estimator (MLE) as [30]

$$\Delta\varphi_{N_\mathrm{acq},R_\mathrm{tot}} = \frac{1}{\sqrt{\sum_{i=1}^{N_\mathrm{acq}} \frac{1}{\Delta\varphi_i^2}}}, \tag{4.6}$$

being $\Delta\varphi_i$ the phase error estimated from the i-th acquisition. From TanDEM-X InSAR data, the phase error has been estimated following the method presented in [82], which is shortly recalled in the following: for each image pixel with indices $\{m,n\}$ the standard deviation of the single-point phase error $\sigma_{\Delta\varphi}[m,n]$ is estimated according to the model as in [80] and expressed by (2.63), by using the corresponding coherence value $\hat{\gamma}[m,n]$ and the number of looks N_l, as shown in Figure 2.11 in Chapter 2. The error probability function is then approximated as a Gaussian pdf with zero mean and standard deviation $\sigma_{\Delta\varphi}[m,n]$. Then, the normalized sum of the pdfs derived for all pixels represents the phase error distribution for the entire SAR image, and its standard deviation $\sigma_{\Delta\varphi}$ finally expresses the measure to be considered for performance assessment, i.e., for each acquisition $\Delta\varphi_i = \sigma_{\Delta\varphi}$ in (4.6).

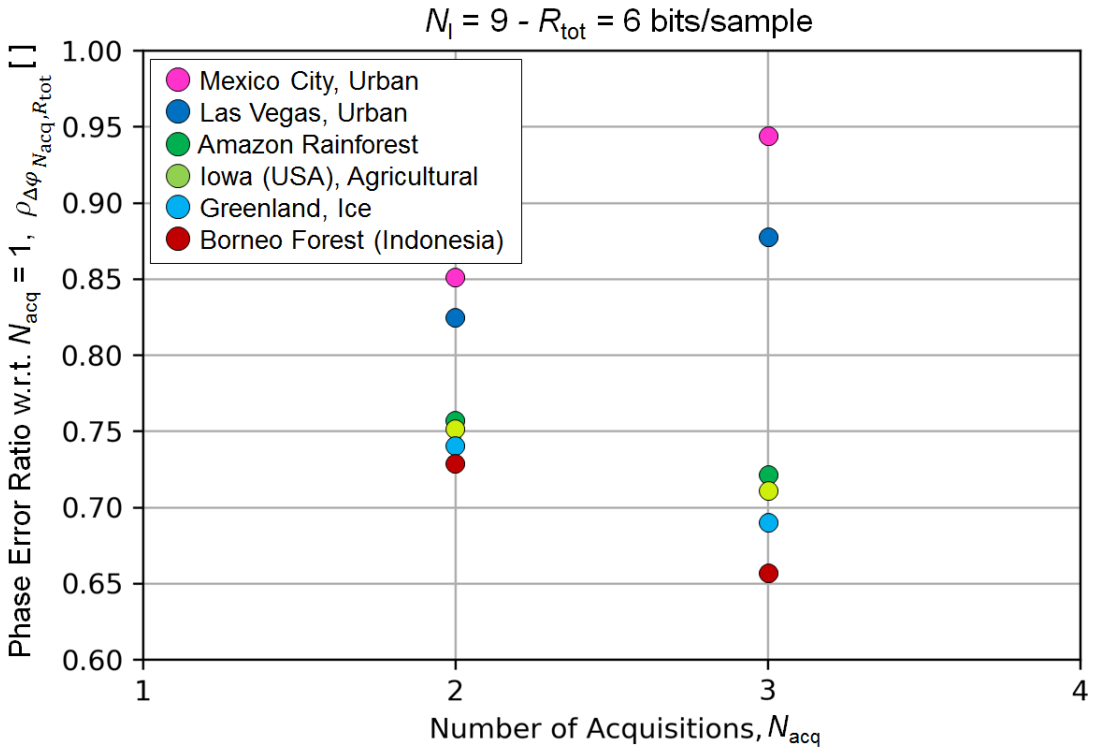

Figure 4.18: Phase error ratio obtained as in (4.7) for $N_l = 9$ looks and a total data rate $R_{tot} = 6$ bits/sample. The resulting BAQ rate is derived from (4.5). According to it, the performance is calculated for the cases $N_{acq} = 2$ with $N_b = 3$ bits/sample and $N_{acq} = 3$ with $N_b = 2$ bits/sample. The case of $N_{acq} = 1$ with $N_b = 6$ bits/sample is used as reference.

For this analysis the ratio of the phase error resulting from the combination of $N_{acq} > 1$ acquisitions, $\Delta\varphi_{N_{acq},R_{tot}}$, to the one resulting from $N_{acq} = 1$, $\Delta\varphi_{R_{tot}}$, has been considered

$$\rho_{\Delta\varphi_{N_{acq},R_{tot}}} = \frac{\Delta\varphi_{N_{acq},R_{tot}}}{\Delta\varphi_{R_{tot}}}, \tag{4.7}$$

for different values R_{tot}. Figure 4.18 shows the phase error ratio $\rho_{\Delta\varphi_{N_{acq},R_{tot}}}$ for the cases $N_{acq} = 2$ and $N_{acq} = 3$ for a total data rate $R_{tot} = 6$ bits/sample, for which BAQ rates of 3 bits/sample and 2 bits/sample are employed, respectively. The performance is assessed for $N_l = 9$ looks and for different test sites (as in Table 4.3). It can be seen that a performance gain is in general obtained when combining more acquisitions (i.e., $\rho_{\Delta\varphi_{N_{acq},R_{tot}}} < 1$). However, this is not the case for highly inhomogeneous test sites like the urban area of Mexico City and Las Vegas (depicted in pink and blue, respectively), for

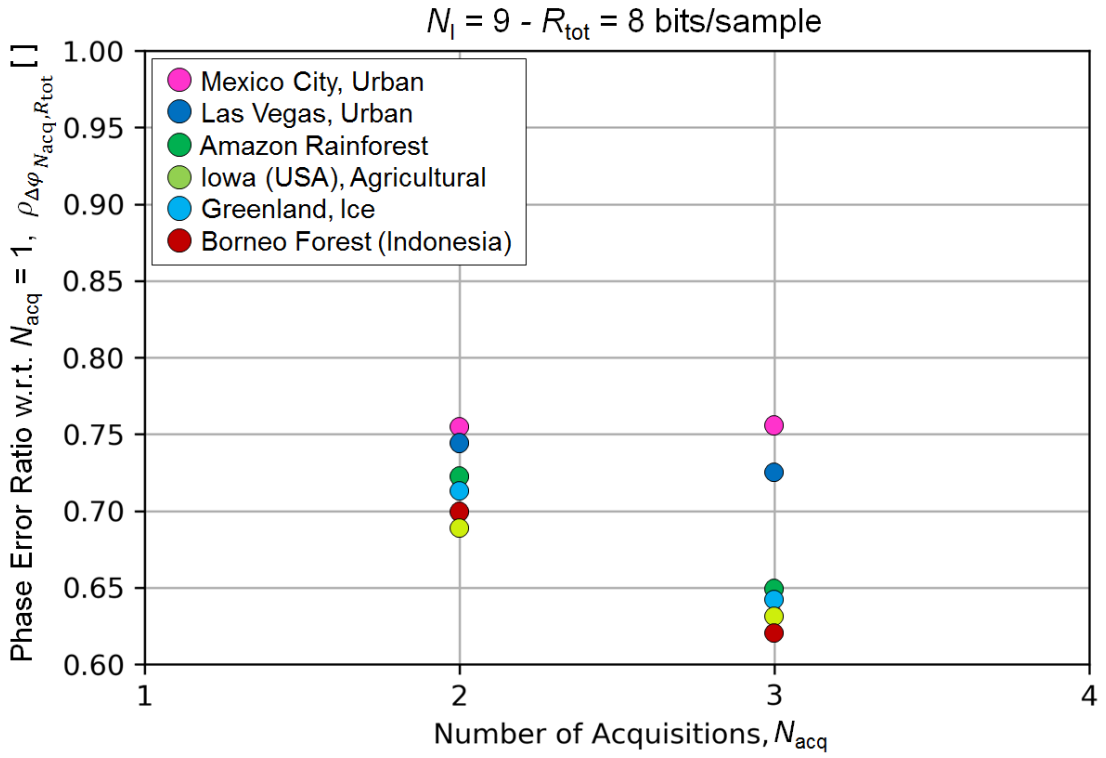

Figure 4.19: Phase error ratio obtained as in (4.7) for $N_l = 9$ looks and a total data rate $R_{tot} = 8$ bits/sample. The resulting BAQ rate is derived from (4.5). According to it, the performance is calculated for the cases $N_{acq} = 2$ with $N_b = 4$ bits/sample and $N_{acq} = 3$ using for two acquisitions $N_b = 3$ bits/sample and for one acquisition $N_b = 2$ bits/sample. The case of $N_{acq} = 1$ with $N_b = 8$ bits/sample is used as reference.

which the phase error for $N_{acq} = 3$ is higher than for $N_{acq} = 2$. This fact can be explained by the very large performance degradation obtained when using lower BAQ rates over such heterogeneous areas, which prevails on the performance improvement which results from the combination of $N_{acq} > 1$ acquisitions. Nevertheless, in real mission scenarios, the number of data takes which can be commanded over the same area within a certain time interval, which is referred to as " system duty cycle", is typically rather limited. As an example, TanDEM-X can acquire for about 180 seconds within each 95-minute orbit, hence the number of acquisitions N_{acq} is typically kept as small as possible. Figure 4.19 and 4.20 show the same plot for a total data rate $R_{tot} = 8$ and $R_{tot} = 12$ bits/sample, which show similar results. In particular, for Figure 4.20 the performance is calculated taking as reference the case of $N_{acq} = 2$ and $N_b = 6$ bits/sample. It can be concluded that for most natural land cover types an increase of the number of acquisitions, for a con-

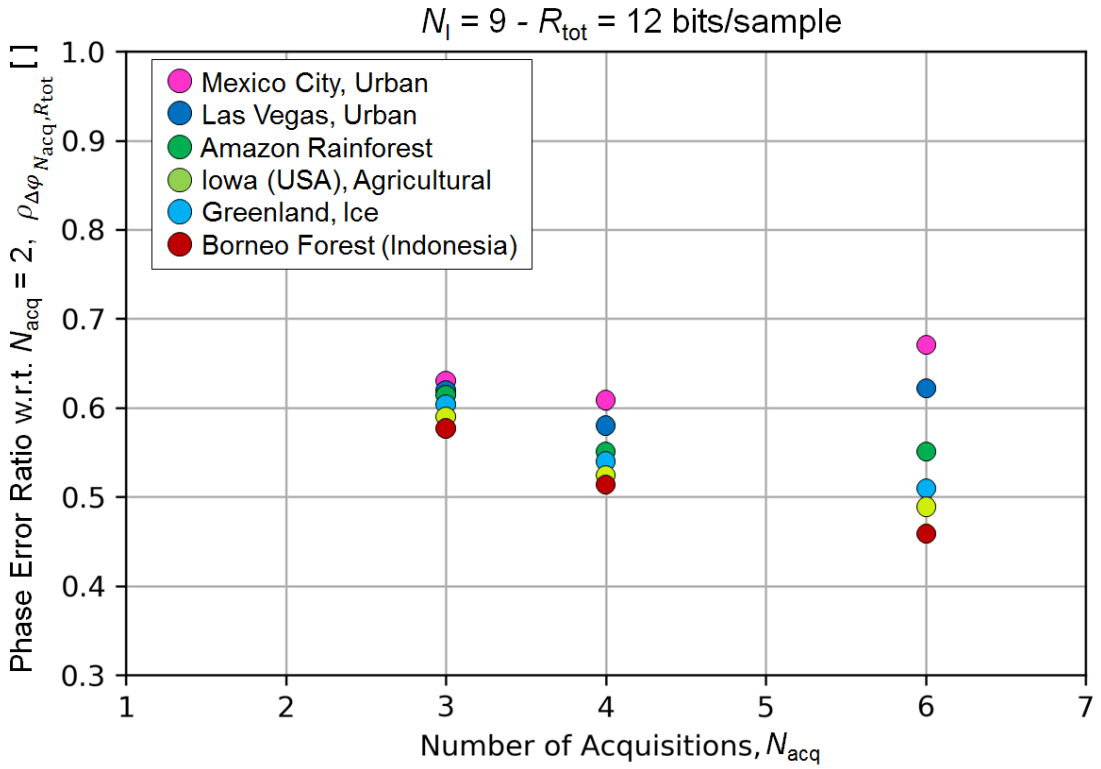

Figure 4.20: Phase error ratio obtained as in (4.7) for $N_l = 9$ looks and a total data rate $R_{tot} = 12$ bits/sample. The resulting BAQ rate is derived from (4.5). According to it, the performance is calculated for the cases $N_{acq} = 3$ with $N_b = 4$ bits/sample, $N_{acq} = 4$ with $N_b = 3$ bits/sample, and $N_{acq} = 6$ with $N_b = 2$ bits/sample. The case of $N_{acq} = 2$ with $N_b = 6$ bits/sample is used as reference.

stant total data rate, improves the overall quantization performance, whereas for areas characterized by large dynamic range in backscatter the use of low BAQ rates should be avoided, as the resulting performance may be dramatically degraded.

If, on the other hand, the number of acquisitions is increased by keeping the same bit rate N_b for each acquisition (hence without imposing the constraint in (4.5)), according to the maximum likelihood estimation (MLE) the phase error after combination is reduced by the square root of number of acquisitions as [30]

$$\Delta\varphi_{N_{acq},N_b} = \frac{\Delta\varphi_{N_b}}{\sqrt{N_{acq}}}, \tag{4.8}$$

being $\Delta\varphi_{N_b}$ the phase error resulting from a single acquisition which has been quantized using N_b bits/sample as defined in (4.3).

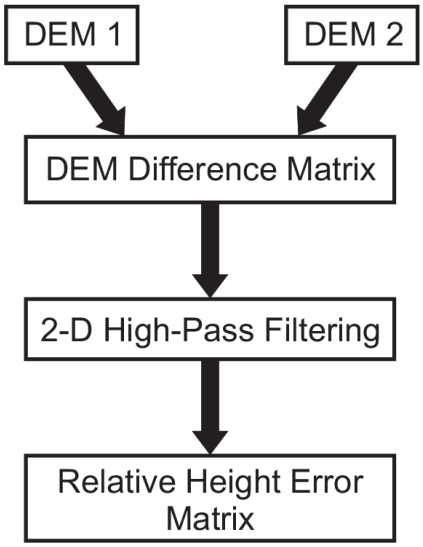

Figure 4.21: Workflow for relative height error analysis from repeat-pass DEMs.

4.3.4 Relative Height Error

Once the interferometric phase error has been estimated, the relative height accuracy of a DEM Δh can be understood as the uncertainty of a height estimation due to noise-like disturbance contributions. Its expression is provided in (2.68) and is recalled in the following

$$\Delta h = h_{\text{amb}} \cdot \frac{\Delta \varphi}{2\pi}. \tag{4.9}$$

In particular, the relative height error is proportional to the height of ambiguity h_{amb}, which represents the height difference corresponding to a complete 2π cycle of the interferometric phase and its expression is provided in (2.56). The estimation of the point-to-point relative height error requires the computation of the probability density function obtained by evaluating the difference between two random variables, each of them describing the fluctuation of the height estimate within one digital elevation model (DEM) [30]. From real data, the point-to-point relative height accuracy can be estimated by evaluating the difference between repeated DEM acquisitions with identical imaging geometry and configuration parameters, each of them affected by independent noise components [82], as shown in Figure 4.21. A high-pass filtering is then performed to remove slowly-varying error sources, such as baseline or attitude uncertainties, which will be calibrated out during the final DEM generation process [83]. Due to a baseline estimation error in the order of millimeters, the resulting DEM horizontal localization accuracy, for typical TanDEM-X baselines and incidence angles, is in the order of a few meters [115]. Together with the dominant noise-like contribution, additional error sources may be due

Table 4.4: Test sites for relative height error analysis. For each test site, repeated bistatic TanDEM-X acquisitions have been commanded with BAQ bypass and with identical imaging geometry.

Test Site	**1st Pass**	**2nd Pass**	$h_{\mathbf{amb}}$
Salar de Uyuni (Bolivia)	2010-11-16	2012-06-10	36 m
Mexico City	2012-02-07	2012-02-29	67 m
Greenland	2012-01-15	2012-02-06	81 m
Amazon Forest (Brazil)	2012-01-17	2012-02-19	84 m
Death Valley (USA)	2010-11-24	2010-12-05	150 m

to phase unwrapping errors, as well as temporal changes in the scene occurring between the two bistatic data takes. For the present analysis, we have considered repeated bistatic TanDEM-X acquisitions commanded with BAQ bypass. The 90% point-to-point relative height error, as required by TanDEM-X mission specifications [30], [108], has been evaluated for the test areas listed in Table 4.4 (corresponding to the sites 1, 3, 5, 8, and 11 of Table 4.3). It is computed as the 90$^{\text{th}}$ percentile of the absolute value of the height error matrix and is evaluated according to the workflow in Figure 4.21. The relative height error, $\Delta h_{90\%}$, resulting from different compression rates is shown in Figure 4.22 (a). Each value represents the 90% point-to-point relative height error obtained from two repeat-pass DEM acquisitions, and for each height error estimation both DEMs result from data takes that all use the same compression rates. According to (4.9) the relative height accuracy is directly proportional to the height of ambiguity h_{amb}. Indeed, looking again at Figure 4.22 (a), it can be noticed that the highest height error values are obtained for the test area of Death Valley (from 6 m to 8 m), acquired with a height of ambiguity of about 150 m. On the other hand, the height errors estimated over the Uyuni salt lake are about four times smaller (approximately 2 m), which is consistent with the ratio of the heights of ambiguity of the corresponding DEM acquisitions (150 m/36 m). Therefore, in order to consistently compare the performance between the different test areas, a normalization with respect to the height of ambiguity characterizing each acquisition pair is needed. The normalized relative height error degradation can be defined, for a single data take, as the difference between the 90% point-to-point height error, derived from non-compressed DEMs, and the ones originated from different rate values N_{b} as

$$\Delta h_{90\%,h_{\text{amb}}} = \frac{1}{h_{\text{amb}}}(\Delta h_{90\%,\text{bypass}} - \Delta h_{90\%,N_{\text{b}}}). \tag{4.10}$$

The resulting normalized height error degradation, expressed in percent of h_{amb}, is depicted in Figure 4.22 (b) for different compression rates. It is worth pointing out once

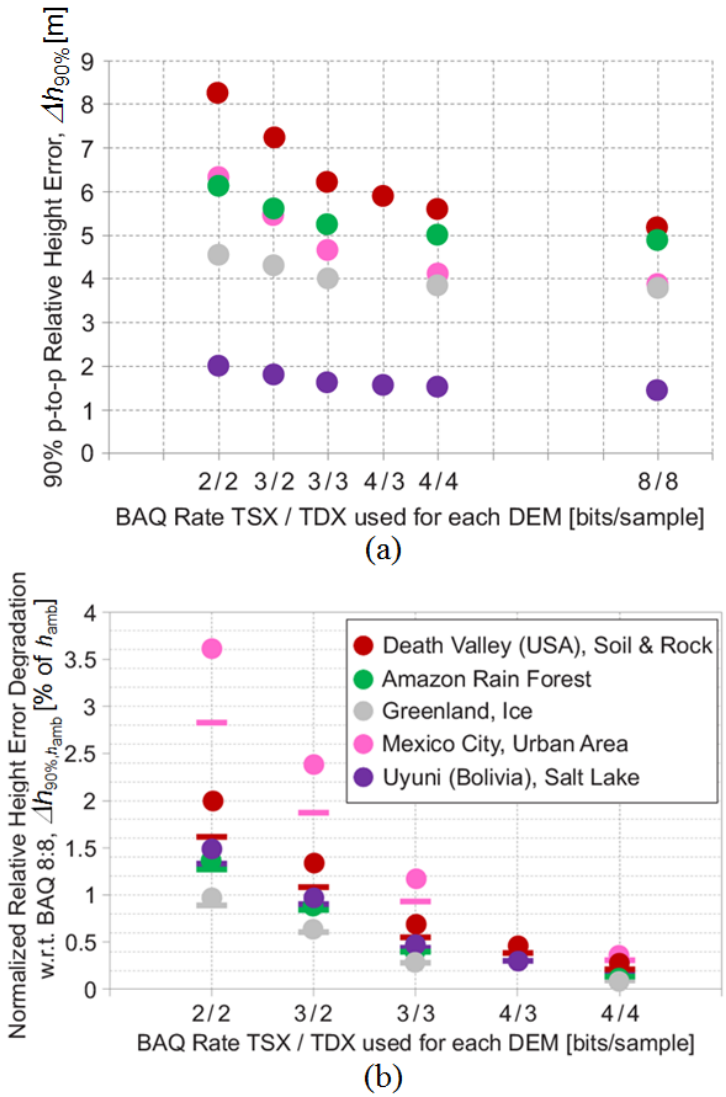

Figure 4.22: (a) 90% point-to-point (p-to-p) relative height error as a function of the compression rate for the repeated acquisitions listed in Table 4.4. (b) Normalized degradation of the relative height error with respect to the bypass case, expressed as a fraction of the height of ambiguity, derived as in (4.10). The horizontal lines represent the corresponding height error degradation obtained from the theoretical model in [80].

more that, for a given test site, the DEMs used for comparison have been created from the same original raw data, i.e., they differ only in the quantization rate employed for compression. Therefore, the observed height accuracy degradation represents the contribution to the total relative height error in the DEM which is produced uniquely by

the quantization process. As expected, the performance degrades more severely over the urban area of Mexico City, for which a degradation up to 4% of h_{amb} is observed. If considering typical heights of ambiguity employed for TanDEM-X nominal acquisitions (between 30 to 50 m), the use of 2 bits/sample for both coverages would in this case have resulted in an increase between 1.2 m and 2 m in terms of relative height accuracy, ultimately leading to a probable violation of the DEM specifications. As previously mentioned, for most of the global DEM acquisitions of TanDEM-X, BAQ 8:3 (mainly) and BAQ 8:4 are employed, which cause a mean additional error of about 30 cm with respect to the uncompressed data (and below 60 cm for the worst case).

The present results have been also validated with the well-established theoretical model proposed in [80], which has been recalled in Section 2.4 and Section 4.3.3. According to the model, the interferometric phase error $\Delta\varphi$ can be directly estimated from the interferometric coherence γ and the independent number of looks N_{l} employed within the multi-looking process as in (2.63) [80]. In particular, for each pixel of a processed interferogram, the 90% relative height error, $\Delta h_{90\%}$, is estimated, and the mean value per scene is then considered. The relative height error degradation derived from the model in [80] is given by the horizontal bars in Figure 4.22 (b). A good agreement between the two approaches can be seen for the sites of "Amazon Rain Forest", "Greenland", and "Uyuni". These areas are characterized by flat and regular height profiles, which are free of phase unwrapping errors. On the other hand, for the "Death Valley" and "Mexico City" test sites the theoretical model underestimates the height error degradation derived from the data. As previously mentioned, both test areas are characterized by an inhomogeneous backscatter distribution, together with rugged topography, where suppression of low scatterers causes an additional performance degradation. The combination of the described effects, together with the possible increase of phase unwrapping errors (which may be more severe in the case that fewer bits are employed for quantization), leads to incorrect height estimates in the resulting DEM. Such errors, as well as possible temporal changes in the scene occurring between the two repeated acquisitions, are not taken into account in the theoretical model used for comparison, which explains the observed discrepancy.

4.3.5 Resource Allocation for the TanDEM-X DEM Acquisition

For nominal mission operation, mainly BAQ 8:3 for TerraSAR-X and TanDEM-X has been employed for the acquisition of two global DEMs in bistatic configuration. Indeed, both satellites have a relatively limited downlink capacity, which is due to an average contact time with the ground station network of about 10 min/orbit at a total net data rate of about 260 Mbits/s, as indicated in Table 4.1 (the downlink time has to be shared among the two spacecraft, since the close satellite formation does not permit the simultaneous downlink of the data). If nominal acquisition parameters are considered, this implies an allowed time for bistatic data takes of about 180 s per orbit, for the case of a quantization

with 3 bits/sample [30]. Based on the analyses presented in this chapter, the strategy for optimizing the resource allocation for the second global acquisition of TanDEM-X was consequently adapted. Areas showing very good performance as well as homogeneous backscatter characteristics have been acquired with reduced BAQ rates. These have been identified by considering the coefficient of variation of the interferometric coherence. The coefficient of variation c_{v} is defined as the ratio of the standard deviation σ_γ and the mean μ_γ of the coherence γ

$$c_{\mathrm{v}} = \frac{\sigma_\gamma}{\mu_\gamma}. \tag{4.11}$$

It is calculated for each processed scene, which extends for an azimuth length of about 50 km, and a range width of about 30 km, and is shown in Figure 4.23 for the first global DEM coverage of TanDEM-X (acquired between the end of 2010 and the beginning of 2012). Usually, high variations in amplitude are associated with high variation in the coherence distribution. On the other hand, for high coherence, smaller variation has been typically observed ($c_{\mathrm{v}} < 0.2$) for the most part of natural land areas. The main regions, which have been selected for resource optimization, are highlighted in the black circles. Here, high coherence (usually bigger than 0.8), homogeneous backscatter distribution, as well as good unwrapping quality is observed. In particular, quantization rates of 2 bits/sample and 2.5 bits/sample (the latter obtained using 3 bits/sample on one satellite and 2 bits/sample on the other satellite), have been employed over such selected areas. The mean BAQ rate was then reduced from 3.09 bits/sample for the first global DEM acquisition to 2.95 bits/sample for the second one, and a consequent reduction in terms of mean data rate of about 5% was gained, without impacting on the overall mission performance (for many of these areas a single acquisition was already sufficient to fulfill the relative height error mission requirements [71], [116]). The resulting freed-up orbit usage (about 125 seconds more per day) was exploited for re-acquisition with optimized imaging geometry of areas affected by poor performance [117], [118], [119], such as forest areas and difficult terrain (depicted in yellow and red in Figure 4.23) to improve their final DEM quality [109], [120].

4.4 Performance-Optimized Quantization for InSAR Applications

The influence of several parameters on phase errors due to quantization in TanDEM-X interferometric data has been assessed in Section 4.3.3. Further, these have been investigated for all the available test sites characterized by different terrain and land cover types and listed in Table 4.3. To this purpose, each complex SAR image matrix has been divided into blocks, each one extending by the chirp length L_{chirp} and the synthetic aperture L_{s} in range and azimuth, respectively. As it has been explained in Section 3.3, the responses of the scatterers under illumination overlap in the raw data domain within an

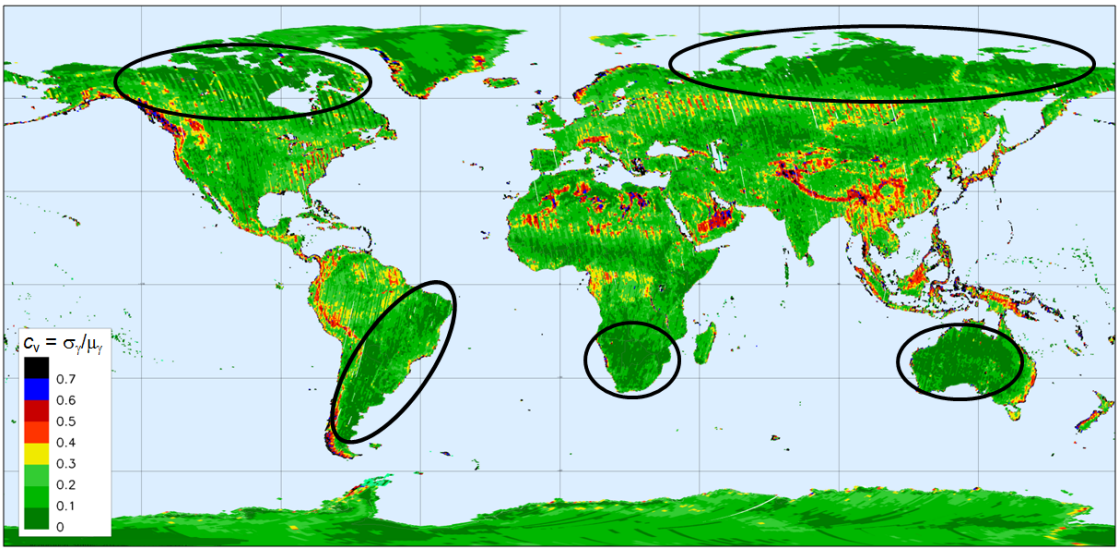

Figure 4.23: Variation coefficient c_v of the interferometric coherence for the first global DEM acquisition. For each scene (50 km x 30 km), c_v is calculated as the ratio of the standard deviation and the mean coherence, according to (4.11). The main regions considered for resource optimization for the second global acquisition are outlined with black circles. Here, homogeneous backscatter distribution and very good performance ($\gamma > 0.8$) is usually observed. On the other hand, yellow and red areas require additional acquisitions with optimized imaging geometry to further improve the overall DEM performance.

area

$$A_{\mathrm{SAR}} = L_s \times L_{\mathrm{chirp}}. \tag{4.12}$$

In this way, each block has been independently analyzed from the others, in terms of local statistics and resulting performance.

Figure 4.24 shows the standard deviation of the single-point phase error $\sigma_{\Delta\varphi}$ as function of the standard deviation of the SAR backscatter σ_{σ^0} derived from single-look interferograms (i.e., $N_l = 1$). Each dot represents the value obtained from a single SAR image block of area A_{SAR} as defined in (4.12). The colors represent different quantization rates and the legend indicates the number of bits used for the master and the slave acquisition $[N_{b,M}, N_{b,S}]$, respectively (the combination of, e.g., $N_{b,M} = 3$ and $N_{b,S} = 2$ results in an equivalent BAQ rate of 2.5 bits/sample). Figures 4.25, 4.26, and 4.27 show the same plot for $N_l = 9$ looks, $N_l = 16$ looks, and $N_l = 25$ looks, respectively. It is worth pointing out that for this analysis the multi-looking has been applied for the calculation of the phase error only, and not for the calculation of σ_{σ^0}, which has been always derived from single-look SAR images. From the figures, it can be verified that σ_{σ^0} and $\sigma_{\Delta\varphi}$ are positively

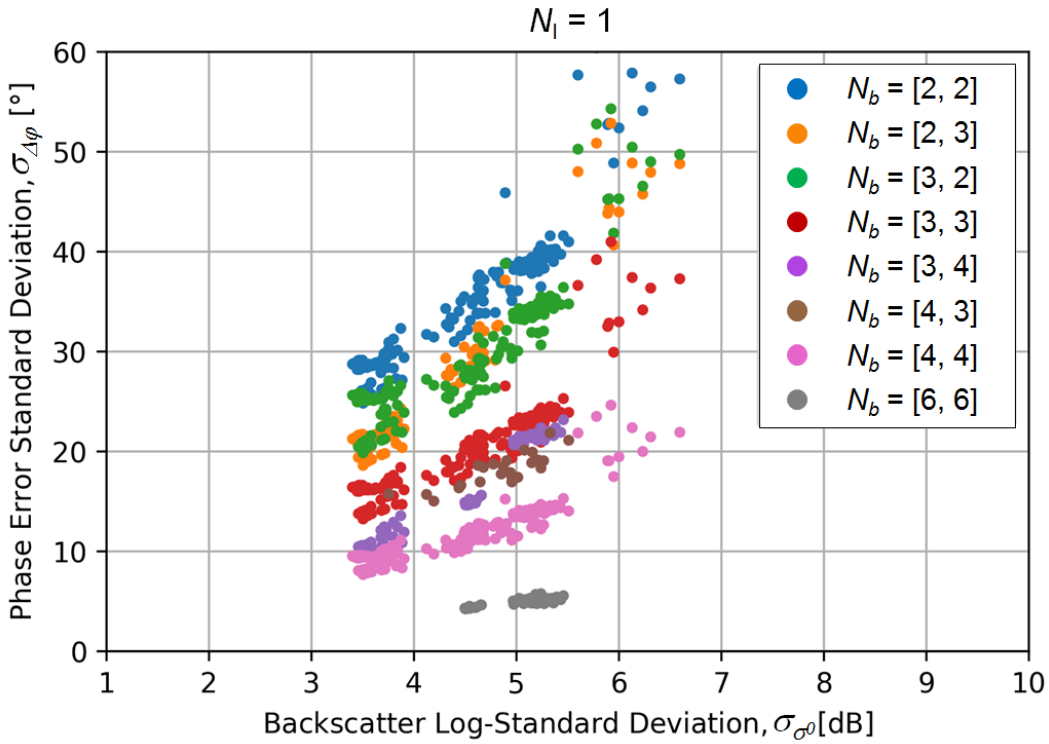

Figure 4.24: Single-point standard deviation of the interferometric phase error due to quantization $\sigma_{\Delta\varphi}$ as a function of the standard deviation of the backscatter coefficient σ_{σ^0} for $N_l = 1$ look and different BAQ rates, depicted with different colors. The BAQ rates in the legend indicate the number of bits used for the master and the slave acquisition $[N_{b,M}, N_{b,S}]$, respectively.

correlated and, as expected, larger phase errors are obtained for heterogeneous areas. As an example, if one considers Figure 4.26, values of σ_{σ^0} smaller than 5.5 dB are typically obtained for natural scenes, such as forests, snow/ice areas, agricultural, and bare soil regions, both with flat and rugged topography characteristics. For these, if considering the 2-bit BAQ case (blue dots), $\sigma_{\Delta\varphi}$ varies in the range between 8° and 20°. On the other hand, σ_{σ^0} values larger than 5.5 dB are typically observed over urban areas, where quantization errors further increase leading to still larger interferometric phase errors (e.g., $\sigma_{\Delta\varphi}$ is typically in the range from 10° up to 30° for $N_l = 16$ looks).

The present results can be exploited to optimize the resource allocation (i.e., the commanded BAQ rate) by controlling, at the same time, the resulting phase error degradation.

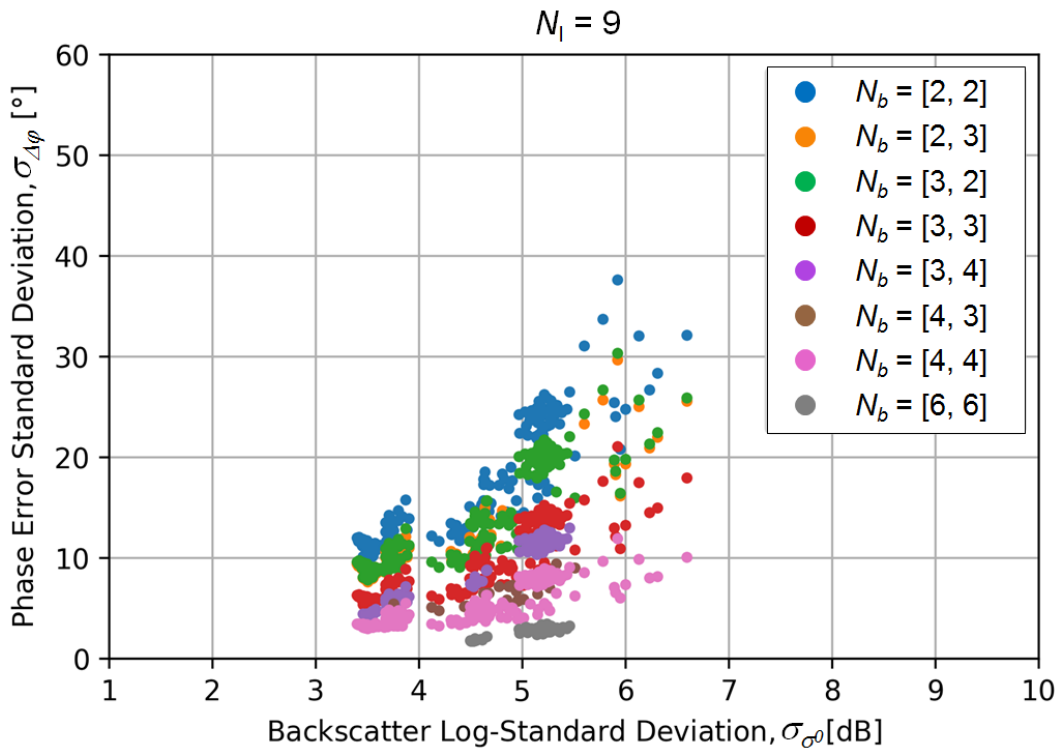

Figure 4.25: Single-point standard deviation of the interferometric phase error due to quantization $\sigma_{\Delta\varphi}$ as a function of the standard deviation of the backscatter coefficient σ_{σ^0} for $N_l = 9$ looks and different quantization rates, depicted with different colors. The BAQ rates in the legend indicate the number of bits used for the master and the slave acquisition $[N_{b,M}, N_{b,S}]$, respectively.

For this, a novel method for SAR raw data compression, named performance-optimized block-adaptive quantization (PO-BAQ), is introduced, according to which the bit rate $N_{b,req}$ to be employed for SAR raw data compression is determined as a function of the considered parameters as

$$N_{b,req} = f\left(N_l, N_{acq}, \Delta\varphi_{req}, \sigma_{\sigma^0}\right). \tag{4.13}$$

In the above equation, the number of looks N_l is defined by the system resolution and by the target posting as in (2.67), the number of available acquisitions N_{acq} is typically determined at mission planning, and σ_{σ^0} is estimated from the local backscatter information, which must be therefore provided as external input before data take commanding. $\Delta\varphi_{req}$ indicates the required phase error degradation (i.e., the maximum allowed phase error due to quantization determined from the performance budget), and can be expressed in terms of, e.g., the standard deviation or the 90th percentile of the single-point or point-

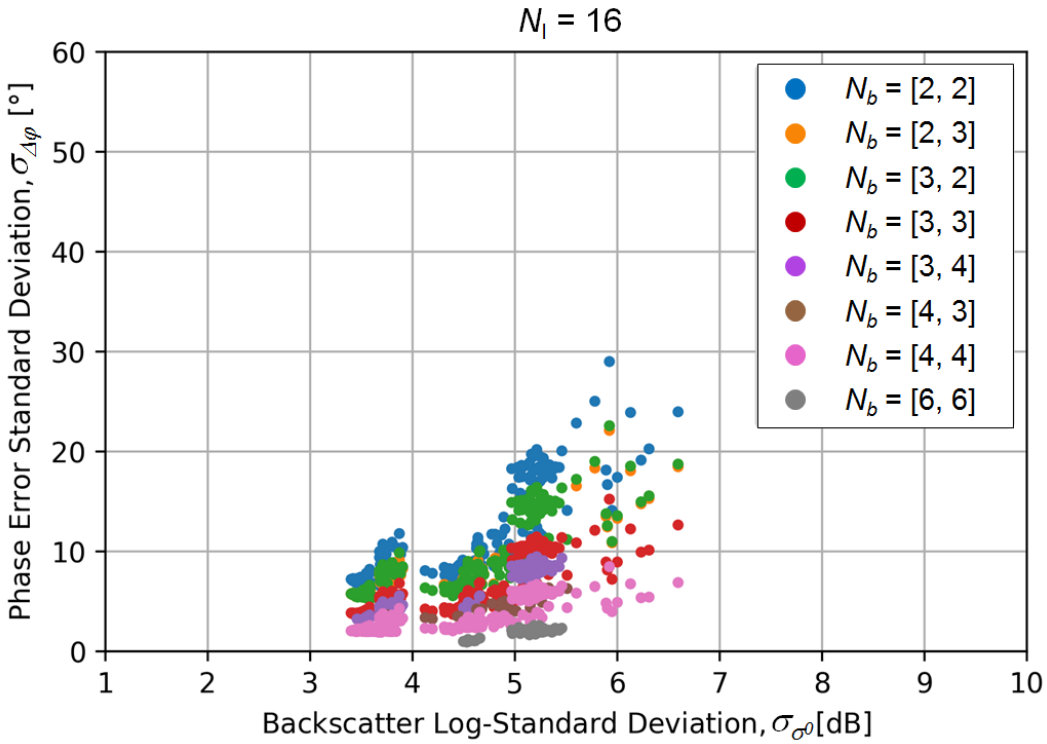

Figure 4.26: Single-point standard deviation of the interferometric phase error due to quantization $\sigma_{\Delta\varphi}$ as a function of the standard deviation of the backscatter coefficient σ_{σ^0} for $N_l = 16$ looks and different BAQ rates, depicted with different colors. The BAQ rates in the legend indicate the number of bits used for the master and the slave acquisition $[N_{b,M}, N_{b,S}]$, respectively.

to-point interferometric phase errors. The function $f(\cdot)$ in (4.13) is described by the information shown, e.g., in Figures 4.24-4.27. These can be regarded as a sort of look-up-tables (LUTs) providing a statistical characterization of the performance degradation, estimated from real data, and can be in principle generated for any value of N_l.

According to the proposed method, the procedure to estimate the bit rate to quantize the raw data associated to a given SAR image block is determined as follows:

Step 1: Once $\Delta\varphi_{req}$, N_l, and N_{acq} are fixed, the standard deviation of the SAR backscatter block σ_{σ^0} is calculated. In the following, without loss of generality the performance requirement is expressed in terms of the single-point standard deviation of the phase error, i.e., $\Delta\varphi_{req} = \sigma_{\Delta\varphi,req}$, as depicted in Figures 4.24-4.27. In addition, $N_{acq} = 1$ is assumed, whereas the performance improvement obtained when combining a stack of acquisitions is discussed in Section 4.3.3.

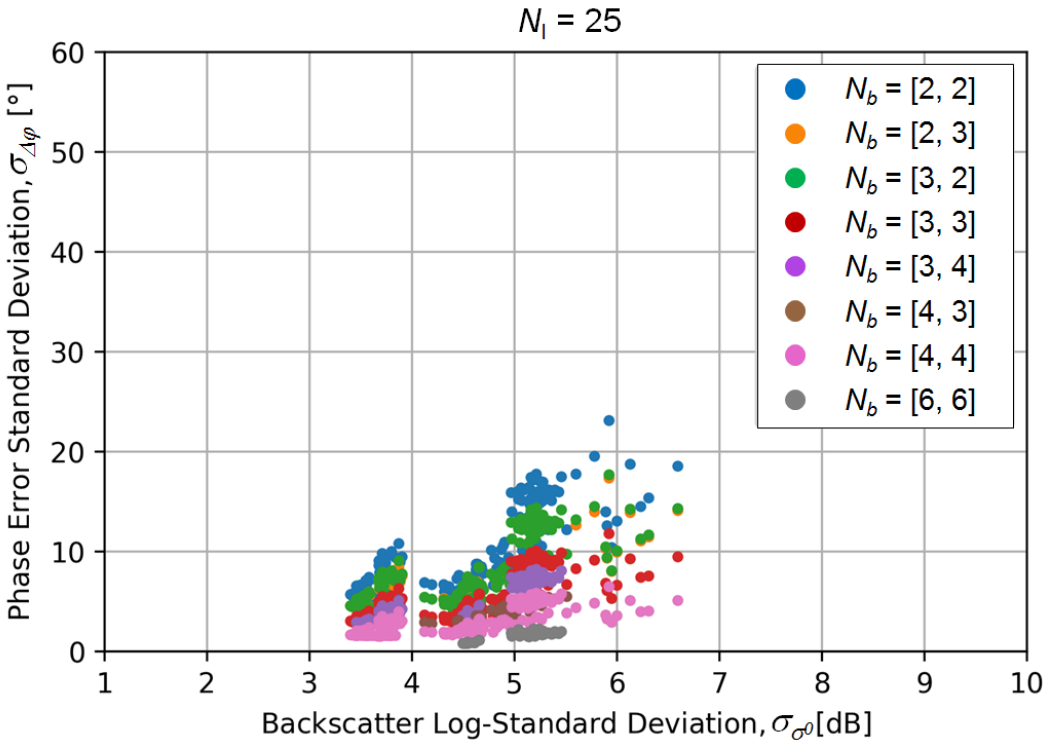

Figure 4.27: Single-point standard deviation of the interferometric phase error due to quantization $\sigma_{\Delta\varphi}$ as a function of the standard deviation of the backscatter coefficient σ_{σ^0} for $N_\mathrm{l} = 25$ looks and different BAQ rates, depicted with different colors. The BAQ rates in the legend indicate the number of bits used for the master and the slave acquisition $[N_{\mathrm{b,M}}, N_{\mathrm{b,S}}]$, respectively.

Step 2: The phase error values $\sigma_{\Delta\varphi}$ associated with the estimated σ_{σ^0} are fetched from the corresponding LUT, which is determined by the actual number of looks N_l, for all the available bit rate combinations $[N_{\mathrm{b,M}}, N_{\mathrm{b,S}}]$. In order to get a sufficient number of samples, the values of σ_{σ^0} must be considered within a reasonable interval of, e.g., ± 0.25 dB. Figure 4.28 shows the phase error values (depicted in blue) as function of the bit rate N_b obtained for an exemplary image block with σ_{σ^0} between 3.25 dB and 3.75 dB and for $N_\mathrm{l} = 9$ looks (i.e., the values are taken from Figure 4.25). The bit rate values used on the abscissa of Figure 4.28 are simply the average of the corresponding master and slave rates, i.e., $N_\mathrm{b} = \left(N_{\mathrm{b,M}} + N_{\mathrm{b,S}}\right)/2$.

Step 3: For each available N_b, the phase error $\sigma_{\Delta\varphi}$ is estimated as, e.g., the 90^{th} percentile of the corresponding values distribution (blue dots in Figure 4.28), which is indicated by the red dots (instead of the 90^{th} percentile, the maximum value can be alternatively used; however, this choice could result in significantly larger phase error

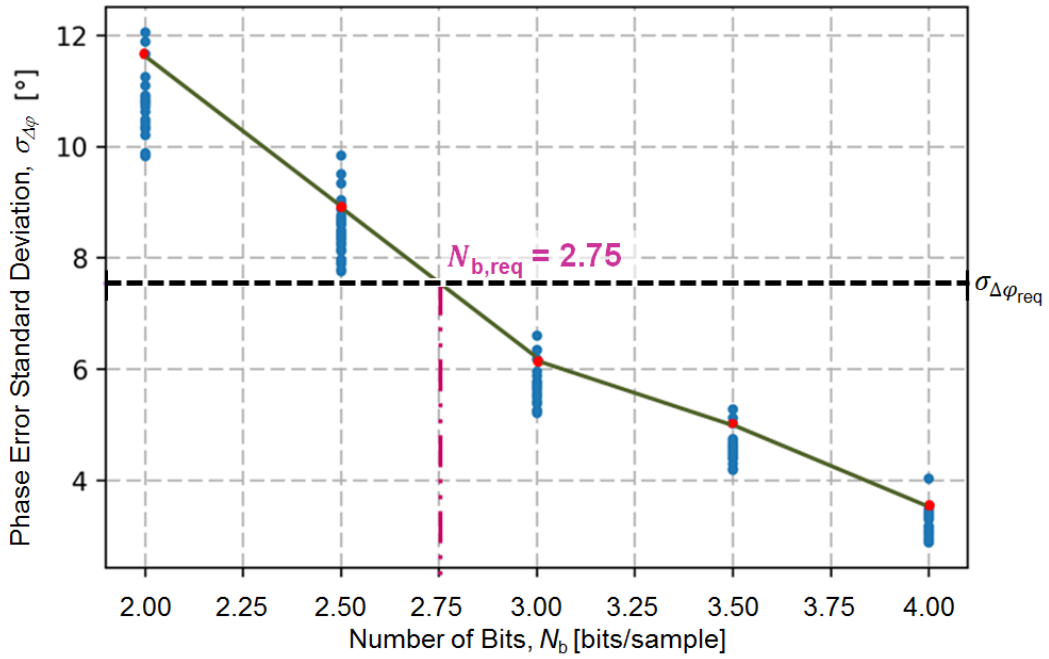

Figure 4.28: Estimation of the required number of bits $N_{b,req}$ according to the proposed PO-BAQ for a SAR backscatter block with σ_{σ^0} between 3.25 dB and 3.75 dB for $N_l = 9$ looks.

values due to the presence of possible outliers in the corresponding LUT estimation interval). The resulting values are then interpolated, as indicated by the dark green line in Figure 4.28.

Step 4: The number of bits $N_{b,req}$ required for quantizing the considered SAR raw data block is finally derived as

$$N_{b,req} = \underset{N_b \in [N_{b,min}, N_{b,max}]}{\arg\max} \quad \Delta\varphi\,(N_l, \sigma_{\sigma^0}) \quad \text{for} \quad \Delta\varphi \leq \Delta\varphi_{req}, \tag{4.14}$$

being $N_{b,min}$ and $N_{b,max}$ the minimum and maximum allowed bit rates. As an example, in Figure 4.28 $\Delta\varphi_{req} = \sigma_{\Delta\varphi,req} = 7.5°$ is set, which is sketched by the dashed horizontal line, $N_{b,min} = 2$ bits/sample, $N_{b,max} = 4$ bits/sample, and $N_{b,req} \approx 2.75$ bits/sample is finally determined as the abscissa corresponding to the intercept between the green line (expected degradation) and the black one (maximum allowed degradation).

Step 5: The procedure described above (Steps 1 to 4) is repeated for each SAR image block of the area to be acquired. In particular, for this purpose a certain step length,

corresponding to the distance d_{step} used for sliding the SAR image block at each iteration, has to be defined. Once all iterations are completed, the output of the PO-BAQ is a two dimensional *bit rate map* (BRM), which contains the quantization rates to be employed for SAR raw data compression. As it is shown in Figure 4.28, the resulting rates are typically non-integer numbers. These can be implemented by including additional hardware (e.g., a Huffman coder) prior to the quantizer block, as proposed in [96], [97]. Alternatively, although a standard BAQ scheme implements integer quantization rates only, non-integer compression rates can be effectively synthesized by toggling the integer BAQ rates along azimuth and/or range according to predefined bit rate sequences, as it is proposed in [121] and discussed in the next chapter.

As an example, Figure 4.29 shows the SAR backscatter map σ^0 acquired by TanDEM-X over the area of Berlin (Germany). The region includes urban settlements, characterized by a large dynamic range in σ^0, surrounded by farmland, rivers, and small lakes, showing a more homogeneous backscatter distribution. Figure 4.30 depicts two bit rate maps generated according to the proposed PO-BAQ for the same area of Figure 4.29 and for $N_{\text{l}} = 9$ looks. In particular, Figure 4.30 (a) shows the BRM for $\sigma_{\Delta\varphi,\text{req}} = 5^\circ$ while Figure 4.30 (b) for $\sigma_{\Delta\varphi,\text{req}} = 10^\circ$. For this example, a step length $d_{\text{step}} = 500$ m in azimuth and range was set, which is comparable to the range extension of one BAQ block for TanDEM-X (128 samples) and corresponds to the pixel size for the BRMs shown in Figure 4.30. As expected, larger values of $N_{\text{b,req}}$ are obtained in the neighborhood of the urban region with respect to the surrounding agricultural area, for which smaller bit rates are sufficient. In Figure 4.30 (a) ($\sigma_{\Delta\varphi,\text{req}} = 5^\circ$), $N_{\text{b,req}}$ ranges typically from about 4 bits/sample to 6 bits/sample. If the specification in terms of performance degradation is relaxed (Figure 4.30 (b), $\sigma_{\Delta\varphi,\text{req}} = 10^\circ$), the required bit rates significantly decrease, ranging from about 2 bits/sample over the homogeneous regions up to 4.5 bits/sample over the city area.

The proposed method has been tested on other test sites, showing different backscatter characteristics and for different number of looks and allowed degradation $\sigma_{\Delta\varphi,\text{req}}$, and consistent bit rate maps have been obtained. The next step is then to validate the PO-BAQ on real data, to verify that the degradation resulting from the raw data quantization according to the derived BRM matches with the expected one. At the moment this has not be done yet and will be investigated in following research studies. Moreover, since the responses of the scatterers under illumination overlap in the raw data domain within a certain area A_{SAR} defined in (4.12) (for this, the responses are opportunely weighted by the azimuth and elevation antenna pattern), the use of a given bit rate N_{b} applied to a certain subset of the raw data, affects the performance, in the focused image, also in areas located in close vicinity, as it is sketched by the red arrows in Figure 4.31. In turn, the performance of the central block is impacted by the bit rates used for quantizing the

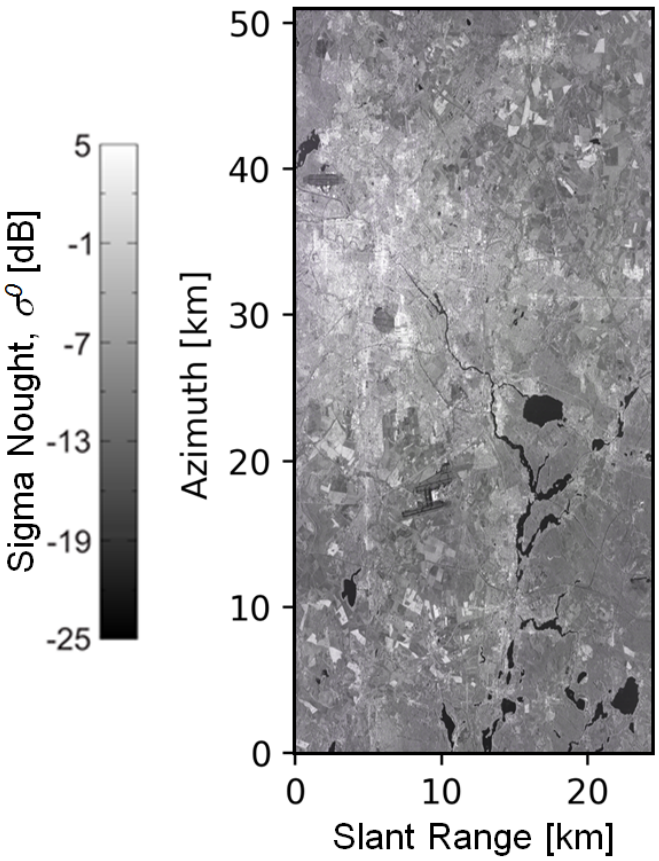

Figure 4.29: SAR backscatter map σ^0 of the area of Berlin (Germany) acquired by TanDEM-X on June 20, 2011. The region is characterized by the presence of urban settlements surrounded by farmland, rivers, and small lakes.

raw data located within the same area A_{SAR}, an effect which is ideally represented by the blue arrows in Figure 4.31 (for TanDEM-X, the synthetic aperture L_{s} and the chirp length L_{chirp} are in the order of a few kilometers). The described mixing effect of the target responses in the raw data results in a sort of low-pass filtering in the resulting bit rate map, for which smooth transitions between different values of N_{b} are typically observed. In the figure, the green segment d_{step} indicates the step length, assumed for simplicity the same in azimuth and range, used for sliding the SAR image block at each PO-BAQ iteration, which also defines the pixel size of the resulting bit rate map. All that considered, in the context of the proposed PO-BAQ it is of relevance to investigate the degree of granularity (i.e., the effective "resolution" of the bit rate maps shown in Figure 4.30) that can be achieved by the space-variant bit allocation when dealing with SAR data, an aspect which will be further investigated as well.

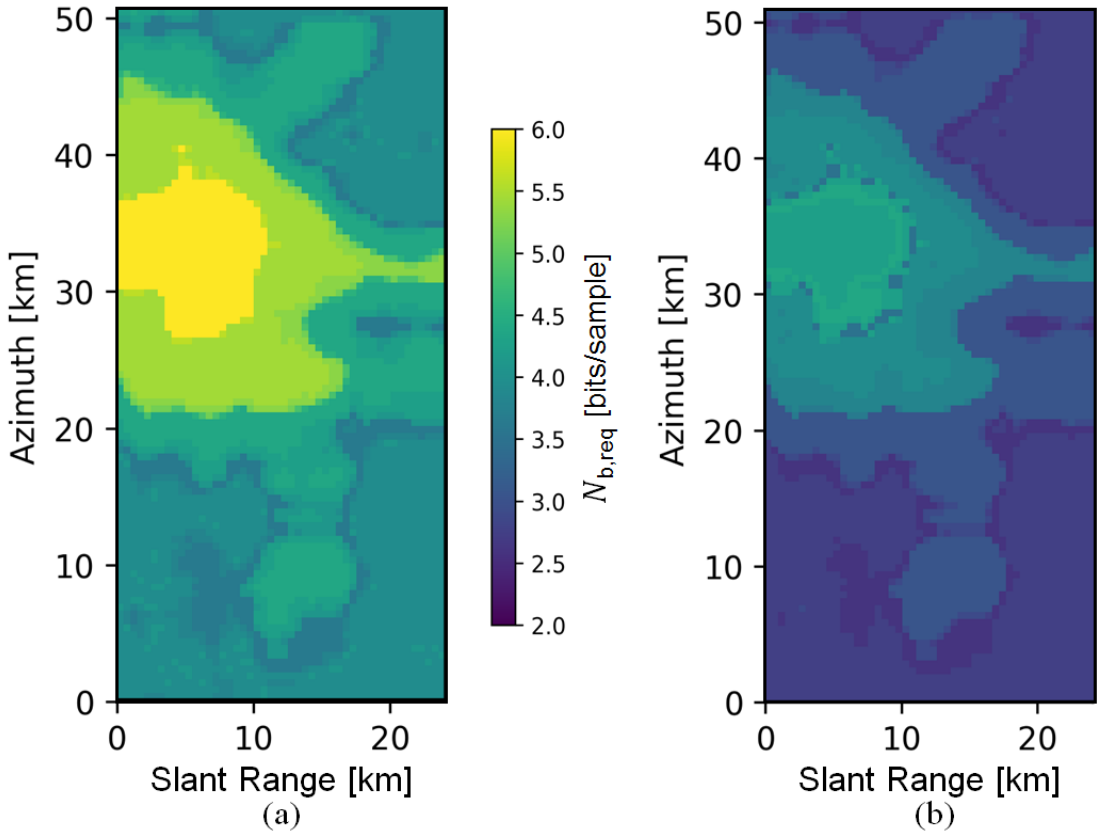

Figure 4.30: Bit rate maps generated according to the proposed PO-BAQ ($N_{b,req}$ in (4.14)) for the area of Berlin depicted in Figure 4.29, $N_l = 9$ looks, and (a) $\sigma_{\Delta\varphi,req} = 5^\circ$ and (b) $\sigma_{\Delta\varphi,req} = 10^\circ$.

Although a number of aspects still deserve to be carefully taken into account, the main advantage of the proposed PO-BAQ with respect to the existing quantization methods is that it aims at optimizing the performance of the processed SAR and InSAR data (and not of the raw data, as it is suggested, e.g., in [96]). This allows for achieving a targeted bit rate allocation depending on a predefined performance degradation, which can be therefore adapted to the specific SAR application and to the corresponding performance requirements. Moreover, since the bit rate definition is performed on ground before the data take commanding, the total required volume of data is known in advance. On the other hand, the bit rate map needs to be uplinked to the sensor, and the resulting bit rate selection must be properly implemented on board, which may require additional computational and processing effort.

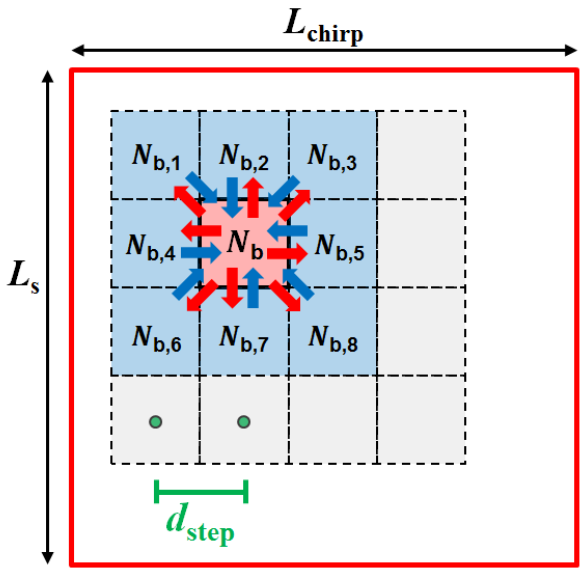

Figure 4.31: The responses of the scatterers under illumination overlap in the raw data domain within an area A_{SAR} as defined in (4.12), which for typical spaceborne SAR extends of several tens of square kilometers. Hence, the use of a given bit rate for a certain subset of raw data (e.g., N_{b} in the central block) affects the performance, in the focused data, in the areas located in close vicinity, an effect which is ideally sketched by the red arrows. In turn, the degradation observed in the area corresponding to the red image block is affected by the bit rates used for quantizing the raw data located within the area A_{SAR} (for this, the weighting carried out by the antenna pattern in azimuth and elevation must be taken into account as well). The closest blocks are indicated by $N_{\text{b},i}$, for $i \in [1,8]$ and the effect is represented by the blue arrows. Finally, the green segment d_{step} indicates the step length, assumed for simplicity the same in azimuth and range, which defines the pixel size of the resulting bit rate map.

4.5 Chapter Summary

In this chapter the effects of raw data quantization on TanDEM-X bistatic data have been investigated. Experimental data sets were acquired with 8 bits/sample (i.e., bypassing BAQ compression). On ground, all available quantization rates have been synthetically applied to the SAR raw data providing multiple data sets per satellite stream. Reprocessing with the interferometric chain was performed, even combining mixed data rates: as an example, 2 bits/sample from one satellite data and 3 bits/sample from the other satellite data result in an equivalent compression rate of 2.5 bits/sample. By this,

a dedicated comparison to the original data was possible, isolating the quantization effects from other error sources. Key parameters in determining SAR and interferometric performance have been evaluated over test areas showing different land cover types and topographic characteristics. The radiometric sensitivity of a radar system (the noise equivalent sigma zero, NESZ) is severely affected by quantization, and a degradation of up to 4 to 6 dB when using 2-bit BAQ with respect to the bypass case has been obtained. Quantization effects on the interferometric coherence are strongly dependent on the backscatter distribution of the imaged scene (low scatterer suppression), and the observed decorrelation for, e.g., the 2-bit case varies between 8% for flat and homogeneous areas, and 20% for irregular regions, such as urban areas. Consistent results have been observed for the interferometric phase errors, and for this several scene and system parameters which critically affect quantization errors have been investigated. In addition, of course, to the quantization rate N_b, these are identified with the degree of inhomogeneities in the backscatter response, described by the standard deviation of the SAR backscatter σ_{σ^0}, the number of interferometric acquisitions N_acq, and the number of looks N_l. Further, quantization effects on the relative height accuracy of the DEM have been assessed, and it has been verified that for typical TanDEM-X acquisition configurations, the employment of 2-bit BAQ for both coverages could have resulted in increased height errors ranging from 0.5 m to 1.8 m, leading in many areas to a violation of the DEM specifications. Therefore, for the first global DEM acquisition of TanDEM-X, mainly 3 bits/sample on both satellites are employed, which grant an acceptable performance degradation and, at the same time, a sufficient compression ratio in consideration of the nominal mission duration. Based on the presented analyses, an optimization of the resource allocation strategy for the second global DEM acquisition of TanDEM-X has been carried out. Acquisitions over areas showing very good performance as well as homogeneous backscatter distribution have been commanded with reduced quantization rates of 2 bits/sample and 2.5 bits/sample. On the other hand, the resulting free onboard resources could be exploited for reacquisition of areas affected by poor performance to further improve the global DEM performance.

Looking at present and next-generation spaceborne SAR missions, an increasing volume of onboard data is going to be demanded, which implies, from the mission design point of view, more stringent requirements in terms of onboard memory and downlink capacity. In this scenario, SAR raw data quantization represents an aspect of primary importance, since the data rate employed for raw data digitization defines the amount of data to be stored and transmitted to the ground, but also, at the same time, it directly affects the performance of the SAR products. Exploiting the state-of-the-art quantization algorithms for SAR systems, a novel method, named performance-optimized block-adaptive quantization (PO-BAQ), has been introduced, which aims at optimizing the resource allocation and, at the same time, the resulting interferometric performance, by exploiting a priori knowledge about the SAR backscatter information. This allows for achieving a targeted bit rate allocation depending on a predefined performance degradation, which

can be therefore adapted to the specific SAR application and to the corresponding performance requirements. The results presented in this chapter can be therefore combined with the precise, high-resolution knowledge of the Earth's topography and backscatter characteristics produced by the TanDEM-X global data set [122], [123], [124], in order to provide a helpful tool for performance budget definition and optimization of the resource allocation strategies for future SAR missions.

5 Azimuth-Switched Quantization for Fractional Bit Rate Implementation

In this chapter, a novel azimuth-switched quantization (ASQ) technique is introduced, which allows for the implementation of non-integer quantization rates in a new, efficient way. This grants higher flexibility in terms of performance design and resource allocation, without increasing the complexity and the computational load of the quantization scheme. The proposed method has been patented [125] and verified on interferometric SAR data acquired by the TanDEM-X mission, as discussed in [121].

5.1 Introduction

One of the most widely recognized methods for raw data digitization is the block-adaptive quantization (BAQ). As it has been recalled in Section 3.2, BAQ is a lossy data reduction technique (i.e., the data reconstructed after decompression are a distorted copy of the original input samples) which performs a space-varying estimation of the raw data statistics, to be calculated for each block (with fixed size) of input data. This information is employed to set the quantization decision levels that best match with the observed statistics [38], [39]. The compression rates N_b are typically fixed to integer numbers of bits and, clearly, the fewer the bits employed for data compression, the higher the resulting quantization noise power, which directly affects the SAR image quality. Despite its simplicity, BAQ has shown itself as an efficient solution for spaceborne SAR systems, where a huge amount of onboard data needs to be stored and then transmitted to the ground. In the last years, non-integer quantization rates have been implemented to allow for a finer performance and resource optimization, by complementing the quantizer (commonly based on a BAQ scheme) with additional software/hardware blocks (as, e.g., an entropy or Huffman coder) at the cost of increasing the overall system complexity [97], [96], [98]. Moreover, for such quantization schemes part of the optimization process is performed on board and, therefore, the amount of data required for an acquisition cannot be exactly calculated during mission planning.

In this chapter, a novel azimuth-switched quantization (ASQ) technique is introduced, which provides the capability of synthesizing fractional quantization rates without impacting the complexity and computational load of the quantization scheme. The impact on SAR and interferometric product quality is evaluated, and it is shown that performance and resources can be dynamically scaled with a very fine discretization. For this, investigations have been carried out in the frame of the TanDEM-X mission. As it has been introduced in Chapter 4, TanDEM-X (TerraSAR-X add-on for Digital Elevation Measurement) is the first operational spaceborne bistatic SAR mission and is served by the twin satellites TerraSAR-X and TanDEM-X, launched in 2007 and 2010,

respectively. The primary objective of TanDEM-X is to generate a worldwide, consistent, and highly accurate DEM in bistatic configuration [30], [104]. On the TerraSAR-X and TanDEM-x satellites the received backscattered signal is first digitized by an 8-bit ADC and then further compressed by the block-adaptive quantizer. Available BAQ compression rates are 2, 3, 4, and 6 bits/sample. Full resolution 8-bit data can be obtained as well by bypassing the BAQ. [27], [93]. By taking into account the limited downlink capacity and onboard memory of TanDEM-X, mainly 3 bits/sample have been selected for operational DEM acquisitions. Furthermore, 2.5 bits/sample (obtained by selecting 3-bit BAQ on one satellite and 2 bits-BAQ on the other one) and 2 bits/sample have been employed over highly coherent (i.e., flat and non-vegetated) areas. This allowed for the completion of two global acquisitions and several additional coverages on selected regions [117] within the nominal mission duration [30], [94]. However, the main drawback of employing constant and integer compression rates is the coarse discretization in terms of achievable data rate, and hence of the corresponding image performance, especially for long data acquisitions. The proposed ASQ can overcome such limitations, allowing for a finer optimization of memory resources and performance. Moreover, the amount of data to be stored and transmitted to the ground can be precisely calculated during mission planning.

The chapter is organized as follows. The principle of azimuth-switched quantization (ASQ) is introduced in the next section and a performance analysis on experimental TanDEM-X data is presented in Section 5.3. The impact of ASQ on the noise equivalent sigma zero (NESZ), azimuth ambiguities, and interferometric coherence is investigated in detail, verifying that ASQ can successfully be employed for state-of-the-art SAR systems. The chapter ends in Section 5.4, where the conclusions and a short summary are provided.

5.2 The Azimuth-Switched Quantization (ASQ) Principle

The basic principle of azimuth-switched quantization is explained as follows. During the data collection by the SAR system, integer compression rates are toggled along the azimuth direction, from echo to echo (within a range line the quantization rate is kept constant). After performing the azimuth focusing over one synthetic aperture, an equivalent non-integer quantization rate is synthesized, which results from an average of the different rates used. This way, highly flexible adaptation of SAR performance and calculation of memory resources are possible, by just exploiting the peculiar SAR acquisition concept. Indeed, only a simple quantizer with integer rates is required (the capability of changing acquisition parameters during a SAR data take is a feature normally provided by state-of-the-art technology). Figure 5.1 depicts the ASQ workflow for a target output bit rate of 2.5 bits/sample. During the acquisition, the quantization setting is switched between 2 and 3 bits/sample at every range line (left part of the figure). The image is

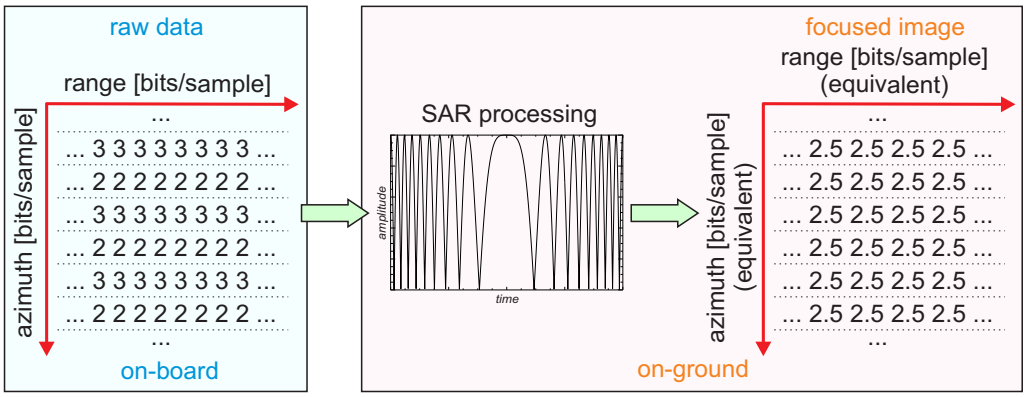

Figure 5.1: Workflow for the implementation of the azimuth-switched quantization (ASQ) on a SAR system. Integer rates are switched along the azimuth direction during the data take. After SAR processing, the focused image shows performance equivalent to as if the raw data were acquired with an "average" of the original sequence. In the example, a fractional quantization rate of 2.5 bits/sample is obtained as a result of switching between 2 bits/sample and 3 bits/sample, range line by range line.

then processed (central part), showing performance equivalent to the average of the compression rates used along azimuth. It is worth recalling that such a fractional rate is not the one of the focused image, for which an always constant bit-rate is used (e.g., 8 or 16 bits/pixel). Instead, it refers to an equivalent compression rate employed for the raw data, i.e., the processed image shows a performance as if the raw data were acquired with the rate resulting from the average of the original sequence.

On the TerraSAR-X and TanDEM-X satellites the BAQ rate can be set for each range line, to support different compression rates for, e.g., dual polarization data. Anyhow, one could think to further extend the presented technique, by adapting the quantization settings for each block within one echo window (i.e., range line). This capability allows for achieving an even finer granularity in terms of performance and resource allocation, such as the FDBAQ technique operated on the Sentinel-1 mission [96], or for the implementation of the Performance Optimized (PO-BAQ) method discussed in Chapter 4. As the compression rate can be theoretically changed from PRI to PRI, the maximum number of range lines ($n_{\mathrm{rg,\,max}}$) to be taken into account for determining the effective average quantization rate are those lying inside one synthetic aperture L_{s} (2.2):

$$n_{\mathrm{rg,\,max}} = \frac{t_{\mathrm{int}}}{\mathrm{PRI}} = \frac{L_{\mathrm{s}}}{v_{\mathrm{s}}} \cdot \frac{1}{\mathrm{PRI}}, \tag{5.1}$$

where v_{s} is the satellite velocity and t_{int} is the integration time defined in (2.24). For the TanDEM-X mission (and typical space-borne configurations), v_{s} is of about 7 km/s,

the synthetic aperture L_s is of about 3-4 km, and the pulse repetition frequency (PRF) is bigger than 2 kHz (i.e., PRI < 0.5 ms). The resulting $n_{\text{rg, max}}$ is around 1000: in practice, with the presented technique, bit rates until a fraction of a thousandth of a bit can be effectively implemented. A given ASQ rate $N_{\text{b,ASQ}}$ is synthesized by replicating along azimuth direction the appropriate sequence of integer BAQ rates of length N_{seq} whose average is just $N_{\text{b,ASQ}}$

$$S_{N_{\text{b,ASQ}}} = [N_{\text{b},1}, N_{\text{b},2}, N_{\text{b},3}, ..., N_{\text{b},N_{\text{seq}}}] : \;\; N_{\text{b,ASQ}} = \frac{1}{N_{\text{seq}}} \sum_{k=1}^{N_{\text{seq}}} N_{\text{b},k}. \tag{5.2}$$

In principle, given a certain $N_{\text{b,ASQ}}$, the corresponding $S_{N_{\text{b,ASQ}}}$ has to be as short as possible, and the distribution of the rates needs to be homogeneous, in order to avoid biases in terms of performance loss within one synthetic aperture.

In the next section, the impact of the proposed ASQ on TanDEM-X interferometric and SAR performance is discussed and evaluated. For this purpose, experimental acquisitions with BAQ bypass (i.e., 8 bits/sample) have been recompressed on ground using different ASQ rates. The obtained products have then been focused to SAR images, allowing for the generation of interferograms and coherence maps.

5.3 Performance Analysis

In this section a performance analysis of ASQ on TanDEM-X data is presented. The impact on the NESZ (Section 5.3.1), azimuth ambiguities (Section 5.3.2), and interferometric coherence (Section 5.3.3) is investigated. The ASQ rates and the corresponding azimuth sequences used for the present investigations are listed in Table 5.1 for $N_{\text{seq}} = 10$. Each element of a sequence represents the compression rate employed for one range line, and the corresponding sequence is then replicated along azimuth direction in the raw data matrix.

5.3.1 Noise Equivalent Sigma Zero (NESZ)

As it has been introduced in Chapter 2, the signal-to-noise ratio (SNR) is a measure to describe the image quality of remote sensing systems, estimating how much a signal has been corrupted by noise (just as coherence does for interferograms). From a SAR image, the SNR is computed according to the definition in (2.43) as follows:

$$\text{SNR} = \frac{\sigma^0}{\text{NESZ}}, \tag{5.3}$$

where σ^0 is the backscatter coefficient (2.42) and NESZ stands for Noise Equivalent Sigma Zero, which accounts for the several noise sources affecting the data, and has

ASQ Rate [bits/sample]	Azimuth Sequence [bits/sample]
2.1	2 2 2 2 2 2 2 2 2 3
2.2	2 2 2 2 3 2 2 2 2 3
2.3	2 2 3 2 2 3 2 2 3 2
2.4	2 3 2 2 3 2 3 2 2 3
2.5	2 3 2 3 2 3 2 3 2 3
2.6	2 3 2 3 2 3 2 3 3 3
2.7	2 3 2 3 3 3 2 3 3 3
2.8	2 3 3 3 3 2 3 3 3 3
2.9	2 3 3 3 3 3 3 3 3 3

Table 5.1: ASQ rates ($N_{\mathrm{b,ASQ}}$) and corresponding azimuth sequences $S_{N_{\mathrm{b,ASQ}}}$ with $N_{\mathrm{seq}} = 10$.

been defined in (2.44). For the present analysis, the NESZ can be formally decomposed into the sum of two main contributions

$$\mathrm{NESZ} = \mathrm{NESZ}_{\mathrm{sys}} + \mathrm{NESZ}_{\mathrm{quant}}. \tag{5.4}$$

The first term on the right-hand side $\mathrm{NESZ}_{\mathrm{sys}}$ includes all noise contributions induced by the system, like antenna pattern, instrument thermal noise, as well as processing filters [30]. The second term describes the noise power solely due to quantization, which directly affects the radiometric resolution of the focused data. In order to estimate noise power from SAR images a distributed target analysis over regions showing very low backscatter response has been carried out. For our investigations, the area depicted in Figure 5.2 has been considered. It is located in the Amazon rainforest and is crossed by two rivers entirely from near to far range: in particular, areas covered by flat water reflect almost completely the incident radar signal to specular direction, and, therefore, the recorded signal is of the same order of magnitude as the system noise (in this case, over the two rivers $\sigma^0 < -19$ dB). After an averaging of the corresponding pixels along azimuth direction the NESZ for different ASQ rates could be evaluated. The results are depicted on the left-hand side of Figure 5.3. The dots indicate the measured values from a distributed target analysis. By interpolating along range direction, the resulting NESZ profile curves are derived (the integer rates have been obtained by using "pure" BAQ). On the right-hand side of Figure 5.3, the NESZ degradation with respect to the bypass case is shown. Being all the acquisition and processing parameters the same except the ASQ rate employed, it can be concluded that the obtained profiles correspond just to the degradation term $\mathrm{NESZ}_{\mathrm{quant}}$ in (5.4). As expected, a higher compression ratio corresponds to a higher degradation, varying between about 1 dB to 3.5 dB for the case of 3

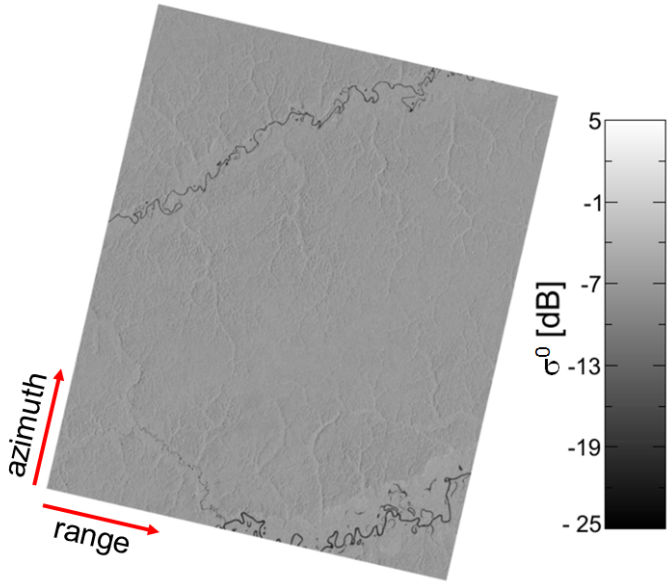

Figure 5.2: Test area for NESZ estimation, located in Amazon rainforest (Stripmap mode, HH polarization, acquired on June 21, 2012). NESZ profiles for different ASQ rates are estimated considering the backscatter response over the two rivers located on the upper-left and lower-right part of the scene.

bits/sample and 2 bits/sample, respectively.

5.3.2 Azimuth Ambiguities

Azimuth-switched quantization can be exploited to reduce the impact, among the others, of the azimuth ambiguities for a given data rate. In order to satisfy the sampling requirement, the PRF must be sufficiently high, depending mainly on the antenna flight velocity and on its azimuth length. In general, the higher the PRF, the smaller the azimuth-ambiguity-to-signal ratio (AASR). For a SAR system, the amount of data stored during an acquisition is proportional to the data rate DR and the acquisition duration ΔT_{acq}. The data rate is, in turn, proportional to the quantization rate N_{b} and the PRF, as expressed in (3.1)

$$DR \propto N_{\text{b}} \cdot \text{PRF}, \tag{5.5}$$

and often represents a bottleneck for spaceborne SAR systems. In order to evaluate the combined effect of quantization and PRF, simulations of a one-dimensional azimuth-compressed point target were carried out. In Figure 5.4, the peak AASR is depicted for ASQ rates between 2 bits/sample and 5 bits/sample and for different azimuth data rates (8 kbits/s, 9 kbits/s, and 10 kbits/s; only one sample has been considered in range direction). The corresponding PRFs are in the range between 1500 Hz and 5000 Hz. As expected,

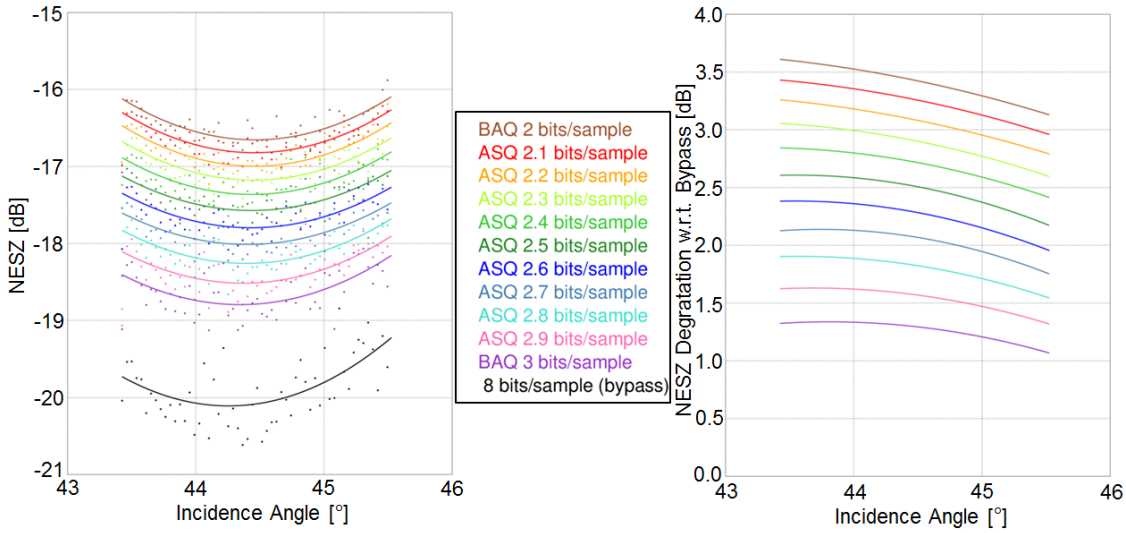

Figure 5.3: (Left) NESZ for different ASQ rates, estimated from the rivers in the data take in Figure 5.2. The points show the recorded values from a distributed target analysis. By interpolating them, corresponding NESZ profiles are obtained, which are depicted with different colors. The highest (brown) and lowest (black) curve indicate the NESZ for the case of BAQ 8:2 and BAQ bypass, respectively. (Right) NESZ degradation introduced by quantization with respect to the 8-bit case (BAQ bypass).

when fewer bits are employed for quantization (i.e., higher PRFs are allowed for the given data rate), smaller values of AASR are observed. In particular, for a fixed data rate, a reduced ambiguous signal power can be obtained by reducing the quantization rate (i.e., moving to the left along one of the curves in Figure 5.4 and thus allowing for an increased PRF). Alternatively, one can exploit a much finer-grained set in terms of acquisition parameters design and resource allocation in order to keep the ambiguous signal below a certain threshold (i.e., "jumping" horizontally from one curve to another one). However, one has to be aware that for too high PRFs it may happen that several successive pulses arrive at the receiving antenna at the same time, as discussed in Section 2.3.4. This produces artifacts in the SAR images known as range ambiguities, and a non-negligible worsening of the resulting range-ambiguity-to-signal ratio (RASR) can be obtained, which depends on the characteristics of the target under illumination together with the specific acquisition geometry and system parameters [30], [42], [126].

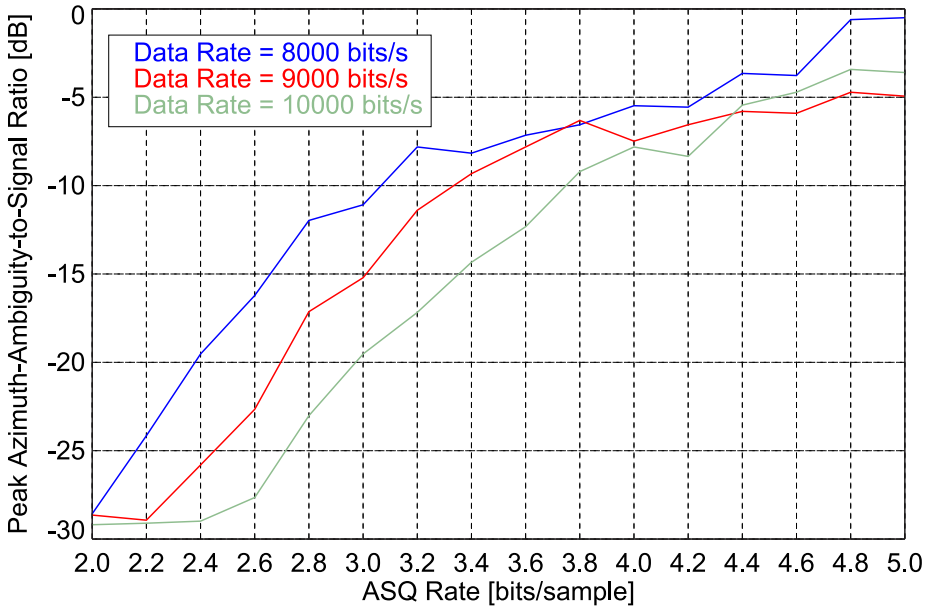

Figure 5.4: Azimuth-ambiguity-to-signal ratio (AASR) over ASQ rates, for different data rates (depicted with different colors). For the described scenario, the resulting PRFs are in the range between 1500 Hz and 5000 Hz.

5.3.3 Interferometric Coherence

The key quantity to evaluate interferometric SAR (InSAR) performance is the coherence. It represents the normalized correlation coefficient between master (monostatic channel) and slave (bistatic channel) acquisition and several error sources may contribute to a coherence loss [30], [63], [69], [70], [71], as it has been described in Section 2.4.2. Figure 5.5 shows the interferometric coherence for rates between 2 bits/sample and 3 bits/sample and for different test sites, and the performance resulting from uncompressed data is shown as well for comparison. Each curve shows the mean coherence values derived from a single bistatic acquisition (extending by about 30 km by 50 km in range and azimuth, respectively), which has been compressed to different ASQ rates. The corresponding sequences are listed in Table 5.1. As expected, when fewer bits are employed for quantization, lower coherence values are obtained for the same test site. Figure 5.6 depicts the corresponding coherence degradation with respect to the bypass case (8:8) for the same test sites. The black bars represent the average and the standard deviation of the estimations for each ASQ rate, and good agreement with the theoretic prediction is observed, marked by the green lines for the case of two and three bits [30]. Moreover, it can be noticed that the dispersion of the estimations increases with a decreasing of the quantization rate. The reason for that is the presence of different backscatter distributions within the analyzed scenes. Figure 5.7 shows the histograms for σ^0 of two areas

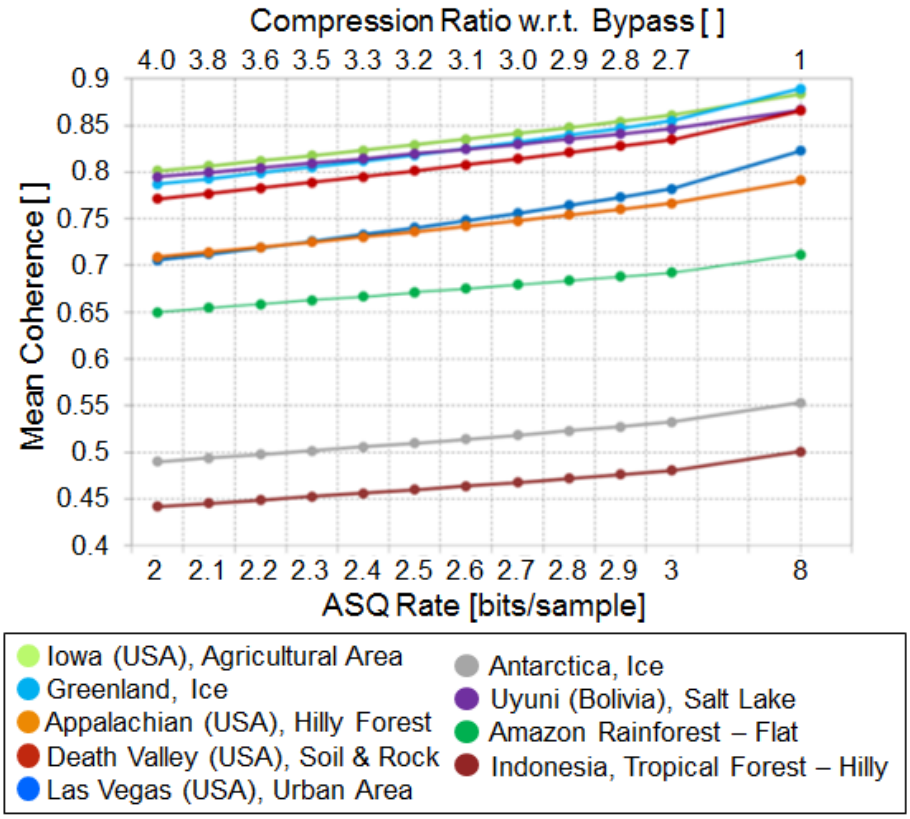

Figure 5.5: Interferometric coherence over ASQ rates for different test sites (depicted with different colors). Each curve corresponds to one acquisition at different ASQ rates. On the upper part of the chart, the compression ratio for each ASQ rate is specified.

with different backscatter characteristics. The salt lake of Uyuni (Bolivia), depicted in blue, is a quite homogeneous region, and the corresponding coherence loss (violet dots in Figure 5.6) goes from about 2% to 8%. On the other hand, the urban area of Las Vegas (USA), represented in red in Figure 5.7, shows a very inhomogeneous backscatter distribution, and a higher coherence degradation is observed (between 5% and 14%, marked in blue in Figure 5.6). This discrepancy in terms of performance is due to the so-called low scatterer suppression, which has been recalled in Chapter 3 and detailed in [94] and [103], and which occurs if the responses from neighboring targets (with respect to the synthetic antenna and the chirp length) overlap considerably in the raw data domain. The decision levels as well as the clipping threshold for the quantization process are set according to the mean power of the raw data block. Therefore, if two targets have different magnitude response, the quantizer best matches with the strong signal, whereas the low one is heavily distorted. Such an effect represents an additional nonlinear and

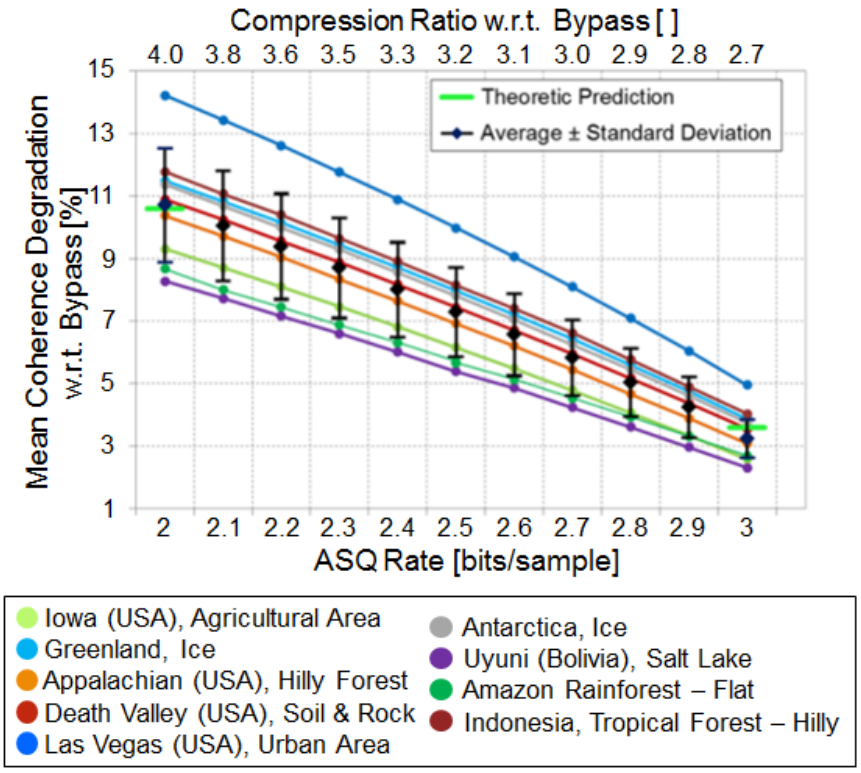

Figure 5.6: Coherence degradation with respect to the bypass case, for different test sites (depicted with different colors). The black bars represent the average and the standard deviation of the estimated degradations for each ASQ rate, and the short horizontal green lines indicate the theoretic prediction for the case of two and three bits [30]. Each curve corresponds to one acquisition at different ASQ rates. On the upper part of the charts, the compression ratio for each ASQ rate is specified.

signal-dependent error source in the SAR data which does not appear in the raw data but becomes visible only in the SAR focused image.

TerraSAR-X and TanDEM-X have a relatively limited downlink capacity, which is due to an average contact time with the ground station network of about 10 min/orbit at a total net data rate of about 260 Mbits/s. If considering nominal acquisition parameters, this implies a maximum allowed time for data takes of about 180 s per orbit, in the case a quantization rate of 3 bits/sample is employed [30]. In order to speed up the completion of the global DEM acquisition, the opportunity to further reduce the quantization rate has been considered: in particular, a “hybrid” quantization of 2.5 bits/sample has been exploited, using 3 bits/sample on one satellite and 2 bits/sample on the other, for

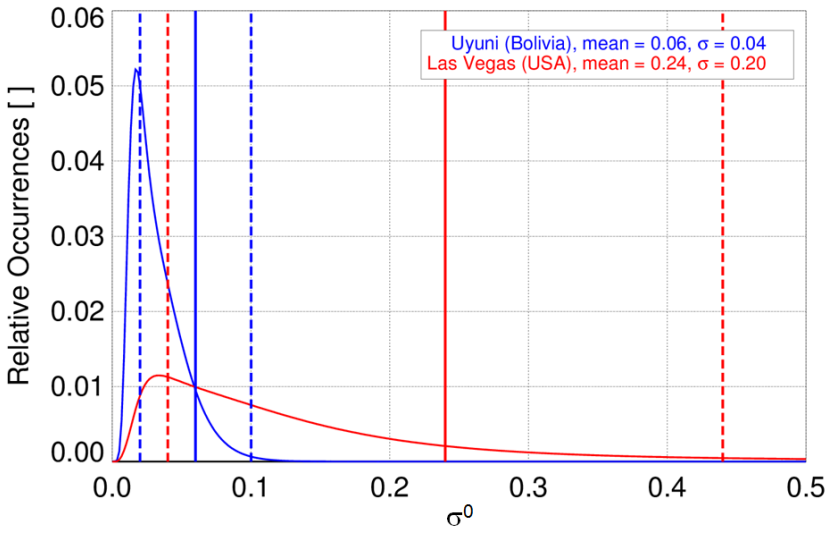

Figure 5.7: Histogram for σ^0 measured over the salt lake of Uyuni (Bolivia) and the urban area of Las Vegas (USA). The continuous (dotted) lines indicate the mean (standard deviation) for each distribution. The linear scale highlights the difference in terms of dynamic range in backscatter.

the acquisition of areas showing very good performance and homogeneous backscatter response, as described in Section 4.3.5. It has been verified that the interferometric performance was essentially the same as that employing an ASQ rate of 2.5 bits/sample, and that a considerable increase, in terms of allowed acquisition time, of about 40 s per orbit (compared to a quantization with 3 bits/sample) could be obtained.

5.4 Chapter Summary

In this chapter, a novel azimuth-switched quantization (ASQ) scheme for SAR raw data has been introduced, which allows for implementing non-integer compression rates in a new, efficient way. The principle of the proposed technique has been described and the impact on SAR and interferometric performance of TanDEM-X experimental data has been evaluated and quantified. It has been shown that highly flexible adaptation of SAR performance and calculation of memory consumption is achievable. This provides more freedom in the design and operation of SAR missions, when memory and downlink resources are limited.

6 Efficient Onboard Quantization for Multi-Channel SAR Systems

In this chapter, a novel method for onboard data reduction for multi-channel synthetic aperture radar (SAR) systems is presented. Such systems allow for high-resolution imaging of a wide swath but require for their operation the acquisition and downlink of a considerable volume of data. Together with the intrinsic requirement related to resolution and swath width, this is due to the use of a pulse repetition frequency (PRF) typically higher than the processed Doppler bandwidth, which introduces a certain oversampling in the azimuth raw data. In this context, a convenient data reduction strategy is proposed, named multi-channel block-adaptive quantization (MC-BAQ), which exploits the existing correlation between subsequent azimuth samples by performing a discrete Fourier transform of the multi-channel SAR data block. Then, a variable-bit quantization is applied, which allows for the optimization of the resulting performance and data rate. Simulations have been carried out on scenes with distributed scatterers showing different backscatter characteristics, to demonstrate that the proposed MC-BAQ allows for a significant reduction of the data volume to be downlinked to the ground at the cost of a modest increase of the onboard computational effort. The proposed method has been first introduced in [127], and then further investigated and detailed in [100].

6.1 Introduction

For conventional single-channel SAR systems, it is well known that the pulse repetition frequency (PRF) poses opposite constraints for the imaging of wide swaths and, at the same time, of fine azimuth resolutions. Indeed, the former dictates a low PRF to allow for a sufficient temporal separation between subsequent SAR pulses, whereas the latter requires a large Doppler bandwidth and, therefore, high PRFs. Such inherent limitations can be overcome by exploiting multiple receiving apertures which are mutually displaced in along-track. The coherent combination of the individual received signals allows for adequate suppression of the ambiguous parts of the Doppler spectra and, in this way, high-resolution wide-swath imaging is achieved [40], [58]. Besides an increased system complexity, the downside for such an improvement of swath coverage and resolution is represented by a significantly larger data volume to be acquired and transmitted to the ground, which poses more stringent demands on the onboard memory and downlink capacity. In this scenario, efficient data volume reduction is of utmost importance, as the data rate selected for the digitization of the recorded radar signals directly affects the quality of the resulting SAR products. In the context of single-channel staggered SAR, a method for data volume reduction based on onboard Doppler filtering (i.e., exploiting the lower processed Doppler bandwidth with respect to the PRF) and decimation is pro-

posed in [128]. However, this technique cannot be directly applied to the multi-channel case since the data of the individual receive channels are highly ambiguous. In the last years, a data-driven data reduction technique for multi-channel SAR based on a principal component decomposition has been proposed in [99], at the cost of a large onboard implementation effort.

The approach described in this chapter aims at exploiting the intrinsic correlation among the azimuth samples. In particular, the multi-channel SAR data are decomposed by means of a non-adaptive orthogonal transformation (a simple discrete Fourier transform). Then, an optimized allocation of the quantization rates is applied to the transformed coefficients, allowing for an increase of the resulting performance for a preselected data rate. For data digitization, a standard block-adaptive quantizer (BAQ) is considered. In particular, in this chapter a quantitative assessment in terms of achievable data volume reduction is presented, and the optimization of the bit allocation for the transformed coefficients is discussed in detail.

The chapter is structured as follows: the principle of multi-channel block-adaptive quantization (MC-BAQ) for efficient data volume reduction is introduced in the next section. Section 6.3 presents simulations for the considered C-band single-platform multi-channel SAR, proving the effectiveness of the proposed compression scheme. Finally, conclusions and chapter remarks are summarized in Section 6.4.

6.2 Multi-Channel Block-Adaptive Quantization

Let us consider a multi-channel SAR with N_{ch} receiving azimuth apertures which flies at velocity v_{s}, $\mathrm{PRF}_{\mathrm{sys}}$ is its transmit PRF, and l is the azimuth separation between the sub-apertures, i.e., the total azimuth antenna length $L_{\mathrm{a}} = N_{\mathrm{ch}} \cdot l$. If the following constraint on the PRF is fulfilled

$$\mathrm{PRF}_{\mathrm{sys}} = \frac{2v_{\mathrm{s}}}{L_{\mathrm{a}}}, \tag{6.1}$$

then the azimuth raw data stream is uniformly sampled, hence the resulting system is equivalent to a single-channel SAR with $\mathrm{PRF}_{\mathrm{eff}} = N_{\mathrm{ch}} \cdot \mathrm{PRF}_{\mathrm{sys}}$ and basically a conventional SAR processing can be applied. More in general, due to timing constraints and requirements on the ambiguity-to-signal ratio, the PRF is often selected slightly deviating from (6.1). In this case, an appropriate signal reconstruction of the unambiguous Doppler spectrum from the non-uniform azimuth data, based on the generalized sampling expansion, needs to be carried out on ground by properly combining the N_{ch} subsampled channels as in [40], [129]. On the other hand, the Doppler bandwidth of the reconstructed multi-channel signal is larger than the system (transmit) PRF, i.e., a finer azimuth resolution is achieved with respect to the corresponding single-channel SAR operating with the full antenna length L_{a} and at the same $\mathrm{PRF}_{\mathrm{sys}}$. Indeed, with multi-channel SAR systems a swath width of hundred kilometers and more can be imaged with an azimuth

resolution in the order of one meter [58], [130]. For such a system, the raw data samples received by its N_{ch} azimuth channels exhibit a certain degree of correlation, which is introduced by the specific antenna pattern (or Doppler spectrum) together with a certain signal oversampling (defined by $\mathrm{PRF}_{\mathrm{sys}}$) of the azimuth data stream [131]. Typically, for multi-channel SAR a processed Doppler bandwidth B_{D} that is significantly smaller than the product of the number of apertures and the PRF ($B_{\mathrm{D}} < N_{\mathrm{ch}} \cdot \mathrm{PRF}_{\mathrm{sys}}$) is required in order to get a sufficient azimuth ambiguity-to-signal ratio (AASR) [40], [58]. However, a direct downlink of the acquired multi-channel data is associated with an unnecessarily high data rate, as the effective PRF is significantly higher than the processed Doppler bandwidth. On the other hand, according to the specific system configuration, i.e., its antenna patterns, PRF, and processed bandwidth, one simple way to exploit the existing spectral selectivity is to perform a (lossless) discrete Fourier transform (DFT) on the multi-channel azimuth block before data compression. The DFT is chosen because of the intuitive correspondence between Doppler spectrum and antenna pattern, but in general other orthogonal transformations could be used for this purpose as well. Then, an efficient quantization strategy is implemented, which allocates less resources for those sub-bands which carry a smaller amount of information, i.e., that are located outside the processed bandwidth, and vice-versa for those sub-bands lying in the more "useful" portion of the Doppler spectrum. By applying the transform coding paradigm, this strategy aims at removing the redundancy existing in the multi-channel data block and enables a better (more targeted) quantization, hence resulting in an increased quality of the final SAR image. For single-channel SAR, a similar compression scheme has been introduced in [92].

The workflow for the proposed onboard data reduction strategy for a multi-channel SAR with N_{ch} receiving azimuth apertures is sketched in Figure 6.1: for each instant of time n, the signal received by the i-th azimuth channel $x_{\mathrm{in},i}$ ($\boldsymbol{x} \in \mathbb{R}^{N_{\mathrm{ch}}}$) is first digitized by a high-resolution analog-to-digital converter (the input to an ADC is typically continuous-time, but here it is assumed to be already a discrete-time signal). The multi-channel raw data block $\boldsymbol{x}_{\mathrm{ADC}}$ is then decomposed by the orthogonal transformation $\boldsymbol{F}$ into a set of K azimuth beams $\boldsymbol{y} = \boldsymbol{F}\boldsymbol{x}$ ($\boldsymbol{F}$ corresponds to the discrete Fourier transformation matrix and $\boldsymbol{y} \in \mathbb{R}^{K}$), each one corresponding to a different portion of the Doppler spectrum, and derived as

$$y_k[\mathrm{n}] = \sum_{i=1}^{N_{\mathrm{ch}}} \left(x_{\mathrm{ADC},i}[\mathrm{n}]\right) e^{-j2\pi i(k-\frac{K}{2})/N_{\mathrm{ch}}}, \quad k = 1,2,...,K. \tag{6.2}$$

In the above equation, the term $\frac{K}{2}$ in the argument of the complex exponential implies that the DC component arises for $k = \frac{K}{2}$. In our case, without loss of generality, the number of output coefficients K is assumed to be equal to the number of the input samples, i.e., $K = N_{\mathrm{ch}}$ and $\boldsymbol{F} \in \mathbb{R}^{K \times N_{\mathrm{ch}}}$ (for $K < N_{\mathrm{ch}}$ the transformation is not strictly orthogonal). The output transformed coefficients are then further compressed by means of a set of block-

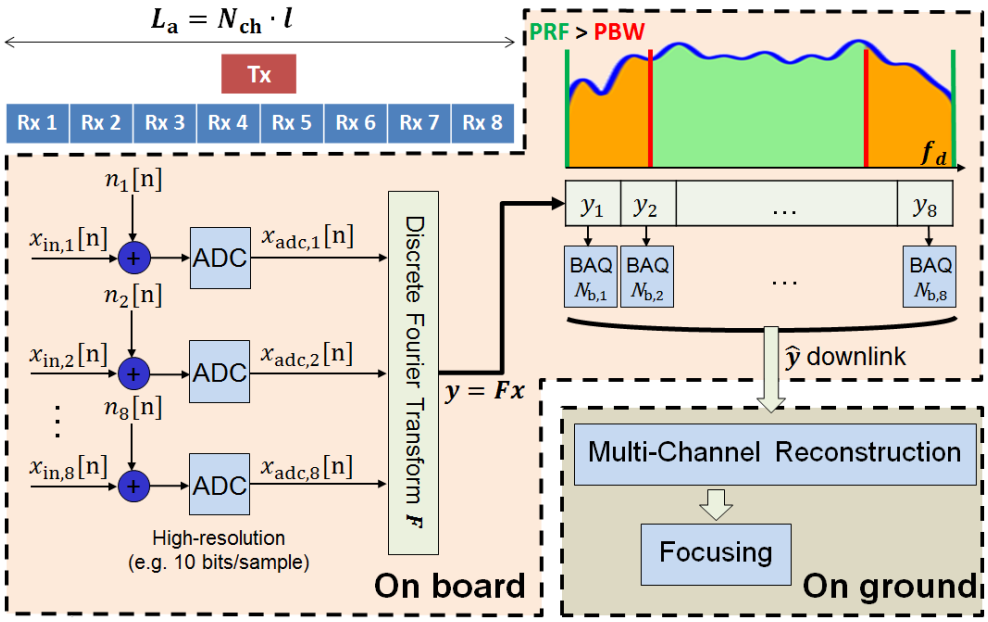

Figure 6.1: MC-BAQ for onboard data reduction for a SAR system with multiple azimuth channels: for each time instant n, the signal received by the i-th azimuth channel, $x_{\mathrm{in},i}$ is first digitized by a high-precision analog-to-digital converter (e.g., 10-bit ADC). The multi-channel azimuth block $\boldsymbol{x}_{\mathrm{ADC}}$ of length N_{ch} is then decomposed by means of a discrete Fourier transform. As a next step, a proper bit allocation is applied to the transformed coefficients (the BAQ $N_{\mathrm{b},k}$ blocks on the right-hand side) to optimize the resulting data volume and performance. The quantized coefficients $\hat{\boldsymbol{y}}$ are then downloaded to the ground, where inverse Fourier transform, multi-channel reconstruction, and SAR focusing are performed.

adaptive quantizers (BAQ) [39], which are indicated on the right-hand side of Figure 6.1. For this, a proper selection of each compression rate $N_{\mathrm{b},k}$ associated to the k-th coefficient y_k needs to be applied. The set of quantized coefficients $\hat{\boldsymbol{y}}$ is then downloaded to the ground, where the inverse Fourier transform, multi-channel reconstruction, and SAR focusing are finally carried out. The optimum bit rate to be selected for the k-th output channel is derived from rate-distortion theory [85] as

$$N_{\mathrm{b},k} = \bar{N}_{\mathrm{b}} + \frac{1}{2}\log_2 \frac{\sigma_k^2}{\left[\prod_{m=1}^{K} \sigma_m^2\right]^{1/K}} = \bar{N}_{\mathrm{b}} + \Delta N_{\mathrm{b},k}, \tag{6.3}$$

where $\bar{N}_{\mathrm{b}}$ is the mean allowed bit rate, σ_k^2 is the power associated to the k-th sub-band, and $\Delta N_{\mathrm{b},k}$ is the resulting bit rate contribution to be added ($\Delta N_{\mathrm{b},k} > 0$) or subtracted ($\Delta N_{\mathrm{b},k} < 0$) for the k-th channel. Clearly, $\sum_{k=1}^{N_{\mathrm{ch}}} \Delta N_{\mathrm{b},k} = 0$ (the above equation strictly

holds for high rates, when the pdf of the quantization error is approximately uniform in the decision interval, which may not be representative for the typical spaceborne SAR scenarios). The power contribution σ_k^2 is estimated as the fraction of the corresponding power spectrum integrated over the processed Doppler bandwidth as

$$\sigma_k^2 = \frac{P_k}{K^2} \int_{-B_\mathrm{D}/2}^{B_\mathrm{D}/2} \left| \frac{\sin\left(\pi K \frac{f+\mathrm{PRF}(K/2-k)/K}{\mathrm{PRF}}\right)}{\sin\left(\pi \frac{f+\mathrm{PRF}(K/2-k)/K}{\mathrm{PRF}}\right)} \right|^2 df. \tag{6.4}$$

Hence, aside from the normalization factor $1/K^2$, σ_k^2 is proportional to the integral of the Dirichlet kernel of the discrete Fourier transform over the processed bandwidth B_D, scaled by the power associated to the k-th transformed coefficient P_k. This latter term, in turn, represents the contribution of the antenna pattern in the corresponding portion of the Doppler spectrum, and can be numerically estimated by means of Monte-Carlo simulations for sequences of coefficients y_k of sufficient length L_P as

$$P_k = \frac{1}{L_P} \sum_{\mathrm{p}=1}^{L_P} |y_k[\mathrm{p}]|^2. \tag{6.5}$$

Moreover, the term $\frac{K}{2}$ in the argument of the Dirichlet kernel in (6.4) implies that the DC component arises for $k = \frac{K}{2}$, which is consistent with (6.2).

As a result from (6.3), $N_{\mathrm{b},k}$ is typically a non-integer number: fractional quantization rates can be implemented by toggling the bit rate selection of an integer-bit BAQ along azimuth and/or range as introduced in Chapter 5 and in [121]. This way, higher flexibility of compression is achieved without increasing the overall scheme complexity.

6.3 Simulation Results and Bit Rate Optimization

In this context a single-platform C-band multi-channel SAR with $N_\mathrm{ch} = 8$ azimuth channels is considered, which is described in Table 6.1. Figure 6.2 shows the patterns for the transmit antenna (in blue) and a single receiver element (in red) for the considered system. Phase spoiling is applied in transmission [132], and a system $\mathrm{PRF}_\mathrm{sys}$ of 1265 Hz is selected. The actual processed bandwidth B_D is represented by the shaded orange area and is of about 5.6 kHz, which corresponds to about 55% of the effective PRF (delimited by the dashed green lines). According to these system assumptions, the azimuth raw data stream is non-uniformly sampled (i.e., the relation in (6.1) is not fulfilled), hence a reconstruction of the unambiguous Doppler spectrum needs to be carried out on ground. According to, e.g., [40], this essentially consists of N_ch linear filters that are individually applied to the subsampled signals of the receive channels and then superimposed. Figure 6.3 shows the power spectrum for the antenna pattern displayed in Figure 6.2 for the $N_\mathrm{ch} = 8$ azimuth channels, each one depicted with a different color. The effective

Table 6.1: System parameters for the considered multi-channel SAR.

Parameter	**Value**
Satellite height, h_s	700 km
Carrier frequency, f_c	5.5 GHz (C-band)
Antenna type	Planar array
Azimuth antenna length, L_a	12.8 m
Number of azimuth channels, N_{ch}	8
Pulse repetition frequency, PRF_{sys}	1265 Hz
Total processed bandwidth, B_D	5630 Hz
Target azimuth resolution, δ_a	1.2 m
Swath width, W_g	100 km
ADC Resolution	10 bits

PRF and the processed bandwidth intervals are delimited by the dashed black and red lines, respectively. For any arbitrary average rate $\bar{N}_b$, the set of quantization rates to be used for the transformed coefficients is entirely described by the array $\Delta N_b = \{\Delta N_{b,k}\}$, defined according to (6.3). For the system configuration as in Figure 6.3 one obtains

$$\Delta N_b = [-2.0, -1.3, +0.9, +0.8, +0.9, +0.8, +1.0, -1.1] \quad \text{bits/sample}, \tag{6.6}$$

i.e., the three (high-Doppler) channels depicted in black, blue and brown in Figure 6.3, respectively, will be quantized with less bits than the average rate $\bar{N}_b$, whereas, for the five channels lying in the center of the Doppler spectrum, about one bit/sample more will be allocated.

To assess the performance of the proposed MC-BAQ method the signal-to-quantization noise ratio (SQNR) has been evaluated on the focused SAR image. For this purpose, an artificial SAR scene is simulated and the raw data are generated by using the inverse focusing kernel. The multi-channel raw data are then Fourier transformed and input to the BAQ which compresses them to available bit rates. The quantized raw data are then focused back to obtain a distorted version of the original simulated image. According to the definition in (3.44), the SQNR is defined as the power ratio of the non-compressed SAR image ι, composed of P pixels, to the quantization error affecting the reconstructed SAR image $\hat{\iota}$, which is calculated as

$$\text{SQNR} = \frac{\sum_{p=1}^{P} |\iota_p|^2}{\sum_{p=1}^{P} |\iota_p - \hat{\iota}_p|^2}. \tag{6.7}$$

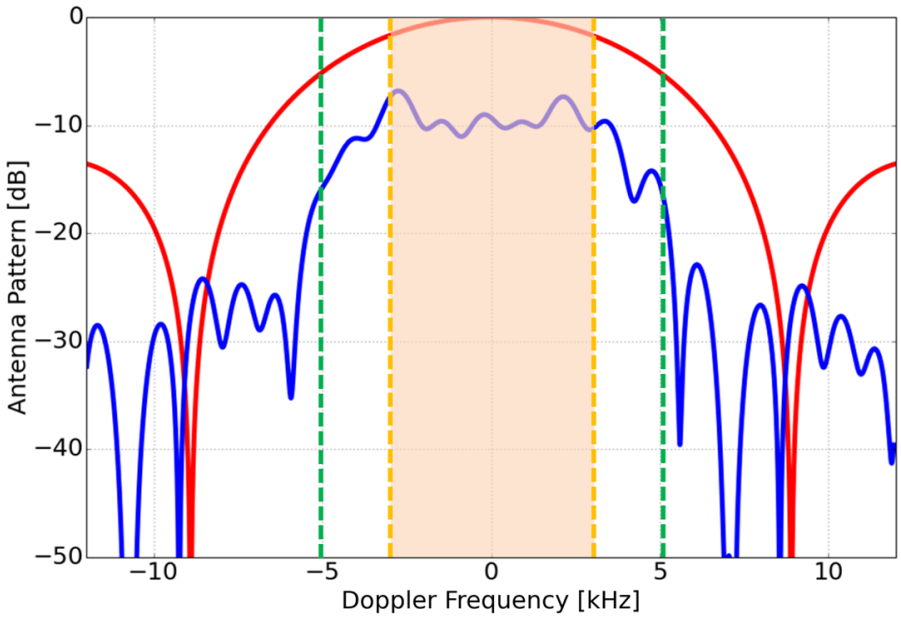

Figure 6.2: Transmit (blue) and single element receive patterns (red) versus Doppler frequency (in transmission a phase spoiled pattern is employed). The shaded orange area indicates the processed bandwidth, whereas the effective sampling bandwidth ($N_{\mathrm{ch}} \cdot \mathrm{PRF}_{\mathrm{sys}}$) is delimited by the dashed green lines.

As an example, Figure 6.4 shows the SQNR obtained for a homogeneous scene, as a function of the average rate $\bar{N}_{\mathrm{b}}$, for the system parameters in Table 6.1 and for different quantization schemes: the performance of a standard BAQ is taken as reference and is depicted in red. Then, the SQNR for the proposed MC-BAQ with the bit allocation derived from rate distortion theory (R-D) as in (6.3) is shown in turquoise: as an example, a 4-bit BAQ has the same SQNR as a 3.5-bit MC-BAQ (both around 20 dB), hence allowing for a saving of about 0.5 bits/sample. However, it could be verified that the rate sequences derived as in (6.3) do not actually correspond to the optimum ones, i.e., there exist other sets of quantization rates that lead to a better performance. A reason for this could be that the SQNR associated to the typically fractional bit rate $N_{\mathrm{b},k}$ resulting from (6.3) is a nonlinear function of the SQNR values associated to the integer BAQ rates used for its implementation according to [121], which further impacts the final performance, as it is discussed in Section 7.3. Hence, for the given system PRF, B_{D}, and antenna patterns, the optimum rate sequence has been derived by an iterative search. For this, as initial point the values obtained from R-D theory were used, and then the set of quantization rates which provides the best SQNR was found by means of iterative search. The result is shown by the green curve and dots in Figure 6.4. Again, if one considers as target performance the one obtained with a 4-bit BAQ, with the proposed MC-BAQ one would achieve a gain of about 4 dB with respect to a standard BAQ operating at the

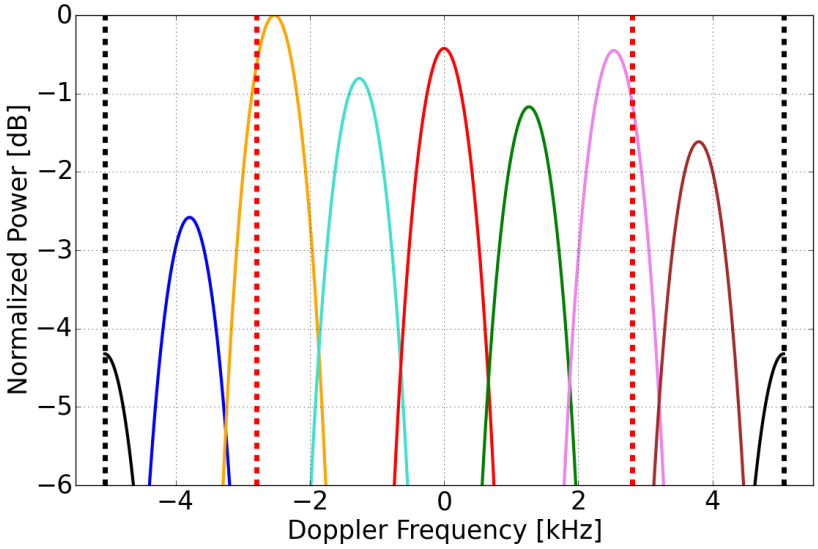

Figure 6.3: Doppler power spectrum for the $N_{\mathrm{ch}} = 8$ azimuth channels, depicted with different colors, each one scaled by the corresponding power contribution P_k, as in (6.5). The power associated to each channel σ_k^2 is estimated by integrating the corresponding power spectrum in the range between $-B_{\mathrm{D}}/2$ and $B_{\mathrm{D}}/2$ (indicated by the dashed red lines), according to (6.4). The dashed black lines delimit the PRF interval.

same rate. Alternatively, the same SQNR is shown by the MC-BAQ at 3.25 bits/sample, hence achieving a data reduction of about 18-20%. On the other hand, if a 3-bit BAQ is used as reference, the resulting data reduction is around 25%.

An example of the optimization procedure for the MC-BAQ bit rate allocation described above (i.e., the green line in Figure 6.4) is shown in Figure 6.5, which depicts the SQNR as a function of different combinations of quantization rate sets for an average rate $\bar{N}_{\mathrm{b}} = 4$ bits/sample. Based on the symmetry shown by the power channel distribution in Figure 6.3 any possible rate sequence can be described, with reasonable approximation, by means of a set of three bit rate values $\{N_{\mathrm{b,high}}, N_{\mathrm{b,mid}}, N_{\mathrm{b,low}}\}$: $N_{\mathrm{b,high}}$ (the largest rate) is associated to the five sub-bands located in the center of the Doppler spectrum of Figure 6.3, $N_{\mathrm{b,mid}}$ refers to the bit rate for the two adjacent channels (blue and brown sub-bands in Figure 6.3), and $N_{\mathrm{b,low}}$ is for the black sub-band in Figure 6.3. The latter represents the lowest rate and, once the average rate $\bar{N}_{\mathrm{b}}$ has been defined, it is uniquely determined as

$$N_{\mathrm{b,low}} = 8 \cdot \bar{N}_{\mathrm{b}} - 5 \cdot N_{\mathrm{b,high}} - 2 \cdot N_{\mathrm{b,mid}}. \tag{6.8}$$

According to this, the best SQNR, of about 23.5 dB, is achieved for

$$\{N_{\mathrm{b,high}}, N_{\mathrm{b,mid}}, N_{\mathrm{b,low}}\} = \{5.6, 2.0, 0.0\} \quad \text{bits/sample}, \tag{6.9}$$

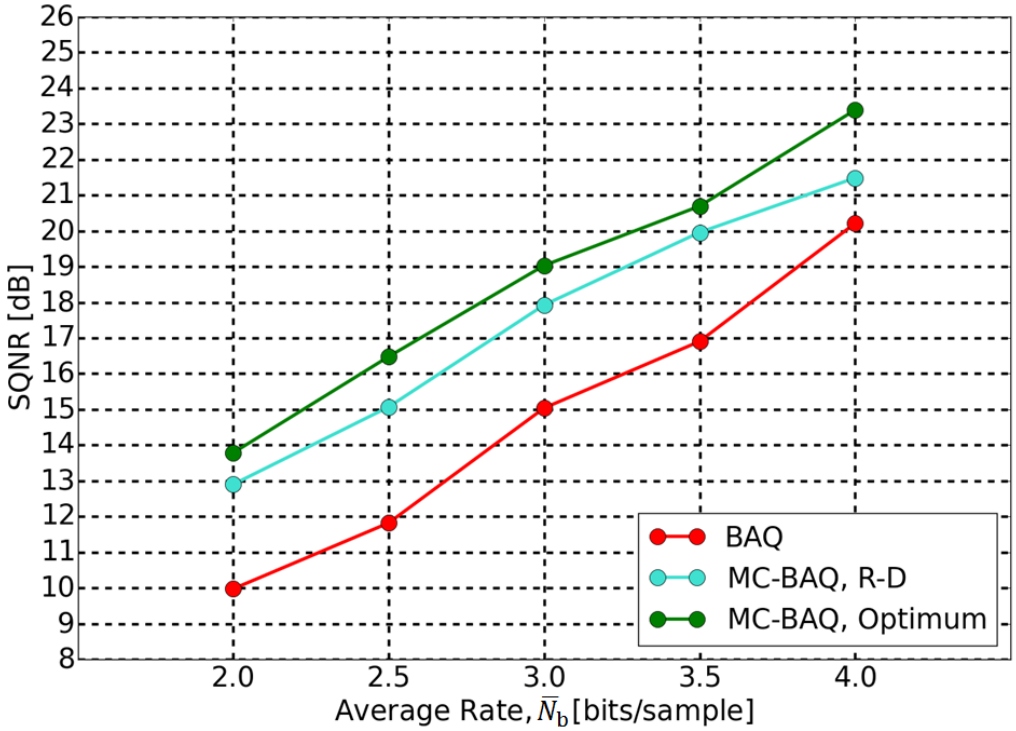

Figure 6.4: Signal-to-quantization noise ratio (SQNR) for a homogeneous scene for different quantization schemes: standard BAQ (red), MC-BAQ with bit allocation derived from rate distortion theory (R-D, turquoise), and MC-BAQ with optimum bit allocation (green), as a function of the average rate $\bar{N}_b$.

as indicated by the dashed black lines sketched in Figure 6.5. Clearly, setting $N_{b,low} = 0$ means that the corresponding DFT coefficient is just discarded on board and hence not downlinked at all.

In addition, the proposed method has been assessed for the backscatter profile depicted in Figure 6.6 in black, which shows a "jump" of 10 dB (left vertical axis) along azimuth, typically occurring over highly inhomogeneous scenes, such as, e.g., urban areas. The resulting SQNR profiles (right vertical axis) are shown for a standard BAQ in red and for the proposed MC-BAQ in green (for this, the optimum bit allocation was chosen as in Figure 6.5), and a consistent performance gain can be observed. In particular, a significant loss in terms of SQNR is observed for both compression techniques in the part of the low backscatter area (with a mean backscatter of -10 dB) close to the high backscatter one. This is due the masking effect which is induced by the presence of high backscatter targets within a distance comparable to the synthetic aperture L_s [94], [103] (for the considered system, L_s is in the order of a few tens of kilometers). As already pointed out, the performance of the proposed method strongly depends on the

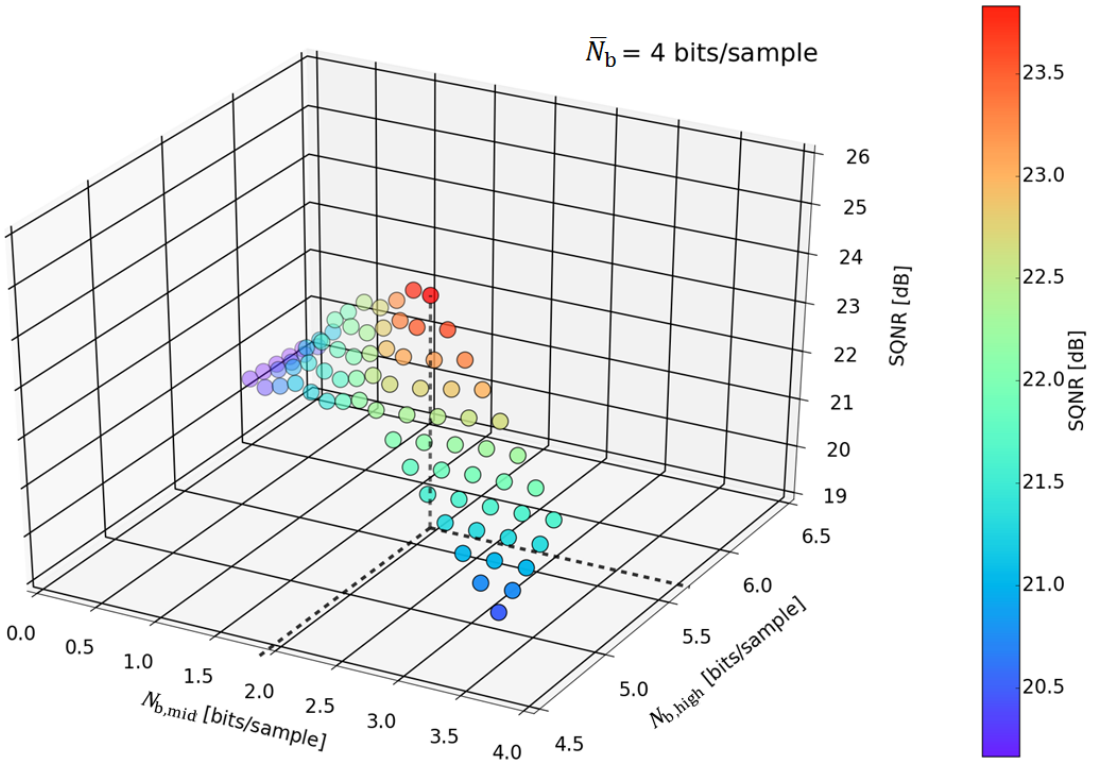

Figure 6.5: SQNR for different combinations of quantization rates applied for the proposed MC-BAQ for $\bar{N}_b = 4$ bits/sample. Based on the symmetry shown by the power channels distribution in Figure 6.3, any sequence is approximated by a set of three bit rates $\{N_{b,high}, N_{b,mid}, N_{b,low}\}$, each one associated to different Doppler sub-bands of Figure 6.3. The dashed black lines indicate the maximum SQNR, of about 23.5 dB, which is achieved by setting $N_{b,high}$= 5.6 bits/sample and $N_{b,mid}$ = 2 bits/sample.

oversampling factor $o_f = PRF_{eff}/B_D$, i.e., the closer o_f is to one, the lower the resulting gain. Different values of o_f have been considered by varying the processed bandwidth only. As an example, for $o_f = 1.67$ the data rate can be reduced by about 0.5 bits/sample, whereas for $o_f = 1.43$ only a negligible SQNR gain is obtained with respect to a nominal BAQ, making the proposed method not suitable for data reduction purposes. On the other hand, the number of azimuth receiving channels N_{ch} also plays a key role in determining the achievable performance of MC-BAQ: the larger N_{ch} is, the better the power spectrum of the transformed coefficients (shown in Figure 6.3 for $N_{ch} = 8$) approximates the actual one, hence more accurate bit allocation and ultimately more effective data reduction can be achieved. Regarding the required onboard complexity, the proposed multi-channel compression technique can be performed in real time by using a state-of-the-art FPGA without excessive memory storage and retrieval capability. For the implementation of

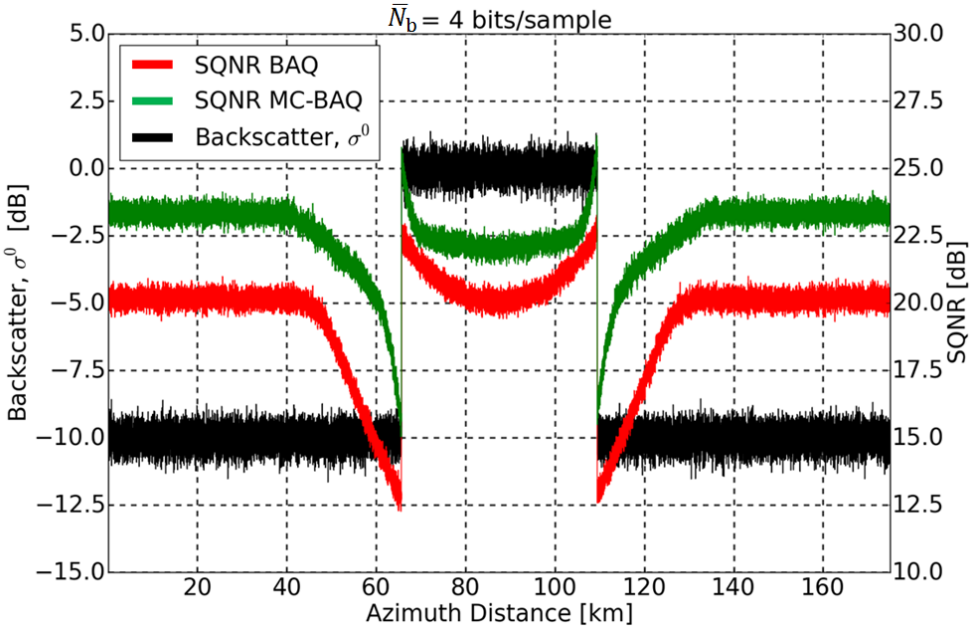

Figure 6.6: Backscatter profile (σ^0, in black) and corresponding SQNR as a function of the azimuth distance for BAQ (red) and MC-BAQ (green) for an average rate $\bar{N}_b$ of 4 bits/sample. The performance gain obtained with the proposed method can be exploited to reduce the resulting data rate.

a N_{ch} points DFT (being N_{ch} the number of azimuth channels) a limited amount, in the order of a few tens, of additional operations N_{op} is required for each multi-channel data block (consisting, in this case, of N_{ch} samples), being $N_{op} = \mathcal{O}\left(N_{ch} \cdot \log_2\left(N_{ch}\right)\right)$.

6.4 Chapter Summary

In this chapter a novel method for onboard data volume reduction for multi-channel SAR systems has been proposed. Such systems require the acquisition of an increased volume of data in order to achieve high-resolution imaging of a wide swath width. The suggested approach exploits the intrinsic correlation exhibited by the received multi-channel SAR raw data samples. For this purpose, a discrete Fourier transform combined with an optimized selection of the quantization rates is applied to the multi-channel azimuth data samples. Simulations are carried out for a single-platform C-band system with eight azimuth receive channels, and for different SAR backscatter distributions, showing that with the proposed method a data volume reduction of 20%-25% can be achieved for typical BAQ rates employed for SAR applications. Future studies will include the inves-

tigation of alternative orthogonal transformations and the detailed analysis of different system configurations, in terms of, e.g., antenna patterns, number of azimuth channels, and required processed bandwidth and PRF. MC-BAQ can also be exploited in the context of polarimetric SAR data, by applying it on each polarization channel independently. Since the power spectrum of the azimuth antenna pattern is approximately the same for all polarization channels, one could practically employ the same set of bit rates $\{N_{\mathrm{b},k}\}$ for each of the available polarimetric combinations. Finally, the proposed method could be extended to multiple transmit pulses by combining transform coding in the Doppler domain with alternative compression schemes such as, e.g., vector quantization [92], to achieve a more effective data reduction.

7 Predictive Quantization for Data Volume Reduction in Staggered SAR Systems

Staggered synthetic aperture radar (SAR) is an innovative SAR acquisition concept which exploits digital beamforming (DBF) in elevation to form multiple receive beams and continuous variation of the pulse repetition interval to achieve high-resolution imaging of a wide continuous swath. Staggered SAR requires an azimuth oversampling higher than a SAR with constant PRI, which results in an increased volume of data. In this chapter the use of linear predictive coding is investigated, which exploits the correlation properties exhibited by the non-uniform azimuth raw data stream. According to this, a prediction of each sample is calculated on board as a linear combination of a set of previous samples. The resulting prediction error is then quantized and downlinked (instead of the original value), which allows for a reduction of the signal entropy and, in turn, of the onboard data rate achievable for a given target performance. In addition, the a priori knowledge of the gap positions can be exploited to dynamically adapt the bit rate allocation and the prediction order to further improve the performance. Simulations of the proposed dynamic predictive block-adaptive quantization (DP-BAQ) are carried out considering a Tandem-L-like staggered SAR system for different orders of prediction and target scenarios, demonstrating that a significant data reduction can be achieved with a modest increase of system complexity. The proposed method has been first investigated in [133] and [134], and then further elaborated in [101].

7.1 Introduction

Nowadays, synthetic aperture radar (SAR) represents a well-recognized technique for a broad variety of remote sensing applications, being able to acquire high-resolution images of the Earth's surface independently of daylight and weather conditions. However, conventional SAR is constrained by the pulse repetition frequency (PRF) for the imaging of wide swaths and, at the same time, of fine azimuth resolutions. To overcome these limitations, in the last decades innovative spaceborne radar techniques have been proposed, which allow for high-resolution imaging of a wide swath by exploiting multiple azimuth channels (MAC) and digital beamforming (DBF) in elevation to achieve Scan-on-Receive (SCORE) [40], [54], [55], [56], [57], [58]. Alternatively, single-channel SAR based on the simultaneous recording of multiple echo pulses received from different elevation directions (so-called "multibeam" mode) [135], [136] enables a further increase of the imaged area by keeping the antenna length within reasonable limits and avoiding the employment of burst modes. Such systems are still limited by the presence of blind ranges across the swath, which arise since the radar cannot receive while transmitting. The opportunity of exploiting the variation of the PRI to solve the blind ranges problem

was first independently proposed in [137] and in [135], [138]. Then, the idea culminated in the staggered SAR concept, which includes a refined design of the PRI sequences, the use of proper interpolation on the raw data and consideration of the ambiguities [41], [102], [139], [140]. By cyclically changing the pulse repetition interval (PRI), staggered SAR allows to vary (i.e., to "stagger") the range positions of such data gaps along the azimuth dimension. In this way, high-resolution imaging of a large continuous swath of up to 350 km without the need for a long antenna with multiple apertures becomes possible [41].

The requirement on swath width and resolution, together with the use of large bandwidths and multiple acquisition channels, is clearly associated to the generation of a large volume of data, which implies, from the mission design point of view, stringent requirements in terms of onboard memory and downlink capacity. In the context of single-channel staggered SAR systems, a method consisting of an interpolation combined with low-pass Doppler filtering and decimation of the acquired raw data has been proposed in [102], [128], which allows for achieving a data reduction of up to 50% at the cost of a significant onboard computational effort. In this scenario, SAR raw data quantization represents an aspect of utmost importance, since the number of bits employed to digitize the recorded radar signal, on the one hand, directly affects the performance of the resulting SAR products and, on the other hand, defines the total amount of data to be managed by the system.

Conventional SAR raw data usually show very little correlation among nearby samples, which, therefore, can be only partially used for compression algorithms. On the other hand, in staggered SAR a significant azimuth oversampling is mandatory to properly reconstruct the information lost within the blind ranges [102]. The resulting data redundancy can be exploited to reduce the data volume to be acquired and stored on board.

This chapter addresses the use of linear predictive coding for onboard data reduction in staggered SAR systems. Linear predictive coding [85] exploits the existing correlation between adjacent azimuth samples, i.e., samples which are located at successive range lines and within the same range bin. Such a correlation is introduced by the antenna pattern and a significant azimuth oversampling: a prediction of each sample is estimated on board through a linear combination of a set of previously received samples in the azimuth dimension. The resulting prediction error is characterized by a signal entropy which is smaller than the one of the original SAR raw data. This allows for a reduction of the number of quantization bits for a given target performance, at the cost of a modest computational burden. Moreover, the proposed method preserves the nonuniform sampling of the staggered SAR data, allowing for the use of more advanced processing techniques on ground, which would be more difficult to apply to resampled raw data as proposed, e.g., in [141]. The use of predictive quantization in the context of conventional SAR has been previously investigated in [142], [143].

The chapter is organized as follows: the proposed method for data volume reduction

based on linear predictive quantization, its detailed mathematical formulation, and application for onboard data volume reduction in staggered SAR are discussed in Section 7.2. Moreover, a strategy to effectively reconstruct the blind ranges, through a dynamic selection of the prediction order together with a variable bit allocation in the vicinity of the gap position, is proposed as well. Simulations for different orders of prediction and different target scenarios are presented in Section 7.3 for a Tandem-L-like staggered SAR system and demonstrate the effectiveness of the proposed compression scheme. Finally, Section 7.4 concludes the chapter with a summary and further research outlook.

7.2 Dynamic Predictive Block-Adaptive Quantization

7.2.1 SAR Signal Statistical Characterization

It is well known that the In-phase (I) and Quadrature (Q) components of the received SAR raw signal $x(t)$ can be described as zero-mean Gaussian stationary and independent processes with a slowly changing variance in both range and azimuth directions [144]. This assumption holds as a consequence of the central limit theorem (CLT) and is almost independent of the type of spaceborne SAR sensor used (frequency, resolution) as well as of the characteristics of the scene under illumination: indeed, a very large number of targets overlap their response in the raw data domain within the imaged scene. This is due, in turn, to the large extension on ground of the azimuth antenna footprint and of the range pulse, which, for the considered spaceborne SAR systems, are in the order of several kilometers. The samples of the SAR raw azimuth signal, received at different time instants, can be modeled as partially correlated random variables. Such a correlation is introduced by the azimuth antenna pattern (or Doppler spectrum) and by the selected pulse repetition frequency (PRF), and can be described by the normalized autocorrelation function $R_x(\tau)$ as

$$R_x(\tau) = \mathbb{E}\{x^*(t) \cdot x(t+\tau)\} / \mathbb{E}\{|x(t)|^2\}, \tag{7.1}$$

where τ represents the time lag in the azimuth dimension. Correlation in the range dimension is not considered here due to the negligible data oversampling (indeed, the range bandwidth is typically sharply limited and only a small oversampling is usually employed). The azimuth autocorrelation function can be expressed as the inverse Fourier transform of the Doppler power spectral density $P_x(f)$

$$R_x(\tau) = \mathcal{F}^{-1}\{P_x(f)\}, \tag{7.2}$$

where f is the Doppler frequency. If a uniformly illuminated rectangular azimuth aperture of length L_a is considered, the power spectral density can be expressed as [145], [131]

$$P_x(f) = X(f)X^*(f) = \sin^4\left(\pi \frac{L_\mathrm{a}}{2v_\mathrm{s}} f\right) \Big/ \left(\pi \frac{L_\mathrm{a}}{2v_\mathrm{s}} f\right)^4, \tag{7.3}$$

being $X(f)$ the spectrum of $x(t)$ and v_s the satellite velocity. The above equation allows for the derivation of the autocorrelation in closed form as [145]

$$R_x(\tau) = \begin{cases} \frac{3}{4}(B_R \cdot \tau)^3 - \frac{3}{2}(B_R \cdot \tau)^2 + 1 & 0 \leq \tau \leq \frac{1}{B_R} \\ -\frac{1}{4}(B_R \cdot \tau - 2)^3 & \frac{1}{B_R} \leq \tau \leq \frac{2}{B_R} \\ 0 & \text{elsewhere.} \end{cases} \tag{7.4}$$

In the above equation B_R represents the bandwidth of the spectral power density function and is defined as

$$B_R = \frac{2v_\mathrm{s}}{L_\mathrm{a}}. \tag{7.5}$$

Hence, longer antennas give a more directive beam, which can be considered as a narrower low-pass filter in the Doppler domain. On the other hand, a lower satellite velocity results in a higher correlation time, since, for a given time lag τ, two targets will be more overlapped in the raw data space and therefore more similar to each other.

It is worth pointing out that the function in (7.4) represents the correlation which is introduced by the system for a white noise input. Indeed, there could be additional correlation due to the properties of the scene under illumination (e.g., point-like targets). Hence, using only the system-induced correlation also represents a sort of worst case scenario, i.e., assuming fully developed speckle.

As already mentioned, for staggered SAR systems a certain azimuth oversampling is necessary to properly recover the raw data information in the neighborhood of gaps introduced during the SAR acquisition. The azimuth oversampling factor o_f is defined as the ratio between the pulse repetition frequency and the processed Doppler bandwidth, $o_\mathrm{f} = \mathrm{PRF}/B_\mathrm{D}$. In this scenario, a compression algorithm based on differential pulse code modulation (DPCM) is proposed, which aims at exploiting the correlation exhibited by adjacent azimuth samples by encoding, instead of the original raw data sample, the difference between the original one and its prediction. This allows for a reduction of the signal dynamic (i.e., its entropy), and hence for a decrease of the required bit rate for a given quantization performance [85]. By having a priori information on the raw signal statistics, a proper design of the predictor can be implemented, as it is detailed in the following.

7.2.2 Mathematical Formulation and Algorithm Implementation

Let $x[\mathrm{n}]$ be the raw azimuth sample received by the SAR system at the discrete time instant n. According to the linear prediction theory, the estimate of the sample $x[\mathrm{n}]$, $\tilde{x}[\mathrm{n}]$, is a linear combination of its N_P preceding samples

$$\tilde{x}[\mathrm{n}] = \sum_{k=1}^{N_\mathrm{P}} \beta_k \, x[\mathrm{n\text{-}k}], \tag{7.6}$$

where N_P defines the so-called prediction order, while β_k is the weight associated to the k-th previous sample $x[\mathrm{n}-\mathrm{k}]$. From this, the prediction error $\varepsilon[\mathrm{n}]$ is defined as

$$\varepsilon[\mathrm{n}] = x[\mathrm{n}] - \tilde{x}[\mathrm{n}]. \tag{7.7}$$

The set of weights $\boldsymbol{\beta} = \{\beta_1, \beta_2, ..., \beta_{N_\mathrm{P}}\}$ is chosen to minimize the mean square prediction error and is derived as [85]

$$\boldsymbol{\beta} = \boldsymbol{C}^{-1}\boldsymbol{\rho}, \tag{7.8}$$

where $\boldsymbol{C} \in \mathbb{R}^{N_\mathrm{P} \times N_\mathrm{P}}$ is the covariance matrix of the random process $x[\mathrm{n}]$ and is populated by the correlation values among the N_P preceding samples used for the prediction (i.e., considering two samples at discrete time instants i and j,

$$C_{i,j} = R_x\big[|i-j| \cdot \mathrm{PRI}\big]. \tag{7.9}$$

Furthermore, $\boldsymbol{\rho} \in \mathbb{R}^{N_\mathrm{P}}$ represents the vector of the correlation values between the N_P previous samples and the sample to be predicted at the time instant n, i.e.,

$$\rho_k = R_x\big[k \cdot \mathrm{PRI}\big]. \tag{7.10}$$

The encoding process is shown in Figure 7.1. The prediction error $\varepsilon[\mathrm{n}]$, derived as in (7.7), is given as input to the block-adaptive quantizer (block "BAQ"). The quantized prediction error $\varepsilon_\mathrm{q}[\mathrm{n}]$ is the information which is actually downlinked to the ground, but it is also used on board in a feedback loop, together with the sample prediction $\tilde{x}[\mathrm{n}]$, in order to obtain a quantized version of the true input signal $\hat{x}[\mathrm{n}]$ as

$$\hat{x}[\mathrm{n}] = \tilde{x}[\mathrm{n}] + \varepsilon_\mathrm{q}[\mathrm{n}]. \tag{7.11}$$

This quantity, in turn, is then used as input for the prediction of the next sample. The decoding process is shown in Figure 7.2: the received signal is first decoded (block "BAQ^{-1}") and then the same prediction loop is implemented to finally get a quantized version of the original SAR raw data sample $\hat{x}[\mathrm{n}]$ as in (7.11). It is worth to point out that the prediction block takes as input the quantized version of the prediction error. In this way, the exact same sample value $\varepsilon_\mathrm{q}[\mathrm{n}]$ is employed both, at encoding and decoding stage, hence avoiding stability problems due to the propagation and accumulation of reconstruction errors in the feedback loop. The scheme depicted in Figure 7.1 and Figure 7.2 refers to a prediction order $N_\mathrm{P} = 1$. Obviously, if $N_\mathrm{P} > 1$ a corresponding number of preceding samples needs to be used for prediction in the feedback loop as in (7.6).

It is worth to point out that, for the present investigations, a causal predictor has been considered, i.e., only preceding samples are used in the prediction process, according to (7.6). A causal filter represents the simplest prediction scheme, which minimizes the required onboard storage and computational effort, if compared to other predictor types

and, e.g., the alternative method proposed in [128]. For a causal predictor, the decoder reconstructs each sample by using the information (i.e., the quantized prediction errors) received at previous time instants, and both the encoding and decoding loops are implemented by a recursive filter, as shown in Figure 7.1 and Figure 7.2. Equivalently, an anti-causal filter could be also employed: in this case, the encoder cannot operate in real time (since it needs first to "wait" for the future samples needed for the prediction), hence requiring an increased onboard complexity for its implementation. Then, the decoder reconstructs the data stream from the last received sample to the first one (i.e., "in the opposite direction" with respect to a causal prediction scheme). A causal predictor achieves the same performance gain of an anti-causal one of the same order, being the autocorrelation of the SAR raw signal an even function, and both require, for their implementation, the storage in the onboard memory of at least of two range lines at a time, i.e., one for the prediction and the actual one for calculating the prediction error.

Different is the scenario represented by a non-causal filter, where both past and future samples are exploited in the prediction process, and at least three range lines need to be stored at a time (i.e., two for the prediction and the actual one for calculating the prediction error). Similarly to an anti-causal predictor, a non-causal filter must wait for future sample(s) to derive the corresponding prediction value, hence requiring an increased implementation complexity. For this, a relevant issue is represented by the fact that, if for a causal predictor the samples used for the prediction are, in their turn, the result of a prediction and quantization operation within the recursive loop (as in Figure 7.1), this is not true for a non-causal predictor: here, the future samples employed in the prediction filter are used "as is", whereas, at decoding stage, only the quantized version of the prediction errors is available. This inconsistency between the information available at the encoding stage and the one available at the decoding stage must be carefully taken into account in order to avoid stability problems in the reconstruction loop due to possible error propagation caused by quantization. Moreover, for a non-causal predictor the reconstruction process cannot be carried out "sample by sample" (differently from a causal or an anti-causal filter), but must be approached as a linear equations system, where each equation represents the linear combination of the preceding/following samples (this operation requires additional processing effort on ground, which, however, does not represent a critical aspect). To conclude, non-causal prediction can in principle be used for data volume reduction in a staggered SAR system. However, the possible performance improvement with respect to a causal or an anti-causal predictor, which is implied by the better exploitation of the correlation between neighboring samples, must be traded by taking into account the increased scheme complexity and the larger number of samples to be stored on board, and by considering the impact of all the aforementioned aspects. These will be addressed in details in future research studies and investigations.

The performance gain G_{N_P} obtained with a $N_\mathrm{P}^{\mathrm{th}}$-order predictor is expressed as the ratio between the variance of the prediction error $\sigma^2_{\varepsilon,N_\mathrm{P}}$ and the one of the input signal

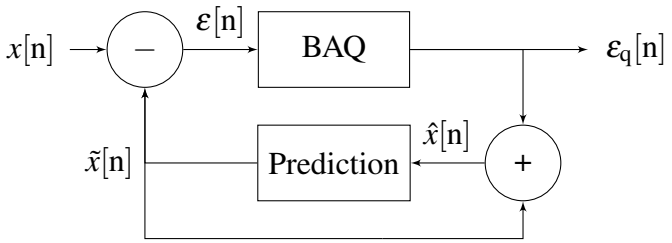

Figure 7.1: Predictive quantization encoding scheme.

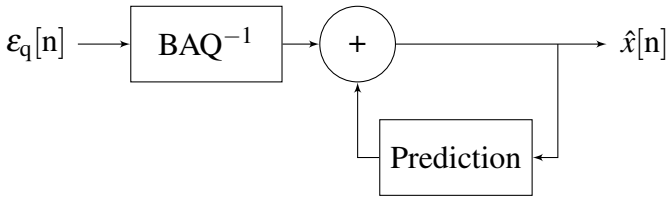

Figure 7.2: Predictive quantization decoding scheme.

σ_x^2 [85], [84]

$$G_{N_\mathrm{P}} = \frac{\sigma_{\varepsilon,N_\mathrm{P}}^2}{\sigma_x^2}, \tag{7.12}$$

that is, the smaller the dynamic of the prediction error (i.e., its entropy), the larger the resulting coding gain.

Since the prediction error is obtained as a linear combination of N_P Gaussian random variables (see Section 7.2.1), according to (7.6) and (7.7), $\varepsilon[\mathrm{n}]$ is also Gaussian (this is strictly true if no quantization is applied in the recursive loop, but holds in practice with reasonable accuracy). The Gaussian nature of the prediction error implies that a reduction of the signal dynamic, achieved by means of the prediction process, results in a decrease of its information entropy. For a given set of system parameters, this allows for the derivation, in closed form, of the prediction gain G_{N_P}, by estimating the standard deviation of the prediction error $\sigma_{\varepsilon,N_\mathrm{P}}$ and substituting it into (7.12). Let us consider the simplest case of a 1$^{\mathrm{st}}$-order predictor, where $N_\mathrm{P} = 1$ and the previous sample only is used in the prediction filter. According to the notation used in (7.7), the random variable $\mathcal{E}$ is obtained as the difference between the random variables X and $\tilde{X}$ as

$$\mathcal{E} = X - \tilde{X} \sim \mathcal{N}\big(0, \sigma_X^2 + \sigma_{\tilde{X}}^2 - 2\rho_1 \cdot \sigma_X\, \sigma_{\tilde{X}}\big), \tag{7.13}$$

being ρ_1 the autocorrelation value obtained for the time lag $\tau = \mathrm{PRI}$, according to (7.10), where, in turn, $R_x(\tau)$ is expressed in (7.4). By modeling the input signal as a stationary

random process (i.e. its unconditional probability distribution does not change in time), due to the weighting introduced in the prediction process, it follows that

$$\sigma_{\tilde{X}} = \beta_1 \sigma_X. \tag{7.14}$$

According to (7.8), $\beta_1 = \rho_1$ (being $C_{1,1} = 1$, see (7.9)) and the variance of the prediction error in (7.13), $\sigma^2_{\varepsilon,N_\mathrm{P}=1}$, can be further simplified as

$$\sigma^2_{\varepsilon,N_\mathrm{P}=1} = \sigma^2_X\left(1-\rho_1^2\right). \tag{7.15}$$

By substituting (7.15) in (7.12), the prediction gain for a 1$^{\mathrm{st}}$-order predictor can be finally expressed as

$$G_1 = (1-\rho_1^2)^{-1}. \tag{7.16}$$

The prediction gains G_{N_P} for $N_\mathrm{P} = \{2,3,4\}$ are derived by following the same procedure and are expressed as

$$G_2 = (1+\beta_1^2+\beta_2^2+2\rho_1(\beta_1\beta_2-\beta_1)-2\rho_2\beta_2)^{-1}, \tag{7.17}$$

$$\begin{aligned} G_3 =& [1+\beta_1^2+\beta_2^2+\beta_3^2+ \\ &+2\rho_1(\beta_1\beta_2+\beta_2\beta_3-\beta_1)+ \\ &+2\rho_2(\beta_1\beta_3-\beta_2)-2\rho_3\beta_3]^{-1}, \end{aligned} \tag{7.18}$$

$$\begin{aligned} G_4 =& [1+\beta_1^2+\beta_2^2+\beta_3^2+\beta_4^2+ \\ &+2\rho_1(\beta_1\beta_2+\beta_2\beta_3+\beta_3\beta_4-\beta_1)+ \\ &+2\rho_2(\beta_1\beta_3+\beta_2\beta_4-\beta_2)+ \\ &+2\rho_3(\beta_1\beta_4-\beta_3)-2\rho_4\beta_4]^{-1}. \end{aligned} \tag{7.19}$$

The weights $\{\beta_n\}$ are obtained from (7.8) for each prediction order. Their expression as function of the autocorrelation values $\{\rho_n\}$ is not included in the above equations to avoid large formulations.

For data digitization, a block-adaptive quantizer (BAQ) is considered, which, as it has been already mentioned, exploits the input signal statistics to perform a block-wise quantization of the SAR raw data [38]. Hence, the encoding/decoding schemes pictured in Figure 7.1 and Figure 7.2 are implemented on samples located in successive range lines and for blocks of N_block range samples: first, the prediction process is carried out for each of the N_block range samples (i.e., located at N_block consecutive range bins) independently;

then, once the difference from the data block and its prediction has been calculated sample by sample for each range bin, the BAQ adapts the quantization levels to the statistics of the corresponding prediction error block, and a Cartesian scheme is usually implemented, i.e., the I and Q components of the complex raw signal are separately treated and quantized.

7.2.3 Gap Considerations

The location of blind ranges (gaps) along the azimuth dimension of a staggered SAR acquisition and their range extension is related to the specific PRI sequence employed, and is therefore known a priori (i.e., at commanding time). This valuable information can be exploited to dynamically optimize the bit rate allocation and to adapt the prediction process for the samples located in the gap vicinity, in order to better recover the missing information and, ultimately, to improve the overall signal reconstruction quality. The left-hand side of Figure 7.3 shows a hypothetical distribution of the blind ranges (black rectangles) within a staggered SAR acquisition. The range and azimuth dimensions are indicated at the bottom-left of the figure. Each vertical stripe represents a single range line, while each gap region ideally extends by many hundreds of samples along the range dimension. In particular, if elaborated non-uniform PRI sequences are employed, gaps can be displaced in range such that two consecutive azimuth samples at the same range are never missed [102]. The right-hand side of Figure 7.3 shows a zoom of the raw data matrix which is affected by a blind range (in black). Each cell corresponds to a raw data sample. The proposed technique is implemented by jointly applying a variable bit rate allocation (which is provided in each box; N_b represents the mean bit rate in bits/sample) together with a dynamic selection of the prediction order in the gap vicinity. In particular, the order of the prediction filter is dynamically set as indicated on the right-hand side of Figure 7.3. The first azimuth sample after the gap is quantized by means of a standard BAQ (i.e., no prediction is applied). Then, the following sample (in red) is encoded through a 1^{st}-order predictor (P-BAQ), which exploits the information carried out by the previous sample only. The next one (in green) is then encoded through a 2^{nd}-order predictor (in general, the n-th sample after the gap is encoded with a predictor filter of order n-1). The operation is repeated until the operative prediction order N_P is reached, where N_P is defined at system design stage as trade off between system complexity and achievable prediction gain (this relevant aspect will be further detailed in the next section). The described precaution, which consists of an adaptive selection of the order of the prediction filter (as sketched by the different colors on the right-hand side of Figure 7.3), aims at excluding the missing samples in the prediction process, hence allowing for a better signal reconstruction. Indeed, the prediction filter is designed under the assumption that the SAR raw data can be modeled as a stationary random process, and therefore the gaps are in principle not taken into account in the weight definition in (7.8). If, on the other hand, a constant $N_\mathrm{P}^{\mathrm{th}}$-order predictor were used, this would result in a larger prediction

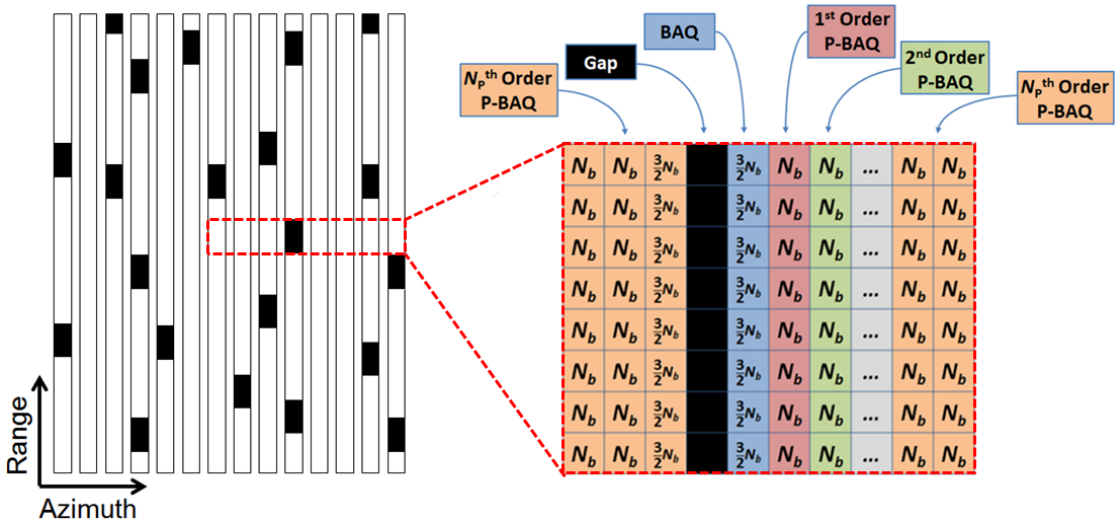

Figure 7.3: (Left) Distribution of the blind ranges (black rectangles) within a staggered SAR acquisition. Each gap region typically extends by several hundreds of samples in the range direction. (Right) Zoom-in of a raw data region affected by gaps. Each cell corresponds to a raw data sample. The proposed method is implemented by jointly applying a variable bit rate allocation (indicated in each box, where N_b represents the mean bit rate in bits/sample) together with a dynamic selection of the prediction order (depicted with different colors and shown on the top of the figure) in the gap vicinity.

error, hence degrading the performance gain in (7.12).

Possible non-stationarities may be caused by temporal changes of the target during the integration time, which, for typical spaceborne SAR systems, are in the order of a few seconds. Such a temporal decorrelation leads to an increase of the Doppler bandwidth and, in turn, to a worsening of the performance (e.g., defocusing) in the resulting SAR image. However, in the present scenario, azimuth samples which are only a few PRI intervals apart are used in the prediction filter. Even for a very long predictor of, e.g., 10^{th} order ($N_\mathrm{p} = 10$), a maximum time lag $\Delta t = N_\mathrm{p} \cdot \mathrm{PRI} \approx 3.7$ ms is obtained, which is much shorter than the decorrelation time typically observed for any kind of vegetation imaged at X band at moderate to high wind speeds, as discussed in [146].

Regarding the variable bit rate allocation to be applied in the gap vicinity, it is worth noting that the bits originally used for a missing sample could be ideally not downloaded at all, i.e., 0 bits are used. Indeed, it could be verified that the best way to exploit the gained N_b bits is, as expected, to allocate them, in equal measure, before and after the gap (i.e., a "distributed" bit allocation), leading to the $N_\mathrm{b} + \frac{1}{2}N_\mathrm{b} = \frac{3}{2}N_\mathrm{b}$ bits/sample for

Table 7.1: Bit allocation applied to the samples in the gap vicinity.

bit rate	**before gap**	**on gap**	**1st after gap**	**2nd after gap**	**3rd after gap**
2	3	0	3	2	2
3	4	0	4	4	3
4	6	0	6	4	4
6	8	0	8	8	6

the samples in the gap vicinity on the right-hand side of Figure 7.3. Since the BAQ operates at certain integer bit rates, the actual bit allocation in the neighborhood of a gap is defined in Table 7.1 for bit rates of 2, 3, 4, and 6 bits/sample, which are indicated in the first column of the table.

To obtain focused images, staggered SAR raw data need to be first interpolated on a uniform grid. For this purpose, a Best Linear Unbiased (BLU) interpolation is employed [41], [128], which exploits the correlation between neighbouring azimuth samples to optimally estimate the values on the output grid and to reconstruct the gap samples. This efficient allocation allows for a consistent mitigation of the errors introduced by the combined effect of quantization and interpolation. Indeed, it has been verified that this simple but effective strategy allows for a quality of the reconstructed signal (in terms of error power) which is practically equivalent to the one obtained for gap-free data.

The proposed method jointly exploits a dynamic bit rate allocation and a variable prediction order in the gap vicinity and is therefore named dynamic predictive block-adaptive quantization (DP-BAQ), whose effectiveness for data volume reduction is demonstrated in the next section for a real mission scenario.

7.3 Simulation Results

Staggered SAR is currently considered as the baseline acquisition mode for Tandem-L, a DLR proposal for a highly innovative L-band single-pass interferometric and fully polarimetric radar satellite mission to monitor dynamic processes on the Earth surface [37], [105]. A list of the system parameters for the Tandem-L mission is given in Table 7.2. In order to assess the proposed method for data volume reduction, simulations of SAR raw data for a Tandem-L-like system in single-pol staggered SAR mode have been carried out, and the performance of different data compression algorithms has been compared.

The azimuth pattern of the Tandem-L reflector antenna, with a diameter of 15 m, can be well approximated by the one generated by a planar array with uniform aperture and azimuth length $L_\mathrm{a} = 10$ m [41]. For the present analyses, the planar approximation has

Table 7.2: Tandem-L system parameters.

Parameter	**Value**
Orbit height, h_s	745 km (@ equator)
Carrier frequency, f_c	1.25 GHz (L band)
Polarization	single/dual/quad
Horizontal baselines	800 m ... 20 km
Revisit time	16 days
Range bandwidth, B_{rg}	up to 84 MHz
Mean (staggered) PRF	2700 Hz
Doppler bandwidth, B_D	1130 Hz
Azimuth resolution, δ_a	7 m
Swath width, W_g	175 km (quad) ... 350 km (single/dual)
Raw data quantization	BAQ @ 4 bits/sample
Downlink capacity	$\sim$8 Terabyte/day
Reflector diameter	15 m
Mission lifetime	10 years

been considered since it allows for the expression of the theoretical autocorrelation function in closed form as in [131], and which is shown in Figure 7.4 as a function of the time lag, $R_x(\tau)$ (in red). For Tandem-L, the mean PRI is about 0.37 ms, hence leading to a correlation between adjacent azimuth samples of about 0.67, which is identified by the dashed black lines in the figure. As introduced in Section 7.1 and summarized in Table 7.2, such a high correlation is caused by the large system oversampling $o_f = \mathrm{PRF}/B_D \sim 2.39$ (i.e., the data volume to be downlinked increases by almost 140%), which is required for the proper staggered SAR operation.

Figure 7.5 shows the theoretical gain as a function of the PRF up to the 6^{th}-order predictor, derived as in (7.16)-(7.19). For this, a constant (i.e., not staggered) PRF has been employed. As expected, the larger the PRF, the larger the correlation among the raw data samples, the higher the resulting prediction gain. In particular, the upper boundary of the prediction gain strictly depends on the system characteristics (i.e., antenna size and shape of the azimuth antenna pattern, satellite velocity, and PRF, according to (7.3)-(7.5)), which directly affect the values of the correlation array $\boldsymbol{\rho}$ and of the covariance matrix $\boldsymbol{C}$. These, in turn, define the resulting gains according to the mathematical expression in (7.8) and (7.16)-(7.19). The best achievable prediction gain can therefore be numerically estimated once the specific system parameters are set (for a given PRF, the

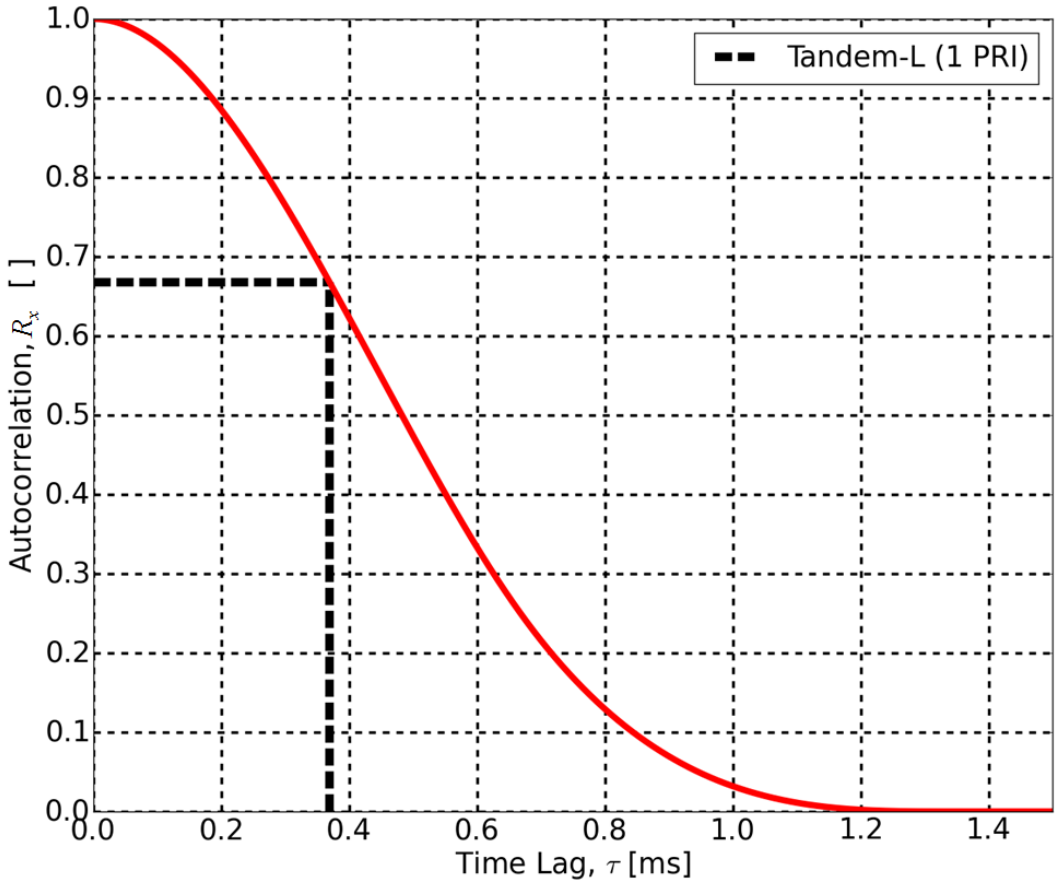

Figure 7.4: Theoretical autocorrelation of the azimuth SAR raw data as a function of the mutual time shift τ. For Tandem-L the mean PRI is of about 0.37 ms, which leads to a correlation of about 0.67 between adjacent azimuth samples (dashed black lines).

gains practically saturate beyond a certain prediction order). The oscillating behavior shown by the higher order predictors is due to the inversion of the covariance matrix $\boldsymbol{C}$ for the weights derivation in (7.8), in presence of very low correlation values: indeed, an N_p-order prediction gain G_{N_p} starts to increase again when a not negligible correlation value of the same order (i.e., ρ_{N_p} derived as in (7.10)) is obtained for the corresponding PRF value.

The mean PRF of the single polarization mode of Tandem-L is 2700 Hz and is indicated by the dashed black line. For this, the prediction gain ranges between 2.5 dB and 5 dB for predictors up to the 4^{th} order (red curve), whereas for higher orders no significant additional gain is obtained.

Let us now focus on the staggered SAR case. Figure 7.6 shows the PRI sequence which has been employed for the present simulations. It consists of about 230 different PRIs,

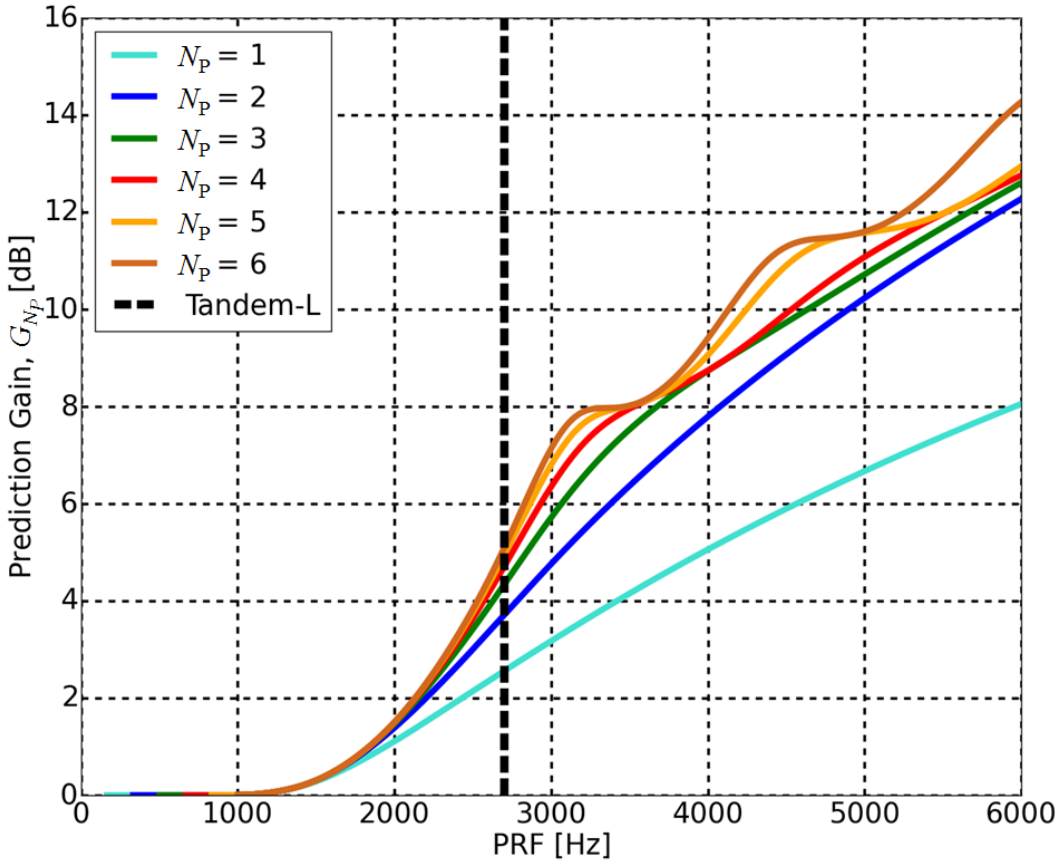

Figure 7.5: Theoretical prediction gain G_{N_P} for up to the 6th order as a function of the PRF for a Tandem-L-like system (see Table 7.2). The gains for a PRF of 2700 Hz are obtained in correspondence to the dashed black line.

which are cyclically repeated during the staggered SAR acquisition (the dashed horizontal red line indicates the mean PRI, which is about 0.37 ms). For the considered system, about 4% of the acquired raw data are affected by gaps [102]. Moreover, a 4-bit BAQ is up to now foreseen for the entire Tandem-L mission, which guarantees an interferometric coherence loss smaller than 1% [94], [71], hence minimizing the effects of quantization errors (the block size for BAQ is set to $N_{\text{block}} = 128$ range samples, which corresponds to a realistic block size implemented on board, e.g., the DLR satellites TerraSAR-X and TanDEM-X [94]). Based on the theoretical coding gains in Figure 7.5 for a mean PRF of 2700 Hz, a prediction order $N_P \leq 4$ is assumed in the following.

As performance measure, the signal-to-quantization noise ratio (SQNR) of the focused SAR image has been evaluated, according to the definition in (6.7). For this analysis, non-uniformly sampled raw data have been generated, which have then been compressed

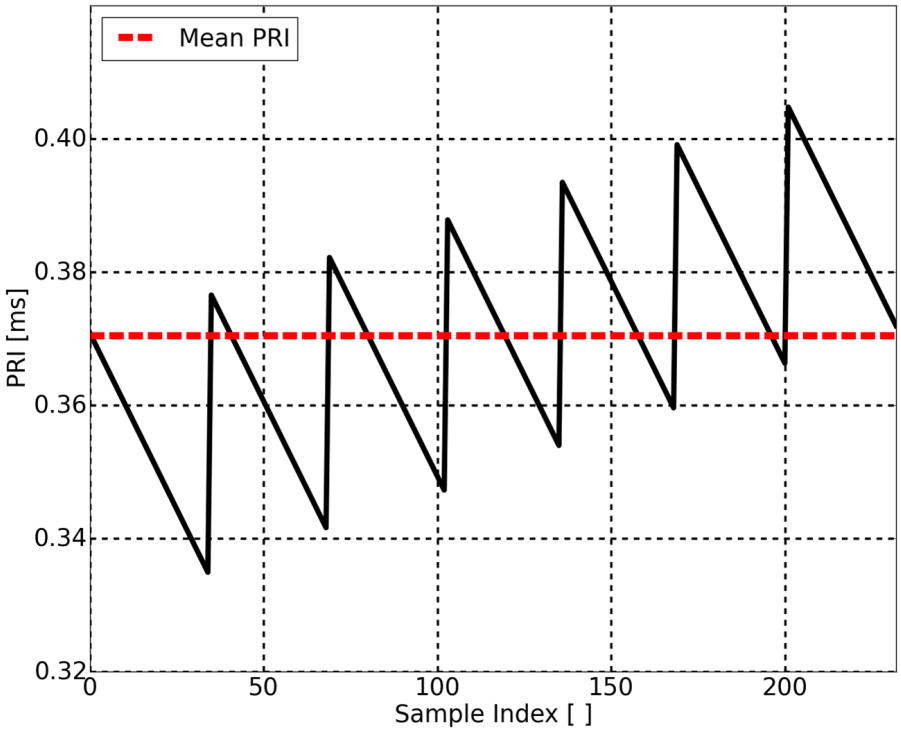

Figure 7.6: Example of a PRI-sequence employed for the present simulations, which is cyclically repeated during a staggered SAR acquisition [102]. The dashed red line indicates the mean PRI, which is of about 0.37 ms.

with the proposed DP-BAQ as well as with a standard BAQ for comparison; then, a Best Linear Unbiased (BLU) interpolation was applied to resample the non-uniform staggered SAR raw data on a uniform grid and, finally, SAR focusing was performed. By selecting the elaborated sequence of PRIs shown in Figure 7.6, one can impose that no more than one sample at a time is missed in the azimuth direction [41]. Figure 7.7 shows the SQNR obtained for a homogeneous target as a function of the average rate $\bar{N}_\mathrm{b}$ and for different quantization schemes. The performance of a BAQ with constant bit rate is taken as reference and is given in black; then, the SQNR for the proposed DP-BAQ for different prediction orders is depicted as follows: 1^{st} order in turquoise, 2^{nd} order in blue, 3^{rd} order in green, and 4^{th} order in red. No significant additional gain is observed for prediction orders $N_\mathrm{P} > 4$. Assuming now as target performance the one obtained with a 4-bit BAQ, the proposed DP-BAQ allows for an improvement of SQNR of up to around 5.5 dB. Alternatively, a 4^{th}-order DP-BAQ at 3 bits/sample approximately provides the same SQNR of a 4-bit BAQ (both around 22 dB), hence allowing for a data reduction of about 25%. Analogously, if a 3-bit BAQ is used as reference, about 2.25 bits/sample

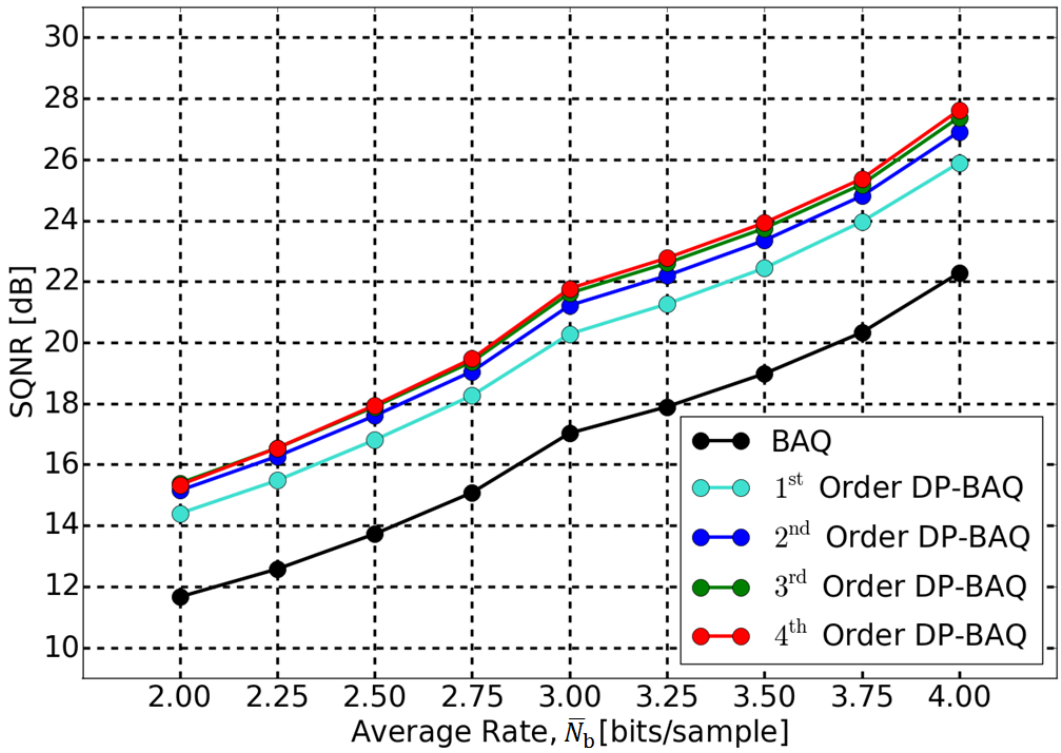

Figure 7.7: Signal-to-quantization noise ratio (SQNR) obtained from a homogeneous SAR scene as a function of the average rate $\bar{N}_b$, for a standard BAQ with constant bit rate (black), and for the proposed DP-BAQ (up to the 4^{th} order), with variable bit rate allocation and dynamic selection of the prediction order in the gap vicinity.

can be used for the proposed method, corresponding again to a data reduction of about 25%. When using lower compression rates, a poorer performance gain can be reasonably expected. This is due to the larger quantization noise affecting the raw data, which implies an additional loss in the azimuth correlation, hence resulting in a more "imprecise" prediction (i.e., a larger $\sigma^2_{\varepsilon,N_P}$ in (7.12)). It is worth highlighting that the estimates of data rate reduction provided above are derived assuming that, for the reference BAQ scenario (black curve), the missing raw data samples are treated as valid (gap-free) signals and are hence quantized with the corresponding number of bits (indicated on the x-axis of Figure 7.7). If one assumes, on the other hand, that the missing samples can be actually "cut" from the raw data matrix and not downlinked at all, the effective data rate to be considered as reference reduces by about 4% (which corresponds to the percentage of acquired raw data affected by gaps for the present staggered SAR system). This implies a slightly lower data reduction of about 22% for both, the 3-bit and 4-bit case.

If compared with the method proposed in [128], DP-BAQ results in a higher data rate, but allows for a simpler and cheaper onboard implementation. Indeed, the prediction process basically consists of a linear combination of $N_P \leq 4$ range lines, which can be performed in real time by using a single state-of-the-art FPGA. In addition to that, the proposed method preserves the non-uniformly sampled SAR raw data that may be used for a more advanced on-ground processing as in [141] and [147]. On the other hand, the data reduction technique in [128] typically requires the storage and processing of more than 15 range lines. For this, a larger number of new-generation FPGAs is required (due to their strong storage limitations), and the number of operations to be executed significantly increases, making the onboard real-time implementation a cost-driving challenge.

Looking at Figure 7.7, it can also be noticed that the SQNR values show, going from one integer rate to the next one, first a slow variation and then a steeper trend, which can be explained as follows: the fractional quantization rates shown in Figure 7.7 are implemented by toggling the bit rate selection of an integer-bit BAQ quantizer along azimuth and/or range, as proposed in [121], hence allowing for higher flexibility of compression without increasing the overall system complexity. For this, let us assume a target non-integer bit rate $N_{b,frac}$. According to [121], $N_{b,frac}$ can be "synthesized" by means of a sequence of integer rates of length N_{seq}, where the next smaller integer rate ($N_{b,inf} = \lfloor N_{b,frac} \rfloor$) occurs with a relative frequency $f_{inf} \in [0,1]$, and the next greater integer one ($N_{b,sup} = \lceil N_{b,frac} \rceil$) occurs with a relative frequency $1 - f_{inf}$. By applying the described rate sequence of length N_{seq} for the quantization of the SAR data, e.g., along azimuth, the expected $SQNR_{frac}$ associated to the resulting non-integer rate is expressed as

$$SQNR_{frac} = \frac{SQNR_{sup} \cdot SQNR_{inf}}{f_{inf} \cdot SQNR_{sup} + (1 - f_{inf}) \cdot SQNR_{inf}}, \tag{7.20}$$

being $SQNR_{inf}$ and $SQNR_{sup}$ the signal-to-quantization noise ratio associated to $N_{b,inf}$ and $N_{b,sup}$, respectively. As an example, the non-integer rate $N_{b,frac} = 3.25$ bits/sample can be implemented by employing a sequence of, e.g., $N_{seq} = 20$ bit rate values and selecting 15 times $N_{b,inf} = 3$ bits/sample (corresponding to a relative occurrence $f_{inf} = 0.75$) and the remaining 5 times $N_{b,sup} = 4$ bits/sample. The above equation is derived by simply weighting the noise power contributions associated to the integer rates according to the factor f_{inf}. Moreover, it explains the non-linear trend shown by the SQNR for fractional bit rates and has been verified by the simulation results in Figure 7.7. It is worth highlighting that possible variations in the image quality among neighboring pixels, resulting from the use of a variable bit rate along azimuth, are actually averaged after SAR processing, provided that the extension L_{seq} (in meters) of the azimuth sequence of length N_{seq}, used to synthesize the target fractional rate, is sufficiently smaller than the synthetic aperture L_s, i.e., $L_{seq} << L_s$ (indeed, L_s represents the azimuth distance within which the targets overlap their response in the raw data domain). These two

quantities are expressed as

$$L_{\text{seq}} = v_{\text{s}} \cdot \text{PRI} \cdot N_{\text{seq}}, \tag{7.21}$$

$$L_{\text{s}} = \lambda \frac{R_0}{L_{\text{a}}}. \tag{7.22}$$

For the aforementioned example of $N_{\text{b,frac}} = 3.25$ bits/sample, the corresponding sequence of length $N_{\text{seq}} = 20$ results in an azimuth extension of about 60 meters. In this case, L_{seq} is (more than) two orders of magnitude smaller than L_{s}, which, for the above listed parameters, is in the order of a few tens of kilometers. As a consequence, the variable quality in the raw data is completely "smoothed" after data focusing and hence not detectable in the resulting SAR and InSAR products, where, instead, a uniform performance loss is observed, as if an equivalent fractional bit rate $N_{\text{b,frac}}$ was used.

As it has been already pointed out, the main advantage of employing azimuth-switched quantization (ASQ) [121] is that it allows for a higher flexibility in terms of achievable compression rate and performance without increasing the onboard computational effort. Alternatively, native non-integer bit rates can be implemented by following a uniform quantizer with additional hardware/software blocks, such as an entropic (Huffman) coder. This solution achieves in general slightly better performance with respect to a traditional May-Lloyd non-uniform quantizer and constant length coding, such as BAQ [148], at the cost of an increased overall system complexity. However, as the length (i.e., the number of bits) of the encoded symbols is determined by the input signal statistics, the use of an entropic coder does not allow to exactly predict the data volume for a certain SAR acquisition (differently from ASQ, where indeed the data rate can be accurately calculated before the SAR survey), which causes additional complexity for the operation of SAR missions. A comparison between the two referred schemes will be subject of future research and investigations.

When considering the variable PRI shown in Figure 7.6, for the application of predictive coding in staggered SAR systems one should in principle take into account the time-variant autocorrelation properties of the non-uniform azimuth SAR raw signal. However, it could be verified that the performance of the predictor obtained by employing a set of weights derived for each one of the around 230 PRI intervals is practically the same as the one obtained by using, for all pulses, the weights derived from the mean PRI of about 0.37 ms (the difference in SQNR is less than 0.1 dB). This means that, once the antenna pattern, the PRI sequence and the prediction order are defined, the resulting weights β_i are constant values that can be derived before commanding, and then stored on board in registers and recalled by the predictor during the SAR data take.

The importance of exploiting the a priori knowledge about the gap locations in order to dynamically adapt the order of the prediction filter is shown in Figure 7.8, which depicts the SQNR estimated on the raw data for a homogeneous target as a function of the azimuth samples (the average over a large number of range samples is considered), and for different quantization schemes. In this example, two gaps are highlighted by

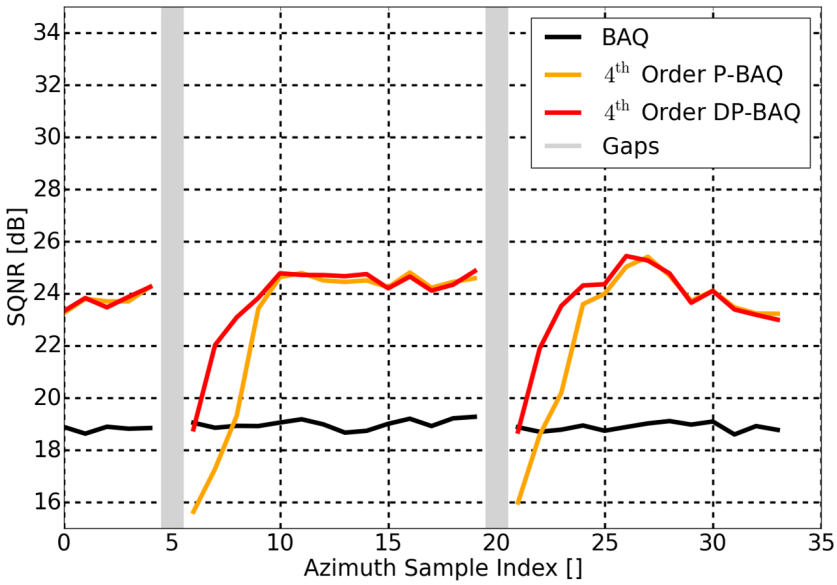

Figure 7.8: Signal-to-quantization noise ratio (SQNR) as a function of the azimuth samples (averaged along range), for different quantization schemes: standard BAQ (black), predictive BAQ with constant bit rate and fixed 4^{th}-order prediction (orange), and the proposed DP-BAQ with dynamic 4^{th}-order prediction and constant bit rate (red). Two gaps are highlighted by the vertical grey lines, and a significant improvement in performance of 3-4 dB can be observed with the proposed method right after the gap occurrence, which outperforms all other considered approaches.

the vertical grey lines. The performance of a standard BAQ is depicted in black and is obviously almost constant for all the samples, since the gaps do not have any impact on it. Then, the performance of a 4^{th}-order prediction (P-BAQ) with fixed predictor order and constant bit rate at 4 bits/sample is shown in orange, and a clear drop of performance is visible after each gap, as a consequence of the larger prediction error introduced by the missing sample. The prediction error gradually reduces (i.e., the SQNR increases) for the following samples, and the method reaches again its "regime" SQNR of about 24 dB after 5 samples, i.e., when the gap is not employed anymore by the prediction filter.

A significant gain of about 3-4 dB is observed if a dynamic prediction order is selected after the gap occurrence (in red), according to the proposed DP-BAQ. It is worth noting that, in this example, the bit rate has been kept constant in the gap vicinity, in order to better highlight the impact of the dynamic prediction order only on the final performance. Moreover, one can notice that the SQNR values observed in Figure 7.8 are different, and in particular smaller, than those shown in Figure 7.7. This is due to the fact that the

latter are calculated on the focused SAR scene, where a processed Doppler bandwidth $B_D = 1130$ Hz is applied, which is less than half of the PRF (being PRF $= 2700$ Hz). Such a low-pass filtering operation contributes to mitigate the effect of digitization errors, since it averages out high-frequency contributions in the focused data and alleviates also the occurrence of saturation effects, ultimately resulting in a better quantization performance (on the other hand, for the raw data the full Doppler bandwidth is used).

In addition, the proposed method has been evaluated for the simulated SAR backscatter profile σ^0 depicted in Figure 7.9 in brown, which shows a "jump" of 10 dB along the azimuth dimension. Such a large dynamic range typically occurs over highly inhomogeneous targets, such as, e.g., urban areas. The two graphs depict the SQNR as a function of the azimuth distance for different quantization schemes: Figure 7.9 (a) shows the BAQ (black) and P-BAQ (1^{st} order in turquoise, 4^{th} order in red) with fixed prediction order and with constant bit rate $\bar{N}_b = 4$ bits/sample; Figure 7.9 (b) depicts the BAQ (black) and the proposed DP-BAQ (1^{st} order in turquoise, 4^{th} order in red), all exploiting variable bit rate in the gap vicinity for $\bar{N}_b = 4$ bits/sample (see Table 7.1). Again, if a fixed prediction order is employed (Figure 7.9 (a)), the presence of gaps (for the considered staggered SAR system, about 4% of the acquired raw data is affected by gaps) degrades the reconstruction so much that a 4^{th}-order predictor performs worse than a 1^{st}-order one. On the other hand, the use of a dynamic prediction order (as for the DP-BAQ in Figure 7.9 (b)), together with a distributed bit rate allocation in the gap neighborhood, significantly improves the resulting performance, which can be exploited to reduce the resulting data rate. In particular, the increase in performance due to the optimized bit rate allocation around the gap (hence, disregarding the gain introduced by the predictive coding) can be noticed when comparing the two black curves depicted in Figure 7.9 (a) and Figure 7.9 (b). Indeed, these show the performance for a "pure" BAQ (i.e., where no prediction is applied), and about 1.5 dB SQNR improvement is observed when an optimized (variable) bit rate is applied around the gap (Figure 7.9 (b)), with respect to the case where a constant bit rate is used (Figure 7.9 (a)). A significant loss in SQNR is observed for all considered compression techniques over the area of low backscatter (with a mean backscatter of -10 dB) close to the high-backscatter one. Such a performance degradation is due to the masking effect caused by the presence of high-backscatter targets in close vicinity and "propagates" up to a distance comparable with the synthetic aperture L_s [94], [103]. Indeed, L_s is expressed in (7.22) and, for the considered system ($\lambda = 23.9$ cm, $L_a = 10$ m, and, for an elevation angle $\theta_e = 40^\circ$ considered in this simulation, $R_0 \approx 900$ km), it results that $L_s \approx 22$ km. This distance approximately corresponds to the extension up to which the SQNR profiles are affected from about 30 km to the first discontinuity at 50 km, and from the second discontinuity at 100 km to 120 km. The described effect strongly affects the reconstruction in the focused SAR image: as an example, in Figure 7.9 (a) the SQNR varies from 15-17.5 dB in the low-backscatter area up to about 25-27.5 dB in the high-backscatter one.

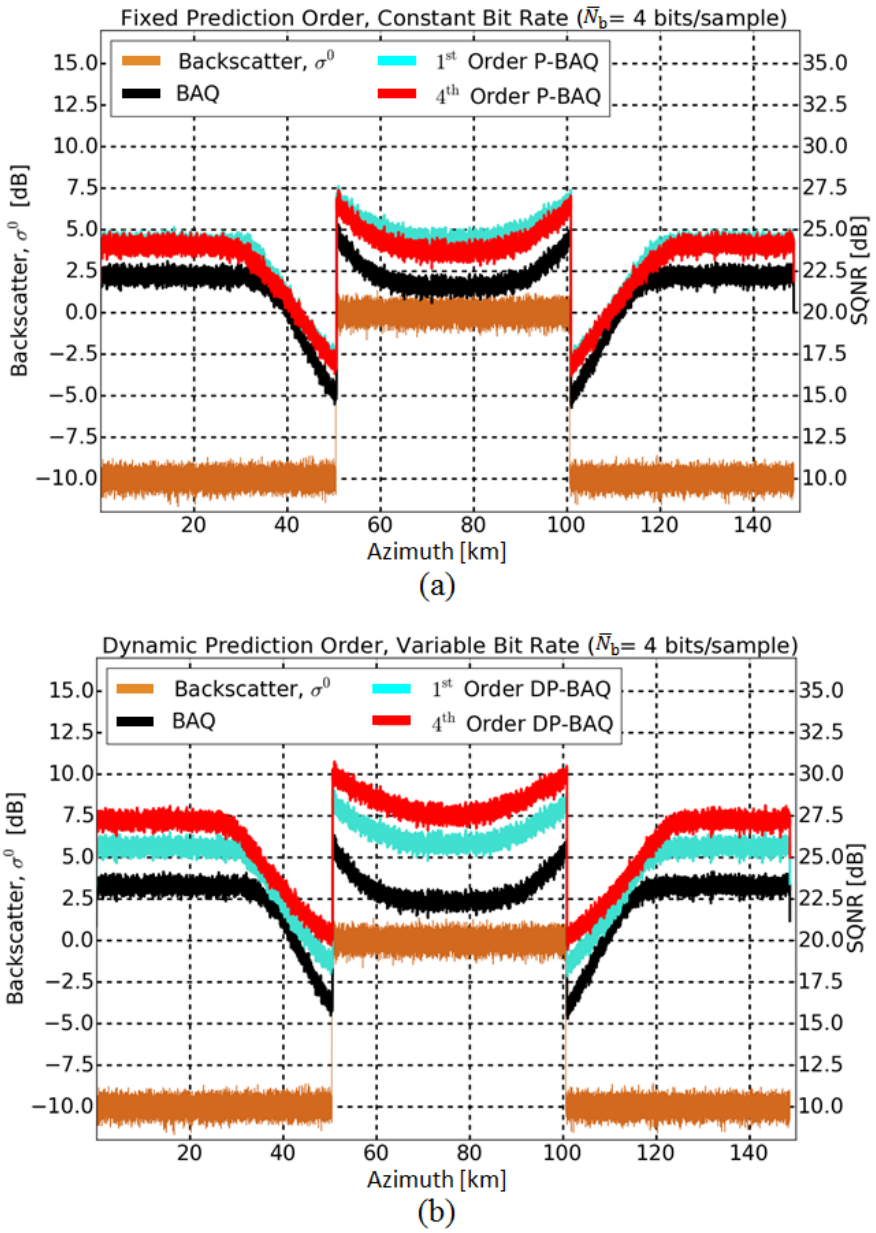

Figure 7.9: Backscatter profile (σ^0, in brown) and corresponding SQNR as a function of the azimuth distance for different quantization schemes: (a) BAQ (black) and P-BAQ with fixed prediction order (1st order in turquoise, 4th order in red) and constant bit rate; (b) BAQ (black) and the proposed DP-BAQ (1st order in turquoise, 4th order in red), by applying variable bit rate in the gap vicinity. The curves are derived for an average rate $\bar{N}_b$ of 4 bits/sample.

7.4 Chapter Summary

In this chapter, onboard data volume reduction in staggered SAR systems is addressed. Such systems require the acquisition of a large volume of data for the imaging of wide swath widths with fine azimuth resolution. Staggered SAR raw data samples exhibit a certain correlation in azimuth, which is introduced by the antenna pattern and a significant oversampling. The proposed method is based on the use of linear predictive coding, which aims at removing the data redundancy by means of an efficient encoding and quantization of the azimuth SAR raw samples. In particular, for the present investigations a causal predictor has been considered, i.e., only preceding samples are used in the prediction process. Dynamic predictive block-adaptive quantization (DP-BAQ) exploits the a priori knowledge of the position of the gaps occurring during the staggered SAR operation, by adaptively selecting the bit rate and the prediction order in the gap vicinity, in order to improve the resulting performance. Simulations for a Tandem-L-like L-band staggered SAR system have been conducted for different compression settings (in terms of quantization scheme, prediction order, and bit rate allocation strategy) and SAR backscatter distributions, showing that the proposed technique allows for a significant reduction of the data volume by requiring, at the same time, a modest processing effort for its onboard implementation. The proposed technique will be applied and verified on real staggered SAR data, similar to [140], as subject of further research and publications. Furthermore, the investigation of alternative prediction techniques, such as non-causal and/or non-linear prediction schemes, or the inclusion of polar quantization methods, will be another topic for possible studies and could be considered for the design of future SAR systems, where the combined use of even larger PRFs and/or oversampling factors will lead to a further improvement of the data reduction capacity.

8 Conclusions

The work presented in this thesis is the result of research activities conducted at the Microwaves and Radar Institute (HR) of DLR, Germany, from 2013 to 2019. Several aspects of onboard quantization for SAR systems have been analyzed and novel quantization algorithms have been developed. In this chapter, the overall research work is summarized, the main results are discussed, and an outlook for further investigations is provided.

8.1 Summary and Discussion

Thanks to its high-resolution, day-night, and weather-independent imaging capabilities, synthetic aperture radar (SAR) represents a powerful and well-recognized technique for a large number of remote sensing applications. For the design of present and next-generation spaceborne SAR missions, the implementation of innovative acquisition modes and system architectures allows for high-resolution imaging of a wide swath, together with the use of large bandwidths, high pulse repetition frequencies (PRFs), and multiple acquisition channels. Such an increased capability implies that a considerable volume of data needs to be acquired and transmitted to the ground, which poses more stringent demands on the onboard memory and downlink capacity. Therefore, a proper quantization of the SAR raw data is of utmost importance, as the compression rate applied for the digitization of the recorded radar signal, on the one hand, directly affects the quality of the resulting SAR products and, on the other hand, defines the volume of data to be stored and managed by the system, being a key aspect for the design of SAR missions.

In Chapter 1, the most important stages in the radar and SAR history, together with an overview of the civilian spaceborne SAR missions are summarized.

Chapter 2 provides a general overview of SAR remote sensing. Relevant system performance parameters are introduced, such as the resolution and sidelobes, which are derived from the impulse response function (IRF), together with the concepts of radar backscatter and speckle. The system sensitivity (NESZ), range/azimuth ambiguities, and nadir returns represent key performance measures to be considered for SAR system design. Furthermore, the basic concept of SAR interferometry (InSAR), the acquisition geometry, and the different operation modes are illustrated. InSAR quality parameters, such as the interferometric coherence, phase errors, and relative height accuracy of the resulting DEM are directly impacted by quantization errors, and are therefore recalled as well.

In Chapter 3, the fundamental background on quantization theory is provided, specifically applied to SAR data. Relevant parameters, which define the type of quantizer and its performance, are recalled, together with a description of the system and signal mod-

els and of the typical sources of quantization errors. The constraints for designing the optimum (Lloyd-Max) quantizer are detailed along with the definition of the quantizing theorem. An overview of the state-of-the-art quantization schemes for SAR systems is given, with particular focus on the widely used block-adaptive quantization (BAQ) [38], [39]. Low-amplitude quantization errors are described as well, which are introduced by the use of adaptive quantizers in SAR data and represent an additional significant error source specifically in presence of heterogeneous SAR backscatter distributions.

The novel contributions of the thesis begin in Chapter 4, where the effects of raw data quantization on TanDEM-X data are investigated in detail. Experimental data takes acquired with best quantization resolution (i.e., 8 bits/sample) are recompressed on ground to all available BAQ rates, hence providing multiple data sets per satellite stream. Key parameters in determining SAR and interferometric performance are evaluated over test areas showing different land cover types and topography characteristics. The effect of system and acquisition parameters which critically affect quantization errors, such as the standard deviation of the SAR backscatter σ_{σ^0}, the number of interferometric acquisitions N_{acq}, and the number of looks N_{l}, are taken into account as well.

As an example, the coherence loss due to quantization for, e.g., the 2-bit BAQ case ranges from 8% for flat and homogeneous areas, to 20% for irregular regions, such as urban areas. Based on the obtained results, a novel method is introduced, named performance-optimized block-adaptive quantization (PO-BAQ), which aims to optimize the required resource allocation and, at the same time, to control the interferometric performance degradation, by exploiting a priori knowledge about the SAR backscatter information. If combined with high-resolution and precise information of the Earth's topography and backscatter, which is by now provided by a variety of SAR sensors operating at different radar wavelengths, the proposed method may represent a helpful tool to adapt the data rate to the specific SAR application, depending on the associated requirements.

State-of-the-art compression schemes (such as the BAQ) are not able to grant a sufficient flexibility in terms of performance and resource allocation, since integer quantization rates only (e.g., 2, 3, or 4 bits/sample) are allowed. For this reason, fractional compression rates can be realized by including additional hardware (e.g., a Huffman coder) prior to the quantizer block [96], [97]. In Chapter 5, a novel compression method, named azimuth-switched quantization (ASQ) has been suggested, whereby non-integer rates are synthetized by properly toggling the integer BAQ rates along azimuth and/or range according to predefined sequences. The performance of the proposed ASQ is evaluated and assessed on SAR and interferometric TanDEM-X experimental data. ASQ enables highly flexible adaptation of SAR performance and resulting onboard data rate, hence providing an increased flexibility for the design and planning of SAR missions.

For conventional single-channel SAR systems, it is well known that the PRF poses contradictory constraints for the imaging of wide swaths and, at the same time, of fine azimuth resolutions. Indeed, the former dictates a low PRF to allow for a sufficient

temporal separation between subsequent SAR pulses, whereas the latter requires a large Doppler bandwidth and, therefore, high PRFs. Such inherent limitations can be overcome by using multiple receiving apertures, which are mutually displaced in the along-track direction. The coherent combination of the individual received signals allows for adequate azimuth ambiguity suppression and, in this way, high-resolution wide-swath imaging is achieved [40], [58]. Besides an increased system complexity, the drawback for such an improvement in swath coverage and resolution is represented by a significantly larger data volume to be acquired and transmitted to the ground, which poses stringent constraints on the onboard memory and downlink capacity. The novel approach proposed in Chapter 6 exploits the intrinsic correlation among the azimuth samples, and the multi-channel SAR data are decomposed by means of a non-adaptive orthogonal transformation (a simple discrete Fourier transform). Then, an optimized allocation of the quantization rates is applied to the transformed coefficients (for data digitization, a standard BAQ is considered), allowing for an increase of the resulting performance for a preselected data rate. Simulations are carried out for a single-platform C-band system with eight azimuth receive channels and show that, with the proposed method, a data volume reduction of about 20%-25% can be achieved for typical BAQ rates employed for SAR applications.

Finally, Chapter 7 addresses onboard data volume reduction in staggered SAR systems. Staggered SAR is an innovative SAR acquisition concept which exploits digital beamforming (DBF) in elevation to form multiple receive beams and continuous variation of the pulse repetition interval to achieve high-resolution imaging of a wide continuous swath. Staggered SAR is currently considered as the baseline acquisition mode for Tandem-L, a DLR proposal for a highly innovative L-band single-pass interferometric and fully polarimetric radar satellite mission to monitor dynamic processes on the Earth surface [37], [105]. The suggested method is based on the use of linear predictive coding, which exploits the correlation exhibited by the azimuth raw data samples, introduced, in turn, by the antenna pattern and by a significant oversampling required for the staggered SAR operation. According to this, a prediction of each sample is calculated on board as a linear combination of a set of previous samples. The resulting prediction error is then quantized and downlinked, which allows for a reduction of the signal entropy and, in turn, of the onboard data rate achievable for a given target performance. In addition, the a priori knowledge of the gap positions can be used to dynamically adapt the bit rate allocation and the prediction order to further improve the performance, as discussed in Section 7.2.3. Simulations for a Tandem-L-like L-band staggered SAR system are conducted for different compression settings, showing that the proposed technique allows for a significant reduction of the data volume of about 20%-25% by requiring, at the same time, a modest processing effort for its onboard implementation. Indeed, the required onboard processing consists of a linear filter typically of a few (around five) coefficients, such that the suggested algorithm can be performed in real time by using a single state-of-the-art FPGA.

8.2 Outlook

A detailed analysis of quantization effects in SAR data is presented in this work, together with the definition of novel compression methods aimed, on the one hand, to achieve a better flexibility in terms of quality and resulting onboard data rate, and, on the other hand, to reduce the volume of the required onboard data for a given performance. Further research developments can lead to improvements in the efficiency of the onboard quantization and of the potentials for data volume reduction for present and next-generation SAR systems, and are summarized in the following.

A description of the performance-optimized block-adaptive quantization (PO-BAQ) is given in Chapter 4. The proposed technique must be validated on real data, to verify that the degradation resulting from the raw data quantized according to the derived bit rate map (BRM) matches with the expected performance. In particular, it is necessary to understand the effective spatial "granularity" in terms of resource allocation achievable with the resulting BRM, since the bit rates used to quantize portions of the raw data matrix, which are close to each other, reciprocally influence the quality of the focused SAR images. In this context, a novel contribution will be represented by the use of innovative acquisition concepts such as cognitive radar [149]. These systems combine intelligent signal processing with an efficient feedback from the receiver to the transmitter, fostered by a continuous learning process through the interaction of the radar with the surrounding environment. This will allow for an efficient resource allocation during the SAR acquisition, such as, e.g., the optimized pointing of the antenna beam and transmit power, but also a dynamic adaptation of the employed sampling and compression rate towards the area of interest, as proposed in [150] for maritime surveillance applications.

In the framework of onboard data volume reduction for multi-channel SAR, it is of interest to investigate the potentials of different orthogonal transformations with respect to the considered discrete Fourier transform (DFT), such as the discrete cosine (DCT) or the principal component transform (PCT), together with the detailed analysis of different system configurations, in terms of, e.g., antenna patterns, number of azimuth channels, and required processed bandwidth and PRF. Moreover, the suggested MC-BAQ can be extended to multiple transmit pulses by combining transform coding in the Doppler domain with alternative compression schemes such as, e.g., vector quantization [92], in order to achieve a more effective data reduction. This approach could become of particular interest if a multi-channel ScanSAR system is considered, as in this case the azimuth time-variant impulse response, introduced by the burst operation, requires the illumination of a significantly wider Doppler bandwidth than required for the focusing of a single target. This means that a receive beam pointing at the edges of the Doppler spectrum suffers from a certain scan loss, which imposes the use of a higher azimuth sampling. Furthermore, similarly to the approach proposed in Chapter 7 in the context of staggered SAR systems, predictive quantization is identified as a promising approach to exploit the redundancy introduced by the large receive PRF for multi-channel SAR and

will be investigated as well. For this purpose, alternative techniques, such as, e.g., non-causal and/or non-linear prediction, or the inclusion of polar quantization schemes, will be subject of further studies to be included for the design of future SAR systems, where the combined use of larger PRFs and/or oversampling factors will lead to an additional improvement of the data reduction capacity.

In the last decades, the radar system technology has experienced significant advancements, which will very likely revolutionize radar system concepts [151]. Recent studies demonstrate that multi-static SAR missions will pave the way for unprecedented potentials in radar remote sensing [152]. In particular, in [153] the new MirrorSAR system concept is proposed, consisting of a fractionated SAR system where the scene illumination and the spatial sampling of the scattered radar signal is carried out by different platforms. The functionality of the receiver satellites is limited to a transponder-like routing of the received radar echoes to the active transmitter(s), hence significantly reducing the hardware and downlink requirements for an affordable implementation cost. The described system architecture can achieve very high resolution SAR imaging of ultra-wide swaths and allows, among other applications, for single-pass tomography for the three-dimensional imaging of volume scatterers, and for multi-baseline cross-track interferometric acquisitions for very high-resolution DEM generation and the monitoring of vector deformation [153], [154]. For such systems, the resulting huge amount of data, collected by the multiple independent apertures, represents a critical challenge. However, the simultaneous availability of all received signals on a centralized node can be exploited by applying, e.g., a proper onboard preprocessing to exploit the mutual redundancy which characterizes multi-static radar signals from close satellite formations. More specific, the described data correlation can be conveniently represented by means of an appropriate three-dimensional "information cube", where the three axes correspond to time, frequency, and direction of arrival of the recorded signals [155]. Thus, an efficient bit-allocation in the transformed space may be derived by applying the general concept of rate distortion analysis to the multi-channel SAR system [87], [156].

Currently, all the compression schemes employed for SAR systems are based on BAQ, which offers a good trade off between scheme complexity and achievable performance for a given compression rate. Looking at latest research trends towards big data and global satellite missions, it is of interest to investigate the capabilities offered by machine learning and deep learning approaches applied to SAR raw data for the development of more powerful and complex onboard quantization schemes. If taking into account the signal-dependent and highly nonlinear behaviour shown by quantization errors in SAR imaging, the potentials of convolutional neural networks (CNNs) for SAR image denoising will be further investigated, following the approaches proposed in [157], [158], [159]. Alternatively, the higher-level information for specific SAR applications can be selectively extracted on board and downloaded. This choice, on the one hand, requires a considerable processing effort and represents a non-reversible data reduction approach, but, on the other hand, it significantly ease the direct data distribution to the users.

Bibliography

[1] H. R. Hertz, "Über Sehr Schnelle Elektrische Schwingungen," *Annalen der Physik*, vol. 267, no. 7, pp. 421–448, 1887.

[2] J. C. Maxwell, "A Dynamical Theory of the Electromagnetic Field," *Philosophical Transaction of the Royal Society of London*, vol. 155, pp. 459–512, 1865.

[3] Hülsmeyer, C., "Hertzian-Wave Projecting and Receiving Apparatus Adapted to Indicate or Give Warning of the Presence of a Metallic Body, Such a Ship or a Train, in the Line of Projection of Such Waves," 22nd Sep. 1904, British Patent no. 13,170.

[4] C. Hülsmeyer, "The Telemobiloscope," *Electrical Magazine*, vol. 2, p. 388, 1904.

[5] A. W. Love, "In Memory of Carl A. Wiley," *IEEE Antennas and Propagation Society Newsletter*, vol. 27, pp. 17–18, Jun. 1985.

[6] F. Lee-Lueng and B. Holt, "Seasat Views Oceans and Sea Ice With Synthetic Aperture Radar," Publication 81-120, NASA, JPL, Feb. 1982.

[7] J. Cimino and C. Elachi, "Shuttle Imaging Radar-A (SIR-A) Experiment," Publication 8277, NASA, JPL, 1982.

[8] C. Elachi, "Shuttle Imaging Radar Experiment," *Science*, vol. 218, no. 4576, pp. 996–1003, 1982.

[9] J. Cimino, C. Elachi, and M. Settle, "SIR-B - The Second Shuttle Imaging Radar Experiment," *IEEE Transactions on Geoscience and Remote Sensing*, vol. GE-24, pp. 445–452, Jul. 1986.

[10] R. Francis and al., "The ERS-1 Spacecraft and its Payload," *ESA Bulletin*, pp. 27–48, Feb. 1991.

[11] R. Francis and al., "The ERS-2 Spacecraft and its Payload," *ESA Bulletin*, pp. 13–31, Aug. 1995.

[12] J. Louet, "The Envisat Mission and System," *ESA Bulletin*, pp. 10–25, Jun. 2001.

[13] P. Potin, B. Rosich, J. Roeder, and P. Bargellini, "Sentinel-1 Mission Operations Concept," in *Proceedings of the IEEE Geoscience and Remote Sensing Symposium (IGARSS)*, (Quebec City, Canada), pp. 1465–1468, Jul. 2014.

[14] A. Mamhood, "RADARSAT-1 Background Mission Monitoring of the Arctic," in *Proceedings of the IEEE Geoscience and Remote Sensing Symposium (IGARSS)*, vol. 1, (Seoul, South Korea), pp. 5–8, Jul. 2005.

[15] A. Hillman, P. Rolland, M. Chabot, R. Periard, P. Ledantec, and N. Martens, "RADARSAT-2 Mission Operations Status," in *Proceedings of the IEEE Geoscience and Remote Sensing Symposium (IGARSS)*, (Vancouver, Canada), pp. 3480–3484, Jul. 2011.

[16] A. Rosenqvist, M. Shimada, and M. Watanabe, "ALOS PALSAR: A Pathfinder Mission for Global-Scale Monitoring of the Environment," *IEEE Transactions on Geoscience and Remote Sensing*, vol. 45, pp. 3307–3316, Nov. 2007.

[17] Y. Okada, S. Nakamura, K. Iribe, Y. Yokota, M. Tsuji, K. Hariu, Y. Kankaku, S. Suzuki, Y. Osawa, and M. Shimada, "System Characteristics for Wide Swath L-Band SAR onboard ALOS-2/PALSAR-2," in *Proceedings of the Asia-Pacific Conference on Synthetic Aperture Radar (APSAR)*, (Tsukuba, Japan), pp. 141–143, Sep. 2013.

[18] "Shuttle Imaging Radar Mission Web Page," Apr. 2018. Available at `http://science.nasa.gov/missions/sir/`.

[19] M. Werner, "Shuttle Radar Topography Mission (SRTM): Mission Overview," *Journal of Telecommunications (Frequenz)*, vol. 55, pp. 75–79, Mar. 2001.

[20] F. Caltagirone, G. De Luca, F. Covello, G. Marano, G. Angino, and M. Piemontese, "Status, Results, Potentiality and Evolution of COSMO-SkyMed, the Italian Earth Observation Constellation for Risk Management and Security," in *Proceedings of the Geoscience and Remote Sensing Symposium (IGARSS)*, (Honolulu, USA), pp. 4393–4396, Jul. 2010.

[21] M. Chakraborty, S. Panigrahy, A. S. Rajawat, R. Kumar, T. V. R. Murthy, D. Haldar, A. Chakraborty, T. Kumar, S. Rode, H. Kumar, M. Mahapatra, and S. Kundu, "Initial Results Using RISAT-1 C-band SAR data," *Current Science*, vol. 104, pp. 490–501, Feb. 2013.

[22] Q. Wang, "Technical System Design and Construction of China's HJ-1 Satellites," *International Journal of Digital Earth*, vol. 5, pp. 202–216, May 2012.

[23] P. Davies, P. Whittaker, R. Bird, L. Gomes, B. Stern, M. Sweeting, M. Cohen, and D. Hall, "NovaSAR-Bringing Radar Capability to the Disaster Monitoring Constellation," in *Proc. AIAA/USU Small Satellites Conference*, (Logan, USA), pp. 1–12, Aug. 2012.

[24] S.-R. Lee, "Overview of KOMPSAT-5 Program, Mission, and System," in *Proceedings of the Geoscience and Remote Sensing Symposium (IGARSS)*, (Honolulu, USA), pp. 797–800, Jul. 2010.

[25] A. S. González, M. Labriola, J. C. Soteras, and J. S. Palma, "PAZ Instrument Design and Performance," in *Proceeding of the International Asia-Pacific Conference on Synthetic Aperture Radar (APSAR)*, (Seoul, South Korea), pp. 1–4, Nov. 2011.

[26] A. E. Giraldez, "SAOCOM-1 Argentina L-band SAR Mission Overview," in *Proceedings of the Coastal and Marine Applications of SAR Symposium*, (Svalbard, Norway), pp. 1–4, Sep. 2003.

[27] J. Mittermayer, M. Younis, R. Metzig, S. Wollstadt, J. Márquez, and A. Meta, "TerraSAR-X System Performance Characterization and Verification," *IEEE Transactions on Geoscience and Remote Sensing*, vol. 48, pp. 660–676, Feb. 2010.

[28] T. Kraus, B. Bräutigam, J. Mittermayer, U. Steinbrecher, C. Grigorov, and D. Schulze, "A Global Performance Assessment Approach for the TerraSAR-X Staring Spotlight and Wide ScanSAR Modes," in *Proceedings of the European Conference on Synthetic Aperture Radar (EUSAR)*, (Berlin, Germany), pp. 997–1000, Jun. 2014.

[29] J. Mittermayer, S. Wollstadt, P. Prats, R. Scheiber, and W. Koppe, "Staring Spotlight Imaging with TerraSAR-X," in *Proceedings of the Geoscience and Remote Sensing Symposium (IGARSS)*, (Munich, Germany), pp. 1606–1609, Jul. 2012.

[30] G. Krieger, A. Moreira, H. Fiedler, I. Hajnsek, M. Werner, M. Younis, and M. Zink, "TanDEM-X: A Satellite Formation for High-Resolution SAR Interferometry," *IEEE Transactions on Geoscience and Remote Sensing*, vol. 45, pp. 3317–3341, Nov. 2007.

[31] M. Bachmann, D. B. Tridon, M. Martone, F. Sica, S. Buckreuss, and M. Zink, "How to Update a Global DEM-Acquisition Concepts for TanDEM-X and Tandem-L," in *Proceedings of the European Conference on Synthetic Aperture Radar (EUSAR)*, (Aachen, Germany), pp. 1–5, Jun. 2018.

[32] M. Nannini, P. Prats-Iraola, F. De Zan, and D. Geudtner, "TOPS Time Series Performance Assessment with TerraSAR-X Data," *IEEE Journal of Selected Topics in Applied Earth Observations and Remote Sensing*, vol. 9, pp. 3832–3848, Aug. 2016.

[33] S. Martinis, J. Kersten, and A. Twele, "A Fully Automated TerraSAR-X Based Flood Service," *ISPRS Journal of Photogrammetry and Remote Sensing*, vol. 104, pp. 203–212, Jun. 2015.

[34] P. Milillo, E. Rignot, P. Rizzoli, B. Scheuchl, J. Mouginot, J. L. Bueso-Bello, and P. Prats-Iraola, "Heterogeneous Retreat and Ice Melt of Thwaites Glacier, West Antarctica," *Science Advances*, vol. 5, pp. 1–8, Jan. 2019.

[35] M. Martone, P. Rizzoli, C. Wecklich, C. González, J.-L. Bueso-Bello, P. Valdo, D. Schulze, M. Zink, G. Krieger, and A. Moreira, "The Global Forest/Non-Forest Map from TanDEM-X Interferometric SAR Data," *Remote Sensing of Environment*, vol. 205, pp. 352–373, Feb. 2018.

[36] G. Krieger, I. Hajnsek, K. Papathanassiou, M. Eineder, M. Younis, F. De Zan, P. Prats, S. Huber, M. Werner, H. Fiedler, A. Freeman, P. Rosen, S. Hensley, W. Johnson, L. Veilleux, B. Grafmueller, R. Werninghaus, R. Bamler, and A. Moreira, "The Tandem-L Mission Proposal: Monitoring Earth's Dynamics with High Resolution SAR Interferometry," in *Proceedings of the Radar Conference, IEEE*, (Pasadena, USA), pp. 1–6, May 2009.

[37] A. Moreira, G. Krieger, I. Hajnsek, K. Papathanassiou, M. Younis, P. Lopez-Dekker, S. Huber, M. Villano, M. Pardini, M. Eineder, F. De Zan, and A. Parizzi, "Tandem-L: A Highly Innovative Bistatic SAR Mission for Global Observation of Dynamic Processes on the Earth's Surface," *IEEE Geoscience and Remote Sensing Magazine*, vol. 3, pp. 8–23, Jul. 2015.

[38] D. Lancashire, B. Barnes, and S. Udall, "Block Adaptive Quantization," 3rd Jul. 2001, US Patent no. 6255987.

[39] R. Kwok and W. T. K. Johnson, "Block Adaptive Quantization of Magellan SAR Data," *IEEE Geoscience and Remote Sensing Letters*, vol. 27, pp. 375–383, Jul. 1989.

[40] G. Krieger, N. Gebert, and A. Moreira, "Unambiguous SAR Signal Reconstruction from Non-Uniform Displaced Phase Center Sampling," *IEEE Geoscience and Remote Sensing Letters*, vol. 1, pp. 260–264, Sep. 2004.

[41] M. Villano, G. Krieger, and A. Moreira, "Staggered SAR: High-Resolution Wide-Swath Imaging by Continuous PRI Variation," *IEEE Transactions on Geoscience and Remote Sensing*, vol. 52, pp. 4462–4479, Jul. 2014.

[42] J. C. Curlander and R. N. McDonough, *Synthetic Aperture Radar*. New York, USA: John Wiley & Sons, 1991.

[43] G. Franceschetti and R. Lanari, *Synthetic Aperture Radar Processing*. Boca Raton, USA: CRC Press, 1999.

[44] M. Soumekh, *Synthetic Aperture Radar Signal Processing*. New York, USA: John Wiley & Sons, 1999.

[45] I. Cumming and F. H. Wong, *Digital Processing of Synthetic Aperture Radar Data*. Norwood, USA: Artech House, 2005.

[46] A. Moreira, P. Prats-Iraola, M. Younis, G. Krieger, I. Hajnsek, and K. Papathanassiou, "A Tutorial on Synthetic Aperture Radar," *IEEE Geoscience and Remote Sensing Magazine*, vol. 1, pp. 6–43, Mar. 2013.

[47] J. Lee and E. Pottier, *Polarimetric Radar Imaging*. Boca Raton, USA: CRC Press, Taylor & Francis Group, 2009.

[48] C. Oliver and S. Quegan, *Understanding Synthtic Aperture Images*. Boston, USA: Artech House, 1998.

[49] A. Freeman, "SAR Calibration: An Overview," *IEEE Transactions on Geoscience and Remote Sensing*, vol. 30, pp. 1107–1121, Nov. 1992.

[50] M. Zink and R. Bamler, "X-SAR Radiometric Calibration and Data Quality," *IEEE Transactions on Geoscience and Remote Sensing*, vol. 33, pp. 840–847, Jul. 1995.

[51] F. De Zan and A. Monti Guarnieri, "TOPSAR: Terrain Observation by Progressive Scans," *IEEE Transactions on Geoscience and Remote Sensing*, vol. 44, pp. 2352–2360, Aug. 2006.

[52] R. Werninghaus and S. Buckreuss, "The TerraSAR-X Mission and System Design," *IEEE Transactions on Geoscience and Remote Sensing*, vol. 48, pp. 606–614, Feb. 2010.

[53] D. Miller and W. Pitz, "The TerraSAR-X Mission and System Design," *IEEE Transactions on Geoscience and Remote Sensing*, vol. 48, pp. 615–622, Feb. 2010.

[54] A. Currie and M. A. Brown, "Wide-Swath SAR," vol. 139, no. 2, pp. 122–135, 1992.

[55] G. D. Callaghan and I. D. Longstaff, "Wide Swath Spaceborne SAR Using a Quad Element Array," vol. 146, no. 3, pp. 159–165, 1999.

[56] M. Suess, B. Grafmüller, and R. Zahn, "A Novel High Resolution, Wideswath SAR System," in *Proceedings of the Geoscience and Remote Sensing Symposium (IGARSS)*, (Sydney, Australia), pp. 1013–1015, Jul. 2001.

[57] M. Younis, C. Fischer, and W. Wiesbeck, "Digital Beamforming in SAR Systems," *IEEE Transactions on Geoscience and Remote Sensing*, vol. 41, pp. 1735–1739, Jul. 2003.

[58] N. Gebert, G. Krieger, and A. Moreira, "Digital Beamforming on Receive: Techniques and Optimization Strategies for High-Resolution Wide-Swath SAR Imaging," *IEEE Transactions on Aerospace and Electronic Systems*, vol. 45, pp. 564–592, Apr. 2009.

[59] F. J. Harris, "On the Use of Windows for Harmonic Analysis with the Discrete Fourier Transform," *Processding of the IEEE*, vol. 66, no. 1.

[60] F. T. Ulaby and M. C. Dobson, *Handbook of Radar Scattering Statistics for Terrain*. Artech House, 1989.

[61] L. C. Graham, "Synthetic Interferometer Radar for Topographic Mapping," *Proceedings of the IEEE*, vol. 62, no. 6, pp. 763–768, 1974.

[62] D. Massonnet and K. L. Feigl, "Radar Interferometry and its Application to Changes in the Earth's Surface," *Reviews of geophysics*, vol. 36, no. 4, pp. 441–500, 1998.

[63] R. Bamler and P. Hartl, "Synthetic Aperture Radar Interferometry," *Inverse Problems*, vol. 14, pp. 1–54, Feb. 1998.

[64] P. A. Rosen, S. Hensley, I. R. Joughin, F. K. Li, S. N. Madsen, E. Rodriguez, and R. M. Goldstein, "Synthetic Aperture Radar Interferometry," *Proceedings of IEEE*, vol. 88, pp. 333–381, Mar. 2000.

[65] R. Goldstein, H. Zebcker, and C. Werner, "Satellite Radar Interferometry: Two-Dimensional Phase Unwrapping," *Radio Science*, vol. 23, pp. 713–720, Jul.-Aug. 1988.

[66] D. Ghiglia and L. Romero, "Robust Two-Dimensional Weighted and Unweighted Phase Unwrapping that Uses Fast Transforms and Iterative Methods," *Journal of the Optical Society of America*, vol. 11, pp. 107–117, Jan. 1994.

[67] M. Costantini, "A Novel Phase Unwrapping Method Based on Network Programming," *IEEE Transactions on Geoscience and Remote Sensing*, vol. 36, pp. 813–821, May 1998.

[68] C. Chen and H. Zebker, "Phase Unwrapping for Large SAR Interferograms: Statistical Segmentation and Generalized Network Models," *IEEE Transactions on Geoscience and Remote Sensing*, vol. 40, pp. 1709–1719, Nov. 2002.

[69] H. A. Zebker and J. Villasenor, "Decorrelation in Interferometric Radar Echoes," *IEEE Transactions on Geoscience and Remote Sensing*, vol. 30, pp. 950–959, Sep. 1992.

[70] R. Touzi, A. Lopes, J. Bruniquel, and P. W. Vachon, "Coherence Estimation for SAR Imagery," *IEEE Transactions on Geoscience and Remote Sensing*, vol. 37, pp. 135–149, Jan. 1999.

[71] M. Martone, B. Bräutigam, P. Rizzoli, C. González, M. Bachmann, and G. Krieger, "Coherence Evaluation of TanDEM-X Interferometric Data," *ISPRS Journal of Photogrammetry and Remote Sensing*, vol. 73, pp. 21–29, Sep. 2012.

[72] M. Martone, B. Bräutigam, and G. Krieger, "Decorrelation Effects in Bistatic TanDEM-X Data," in *Proceedings of the IEEE Geoscience and Remote Sensing Symposium (IGARSS)*, (Munich, Germany), pp. 5558–5561, Jul. 2012.

[73] M. Martone, B. Bräutigam, P. Rizzoli, and G. Krieger, "TanDEM-X Performance over Sandy Areas," in *Proceedings of the European Conference on Synthetic Aperture Radar (EUSAR)*, (Berlin, Germany), pp. 1009–1012, Jun. 2014.

[74] M. Martone, B. Bräutigam, P. Rizzoli, N. Yague-Martinez, and G. Krieger, "Enhancing Interferometric SAR Performance Over Sandy Areas: Experience From the TanDEM-X Mission," *IEEE Journal of Selected Topics in Applied Earth Observations and Remote Sensing*, vol. 9, pp. 1036–1046, Mar. 2016.

[75] M. Martone, P. Rizzoli, and G. Krieger, "Volume Decorrelation Effects in TanDEM-X Interferometric Data," *IEEE Geoscience and Remote Sensing Letters*, pp. 1812–1816, Dec. 2016.

[76] R. N. Treuhaft and P. R. Siqueira, "The Vertical Structure of Vegetated Land Surfaces from Interferometric and Polarimetric Radar," *Radio Science*, vol. 35, pp. 131–177, Jan. 2000.

[77] J. Praks, O. Antropov, and M. T. Hallikainen, "LIDAR-Aided SAR Interferometry Studies in Boreal Forest: Scattering Phase Center and Extinction Coefficient at X- and L-Band,"

[78] M. Martone, P. Rizzoli, B. Bräutigam, and G. Krieger, "A Method for Generating Forest/Non-Forest Maps from TanDEM-X Interferometric Data," in *Proceedings of the IEEE Geoscience and Remote Sensing Symposium (IGARSS)*, (Milan, Italy), pp. 2634–2637, Jul. 2015.

[79] P. Rizzoli, M. Martone, H. Rott, and A. Moreira, "Characterization of Snow Facies on the Greenland Ice Sheet Observed by TanDEM-X Interferometric SAR Data," *Remote Sensing*, vol. 9, Mar. 2017.

[80] J. S. Lee, K. W. Hoppel, S. A. Mango, and A. R. Millerand, "Intensity and Phase Statistics of Multilook Polarimetric and Interferometric SAR Imagery," *IEEE Transactions on Geoscience and Remote Sensing*, vol. 32, pp. 1017–1028, Sep. 1994.

[81] M. Abramowitz and I. Stegun, *Handbook of Mathematical Functions*. New York, USA: Dover, 1965.

[82] P. Rizzoli, B. Bräutigam, T. Kraus, M. Martone, and G. Krieger, "Relative Height Error Analysis of TanDEM-X Elevation Data," *ISPRS Journal of Photogrammetry and Remote Sensing*, vol. 73, pp. 30–38, Sep. 2012.

[83] A. Gruber, B. Wessel, M. Huber, and A. Roth, "Operational TanDEM-X DEM Calibration and First Validation Results," *ISPRS Journal of Photogrammetry and Remote Sensing*, vol. 73, pp. 39–49, Sep. 2012.

[84] A. Gersho and R. M. Gray, *Vector Quantization and Signal Compression*. Springer Science & Business Media, 2012.

[85] N. Jayant and P. Noll, *Digital Coding of Waveforms–Principles and Applications to Speech and Video*. New Jersey: Prentice-Hall, 1984.

[86] B. Widrow and I. Kollár, *Quantization Noise: Roundoff Error in Digital Computation, Signal Processing, Control, and Communications* . Cambridge, UK: Cambridge University Press, 2008.

[87] B. Widrow, I. Kollár, and M.-C. Liu, "Statistical Theory of Quantization," *IEEE Transactions on Instrumentation and Measurement*, vol. 45, no. 2, pp. 353–361, 1996.

[88] D. T. Sherwood, "Some Theorems on Quantization and an Example Using Dither," in *Asilomar Conference on Circuits, Systems and Computers*, (Pacific Grove, USA), pp. 207–212, Nov.

[89] S. P. Lipshitz, R. A. Wannamaker, and J. Vanderkooy, "Quantization and Dither: A Theoretical Qurvey," *Journal of the audio engineering society*, vol. 40, no. 5, pp. 355–375, 1992.

[90] R. M. Gray and T. G. Stockham, "Dithered Quantizers," *IEEE Transactions on Information Theory*, vol. 39, no. 3, pp. 805–812, 1993.

[91] J. Max, "Quantizing for Minimum Distortion," *IEEE Transactions on Information Theory*, vol. 6, no. 1, pp. 7–12, 1960.

[92] U. Benz, K. Strodl, and A. Moreira, "A Comparison of Several Algorithms for SAR Raw Data Compression," *IEEE Transactions on Geoscience and Remote Sensing*, vol. 33, pp. 1266–1276, Sep. 1995.

[93] M. Younis, J. Böer, C. Ortega-Míguez, D. Schulze, S. Huber, and J. Mittermayer, "Determining the Optimum Compromise Between SAR Data Compression and Radiometric Performance - An Approach Based on the Analysis of TerraSAR-X Data," in *Proceedings of the Geoscience and Remote Sensing Symposium (IGARSS)*, (Boston, USA), pp. 107–110, Jul. 2008.

[94] M. Martone, B. Bräutigam, and G. Krieger, "Quantization Effects in TanDEM-X Data," *IEEE Transactions on Geoscience and Remote Sensing*, vol. 53, pp. 583–597, Feb. 2015.

[95] C. P. Niebla and G. Krieger, "Optimization of Block-Adaptive Quantization for SAR Raw Data," *Space Technol.*, vol. 23, pp. 131–141, Jan. 2003.

[96] E. Attema, C. Cafforio, M. Gottwald, P. Guccione, A. M. Guarnieri, F. Rocca, and P. Snoeij, "Flexible Dynamic Block Adaptive Quantization for Sentinel-1 SAR Missions," *IEEE Geoscience and Remote Sensing Letters*, vol. 7, pp. 766–770, Oct. 2010.

[97] T. Algra, "Data Compression for Operational SAR Missions Using Entropy-Constrained Block Adaptive Quantization," in *Proceedings of the Geoscience and Remote Sensing Symposium (IGARSS)*, (Toronto, Canada), pp. 1135–1138, Jun. 2002.

[98] P. Guccione and A. M. Guarnieri, "A Space Adaptive Quantizer for Spaceborne SAR," *IEEE Transactions on Geoscience and Remote Sensing*, vol. 49, pp. 3564–3573, Oct. 2011.

[99] P. Guccione, M. Scagliola, and D. Giudici, "Principal Components Dynamic Block Quantization for Multichannel SAR," in *Proceedings of the Geoscience and Remote Sensing Symposium (IGARSS)*, (Bejing, China), pp. 2090–2093.

[100] M. Martone, M. Villano, M. Younis, and G. Krieger, "Efficient Onboard Quantization for Multi-Channel SAR Systems," *IEEE Geoscience and Remote Sensing Letters*, vol. 16, pp. 1859–1863, Dec. 2019.

[101] M. Martone, N. Gollin, M. Villano, P. Rizzoli, and G. Krieger, "Predictive Quantization for Data Volume Reduction in Staggered SAR Systems," *Submitted to IEEE Transactions on Geoscience and Remote Sensing*, 2019.

[102] M. Villano, *Staggered Synthetic Aperture Radar*. PhD thesis, Karlsruhe Institute of Technology, Wessling, Germany, 2016. DLR-Forschungsbericht 2016-16, ISSN 1434-8454.

[103] S. Huber, M. Younis, and G. Krieger, "The TanDEM-X Mission: Overview and Interferometric Performance," *Int. J. Microw. Wireless Technol.*, vol. 2, pp. 379–389, Jul. 2010.

[104] P. Rizzoli, M. Martone, C. González, C. Wecklich, B. Bräutigam, D. Borla Tridon, M. Bachmann, D. Schulze, T. Fritz, M. Huber, B. Wessel, G. Krieger, M. Zink, and A. Moreira, "Generation and Performance Assessment of the Global TanDEM-X Digital Elevation Model," *ISPRS Journal of Photogrammetry and Remote Sensing*, vol. 132, pp. 119–139, Oct. 2017.

[105] A. Moreira, G. Krieger, M. Younis, I. Hajnsek, K. Papathanassiou, M. Eineder, and F. De Zan, "Tandem-L: A Mission Proposal for Monitoring Dynamic Earth Processes," in *Proceedings of the Geoscience and Remote Sensing Symposium (IGARSS)*, (Vancouver, Canada), pp. 1385–1388, Jul. 2011.

[106] M. Zink, G. Krieger, H. Fiedler, I. Hajnsek, and A. Moreira, "The TanDEM-X Mission Concept," in *Proceedings of the European Conference on Synthetic Aperture Radar (EUSAR)*, (Friedrichshafen, Germany), pp. 1–4, Jun. 2008.

[107] E. Rodriguez, C. S. Morris, and J. E. Belz, "A Global Assessment of the SRTM Performance," *Photogrammetric Engineering and Remote Sensing*, vol. 72, pp. 249–260, Mar. 2006.

[108] EOC - TanDEM-X Ground Segment, "DEM Products Specification Document." `http://tandemx-science.dlr.de/pdfs/TD-GS-PS-0021_DEM-Product-Specification_v1.7.pdf`. Online accessed February 1st 2012.

[109] M. Martone, P. Rizzoli, B. Bräutigam, and G. Krieger, "First Two Years of TanDEM-X Mission: Interferometric Performance Overview," *Radio Science*, vol. 48, pp. 617–627, Sep. 2013.

[110] M. Lachaise, T. Fritz, and R. Bamler, "The Dual-Baseline Phase Unwrapping Correction Framework for the TanDEM-X Mission Part 1: Theoretical Description and Algorithms," *IEEE Transactions on Geoscience and Remote Sensing*, vol. 56, pp. 780–798, Feb. 2018.

[111] T. Fritz, C. Rossi, N. Yague-Martinez, F. Rodriguez-González, M. Lachaise, and H. Breit, "Interferometric Processing of TanDEM-X Data," in *Proceedings of*

the IEEE Geoscience and Remote Sensing Symposium (IGARSS), (Vancouver, Canada), pp. 2428–2431, Jul. 2011.

[112] T. Kraus, D. Schrank, P. Rizzoli, and B. Bräutigam, "In-Orbit SAR performance of TerraSAR-X and TanDEM-X satellites," in *Proceedings of the URSI Commission-F Triennial Open Symposium on Radio Wave Propagation and Remote Sensing*, (Garmisch-Partenkirchen, Germany), pp. 1–6, Mar. 2011.

[113] M. Schwerdt, J. H. González, M. Bachmann, and D. Schrank, "Monostatic calibration of both TanDEM-X satellites," in *Proceedings of the Geoscience and Remote Sensing Symposium (IGARSS)*, (Honolulu, Hawaii), pp. 2636–2639, July 2010.

[114] P. Prats, M. Rodriguez-Cassola, L. Marotti, M. Nannini, S. Wollstadt, D. Schulze, N. Tous-Ramon, M. Younis, G. Krieger, and A. Reigber, "TAXI: a Versatile Processing Chain for Experimental TanDEM-X Product Evaluation," in *Proceedings of the Geoscience and Remote Sensing Symposium (IGARSS)*, (Honolulu, USA), pp. 4059–4062, Jul. 2010.

[115] J. H. González, J. W. Anthony, M. Bachmann, G. Krieger, M. Schwerdt, and M. Zink, "Tests of the TanDEM-X DEM Calibration Performance," in *Proceedings of the Geoscience and Remote Sensing Symposium (IGARSS)*, (Munich, Germany), pp. 303–306, July 2012.

[116] B. Bräutigam, P. Rizzoli, M. Martone, M. Bachmann, D. Schulze, G. Krieger, and M. Zink, "TanDEM-X Acquisition and Quality Overview with Two Global Coverages," in *Proceedings of the Geoscience and Remote Sensing Symposium (IGARSS)*, (Melbourne, Australia), pp. 2958–2961, July 2013.

[117] D. Borla Tridon, M. Bachmann, D. Schulze, C. Ortega-Miguez, M. Polimeni, M. Martone, J. Böer, and M. Zink, "TanDEM-X: DEM Acquisition in the Third Year," *International Journal of Space Science and Engineering*, vol. 1, no. 4, pp. 367–381, 2013.

[118] C. Ortega-Míguez, D. Schulze, M. Polimeni, J. Böer, P. Rizzoli, and M. Bachmann, "TanDEM-X Acquisition Planner," in *Proceedings of the European Conference on Synthetic Aperture Radar (EUSAR)*, (Nuremberg, Germany), pp. 418–421, April 2012.

[119] D. Borla Tridon, M. Bachmann, D. Schulze, M. Polimeni, M. Martone, J. Böer, and M. Zink, "TanDEM-X DEM Difficult Terrain and Antarctica Acquisitions towards the Planning of the Science Phase," in *Proceedings of the European Conference on Synthetic Aperture Radar (EUSAR)*, (Berlin, Germany), pp. 1133–1136, Jun. 2014.

[120] G. Krieger, M. Zink, M. Bachmann, B. Bräutigam, D. Schulze, M. Martone, P. Rizzoli, U. Steinbrecher, J. W. Antony, F. De Zan, I. Hajnsek, K. Papathanassiou, F. Kugler, M. Rodriguez Cassola, M. Younis, S. Baumgartner, P. López-Dekker, P. Prats, and A. Moreira, "TanDEM-X: A radar interferometer with two formation-flying satellites," *Acta Astronautica*, vol. 89, pp. 83–98, Aug.-Sep. 2013.

[121] M. Martone, B. Bräutigam, and G. Krieger, "Azimuth-Switched Quantization for SAR Systems and Performance Analysis on TanDEM-X Data," *IEEE Geoscience and Remote Sensing Letters*, vol. 11, pp. 181–185, Jan. 2014.

[122] P. Rizzoli, B. Bräutigam, S. Wollstadt, and J. Mittermayer, "Radar Backscatter Mapping Using TerraSAR-X," *IEEE Transactions on Geoscience and Remote Sensing*, vol. 49, pp. 3538–3547, Oct. 2011.

[123] P. Rizzoli and B. Bräutigam, "Radar Backscatter Characterization Approach Combining Global TanDEM-X Data," in *Proceedings of the IEEE Geoscience and Remote Sensing Symposium (IGARSS)*, (Munich, Germany), pp. 3305–3308, July 2012.

[124] C. González, B. Bräutigam, and P. Rizzoli, "SAR Performance Enhancements Using Radar Backscatter Map of TerraSAR-X," in *Proceedings of the European Conference on Synthetic Aperture Radar (EUSAR)*, (Nuremberg, Germany), pp. 446–449, April 2012.

[125] M. Martone, G. Krieger, and B. Bräutigam, "Verfahren und Vorrichtung zur rechnergestützten Verarbeitung von SAR-Rohdaten," 2nd Jun. 2016, DE Patent no. 102012209113B4.

[126] M. Martone, C. González, J. L. Bueso-Bello, and B. Bräutigam, "Bandwidth Considerations for Interferometric Applications Based on TanDEM-X," *IEEE Geoscience and Remote Sensing Letters*, vol. 14, no. 2, pp. 203–207, 2017.

[127] M. Martone, M. Villano, M. Younis, and G. Krieger, "An Efficient Onboard Quantization Strategy for Multi-Channel SAR Systems," in *Proceedings of the European Conference on Synthetic Aperture Radar (EUSAR)*, (Aachen, Germany), pp. 1–6, Jun. 2018.

[128] M. Villano, G. Krieger, and A. Moreira, "Onboard Processing for Data Volume Reduction in High-Resolution Wide-Swath SAR," *IEEE Geoscience and Remote Sensing Letters*, vol. 13, pp. 1173–1177, Aug. 2016.

[129] D. Cerutti-Maori, I. Sikaneta, J. Klare, and C. H. Gierull, "MIMO SAR Processing for Multichannel High-Resolution Wide-Swath Radars," *IEEE Transactions on Geoscience and Remote Sensing*, vol. 52, pp. 5034–5055, Aug. 2014.

[130] F. Q. de Almeida, M. Younis, G. Krieger, and A. Moreira, "Multichannel Staggered SAR Azimuth Processing," *IEEE Transactions on Geoscience and Remote Sensing*, vol. 56, pp. 2772–2788, Feb. 2015.

[131] S. Barbarossa, "Detection and Imaging of Moving Objects with Synthetic Aperture Radar. Part 1. Optimal Detection and Parameter Estimation Theory," *IEE Proceedings F - Radar Signal Processing*, vol. 139, pp. 79–88, Jan. 1992.

[132] M. Villano, G. Krieger, and A. Moreira, "Advanced Spaceborne SAR Systems with Planar Antenna," in *IEEE Radar Conference*, (Seattle, USA), pp. 152–156, May 2017.

[133] N. Gollin, "Predictive Quantization for Staggered Synthetic Aperture Radar Systems," Master's thesis, Università degli Studi di Trento, Wessling, Germany, 2018.

[134] N. Gollin, M. Martone, M. Villano, P. Rizzoli, and G. Krieger, "Predictive Quantization for Staggered Synthetic Aperture Radar," in *German Microwave Conference (GeMiC)*, pp. 83–86, Mar. 2019.

[135] G. Krieger, N. Gebert, M. Younis, and A. Moreira, "Advanced Synthetic Aperture Radar Based on Digital Beamforming and Waveform Diversity," in *Proc. IEEE Radar Conf.*, (Rome, Italy), pp. 767–772, May 2008.

[136] A. Freeman, G. Krieger, P. Rosen, M. Younis, W. Johnson, S. Huber, R. Jordan, and A. Moreira, "SweepSAR: Beam-Forming on Receive Using a Reflector-Phased Array Feed Combination for Spaceborne SAR," in *Proc. IEEE Radar Conf.*, (Pasadena, USA), pp. 1–9, May 2009.

[137] B. Grafmüller and C. Schaefer, "High-Resolution Synthetic Aperture Radar Device and Antenna for One Such Radar," 22nd Dec. 2005, US 8013778 no. 8013778 B2.

[138] G. Krieger, N. Gebert, M. Younis, F. Bordoni, A. Patyuchenko, and A. Moreira, "Advanced Concepts for Ultra-Wide-Swath SAR Imaging," in *Proceedings of the European Conference on Synthetic Aperture Radar (EUSAR)*, (Friedrichshafen, Germany), pp. 1–4, Jun. 2008.

[139] M. Villano, G. Krieger, and A. Moreira, "A Novel Processing Strategy for Staggered SAR," *IEEE Geoscience and Remote Sensing Letters*, vol. 11, pp. 1891–1895, Nov. 2014.

[140] M. Villano, G. Krieger, M. Jäger, and A. Moreira, "Staggered SAR: Performance Analysis and Experiments with Real Data," *IEEE Transactions on Geoscience and Remote Sensing*, vol. 55, pp. 6617–6638, Nov. 2017.

[141] M. Pinheiro, P. Prats-Iraola, M. Rodriguez-Cassola, and M. Villano, "Combining Spectral Estimation and BLU Interpolation for the Reconstruction of Low-Oversampled Staggered SAR Data," in *Proceedings of the European Conference on Synthetic Aperture Radar (EUSAR)*, (Aachen, Germany), pp. 1–6, Jun. 2018.

[142] E. Magli and G. Olmo, "Lossy Predictive Coding of SAR Raw Data," *IEEE Transactions on Geoscience and Remote Sensing*, vol. 41, pp. 977–987, May 2003.

[143] T. Ikuma, M. Naraghi-Pour, and T. Lewis, "Predictive Quantization of Range-Focused SAR Raw Data," *IEEE Transactions on Geoscience and Remote Sensing*, vol. 50, pp. 1340–1348, Apr. 2012.

[144] I. H. McLeod, I. G. Cumming, and M. S. Seymour, "ENVISAT ASAR data reduction: impact on SAR interferometry," *IEEE Transactions on Geoscience and Remote Sensing*, vol. 36, pp. 589–602, March 1998.

[145] G. Schreier, *SAR Geocoding: Data and Systems*. Wichmann, 1993.

[146] R. M. Narayanan, D. W. Doerr, and D. C. Rundquist, "Temporal Decorrelation of X-Band Backscatter from Wind-Influenced Vegetation," *IEEE Transactions on Aerospace and Electronic Systems*, vol. 28, pp. 404–412, April 1992.

[147] G. Krieger, S. Huber, M. Villano, M. Younis, T. Rommel, P. Lopez-Dekker, F. Q. de Almeida, and A. Moreira, "CEBRAS: Cross Elevation Beam Range Ambiguity Suppression for High-Resolution Wide-Swath and MIMO-SAR Imaging," in *Proceedings of the Geoscience and Remote Sensing Symposium (IGARSS)*, (Milan, Italy), pp. 196–199, Jul. 2015.

[148] A. Gersho, "Principles of Quantization," *IEEE Transactions on Circuits and Systems*, vol. 25, pp. 427–436, July 1978.

[149] S. Haykin, "Cognitive Radar: A Way of the Future," *IEEE Signal Processing Magazine*, vol. 23, pp. 30–40, Feb. 2006.

[150] G. Di Martino and A. Iodice, "Coprime Synthetic Aperture Radar (CopSAR): A New Acquisition Mode for Maritime Surveillance," *IEEE Transactions on Geoscience and Remote Sensing*, vol. 53, pp. 3110–3123, Jun. 2015.

[151] W. Wiesbeck, L. Sit, M. Younis, T. Rommel, G. Krieger, and A. Moreira, "Radar 2020: The Future of Radar Systems," in *Proceedings of the Geoscience and Remote Sensing Symposium (IGARSS)*, (Milan, Italy), pp. 188–191, Jul. 2015.

[152] G. Krieger and A. Moreira, "Multistatic SAR Satellite Formations: Potentials and Challenges," in *Proceedings of the Geoscience and Remote Sensing Symposium (IGARSS)*, (Seoul, South Korea), pp. 2680–2684, July 2005.

[153] G. Krieger, M. Zonno, J. Mittermayer, A. Moreira, S. Huber, and M. Rodriguez-Cassola, "MirrorSAR: A Fractionated Space Transponder Concept for the Implementation of Low-Cost Multistatic SAR Missions," in *Proceedings of the European Conference on Synthetic Aperture Radar (EUSAR)*, (Aachen, Germany), pp. 1359–1364, Jun. 2018.

[154] M. Zonno, G. Krieger, M. Rodriguez-Cassola, J. Mittermayer, and A. Moreira, "A MirrorSAR-Based Single-Pass Dual-Baseline SAR Interferometer for the Generation of Very High Quality DEMs," in *Proceedings of the European Conference on Synthetic Aperture Radar (EUSAR)*, (Aachen, Germany), pp. 1256–1261, Jun. 2018.

[155] G. Krieger, "MIMO-SAR: Opportunities and Pitfalls," *IEEE Transactions on Geoscience and Remote Sensing*, vol. 52, pp. 2628–2645, May. 2014.

[156] T. Berger, *Rate Distortion Theory: A Mathematical Basis for Data Compression*. Englewood Cliffs, USA: Prentice Hall, 1971.

[157] V. Jain and S. Seung, "Natural Image Denoising with Convolutional Networks," in *Advances in Neural Information Processing Systems*, (Vancouver, Canada), pp. 769–776, Dec. 2008.

[158] G. Chierchia, D. Cozzolino, G. Poggi, and L. Verdoliva, "SAR Image Despeckling through Convolutional Neural Networks," in *Proceedings of the Geoscience and Remote Sensing Symposium (IGARSS)*, (Fort Worth, USA), pp. 5438–5441, Jul. 2017.

[159] P. Wang, H. Zhang, and V. Patel, "SAR Image Despeckling Using a Convolutional Neural Network," *IEEE Signal Processing Letters*, vol. 24, pp. 1763–1767, Dec. 2017.